Core-Shell Upconversion Nanoparticles

—

Investigation of Dopant Intermixing and Surface Modification

Philipp U. Bastian

Doctoral thesis (cumulative)
in fulfillment of the requirements for the degree

"doctor rerum naturalium"
(Dr. rer. nat.)
in the scientific discipline "Physical Chemistry"

submitted to the

Faculty of Science
Institute of Chemistry
of the University of Potsdam

Potsdam, Mai 2022

Acknowledgement

This page contains personal data and has been removed from the work.

The respective people know I gratefully thank them.

This work presents my research as Ph.D. student at the University of Potsdam (Institute of Chemistry) in the research group Physical Chemistry of Prof. Dr. H.-G. Löhmannsröben (i.R.) and apl. Prof. Dr. M. U. Kumke, as well as JProf. H. Müller-Werkmeister, from March 2016 to December 2021.

1 st *Supervisor* Apl. Prof. Dr. M. U. Kumke*
2 nd *Supervisor* Prof. Dr. R. Haag†

**University of Potsdam, Institute of Chemistry, Physical Chemistry*
†*Freie Universität Berlin, Institute of Chemistry and Biochemistry, Organic Chemistry*

Published online on the
Publication Server of the University of Potsdam:
https://doi.org/10.25932/publishup-55160
https://nbn-resolving.org/urn:nbn:de:kobv:517-opus4-551607

Contents

Abstract

Frequency upconversion nanoparticles (UCNPs) are inorganic nanocrystals capable to up-convert incident photons of the near-infrared electromagnetic spectrum (NIR) into higher energy photons. These photons are re-emitted in the range of the visible (Vis) and even ultraviolet (UV) light. The frequency upconversion process (UC) is realized with nanocrystals doped with trivalent lanthanoid ions (Ln(III)). The Ln(III) ions provide the electronic (excited) states forming a ladder-like electronic structure for the Ln(III) electrons in the nanocrystals. The absorption of at least two low energy photons by the nanoparticle and the subsequent energy transfer to one Ln(III) ion leads to the promotion of one Ln(III) electron into higher excited electronic states. One high energy photon will be emitted during the radiative relaxation of the electron in the excited state back into the electronic ground state of the Ln(III) ion. The excited state electron is the result of the previous absorption of at least two low energy photons.

The UC process is very interesting in the biological/medical context. Biological samples (like organic tissue, blood, urine, and stool) absorb high-energy photons (UV and blue light) more strongly than low-energy photons (red and NIR light). Thanks to a naturally occurring optical window, NIR light can penetrate deeper than UV light into biological samples. Hence, UCNPs in bio-samples can be excited by NIR light. This possibility opens a pathway for in vitro as well as in vivo applications, like optical imaging by cell labeling or staining of specific organic tissue. Furthermore, early detection and diagnosis of diseases by predictive and diagnostic biomarkers can be realized with bio-recognition elements being labeled to the UCNPs. Additionally, "theranostic" becomes possible, in which the identification and the treatment of a disease are tackled simultaneously.

For this to succeed, certain parameters for the UCNPs must be met: high upconversion efficiency, high photoluminescence quantum yield, dispersibility, and dispersion stability in aqueous media, as well as availability of functional groups to introduce fast and easy bio-recognition elements.

The UCNPs used in this work were prepared with a solvothermal decomposition synthesis yielding in particles with $NaYF_4$ or $NaGdF_4$ as host lattice. They have been doped with the Ln(III) ions Yb^{3+} and Er^{3+}, which is only one possible upconversion pair. Their upconversion efficiency and photoluminescence quantum yield were improved by adding a passivating shell to reduce surface quenching.

However, the brightness of core-shell UCNPs stays behind the expectations compared

to their bulk material (being at least μm-sized particles). The core-shell structures are not clearly separated from each other, which is a topic in literature. Instead, there is a transition layer between the core and the shell structure, which relates to the migration of the dopants within the host lattice during the synthesis. The ion migration has been examined by time-resolved laser spectroscopy and the interlanthanoid resonance energy transfer (LRET) in the two different host lattices from above. The results are presented in two publications, which dealt with core-shell-shell structured nanoparticles. The core is doped with the LRET-acceptor (either Nd^{3+} or Pr^{3+}). The intermediate shell serves as an insulation shell of pure host lattice material, whose shell thickness has been varied within one set of samples having the same composition, so that the spatial separation of LRET-acceptor and -donor changes. The outer shell with the same host lattice is doped with the LRET-donor (Eu^{3+}). The effect of the increasing insulation shell thickness is significant, although the LRET cannot be suppressed completely.

Next to the Ln(III) migration within a host lattice, various phase transfer reactions were investigated in order to subsequently perform surface modifications for bio-applications. One result out of this research has been published using a promising ligand, that equips the UCNP with bio-modifiable groups and has good potential for bio-medical applications. This particular ligand mimics natural occurring mechanisms of mussel protein adhesion and of blood coagulation, which is why the UCNPs are encapsulated very effectively. At the same time, bio-functional groups are introduced. In a proof-of-concept, the encapsulated UCNP has been coupled successfully with a dye (which is representative for a biomarker) and the system's photoluminescence properties have been investigated.

Zusammenfassung

Frequenzaufkonvertierende Nanopartikel (UCNP) sind anorganische Nanokristalle, die in der Lage sind, einfallende Photonen des nah-infraroten elektromagnetischen Spektrums (NIR) in höher energetische Photonen im Bereich des sichtbaren Lichtes (Vis) und sogar des ultravioletten Lichtes (UV) umzuwandeln und wieder emittieren zu können. Dieser Frequenzaufkonversionsprozess (UC) basiert auf Nanokristallen, die mit dreiwertigen Lanthanoid-Ionen (Ln(III)) dotiert sind. Somit stehen die elektronisch (angeregten) Zustände der Ln(III)-Ionen zur Verfügung, mit deren Hilfe Elektronen über eine leiterartige elektronische Struktur der elektronisch angeregten Zustände der Ln(III)-Ionen in höher angeregte Zustände gelangen können. Dabei müssen zuvor mindestens zwei niederenergetische Photonen vom Nanopartikel absorbiert werden. Weiterhin muss die absorbierte Energie über einen oder mehrere Energieübertragungen das gleiche Ln(III)-Ion erreichen. Beim strahlenden Relaxieren des Elektrones im angeregten Zustand zurück in den elektronischen Grundzustand des Ln(III)-Ions wird ein höherenergetisches Photon emittiert. Das Elektron im angeregten Zustand resultiert aus der vorhergehenden Absorption von mindestens zwei niederenergetischen Photonen.

Der Frequenzaufkonversionsprozess ist sehr interessant für die Anwendung im biologischen/medizinischen Bereich. Biologische Proben (z.B. organisches Gewebe, Blut, Urin und Stuhl) absorbieren höherenergetische Photonen (UV und blaues Licht) stärker als niederenergetische Photonen (rotes Licht und NIR). Dank eines natürlich vorkommenden optischen Fensters in biologischen Proben kann NIR-Licht tiefer eindringen als UV-Licht. Aufgrund dessen können die UCNPs in biologischen Proben mit NIR-Licht angeregt werden. Dies ermöglicht in vitro als auch in vivo Anwendungen, beispielsweise für die optische Bildgebung durch Markieren von Zellen oder durch Einfärben von bestimmten Bereichen organischer Gewebe. Weiterhin könnte die frühzeitige Erkennung von Krankheiten durch prädiktive und diagnostisch geeignete Biomarker, die mit Erkennungselementen an den UCNPs detektiert werden, realisiert werden. Demnach ist „Theranostic“ ein mögliches Szenario, das die Identifikation und die gleichzeitige Behandlung einer Krankheit ermöglichen könnte.

Um diese Vision zu realisieren, müssen die UCNPs bestimmte Parameter erfüllen: Eine hohe Aufkonversionseffizienz, eine hohe Photolumineszenzquantenausbeute, eine gute Dispergierbarkeit und Stabilität der Dispersion in wässrigen Medien, sowie die Verfügbarkeit von funktionellen Gruppen, um schnell und einfach biologische Erken-

nungselemente daran zu koppeln.

Die UCNPs dieser Arbeit wurden mit Hilfe einer solvothermalen Zersetzungsreaktion durchgeführt. Die Nanopartikel bestanden aus unterschiedlichen Wirtsgittern, entweder aus $NaYF_4$ oder $NaGdF_4$. Die Wirtsgitter wurden mit den Ln(III)-Ionen Yb^{3+} und Er^{3+} dotiert. Dieses Aufkonversionspaar ist nur eines von mehreren Aufkonversionspaaren. Die Aufkonversionseffizienz, somit auch deren Quantenausbeute, konnte mit einer passivierenden Schale verbessert werden, die die Oberflächenlöschung der Lumineszenz des Nanopartikels reduziert.

Dennoch leuchten die Kern-Schale-UCNPs schlechter als es im Vergleich mit µm-großen Partikeln zu erwarten wäre. Die Kern-Schale-Strukturen gehen ineinander über und sind nicht mit einer klaren Grenzschicht voneinander getrennt. Zwischen dem Kern und der Schale existiert eine Übergangsregion, die mit der Wanderung der Ionen des Wirtsgitters und den dotierten Ln(III)-Ionen einhergeht. Diese Beobachtung wird auch in der Literatur diskutiert. Die Ionenwanderung wurde mit Hilfe von zeitaufgelöster Laserspektroskopie und dem Interlanthanoidenergietransfer (LRET) in den beiden, bereits erwähnten Wirtsgittern untersucht. Die Ergebnisse sind in zwei Publikationen veröffentlicht, die auf Kern-Schale-Schale-Strukturen basieren. Der Kern ist mit dem LRET-Akzeptor dotiert (Nd^{3+} oder Pr^{3+}). Die Zwischenschale besteht aus dem gleichen Wirtsgitter ohne Dotierstoffe und dient als Isolationsschale, deren Schalendicke innerhalb einer Experimentierreihe variiert wurde, um eine räumliche Trennung von LRET-Akzeptor und -Donor zu schaffen. Die äußere Schale, aus dem gleichen Wirtsgitter, ist mit dem LRET-donor (Eu^{3+}) dotiert. Der Effekt der wachsenden Isolationsschalendicke ist signifikant, obwohl es nicht möglich gewesen ist, den Energietransfer vom Donor auf den Akzeptor komplett zu unterbinden.

Neben der Untersuchung der Wanderung von Ln(III)-Ionen in einem Wirtsgitter wurden verschiedene Phasentransferreaktionen durchgeführt, um anschließende Oberflächenmodifikationen anzuwenden, damit die Anwendungen der UCNPs im biologischen Kontext prinzipiell demonstriert werden kann. Ein Ergebnis mit einem sehr vielversprechenden Liganden für die bio-medizinische Anwendung wurde in einer Publikation veröffentlicht. Dieser Ligand imitiert natürliche Mechanismen von Muschelproteinen und von Blutkoagulation, sodass die untersuchten Nanopartikel sehr effektiv eingekapselt werden. Gleichzeitig sind funktionelle Gruppen zur Bio-Funktionalisierung vorhanden. In einer Machbarkeitsstudie wurde der eingekapselte UCNP erfolgreich mit einem Farbstoff (der durch einen Biomarker ersetzt werden kann) gekoppelt und die Photolumineszenzeigenschaften des Systems untersucht.

List of Publications

Original Publications

- P. U. Bastian, N. Robel, P. Schmidt, T. Schrumpf, C. Günter, V. Roddatis, M. U. Kumke, "Resonance Energy Transfer to Track the Motion of Lanthanide Ions – What Drives the Intermixing in Core-Shell Upconverting Nanoparticles?", *Biosensors* **11** (12), 515 (2021).

- P. U. Bastian, L. Yu, A. López de Guereñu, R. Haag, M. U. Kumke, "Bioinspired Confinement of Upconversion Nanoparticles for Improved Performance in Aqueous Solution", *The Journal of Physical Chemistry C* **124** (52), 28623–28635 (2020).

- P. U. Bastian, S. Nacak, V. Roddatis, M. U. Kumke, "Tracking the Motion of Lanthanide Ions within Core–Shell–Shell $NaYF_4$ Nanocrystals via Resonance Energy Transfer", *The Journal of Physical Chemistry C* **124** (20), 11229–11238 (2020).

- A. López de Guereñu, P. Bastian, P. Wessig, L. John, M. U. Kumke, "Energy Transfer between Tm-Doped Upconverting Nanoparticles and a Small Organic Dye with Large Stokes Shift", *Biosensors* **9** (1), 9 (2019).

- S. Schimka, D. T. Klier, A. López de Guereñu, P. Bastian, N. Lomadze, M. U. Kumke, S. Santer, "Photo-Isomerization of Azobenzene Containing Surfactants Induced by near-Infrared Light Using Upconversion Nanoparticles as Mediator", *Journal of Physics: Condensed Matter* **31** (12), 125201 (2019).

Oral Presentations

- P. Bastian, M. Kumke, "Surface-modulated upconversion nanoparticles for biosensing – a photophysical investigation", *The 2nd Conference and Spring School on Properties, Design and Applications of Upconversion Nanomaterials, UPCON 2018*, Valencia, Spain (2018).

- P. Bastian, S. Nacak, M. Kumke, "Multiplexed targeting of cells and tissue – novel surface-modulated upconversion nanoparticles for biosensing and -imaging", *JCF-Frühjahrssymposium*, Mainz, Germany (2017).

- P. Bastian, S. Nacak, M. Kumke, "Multiplexed targeting of cells and tissue – novel surface-modulated upconversion nanoparticles for biosensing and -imaging", *DBS EBS BioSensor Symposium 2017*, Potsdam, Germany (2017).
- P. Bastian, "Paul and upconversion nanoparticles", *Elevator Pitch Event by PoGS*, Potsdam, Germany (2016).
- P. Bastian, M. U. Kumke, "Multiplexed targeting of cells and tissue – novel surface-modulated upconversion nanoparticles for biosensing and -imaging", *MacroBio Summer School*, Potsdam, Germany (2016).

Poster Presentations

- P. Bastian, M. Kumke, "Surface-modulated upconversion nanoparticles for biosensing – a photophysical investigation", *The 2nd Conference and Spring School on Properties, Design and Applications of Upconversion Nanomaterials, UPCON 2018*, Valencia, Spain (2018).
- P. Bastian, S. Nacak, L. Yu, M. Kumke, R. Haag, "Multiplexed Targeting of Cells and Tissue – Novel Surface-modulated Upconversion Nanoparticles for Biosensing", *GDCh-Wissenschaftsforum Chemie 2017*, Berlin, Germany (2018).
- S. Nacak, P. Bastian, M. Kumke, "Multiplexed targeting of cells and tissue – novel surface-modulated upconversion nanoparticles for biosensing and -imaging", *116^{th} Bunsentagung*, Kaiserslautern, Germany (2017).

1

Introduction

Upconversion nanoparticles (UCNPs) are nanoparticles, which are able to increase the frequency of incident light by its absorption and subsequent re-emission. In other words: long-wavelength photons are absorbed and shorter-wavelength photons are emitted.

This photoluminescence (PL) phenomenon suits very well in the International Year of Light in 2015, which was declared by the United Nations Educational, Scientific and Cultural Organization (UNESCO). The UNESCO aimed at promoting the awareness of light and light-matter interactions not only in science, but also in the general public perception and its meaning for science, technology, nature, and culture.[1]

The frequency upconversion (UC) describes the effect of the absorption of low energy photons and the subsequent emission of higher energy photons. Basic laws of physics, namely the conservation of energy, are not violated, as at least two low energy photons with a long wavelength, e.g., in the near-infrared (NIR) spectral range, need to be absorbed in order to observe the emission of one higher energy photon with a shorter wavelength, e.g., in the visible (Vis) or ultraviolet (UV) spectral range. Consequently, the theoretical maximum UC quantum efficiency is 50 %, because at least two photons are needed to produce one photon via the UC process. The UC process is based on the particular electronic properties of trivalent lanthanoid cations* (Ln(III)), which is described in more detail in subsection 1.1.1 and Fig. 1.1.

In 2016, the challenges of today and those of the future have been formulated by the United Nations as 17 sustainable development goals (SDGs). The SDGs call for action to all nations for all domains in life and cover topics of poverty, inequality, climate change, environmental degradation, as well as peace and justice.[3] Everything is somehow connected with each other. As the world moves closer together, especially facing globalization, the SDG's importance is emphasized. They became highlighted during 2019 with the Fridays for Future and Scientists for Future (and "*others*" for Future) movements.

*According to IUPAC: The term "lanthanoid ion" is the preferred term over "lanthanide ion", since the suffix "ide" indicates negatively charged ions and the lanthanoid ions are cations.[2]

UC materials can be a contribution for at least SDG #3 and SDG #7 (good health and well-being, as well as affordable and clean energy, respectively). Already in 2003, the German Advisory Council on Global Change has published an assessment of the current energy production with ideas for changing to globally green energy production and sustainability.[4] It should be emphasized, that there is not THE ONE solution. UCNPs and their light interaction properties can be considered as one possible contribution to the SDGs.

Upconversion for photovoltaic cells. SDG #7, affordable and clean energy. In general, photovoltaic/solar cells consist of semiconducting materials with particular bandgaps. The energy of the bandgap defines the photon energy being absorbed. An electron-hole pair is created upon photon absorption and their separation leads to usable electrical energy. Most solar cells consist of polycrystalline silicon. Photons with lower energy (sub-bandgap photons) than the Si-bandgap are not absorbed. Photons with higher energy than the Si-bandgap are absorbed and the desired electron-hole pair is created. But, the photon's excess energy leads to heat, which decreases the solar cell efficiency. This is called thermalization. Semiconducting solar cells have a limited absorption range of the solar spectrum. This limitation can be reduced by multi-layer or tandem solar cells with material combinations of different bandgaps. This kind of solar cells possesses an increased absorption range. But, the multi-layer solar cells are relatively expensive and complicated in production.[5]

Another approach is the "modification" of the incident sun light before the photons enter the absorbing semiconducting material. It could be realized with UC material, which is doped with Ln(III) ions, like Er^{3+} doped Gd_2O_2S. The doped Er^{3+} ions increase the absorption range towards lower photon energies by upconversion, which enhances the efficiency of silicon photovoltaic devices. The Si-bandgap is 1.1 eV ($\approx 9100\,cm^{-1}$; 1100 nm). Sub-bandgap NIR photons are not absorbed. Er^{3+} ions can absorb NIR photons at around 1500 nm ($^4I_{13/2} \leftarrow {}^4I_{15/2}$ transition) and upconvert NIR photons to photons having an energy comparable to the Si-bandgap at around 1000 nm ($^4I_{11/2} \rightarrow {}^4I_{15/2}$ transition of Er^{3+}, see Fig. 1.1). Accordingly, silicon solar cells equipped with $Gd_2O_2S{:}Er^{3+}$ have an increased absorption range and can theoretically enhance the efficiency of such solar cells from 33 % up to 40 %.[6]

If there is upconversion, of course, there will be downconversion.[†] The downconver-

[†]There is also downshifting describing the expected photoluminescence emission (PL) behavior: If one high energy photon is absorbed, in maximum one low energy photon will be emitted. An optically active material goes into an electronic excited state by absorption of high energy photons. An electron is promoted into an vibronic excited state. The electron will reach a lower vibrational ground and

sion (DC), also called quantum cutting, describes the absorption of one high energy UV or Vis photon and the subsequent emission of two or more low energy Vis or NIR photons due to cascaded processes, like resonance, cooperative energy transfers, and/or cross relaxation processes.[7,8] In contrast to UC (max. 50 % quantum efficiency), DC can result in quantum efficiencies larger than 100 %. DC materials can be used to "modify" the incident photons, so that these match the semiconductor bandgap. Known UC material can also perform downconversion depending on the dopants. For example, Gd_2O_2S doped with Tm^{3+} instead of Er^{3+} exhibits downconversion photoluminescence emission at 1000 nm suiting for silicon photovoltaic devices.[8] Further downconversion materials can be (i) YVO_4 doped with Yb^{3+} (λ_{em} = 1000 nm, 185 % efficiency);[7] (ii) $NaYF_4$ doped with Ho^{3+} and Yb^{3+} (155 % efficiency);[5] (iii) $KSrPO_4$ doped with either Tb^{3+} & Yb^{3+}, Ce^{3+} & Tb^{3+} & Yb^{3+} or Eu^{2+} & Yb^{3+} (highest efficiency for Eu^{2+} with 140 %)[9] and (iv) $CsPbCl_3$ perovskites doped with Yb^{3+} (120 % efficiency).[10]

These examples show the possibilities for applications of Ln(III) ions for UC and DC in the photovoltaic technology. The future will show if these investigations find a way in a technical realization.

Upconversion for biological applications. SDG #3, good health and well-being. In 2013, the Federal Ministry of Education and Research (BMBF) of Germany published an action plan for tailored medical treatment with targeted care.[11] The application of light and especially of NIR light in combination with UC materials will be one important contribution for individualized medicine and for in vitro as well as in vivo diagnostics. UCNPs in combination with laser spectroscopy could be used in pre-screening or early stage recognition applications to find and prevent the outbreak of particular diseases. UCNPs can be used for diagnostic measures in order to supervise disease progressions and perhaps even provide therapy applications. This demands for further research on biomarkers.[‡] In this context, the UCNPs present a platform, that can be compared with a toolbox-like system. In combination with a variety of surface modification strategies a wide range of possible bio-applications can be covered. The UCNPs serve "only" as a tool and as optical probe and can be a rather powerful tool in combination with NIR laser excitation.

electronic excited state by inner relaxation, internal conversion, intersystem crossing, and/or cross relaxation processes. Finally, the non-radiative transitions and preferred radiative transitions end in the material's ground state. Emitted photons will have lower energy than incident photons.

[‡]Biomarkers are important medical and biological parameters, that are characteristic for normal or pathological bio-processes. Biomarkers can be measured qualitatively and quantitatively. There are three classes of biomarkers: Predictive biomarkers are risk indicators to find diseases in early stages. Diagnostic biomarkers are indicators for a present disease. Prognostic biomarkers are indicators to estimate the disease progression and adapt the therapy.[11]

This interface of physical chemistry and biology can be addressed with the UCNPs and their unique luminescence properties (PL properties). It opens pathways for biological and medical applications. Tissues and biological media are complicated mixtures with a lot of optical active matter. The excitation with light may lead to autofluorescence, that competes with the desired signal. UCNPs can be excited in the NIR, which leads to less autofluorescence and less damage of organic tissue. In contrast to that, UV excitation leads to strong autofluorescence and damage of organic matter. Additionally, NIR photons can penetrate deeper into organic tissue than photons with the energy of green, blue, or UV light.§[14]

Organic tissues and samples have different absorption properties depending on their origin (e.g., skin, connective tissue, adipose tissue, abdominal tissue, blood plasma, full blood, or urine). The electromagnetic spectrum can be divided into four NIR optical windows, whose limits vary a bit in the literature. These optical windows describe the spectral ranges, at which the absorption of organic samples is low. Furthermore, they promise larger penetration depth for NIR photons. The first NIR optical window addressable with spectroscopic techniques lies between 650–950 nm,[15] or between 700–900 nm.[16] The second NIR optical window lies in the range of 1100–1350 nm. The third NIR optical window is at 1600–1870 nm. The fourth optical window lies around 2100–2350 nm.[17,18] Within those windows, spectroscopic techniques can be applied, because organic samples show less absorption, scattering, and autofluorescence, being well illustrated with the experiment in the footnote §. Hence, UCNPs can help to improve the light penetration and imaging depth.

Fluorescent labels, like dyes, quantum dots, and complexed lanthanoid ions have already been demonstrated as powerful tools for bio-imaging, bio-sensing, and usage in immunoassays with picomolar detection limits.[19–23] UCNPs will complement this list.

1.1. Upconversion Nanoparticles

In general, optical probes as dyes or quantum dots convert high energy photons into low energy photons (Stokes shift). In that point, the UCNPs are outstanding, as they possess the ability to convert low energy photons into high energy photons (anti-Stokes shift). The UCNPs absorb NIR photons and upconvert these into Vis and even UV

§Liu et al. showed a penetration depth of ~2 cm in black mice with $NaLuF_4$:Gd^{3+}, Yb^{3+}, Tm^{3+} UCNPs under 980 nm (NIR) excitation.[12] For comparison: UV light causes sunburn on the skin and UV photons only penetrate a few micrometers into skin.[13]

photons due to the ladder-like electronic structure of the involved Ln(III) ions.[24–27] Narrow absorption and emission bands can be addressed with the real electronic states involved (compare Fig. 1.1). Because of these states, relatively low excitation power densities are needed to produce upconversion photoluminescence. For this, already low-cost continuous wave laser diodes can be used instead of expensive short-pulsed laser systems. The excitation of the Ln(III) ions involves spectroscopically forbidden 4f transitions (Laporte rule),[28] which leads to long excited state live times enabling time-gated detection. In addition to this, background/autofluorescence of biological samples can be further overcome by the NIR excitation increasing the signal-to-noise ratio (being related to the optical window as well). Due to the smaller excitation of biological samples by the NIR photons, less photo-damage of the samples is very likely. [29,30]

UCNPs can be realized in several host lattices, like oxide, phosphate glass, or in fluoride host materials. The fluoride host is used in this work. These materials contribute to the photostability and the chemical stability. The latter is also a challenge for surface-modifications due to its chemical stability. Another advantage is the variety of dopants, that can be used (most commonly Ln(III) ions). Due to the doping, several luminescent centers are present in one nanoparticle, which avoids blinking. In literature, additional applications to the UCNP luminescence are reported as well. They present a combined UCNP application depending on the dopants, e.g., magnetic resonance imaging, computer tomography, single photon emission computer tomography, positron emission tomography, and therapeutic applications such as photothermal or photodynamic therapy, and gene or drug delivery systems.[30]

1.1.1. Upconversion photoluminescence

The photoluminescence emission (PL) of high energy photons upon low energy photon absorption has been described in detail by François Auzel in the 1970s,[33] who called this effect "*addition de photon par transfers d'énergie*" (APTE), which has been later termed energy transfer upconversion (ETU). Initially, the ETU had been suggested by Bloembergen in 1959 for an infrared quantum counter.[34] The interaction of two excited ions via an energy transfer has been doubted until 1966, when Auzel contributed intensively to the major theory for the energy transfer from one excited ion to a second one, that is further excited. The light absorbing ion and energy donor is termed sensitizer. The energy acceptor and UC light emitting ion is termed activator, as illustrated in Fig. 1.1 for Yb^{3+} and Er^{3+} ions. The sensitizers outnumber the activators and absorb the major amount of the incident NIR photons. Subsequent energy transfers (more than one) from

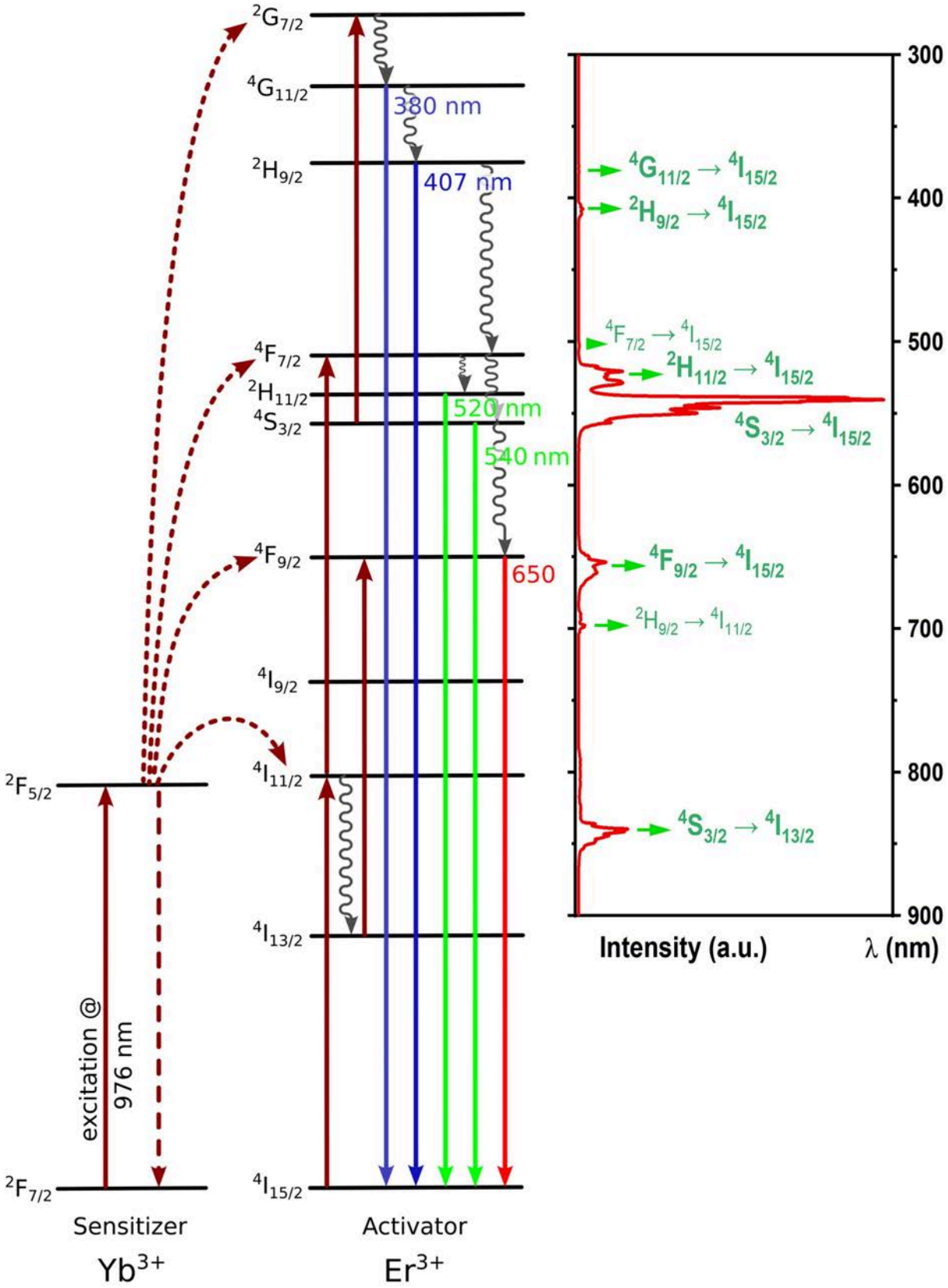

Figure 1.1.: Energy transfer upconversion scheme with energy levels of the Yb^{3+} sensitizer and the Er^{3+} activator. Solid upward arrows are excitation pathways related to absorption or energy transfer (dashed arrows). Solid downward arrows are radiative transitions. Dashed and wavy downward arrows are non-radiative transitions. The upconversion emission spectrum of Yb^{3+}/Er^{3+} doped UCNPs is shown on the right hand side. The energy levels are taken from Dieke's diagram showing free lanthanoid ion energy levels.[31,32]

the sensitizers (many) to the activators (few) increase the population of energetically higher electronic excited states of the activators. Common sensitizers are Nd^{3+} or Yb^{3+} ions for the excitation with 795 nm or with 976 nm, respectively. Common activators are Pr^{3+}, Ho^{3+}, Er^{3+}, or Tm^{3+}. An additional ETU scheme for Nd-Yb-Er-Tm UCNPs is shown in the SI/appendix, Fig. S.6.

The subsequent energy transfer upconversion from the excited sensitizer to the ground state or excited state activator within UCNPs can be split into two mechanisms: (1), the phonon assisted energy transfer and (2), the lanthanoid resonance energy transfer (LRET). The energy differences of the sensitizer and activator electronic states have to match with each other. The refractive index and the phonon energy of the host material, that keeps the sensitizer and activator in spatial proximity to each other, need to match as well to achieve high UC quantum efficiency. The advantages of low phonon energies are the longer living excited states of the sensitizer and activator ions. The longer living excited states lead to larger ETU probabilities.[33]

The phonon assisted energy transfer helps to bridge the energetic mismatches of sensitizer and activator. As the UCNP size decreases, the proportion of the phonon assisted energy transfer on the overall energy transfer decreases, especially as soon as the UCNP size undercuts 10 nm. Consequently, the energy levels of the sensitizers and activators should match well.[35]

The resonance energy transfer is the main ETU mechanism in UCNPs. The 4f Ln(III) ion energy states show only little dependence on the host material. Accordingly, Dieke's diagram, depicted in Fig. 1.1, is valid with only minor deviations for different host lattices. The $4f^n$ Ln(III) ion energy states are defined by the Russel-Saunders notation in $^{2S+1}L_J$ multiplets. Hereby, $2S+1$ is the spin multiplicity, S is the total spin quantum number, L is the total orbital momentum quantum number and J is the total angular momentum quantum number. The J-levels split again into $2J+1$ energy levels due to crystal-field interactions (Stark splitting).[28]

Some energy transfers become possible due to the combination of Stark splitting and vibronic side bands, which bridge energetic mismatches between the energy states of the sensitizer and activator ions. The intra $4f^n$ electronic transitions have weak electron-phonon interactions, so that the vibronic side bands play a minor role in the lower excited states. However, the electron-phonon interactions become more important for efficient energy transfers to reach higher excited states, as the vibronic side bands increase the absorption cross section.[35]

Besides the ETU, probably with the highest expected UC quantum efficiency, there are other upconversion mechanisms listed here briefly: Excited state absorption, photon

avalanche effect, cooperative sensitization, cooperative photoluminescence emission, second and third harmonic generation (SHG or THG, nonlinear optical processes), and two-photon absorption. These effects have their own specific theoretical interpretations and descriptions based on the nature of the electronic interactions.[33]

1.1.2. Tuneability of upconversion efficiency

Tuning the upconversion efficiency affects the total UC luminescence intensity and the UC luminescence color. Next to the choice of the host lattice, the nanoparticle size, dopant ratios, and the excitation power density play a role. Also, these parameters depend on each other. Each variation changes the PL emission color related to the population of the respective energy levels of the activators and their PL decay times.

The UC efficiency can be changed by altering the particle size. Smaller particles suffer from higher surface-to-volume ratios and possess relatively more surface defects than larger particles or their respective bulk material. Accordingly, smaller particles are prone to luminescence quenching, leading to less UC PL intensity and shorter PL decay times.[36]

Next to the overall UC efficiency, single PL emission bands and their PL decay times can be tuned. As described above, the Ln(III) energy levels are only slightly influenced by the chemical environment (which does not account for the Stark levels). The involved intermediate states of the Ln(III) ions doped into the host lattice can influence the population pathways of the different energy levels resulting in luminescence. Different sensitizer/activator doping ratios (e.g., Yb^{3+}/Er^{3+}) or mixture of activators (e.g., Er^{3+}/Tm^{3+}) within the UCNPs alter the UC PL emission. In the latter case, different population pathways are realized and a luminescence mixture of the two activators can be observed.[37–39]

The excitation power density is an important parameter as well to alter the population pathway of the excited states. For example: High excitation power density leads to higher population of the upper energy levels. Accordingly, low excitation power density leads to higher population of the lower energy levels. In the low excitation power density area for Er^{3+} doped UCNPs, the green PL emission at 520 nm and 540 nm ($^2H_{11/2}$ & $^4S_{3/2} \rightarrow {}^4I_{15/2}$) and the red PL emission at 650 nm ($^4F_{9/2} \rightarrow {}^4I_{15/2}$) compete with each other, see Fig. 1.1. The Er^{3+} green PL emission is a two-photon process. The Er^{3+} red PL emission can be a two- and a three-photon process. For the green PL emission, the energy of two absorbed NIR photons needs to be transferred via ETU from the excited sensitizers to one Er^{3+} ion in order to populate the $^2H_{11/2}$ and $^4S_{3/2}$ energy levels. The sensitizer ions are responsible for the energy propagation

within the crystal and serve as an energy reservoir for the UC process. In general, lower excitation power density for Yb^{3+}/Er^{3+} UCNPs leads to larger proportion of Er^{3+} green PL intensity than its red PL intensity.

Higher excitation power density leads to a fuller energy reservoir. But, the parameters, that influence the upconversion population pathway, are coupled with each other: In the high excitation power density area, the red PL emission is also fed by the higher lying "blue" energy level ($^2H_{9/2} \rightarrow {}^4F_{9/2}$ transition) more efficiently than the green one, which corresponds to a three-photon process. Hence, its intensity can increase in relation to the green PL emission if the excitation power density increases. Additionally, the nanoparticle size plays a distinct role. Depending on the size, the Er^{3+} red PL emission can either result from a three-photon process (for large UCNPs > 90 nm), a two-photon process (for small UCNPs < 25 nm), or a mixture of the two- and three-photon process. Consequently, the observed PL emission color of the UCNP changes size-dependent as well.

As illustrated, the excitation power density changes the population pathways of the emissive energy levels, as well as the particle size. Furthermore, solvent influences on the Ln(III) luminescence is small, but different solvents can depopulate effectively some excited states of the sensitizers and the activators, which are mandatory for the ETU, and which can alter the luminescence color of the UCNP.[40–43]

In 2007, the concept of core-shell UCNP structures has been introduced with the aim to increase the total UC PL efficiency and to reduce surface related quenching. [44,45] The shell serves as a passivation layer protecting the core from the influence of the chemical environment. Especially aqueous solvents quench the PL emission of the excited states from the sensitizers and the activators by non-radiative multiphonon relaxation. The third overtone of the OH-vibration matches energetically to the Yb^{3+} (sensitizer) $^2F_{5/2} \rightarrow {}^2F_{7/2}$ transition. Quenching the sensitizer means emptying the energy reservoir and interrupting the energy propagation for the ETU.

It also accounts for the Er^{3+} (activator) $^4I_{11/2} \rightarrow {}^4I_{13/2}$ transition. The $^4I_{11/2}$ energy level is the starting energy level for the upconversion within the Er^{3+} ion. The OH-vibrations favor the population of the $^4F_{9/2}$ energy level (compare Fig. 1.1), which leads to a higher proportion of the Er^{3+} red PL emission ($^4F_{9/2} \rightarrow {}^4I_{15/2}$ transition), because the two Er^{3+} excited energy states, being thermally coupled and responsible for the green PL emission ($^2H_{11/2}$ & $^4S_{3/2} \rightarrow {}^4I_{15/2}$ transition), are less populated.

In contrast to that, the CH-vibrations of organic solvents couple more effectively with the "red" energy level ($^4F_{9/2}$) than with the "green" energy levels ($^2H_{11/2}$ and $^4S_{3/2}$). [46] This may lead to a stronger PL quenching rate of the Er^{3+} red PL emission by

multiphonon relaxation and affect the UC PL emission color.

Comparing the two activator ions Er^{3+} and Tm^{3+} with each other, it is found, that the Tm^{3+} PL emission at 800 nm is less affected by OH-quenching. With the help of a passivating shell, this effect cannot be suppressed, but significantly reduced. The observed UC luminescence intensity increases and the luminescence color may be affected.[40,46–48]

Another application of core-shell structures in terms of tuning the UCNP luminescence can be realized in spatial confinement. Different designs and host materials for the core and for the shell can be chosen. The strategies range from exclusively doping the sensitizers and activator into the core and shell, respectively, to designs with several shells containing the same sensitizers but different activators. With these designs, the sensitizers (energy reservoir) transfer their energy only to the activators. Another design might be an undoped core and a sensitizer/activator doped shell (inert core-active shell) aiming to increase spatial proximity.[49,50]

Different host materials can be applied, like a protective CaF_2 shell[27,51] or SiO_2 shell [12] to suppress energy migration as well as dopant migration towards the nanoparticle surface. The motion of lanthanoid dopants in the host lattice is discussed in more detail in the manuscript 1 (section 2.2) and manuscript2 (section 2.3). Changing the host lattice material is accompanied by changing the phonon energy, the refractive index, and the crystal lattice structure. In literature, successful host lattice changes, that improve the UC efficiency, are often reported. But, failures are very rarely reported.

1.1.3. Trivalent lanthanoid ion migration (Ln(III) migration)

Indeed, core-shell structures contribute to better shielding the luminescent core from the solvent and reduce surface defects as well as surface quenching. But still, the UCNPs will stay behind the expected upconversion brightness comparing to their bulk material. TEM investigations of core-shell UCNPs revealed a Ln(III) ion migration resulting in a transition layer between the core and the shell. Accordingly, the understanding of clearly separated core-shell structures has changed for the UCNPs towards the existence of a transition layer between cores and shells.[52–54] Other investigations concentrated on the amount of surface Ln(III) ions and found a distinct concentration gradient towards the UCNP surface, depending on the synthesis approach.[55] This could be one reason for the reduced brightness, although the core-shell UCNPs show better performance than core-only structures. In this work, this phenomenon is named trivalent lanthanoid ion migration and is investigated with spectroscopic techniques. With better understanding of the Ln(III) migration and how to influence it, the extent

of the transition layer could be reduced. The extent of the transition layer formation is already known to correlate with dopant concentration, synthesis temperature, and synthesis time.[56] The previous investigations all focus on the fluoride host material. It should be kept in mind as well, that the transition layer formation between core-shell structures is not only limited to fluoride host nanoparticles.[57]

The ion migration can be explicitly favored (instead of reduced) by the reaction conditions (different surfactant/solvent ratios, changing the pH value of the nanoparticle synthesis) to alter the crystal size and shape of e.g., Ln(III)-doped fluoride host nanoparticles.[58] Moreover, the migration is not only limited to Ln(III) ions. The migration of all ions in the UCNP can potentially be used for guiding the energy migration and tuning the UC PL emission by synthesis and nanoparticle design. In addition to the ion migration, the excitation power density can be adapted to favor distinct PL emission bands (emission colors).[59,60]

1.1.4. The host lattice and its dopants

The fluoride host has shown the best performance, which is why the $NaYF_4$ lattice is one of the most often used host materials in UCNP research. Another challenge is the fabrication of highly luminescent UCNPs related to their high surface-to-volume ratio and higher luminescence quenching rates in comparison to their bulk material.[35]

The combination of different host lattices and dopants can increase the UC efficiency. $NaYF_4$ in the cubic and hexagonal crystal phase, $NaGdF_4$ (hexagonal) and $NaScF_4$ (either trigonal or monoclinic) have already been investigated. Next to these, several other host lattices can be found in literature.[30] The most often used one is the $NaYF_4$ host lattice in the hexagonal crystal phase.

The question why and which basic rules apply for the interchangeability of dopants and host lattices has already been researched in the geochemistry research field by Victor Goldschmidt, who formulated some general rules in the 1920s referring to ion exchanges and lattice variations without changing the crystal structure family.[61] Three rules can be briefly summarized: (i) The mutual substitution of elements within a crystal will be possible if the ionic radii resemble each other. (ii) If the charges are equal, the element with the smaller ionic radius will be preferred in the crystal structure. (iii) If the ionic radii are equal, the element with the higher charge will be preferred in the crystal structure.[62] The deviations between the exchanged cation radii shall not exceed 15 % if the crystal structure shall be maintained. Breaking these rules leads either to a change in the crystal structure or to a failure in the formation of the nanoparticle design, because the particles do not form as desired. The lanthanoid ions are well

interchangeable between each other, since they are similar in size and in polarizability. The latter is another important parameter for exchanging ions within a lattice without changing the crystal structure.[61]

$NaYF_4$ possesses low phonon energy supporting the ETU in UCNPs. Depending on the synthesis design, it can be obtained in two crystal structures basically: The cubic or the hexagonal crystal structure.[63] This phenomenon is not exclusive to $NaYF_4$ but important for the ETU. The hexagonal phase exhibits higher UC efficiency. The cubic phase forms at low temperatures ($\approx$ 200 °C) in a solvothermal decomposition synthesis. Upon annealing between 300 °C and 400 °C a transition from the cubic to the hexagonal phase takes place. Further heating (up to 700 °C) leads to the high temperature cubic phase. The cubic-to-hexagonal-to-cubic lattice transformation and ion re-ordering upon heating takes place under NaF loss and is irreversible.[64,65] Accordingly, the solvothermal decomposition synthesis is adapted to yield $NaYF_4$ UCNPs in the hexagonal crystal phase.

Laporte rule states, $4f^n$ transitions are parity forbidden for centrosymmetric systems. The hexagonal phase exhibits less centrosymmetry and stronger crystal field coupling than the cubic phase, which leads to higher transition probabilities and higher UC luminescence intensity. Further disordering can be realized by the addition of Gd^{3+} in the nanocrystalline structure. Plus, $NaGdF_4$ nanoparticles tend to crystallize in the hexagonal phase under the applied conditions of this work. Depending on the doping ratio and only up to a certain Gd^{3+} concentration, the symmetry in $NaYF_4$:Yb,Er/Tm UCNPs can be further disordered by Gd^{3+} addition to enhance the UC efficiency.[35,66]

1.1.5. Non-radiative energy transfers: FRET and LRET

The non-radiative energy transfer can be divided into long range and short range energy transfers. The best known long range energy transfer is the Förster resonance energy transfer (FRET), which can reach distances up to 20 nm,[67] whereas the FRET efficiency depends on the donor-acceptor distance by the power of –6 ($1/r^6$, compare Eq. (1.2), further below).

The resonance energy transfer between two Ln(III) ions is termed LRET for lanthanoid resonance energy transfer. The FRET theory describes qualitatively and quantitatively a non-radiative energy transfer based on coulombic dipole-dipole interactions. The FRET theory can be applied for LRET as well, although the energy transfer character between Ln(III) ions doped into UCNPs is not exclusively limited to dipole-dipole interactions, [68] but can be also of the character of dipole-quadrupole[69] or quadrupole-quadrupole interactions.[28,70–72]

For the sake of clarity, the term RET describes the resonance energy transfer from the UCNP (RET-donor) to a dye (RET-acceptor) for this work. To be more precise, the doped Ln(III) activator (here: Er^{3+}) is the RET-donor for the energy transfer from the UCNP to the RET-acceptor (here: TAMRA). The RET can be described and its parameters can be calculated by the FRET theory as well.

Förster resonance energy transfer

In 1948, the FRET-theory has received its deserved scientific attention and today it is an often applied theory.[73,74] Previous ideas and experiments with electromagnetic fields and spectroscopy dating back until the 19th century formed the base for Förster's theoretical interpretation of the energy transfer between two dipoles. Some important researchers of that time contributing with their ideas and work are for instance: Cartio and Franck (1922), who were the first to experimentally observe energy transfers in atom vapor over larger distances than the atomic collision radii; Kallman and London (1928), who developed a quantum mechanical theory for energy transfers in chemical vapors; Weigert, Gaviola, and Pringsheim (1920 and 1924), who experimentally observed energy transfers in solution; and J. Perrin and F. Perrin (around 1930), who developed a simple classical and a quantum mechanical interpretation of energy transfers in solution.[75]

The following theory and FRET equations are mainly from Refs. [28,70,71]. In order to observe FRET from a donor in its excited state (D^*) to an acceptor in its ground state (A), several conditions have to be met. First, the resonance condition, Eq. (1.1):

$$\Delta E\,(D^* \rightarrow D) = \Delta E\,(A^* \leftarrow A) \tag{1.1}$$

After the energy transfer, the FRET-donor is in its ground state (D) and the FRET-acceptor is in its excited state (A^*). The energy differences of the excited-to-ground state transitions (and vice versa) of the donor ($D^* \rightarrow D$) and the acceptor ($A^* \leftarrow A$) must be equal and match with each other as illustrated in Fig. 1.2 (a).

Second, the donor-acceptor distance is limited. The dipole-dipole interaction has a distance dependency of r^{-6}. The FRET rate constant k_{FRET} can be calculated according to Eq. (1.2).

$$k_{FRET} = \left(\frac{1}{\tau_D}\right)\left(\frac{R_0}{r}\right)^6 \tag{1.2}$$

τ_D is the donor luminescence decay time in absence of the acceptor and r the donor-

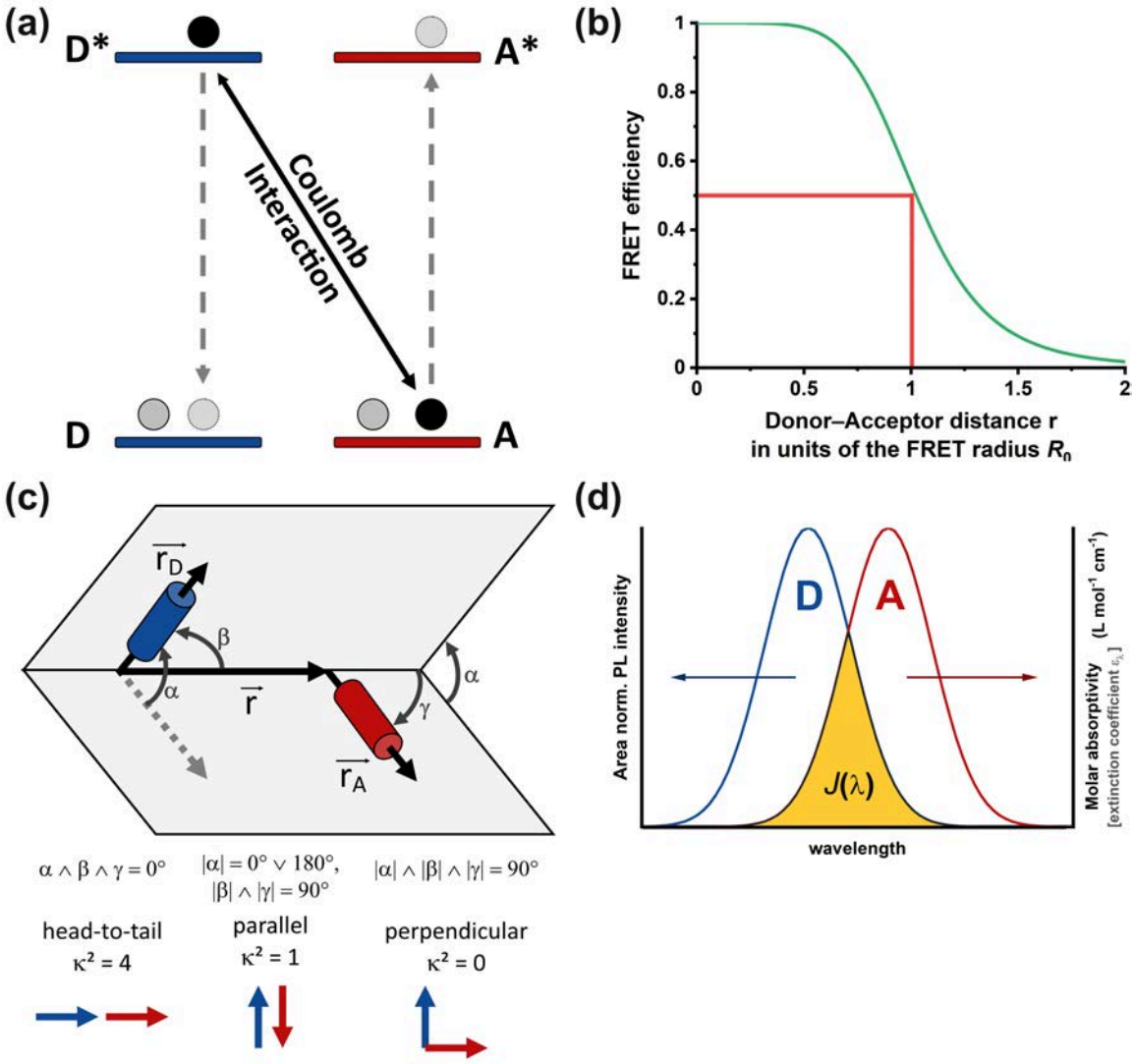

Figure 1.2.: Illustration of Förster resonance energy transfer properties and parameters. (a) FRET mechanism of the resonance condition and energy transfer via coulomb interaction: The excited donor D^* transfers its energy to the acceptor A in the ground state. Upon energy transfer the donor electron returns to the donor's ground state (dashed grey downward arrow), whereas the acceptor is excited (dashed grey upward arrow): $\mathrm{D}^* + \mathrm{A} \rightarrow \mathrm{D} + \mathrm{A}^*$. (b) FRET efficiency dependent on the donor-acceptor distance in units of the Förster radius R_0. (c) Relative orientation of the donor PL emission transition dipole moment ($\vec{r}_\mathrm{D}$, blue) and the acceptor absorption transition dipole moment ($\vec{r}_\mathrm{A}$, red). (d) Illustration of the spectral overlap (in yellow), the area normalized donor PL emission spectrum (in blue) and the acceptor molar absorptivity spectrum (or extinction coefficient spectrum, in red), which are mandatory for FRET. (Inspired by Refs. [70, 71, 76]).

acceptor distance. The Förster radius R_0 can be calculated based on experimental data according to Eq. (1.3). R_0 is the donor-acceptor distance at which the efficiency of the energy transfer is 50 %, as illustrated in Fig. 1.2 (b).

$$R_0^6 = \frac{9 \ln(10) \kappa^2 \Phi_D}{128 \pi^5 n_r^4 N_A} J(\lambda) \tag{1.3}$$

The Förster radius R_0 depends on the transition dipole orientation factor κ^2, the donor quantum efficiency Φ_D, the refractive index n_r representing the chemical environment, and the overlap integral $J(\lambda)$ correlating with the resonance condition. N_A is the Avogadro constant.

$$\kappa^2 = (\cos\alpha - 3 \cos\beta \cos\gamma)^2 = (\sin\beta \sin\gamma \cos\alpha - 2 \cos\beta \cos\gamma)^2 \tag{1.4}$$

The transition dipole orientation factor κ^2 represents the third condition for successful FRET (Eq. (1.4)) and describes the relative orientation of the donor PL emission transition dipole moment $\vec{r_D}$ and the acceptor absorption transition dipole moment $\vec{r_A}$ as illustrated in Fig. 1.2 (c). The maximum value for κ^2 is 4 (head-to-tail orientation). κ^2 can also be 1 (parallel orientation). The minimum value of κ^2 is 0 (zero; perpendicular, no FRET). The orientation factor for random orientation between the donor and acceptor transition dipole moments, which is related to rotational diffusion within the limits of the molecules, is assumed to $\kappa^2 = 2/3$ prior to the energy transfer. This value is most often used to calculate R_0. The influence of κ^2 on the donor-acceptor distance r is only 26 %. The maximum deviation will be 35 % if κ^2 is 2/3. The orientation factor κ^2 can also be assumed to be 0.476 if the donor-acceptor orientation is static but still randomly distributed during the excited state lifetime.[70]

$$J(\lambda) = \int F_D(\lambda) \varepsilon_A(\lambda) \lambda^4 \, d\lambda \tag{1.5}$$

The overlap integral $J(\lambda)$, Eq. (1.5), can be calculated with the area normalized donor PL emission spectrum $F_D(\lambda)$ and the acceptor extinction coefficient spectrum $\varepsilon_A(\lambda)$ depending on the wavelength λ, respectively. The donor PL emission and acceptor absorption spectral overlap is illustrated in Fig. 1.2 (d). If both do not overlap, FRET will not occur.

The efficiency of the resonant energy transfer can be calculated with Eq. (1.6), whereas the FRET efficiency E_{FRET} decreases proportionally to the inverse power of 6 of the

donor-acceptor distance r.

$$E_{\mathrm{FRET}} = \frac{R_0^6}{R_0^6 + r^6} = \frac{k_{\mathrm{FRET}}}{k_{\mathrm{FRET}} + k_{\mathrm{D}} + k_{\mathrm{NR}}} = 1 - \frac{\Phi_{\mathrm{DA}}}{\Phi_{\mathrm{D}}} = 1 - \frac{I_{\mathrm{DA}}}{I_{\mathrm{D}}} = 1 - \frac{\tau_{\mathrm{DA}}}{\tau_{\mathrm{D}}} = 1 - \frac{\tau_{\mathrm{AD}}}{\tau_{\mathrm{D}}} \quad (1.6)$$

k_{D} is the donor luminescence decay rate constant, k_{NR} is the rate constant for non-radiative relaxation, Φ is the photoluminescence quantum yield, τ is the luminescence decay time, and I the luminescence emission intensity. The index DA stands for the respective physical quantity of the donor in presence of the acceptor and the index D stands for the respective physical quantity of the donor in absence of the acceptor. If the acceptor luminescence decay time τ_{A} is significantly smaller than the acceptor luminescence decay time in presence of the donor τ_{AD} (because the donor sensitizes the acceptor via FRET), the donor PL decay time in presence of the acceptor τ_{DA} can be replaced by τ_{AD}.[77–79] Furthermore, kinetic-based FRET experiments should be preferred, since these are not affected by photobleaching of the luminophores. In case of photobleaching, only the total PL emission intensity decreases, which would lead to incorrect FRET efficiencies for intensity based experiments.

As mentioned above, UCNPs exhibit less photobleaching, which renders them in combination with their NIR absorption and upconversion properties to promising light harvesting tools in organic tissues. This concept is demonstrated in a proof of principle experiment with a dye (RET-acceptor) coupled to the UCNP (RET-donor). This experiment has been published in manuscript 3 (section 2.4).

Furthermore, the average acceptor number within the distance of the Förster radius around one single hypothetical donor is calculated based on the equations of the FRET theory. The average acceptor number can be calculated with the donor's luminescence data and its quenching. The FRET derived equation adapted for the UCNP case is termed "LRET equation" and described in subsection 3.1.2 (Eq. (3.1), Eq. (3.2) and Eq. (3.3)), as well as in the respective manuscripts 1 and 2 (section 2.2 and section 2.3).

1.2. Surface Modification for Hydrophilic UCNPs

Various ways for UCNP synthesis are available. One classification can be made by the outcome of the UCNP character from the synthesis: hydrophilic or hydrophobic. Hydrophilic UCNPs can be obtained via hydrothermal synthesis, sol-gel processes in autoclaves, or microwave assisted synthesis.[80,81]

Frequently, UCNPs are synthesized via coprecipitation, thermal decomposition, and solvothermal synthesis, producing hydrophobic nanoparticles. The synthesis in high

boiling solvents (as also performed in this work) promises better control over the UCNP size, size distribution, shape, and long term stability in organic solvents.

In order to apply the UCNPs in biological media and to target specific biological relevant structures, the UCNPs need to be water dispersible and bio-conjugatable, as well as bio-tolerable or bio-compatible. Bio-conjugation means to equip the UCNP surface with bio-recognition elements like antibodies to target cells or proteins.

Different strategies have been well summarized in a review by Sedlmeier et al.[29] Three basic approaches to water dispersible nanoparticles are available: Either, the synthesis is already made with capping agents (surface ligands), that provide water dispersibility, or the hydrophobic capping agents are exchanged against hydrophilic ones. In that case, the new ligands (capping agents) should be used in excess for the phase transfer reaction. Another approach can be the modification of the hydrophobic capping agents to render the UCNPs water dispersible.

Some surface ligands providing water dispersibility can be applied in hydrothermal synthesis, like acetic acid or citric acid.[66] Acid groups on the capping agents work well, due to a little excess of positive charges on the UCNP surface being introduced by the doped Ln(III). A promising approach can also be the usage of polydentate capping agents like ethylenediaminetetraacetic acid (EDTA, a hexadentate chelating capping agent) or polymers like polyacrylic acid (PAA) and polyethylene imine (PEI). The polydentate capping agents can bind via several anchor groups on the UCNP surface. In case of PAA (M_W = 1800 g/mol), the polymer carries about 25 carboxy groups. Mixtures of hydrophobic and hydrophilic capping agents, like 6-aminohexanoic acid and oleic acid ((9Z)-octadecenoic acid) forming a hydrophilic surface around the UCNP have been reported as well.[29]

The capping agents must not be cytotoxic or must not provoke immunologic reactions to be applicable (for purely in vivo applications). Furthermore, the resulting hydrophilic surface needs to have freely available bio-conjugatable groups. Some capping agents can be already equipped with bio-recognition elements or are bio-recognition elements by themselves, e.g., folic acid. PAA is a good agent, too, because it neither leads to cell damage nor cell death. EDTA and PEI are less optimal. EDTA provides less functional groups that need to be used either to "anchor" on the UCNP surface or to bio-conjugate. PEI brings a distinct cytotoxicity.[82]

Despite the challenges of the phase transfer, probably most synthesis result in hydrophobic UCNPs, that are covered with oleic acid or with oleylamine. Post-synthesis surface modifications can be realized with similar capping agents, which are mentioned above, and that coordinate via carboxy groups or amines to the partially posi-

tively charged UCNP surface. The oleic acid (from oleic acid capped UCNPs) can be replaced by citric acid, PAA, or PEI. Furthermore, ligand-free UCNPs can be produced by using acidic condition, under which the hydrophobic oleic acid is protonated and detaches from the UCNP surface. The electrostatic repulsion of ligand-free UCNPs is strongest at pH 4.[83] The "naked" UCNPs can be further surface modified with the desired capping agent. Another oleic acid replacement strategy exists with nitrosonium tetrafluoroborate ($NOBF_4$). The tetrafluoroborate anion attaches loosely on the UCNP surface, but provides sufficient dispersion stability in combination with a mixture of dimethylformamide or dimethyl sulfoxide and water.[84] Subsequent ligand exchange reactions can be further realized after these first surface modifications.

Polymeric ligands are interesting polydentate capping agents, since their properties are variable. Ligands like PAA, polyvinylpyrrolidone (PVP), or polyethylene glycol (PEG) contribute particular properties to the UCNP surface, whereas PAA can suffer from pH changes and protonation under physiological conditions and detach. PEG shows low cytotoxicity, no immunogenecity, and no metabolic degradation during body clearance,[85] which can be advantageous. The combination of PEG and PAA in a copolymer (PEG-PAA) increases the pH stability and reduces possible crosslinking during a ligand exchange reaction than with PAA only. A block-co-polymer like PEG-PLGA (PLGA is poly(lactic-co-glycolic acid)) can be applied if bio-compatibility *and* bio-degradability are desired. Additional approaches being worth to be mentioned are ligand interactions of surfactants with the capping agents on the UCNP surface forming micelles. Polymers like PEG-PLGA or PAA-oleylamine, as well as surfactants like sodium dodecyl sulfate (SDS, negative surface charge) or cetyltrimethylammonium bromide (CTAB, positive surface charge) can be used for that purpose. There is also a layer-by-layer deposition technique in order to achieve particular properties and to control the surface charges via polyanions and/or polycations. Not to forget phospholipid coatings, that mimic cell surfaces, which increase the bio-compatibility and are available in almost any thinkable configuration, and which are adaptable to the desired bio-conjugation approach.[29,86]

Next to ligand interactions and replacements, there are chemical approaches to render UCNPs water dispersible. The oleic acid on UCNP surfaces can be oxidized to azelaic acid (nonanedioic acid) and nonanoic acid by a Lemieux-von-Rudloff reaction. [87,88] The azelaic acid carries two carboxy groups providing water dispersibility and accessible carboxy groups for bio-conjugation. The phase transfer from organic into aqueous phases can also be realized by growing a silica shell on the UCNP surface. There are several protocols in literature showing strategies for silanization to introduce

bio-functional groups via Si-O-Si bonds,[14,29,89] and provide the possibility to bind ligands covalently to the silica shell. Besides a silica shell, CaF_2 can be applied aiming at bio-applications.[82] These surface modifications can be important for in vivo applications, as monodentate ligands as well as polydentate ligands might detach from the UCNPs upon pH changes, dilution effects, or immunologic reactions. These three effects can potentially provoke UCNP coagulation or undesired side effects like accumulation in the lymph nodes or in the liver.

It should be kept in mind, that the transfer into the aqueous phase reduces the overall UC efficiency related to OH-quenching. The phase transfer introduces an additional challenge to the UCNP capping agents. The capping agents should prevent the surface related quenching of the UCNP luminescence by keeping solvent molecules apart and by not quenching the luminescence themselves, e.g., with their hydroxy- or carboxy groups. The growth of a passivating shell on the luminescent UCNP core supports the protection of the UCNP and its luminescence from solvent and capping agent molecules. And as hinted, the usage of surface ligands, that do not only provide water dispersibility, but also protect the UCNP surface from solvent quenching, as discussed in manuscript 3 (section 2.4), can be advantageous.

1.3. Bio-Conjugation Techniques

Bio-conjugation/-labeling is mandatory to use the UCNPs as sensors or labels to detect biomarkers. Those bio-recognition elements can be antibodies, nanobodies, aptamers, oligonucleotides, proteins, lectines, or carbohydrates. They must bind specifically to the desired biomarkers on cell surfaces or in complex biological matrices. The bio-recognition elements on the UCNP surface can be specifically synthesized to meet the desired properties for the application. Different strategies are available for UCNP bio-conjugation, on which a small insight shall be given here.

UCNPs carrying amine, hydroxy, or carboxy groups have a common abundance in proteins and can be conjugated via a Steglich-like esterification with N-hydroxy-succinimide (NHS) or N-hydroxysulfosuccinimide (Sulfo-NHS) and with 1-ethyl-3-(3-dimethylaminopropyl)carbodiimide (EDC) to couple antibodies. Amines or hydroxy groups couple with carboxy groups. Double functionalized linkers could be applied to change from one functional group to the other, although cross-linking between the UCNPs is at high risk and needs often fine tuning. Another approach to bio-conjugate amines can be realized with isothiocyanate functionalized antibodies forming a thiourea group.[29]

The amines, hydroxy, and carboxy groups, as well as aldehydes and thiols, from which the last two are less abundant in proteins, can be addressed for bio-conjugation. This conjugation is not only limited to bio-recognition elements. Other molecules or nanoparticles can be introduced to the UCNP surface as well.[29,90,91] Besides the aforementioned functional groups, there are also epoxides and "click chemistry"-ready functional groups (e.g., used in manuscript 3, section 2.4) usable for bio-functionalization reactions. The "click chemistry"-ready functional group of the polymer, that was used in this study to encapsulate the UCNP, was an azide group. The functionalization was realized with copper(I) catalyzed 1,3-dipolar cycloaddition of the azide with an alkyne group. This can be considered as bio-orthogonal functionalization, becasue biological samples do not react with these groups due to the non-occurrence of those groups in natural samples. Silanization should not be forgotten to complement the list of feasible UCNP bio-conjugations, because with appropriate reagents, that are already equipped with bio-recognition elements, a variety of biomarkers can be targeted.[29]

Some antibodies can be directly immobilized on the UCNP surface. E.g., negatively charged streptavidin can attach on the partially positive charged UCNP surface, if the modifcation is supported by PEG-*b*-PAA as co-ligand to prevent particle aggregation. [29] Another approach for immobilizing streptavidin on a UCNP surface is its coupling to carboxylic acid capped UCNPs.[87] For example, streptavidin-conjugated UCNPs can be used to target biotinylated antibodies (very high binding affinity) to detect methylation of DNA.[92] Another example for direct binding on the UCNP surface is folic acid (Vitamin B_9, B_{11}, or M), which can bind with its carboxylic acid groups on the UCNP surface without loosing its specificity.[29,93] UCNPs carrying folic acid on their surface can target specific cancer cells, that overexpress folic acid receptors on their surface. Other recognition elements can be realized with DNA, glycoprotein, or aptamer surface modified UCNPs.[29]

Strong binding bio-modifications on the UCNP surface are mandatory for bio-relevant applications. In this work (manuscript 3, section 2.4), the UCNPs have been encapsulated in a cage-like system to avoid ligand exchange reactions. The ligand detachment or serious immunologic reactions against bio-functionalized UCNPs, as well as too fast or too slow body clearance is an issue. In this context, the surface polymer used in the presented study to encapsulate the UCNPs showed potentially interesting results on first cells adhesion tests.[94] Depending on the desired application, covalently encapsulated UCNPs may be advantageous over coordinatively encapsulated UCNPs. Other applications may favor the direct immobilization of bio-recognition elements on the UCNP surface (folic acid/DNA). Every surface modification and bio-

conjugation needs in vitro and in vivo testing regarding their bio-compatibility/bio-tolerability prior to be used in bio-medical applications. Unfortunately, the outcomes of in vitro experiments may differ significantly from in vivo reactions, e.g., due to an altered immunologic response of living organisms changing parameters drastically.

1.4. Bio-Relevant Applications

Some examples of possible bio-relevant applications of UCNPs in combination with NIR laser excitation shall be mentioned here without claiming to present a complete list.

Bio-samples are always complex matrices and a challenge for analysis. Only one or a few analytes shall be targeted in a mixture of proteins and optically disturbing substances, that strongly absorb and scatter light. UV excitation suffers from almost no penetration depth in bio-samples due to high absorption and scattering, from auto-fluorescence, and from potential photodamage of the sample. The operation within the limits of the optical windows (vide supra) becomes possible with UCNPs and bio-samples could be examined without purification, e.g., in immunoassays for analysis of full blood, stool, saliva, and urine. For example, the prostate-specific antigen (PSA) is one biomarker for prostate cancer and its concentration in a patient's blood sample could be determined relatively fast with an immunoassay based on UCNPs.[95] Furthermore, UCNPs have several PL emission bands, which can enable multiplexing. Multiplexing means, that several analytes can be determined simultaneously. This could make the examination result for cancer more reliable. In case of prostate cancer, PSA is only one of many predictive and diagnostic biomarkers, that need to be determined.

The UCNP application in combination with NIR excitation is not only limited to applications outside of living organisms. Maybe in the future, UCNPs can be applied in cancer therapy for photodynamic therapy (as one example only). E.g., in 2010, the photodynamic therapy approach has been realized by introducing light via fibers into a cancer infested prostate. A photosensitizer, being optically excited by the Vis-light delivering fibers, produced the desired singlet oxygen.[96] Bio-conjugated UCNPs, that bind specifically to prostate cancer cells and that are equipped with a singlet oxygen producing dye/photosensitizer, can maybe even improve the photodynamic therapy approach and the situation of the patient during the treatment. The therapy from outside of the patient's body could be possible in combination with the NIR excitation. [97] This approach would have a double security mechanism: First, the UCNP binds specifically to the cancer cells due to the UCNP's surface modification. Second, the

bio-conjugated UCNPs are non-toxic until NIR laser irradiation excites the UCNPs. Although this application is adventurous, the implementation of UCNPs in combination with the excitation in the NIR spectral region could be feasible with a reduced harming potential for the patient. This approach is not limited only to prostate cancer and this kind of therapy.

1.5. Scientific Approach

In this work, two parts of the upconversion field are focused. First, the UCNP synthesis was optimized to enhance the UC quantum efficiency and to yield nanoparticles in the hexagonal crystal phase. XRD, Raman, and laser spectroscopic investigations have been performed. The brightest UCNPs have been realized with core-shell structures. Nevertheless, these UCNPs still remain behind their expected brightness in comparison with their bulk material. There is a discrepancy related to dopant migration within the host lattice. This migration leads to a transition layer between the UCNP core and shell resulting in a concentration gradient, which changes the understanding of clearly separated cores and shells towards the existence of a transition layer between those. This work contributes to those investigations using optical methods and an LRET equation based on the interlanthanoid resonance energy transfer (LRET). Several sets of core-shell-shell UCNPs have been synthesized, where the LRET-acceptor and the LRET-donor have been doped in the core and in the outer shell, respectively. The first inner shell serves as an insulation layer, whose thickness gradually increases within one set and accordingly also increases the donor-acceptor distance and decreases the LRET efficiency. These results are published in two manuscripts (section 2.2 and section 2.3).

The second major research focus was a robust and fast phase transfer reaction to prepare UCNPs for applications in biological media. Several approaches have been investigated yielding in very good and less good reproducibility. Some of those experiments, of which some were project related, are summarized in the appendix section S.2. Finally, the most promising UCNP capping ligand has been used to couple an appropriate dye to Er^{3+}-doped UCNPs. The UCNP-to-dye RET of this system has been investigated. The coupling with the dye presents a proof-of-principle reaction for potential bio-conjugation reactions of the UCNPs with the applied ligand. This ligand is a bio-inspired coating polymer and applied for the first time for the encapsulation of UCNPs. The results are published in one manuscript (section 2.4).

2

Manuscripts

2.1. Contribution to the Manuscripts

This section lists the original publications ordered by the research topic and chronologically. The respective supporting information (SI) are listed in the appendix section S.1.

(1) P. U. Bastian, S. Nacak, V. Roddatis, M. U. Kumke, "Tracking the Motion of Lanthanide Ions within Core–Shell–Shell $NaYF_4$ Nanocrystals via Resonance Energy Transfer", *The Journal of Physical Chemistry C* **124** (20), 11229–11238 (2020).[98]

The nanoparticle design, synthesis approach, and analysis methods were discussed between apl. Prof. Dr. Michael Kumke, Dr. Selma Nacak, and me prior to starting with the experiments. I performed the synthesis that I adapted for our purposes from Dr. Julia Hesse thanks to a previous collaboration with Dr. Dennis T. Klier.[99] The steady-state and time-resolved luminescence emission and total luminescence spectroscopy was performed by Dr. Selma Nacak, who taught me the important details of Eu^{3+} spectroscopy. The theoretical evaluation of the spectra was performed by myself, also with the help of an LRET equation derived from the FRET theory. The TEM grids and the XRD silicon sample holders were prepared by me. Dr. Richard Wirth and Dr. Vladimir Roddatis carefully recorded the TEM images at the GFZ in Potsdam. Dr. Christina Günter took care of the prepared XRD sample holders. I wrote the manuscript together with apl. Prof. Dr. Michael Kumke, Dr. Selma Nacak, and Dr. Vladimir Roddatis. The data evaluation and preparation of the figures and illustrations were realized by myself with the help of MATLAB® and OriginLab (OriginPro®), as well as the listed software solutions in the manuscript, Microsoft® tools, and the open source software Inkscape®.

The published manuscript is shown in section 2.2. The corresponding supporting information are shown in the appendix, subsection S.1.1.

(2) P. U. Bastian, N. Robel, P. Schmidt, T. Schrumpf, C. Günter, V. Roddatis, M. U. Kumke, "Resonance Energy Transfer to Track the Motion of Lanthanide Ions – What Drives the Intermixing in Core-Shell Upconverting Nanoparticles?", *Biosensors* **11** (12), 515 (2021).[100]

This publication is based on three bachelor theses, which I supervised. The nanoparticle design and synthesis approach were discussed previously by apl. Prof. Dr. Michael Kumke and me. The synthesis followed a detailed protocol, that was prepared as previously discussed. The synthesis, the optical investigation by laser spectroscopy, as well as the preparation of the TEM grids and the XRD sample holders were performed by the Bachelor students, Nathalie Robel, Tim Schrumpf, and Peter Schmidt. The XRD patterns and the TEM images were recorded by Dr. Christina Günter and by Dr. Vladimir Roddatis, respectively. The experimental data were theoretically evaluated and discussed by the bachelor students, apl. Prof. Dr. Michael Kumke, and me. The spectroscopic data were as well analyzed with an LRET equation derived from the FRET/LRET theory. The bachelor students wrote their theses based on these experiments. I wrote the manuscript based on the findings of the bachelor students together with apl. Prof. Dr. Michael Kumke, Dr. Christina Günter, and Dr. Vladimir Roddatis. The additional data evaluation and preparation of the figures and illustrations were realized with the help of MATLAB® and OriginLab (OriginPro®), as well as the listed software solutions in the manuscript, Microsoft® tools, and the open source software Inkscape®.

The published manuscript is shown in section 2.3.

(3) P. U. Bastian, L. Yu, A. López de Guereñu, R. Haag, M. U. Kumke, "Bioinspired Confinement of Upconversion Nanoparticles for Improved Performance in Aqueous Solution", *The Journal of Physical Chemistry C* **124** (52), 28623–28635 (2020).[101]

The nanoparticle design and synthesis were discussed by apl. Prof. Dr. Michael Kumke, Dr. Anna López de Guereñu, and me. I performed pre-experiments for the appropriate chemical ratios. The particular coating polymer has been provided and the coating procedure has been taught by Dr. Leixiao Yu and Prof. Rainer Haag. I planned, performed, and evaluated the respective experiments. The XRD experiments and the TEM images were recorded by Dr. Christina Günter and Dr. Vladimir Roddatis. I wrote the manuscript together with apl. Prof. Dr. Michael Kumke, Dr. Anna López de Guereñu, Dr. Leixiao Yu, and Prof. Rainer Haag. The data evaluation and preparation of the figures and illustrations were realized by myself with the help of MATLAB® and OriginLab (OriginPro®), as well as the listed software solutions in the manuscript, Microsoft® tools, ChemDraw® and the open source software Inkscape®.

The published manuscript is shown in section 2.4. The corresponding supporting information are shown in appendix subsection S.1.2.

2.2. Trivalent Lanthanoid Cation Migration in the Sodium Yttrium Fluoride Host Lattice – Supervision via the Eu^{3+}-to-Nd^{3+} Lanthanoid Resonance Energy Transfer (Manuscript 1)

"Tracking the Motion of Lanthanide Ions within Core–Shell–Shell $NaYF_4$ Nanocrystals via Resonance Energy Transfer"

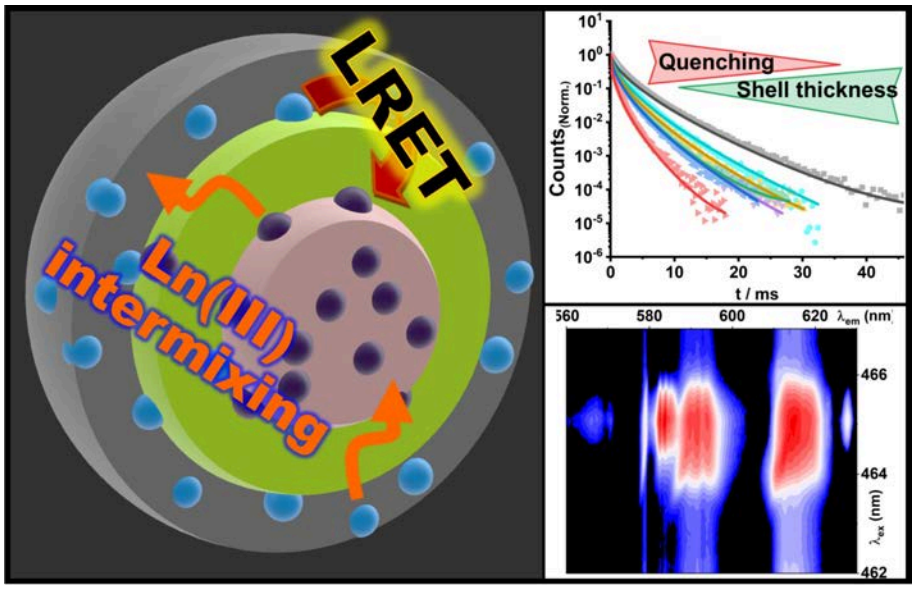

J. Phys. Chem. C **124** (20), 11229–11238 (2020).[98]

Link: https://doi.org/10.1021/acs.jpcc.0c02588

ACS Article on Request author-directed link:
http://pubs.acs.org/articlesonrequest/AOR-GXRJDUNF9HQ58X2NBQIV

THE JOURNAL OF PHYSICAL CHEMISTRY C

pubs.acs.org/JPCC Article

Tracking the Motion of Lanthanide Ions within Core−Shell−Shell $NaYF_4$ Nanocrystals via Resonance Energy Transfer

Philipp U. Bastian, Selma Nacak, Vladimir Roddatis, and Michael U. Kumke*

Cite This: *J. Phys. Chem. C* 2020, 124, 11229−11238 Read Online

ACCESS | Metrics & More | Article Recommendations | Supporting Information

ABSTRACT: Lanthanide resonance energy transfer (LRET) was used to investigate the motion of dopant ions during the synthesis of core−shell−shell nanocrystals (NCs) that are frequently used as frequency upconversion materials. Reaction conditions (temperature, solvent) as well as lattice composition and precursors were adapted from a typical hydrothermal synthesis approach used to obtain upconversion nanoparticles (UCNPs). Instead of adding the lanthanide ions Yb^{3+}/Er^{3+} as the sensitizer/activator couple, Eu^{3+}/Nd^{3+} as the donor/acceptor were added as the LRET pair to the outer shell (Eu^{3+}) and the core (Nd^{3+}). By tailoring the thickness of the insulation shell ("middle shell"), the expected distance between the donor and the acceptor was increased beyond 2 R_0, a distance for which no LRET is expected. The successful synthesis of core−shell−shell NCs with different thicknesses of the insulation layer was demonstrated by high-resolution transmission electron microscopy measurement. The incorporation of the Eu^{3+} ions into the $NaYF_4$ lattice was investigated by high-resolution time-resolved luminescence measurements. Two major Eu^{3+} species (bulk and surface) were found. This was supported by steady-state as well as time-resolved luminescence data. Based on the luminescence decay kinetics, the intermixing of lanthanides during synthesis of core−shell UCNPs was evaluated. The energy transfer between Eu^{3+} (donor) and Nd^{3+} (acceptor) ions was exploited to quantify the motion of the dopant ions. This investigation reveals the migration of Ln^{3+} ions between different compartments in core−shell NCs and affects the concept of using core−shell architectures to increase the efficiency of UCNPs. In order to obtain well-separated core and shell structures with different dopants, alternative concepts are needed.

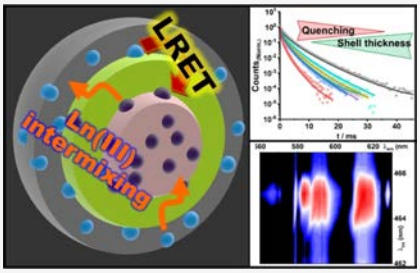

INTRODUCTION

The upconversion effect is a nonlinear optical effect which was predicted by Bloembergen in 1958 with an excited state absorption approach. Upconversion was discussed in detail by Auzel in 1966 who introduced the term APTE effect (for addition de photon par transferts d'énergie). Later, the term ETU (for energy transfer upconversion) was established, which is colloquially called upconversion (UC) in the research field of upconversion nanoparticles (UCNPs). The UC effect opens several application possibilities, for example, light harvesting, counterfeiting, solid-state lasers, and imaging in the biological environment, as well as theranostic platforms.[1−6]

Recently, the UC process has been investigated to find the best synthesis methods as well as the optimal crystal structure and dopants.[7−10] In case of a $NaYF_4$ host lattice, the hexagonal crystal phase (β-phase) shows better UC efficiency than its cubic crystal phase (α-phase).[11] The optical properties of the UC materials can be tuned by the dopants, which are lanthanide (Ln^{3+}) ions because of their outstanding electronic properties, here the ladder-like electronic level scheme. The dopants are chosen depending on the excitation source to be used (Yb^{3+} for 976 nm excitation and Nd^{3+} for 800 nm excitation, called sensitizer) and depending on the desired photoluminescence (luminescence) emission of the so-called activators (e.g., Er^{3+}, Tm^{3+}, Ho^{3+}). Next to the research on the ETU mechanism, it is of major importance to enhance the UC quantum yield for instance by using dye sensitization[12] and/or by adding passivating shells, which has been introduced in 2007.[13,14] One can expect a perfect order of core and shell in such UCNPs, as illustrated in Figure 1. The application of an inert shell with sufficient thickness distinctly reduces surface quenching and consequently enhances the UC efficiency becoming independent on surrounding media or ligands. However, experimental results from luminescence kinetic measurements show that surface quenching still plays a role and subsequently decreases upconversion efficiency significantly. Very similar observations and core/shell intermixing were also reported by Würth et al.[15] and Homann et al.[16] This

Received: March 24, 2020
Revised: April 23, 2020
Published: April 24, 2020

https://dx.doi.org/10.1021/acs.jpcc.0c02588
J. Phys. Chem. C 2020, 124, 11229−11238

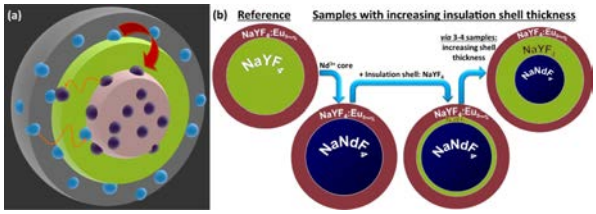

Figure 1. (a) Illustration of the basic idea. Reference = $NaYF_4$ @ $NaYF_4$:$Eu_{(5mol\%)}$ & set 1: $NaNdF_4$ @ $NaYF_4$ @ $NaYF_4$:$Eu_{(5mol\%)}$ & set 2: $NaYF_4$:$Nd_{(20mol\%)}$ @ $NaYF_4$ @ $NaYF_4$:$Eu_{(5mol\%)}$. The first $NaYF_4$ shell serves as the insulation shell to tune the spatial separation of Nd^{3+} and Eu^{3+}. Nd^{3+}/Eu^{3+} samples with no insulation shell are synthesized as reference for maximum quenching efficiency. Wavy orange arrow = Ln^{3+} migration; single curved thick red arrow = energy transfer from Eu^{3+} (in light blue) to Nd^{3+} (in violet). (b) Scheme of stepwise synthesis: $NaYF_4$:$Nd_{(20mol\%)}$ @ $NaYF_4$ @ $NaYF_4$:$Eu_{(5mol\%)}$ NC.

is especially problematic when the UCNPs equipped with a passivating shell are transferred into aqueous media (possessing strong luminescence quenching capacities), which is mandatory for further biosensing applications using UCNPs as luminescence probes. Recent experiments performed by Hudry et al.,[3,17−19] Dong et al.,[20] and by Chen et al.[21] investigated the ion migration using atom mapping techniques to visualize the dopant distribution in core shell UCNPs. The Ln^{3+} ions are distributed in an intermixing layer between the core and shell structure (Hudry et al.). It was shown that Ln^{3+} ions can diffuse within the host lattice (which is built normally from rare earth ions such as Sc^{3+} or Y^{3+}). For instance, Yb^{3+}, Er^{3+}, and Y^{3+} can exchange their positions in the crystal. It was further shown that a CaF_2 shell could inhibit the cation exchange, probably because of the different oxidation state of the Ca^{2+} ions (Dong et al.). The motion of Ln^{3+} ions is assumed to happen via vacancies in the host lattice being favored at elevated temperatures (Chen et al.), whereas elevated temperatures can be as low as 280 °C. At 200 °C, only little Ln^{3+} diffusion was observed by Liu et al. who also demonstrated a dependency on the dopant concentration.[22] Better understanding of the Ln^{3+} diffusion properties could be exploited by adaption of the synthesis approach to optimize luminescence quantum yield[23,24] and to favor or to suppress ion diffusion to aim at particular ion distributions depending on the desired application.[25−27]

In the present paper, the motion of Ln^{3+} ions between different layers was reinvestigated for $NaYF_4$ core−shell-based nanoparticles synthesized via a thermal decomposition synthesis.[28] The dopants, Ln^{3+} ions, Yb^{3+}, and Er^{3+}, which are regularly used in UCNPs, were exchanged for Nd^{3+} and Eu^{3+} in order to introduce a lanthanide resonance energy transfer (LRET) pair into the lattice instead. Because of the spectral overlap between the energy donor (Eu^{3+}) and the energy acceptor (Nd^{3+}), the Eu^{3+} luminescence is quenched depending on the distance between the donor and the acceptor in cases for which the distance between the two Ln^{3+} ions is smaller than twice the Förster radius (see Figure 1a). The Förster radius is a donor−acceptor pair characteristic distance obtained from the respective photophysical properties and defines the distance R_0 between the donor and the acceptor at which the efficiency of resonance energy transfer is 50%. The donor and acceptor ions (Eu^{3+} and Nd^{3+}, respectively) are separated by an insulation shell of different thicknesses. It is supposed that the efficiency of the energy transfer is dependent on the insulation shell thickness. In the case of Ln^{3+} ions migrating toward each other, a deviation from the theoretical distance dependence is expected to be observed. The conceptual approach is illustrated in Figure 1b. In total, two sets of nanocrystals (NCs) were synthesized based on the same general synthesis route regularly used for UCNPs.[29] Both NC sets have their respective reference sample with $NaYF_4$-only cores and a $NaYF_4$:$Eu_{(5mol\%)}$ shell grown directly on top of the core (indicated as Ref). The molar percentage describes the amount of trivalent ions (Ln^{3+} or Y^{3+}). Trivalent ions occupy the same positions in the hexagonal crystal lattice (indicated for the hexagonal unit cell in Figure 2), so that the shell

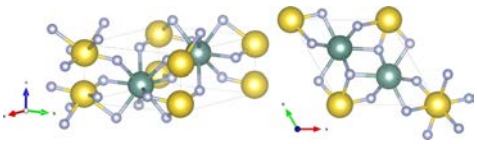

Figure 2. Hexagonal $NaYF_4$ NC unit cell ($P6_3/m$ space group). Yellow = Na^+; grey = F^-; green = Y^{3+} or Ln^{3+}. Two positions in the hexagonal unit cell are available either for vacancies or Y^{3+} or Ln^{3+} ions. (Unit cell structure of hexagonal $NaNdF_4$ ($P\bar{6}$ space group) is illustrated in the Supporting Information, Figure S2). Both space groups are very similar to each other, whereas $P6_3/m$ shows a higher symmetry than $P\bar{6}$.[11] Images are created with open-source software package VESTA.[47]

contains 95 mol % Y^{3+} ions and 5 mol % Eu^{3+} ions. The other NCs consist either of a pure $NaNdF_4$ core (set 1) or of a $NaYF_4$:$Nd_{(20mol\%)}$ core (set 2). The core doping with 20 mol % Nd^{3+} has been chosen on the basis of the common UCNP composition with 18 mol % Yb^{3+} and 2 mol % Er^{3+} or 19 mol % Yb^{3+} and 1 mol % Tm^{3+}. The remaining 80 mol % are Y^{3+} ions. The respective NC core samples were equipped with either no insulation shell (denoted as S0) or insulation shells with increasing thickness (denoted as S1 up to S5, 1st shell = $NaYF_4$ and is referred to as the insulation shell). Increasing sample number indicates increasing insulation shell thickness. The outer shell is always $NaYF_4$:$Eu_{(5mol\%)}$ (see Figure 1b and for more details please refer to Table 1).

EXPERIMENTAL SECTION

Materials. The rare earth chlorides $RECl_3 \cdot 6\,H_2O$ (RE: Y^{3+}; Nd^{3+}; Eu^{3+}, purities >99.99%) and ammonium fluoride (NH_4F, ≥99.99%) were purchased from Sigma-Aldrich. Oleic acid (OA, 90% purity) was purchased from Alfa Aesar. Therminol 66 was purchased from FRAGOL GmbH+Co. KG.

https://dx.doi.org/10.1021/acs.jpcc.0c02588
J. Phys. Chem. C 2020, 124, 11229−11238

Table 1. Size Evaluation by TEM, Showing the Diameter *d*, the Standard Deviation *σ*, and the Layer Thickness of the Insulation Shell[a]

	set 1			set 2		
sample ID	*d*/nm	*σ*/nm	layer thickness/nm	*d*/nm	*σ*/nm	layer thickness/nm
Ref_C [$NaYF_4$]	5	1		5	1	
Ref_CS [$NaYF_4$ @ $NaYF_4$:Eu]	10	3	2.4	9	2	2.3
S0_C [core]	5	1		4	1	
S0_CS [core @ $NaYF_4$:Eu]	9	3	2.4	10	2	2.7
S1_C [core]	4	1		4	1	
S1_CS [core @ $NaYF_4$]	7	2	1.4	6	2	1.0
S1_CSS [core @ $NaYF_4$ @ $NaYF_4$:Eu]	8	2	0.6	8	2	0.9
S2_C [core]	4	1		4	1	
S2_CS [core @ $NaYF_4$]	8	2	1.9	7	2	1.5
S2_CSS [core@ $NaYF_4$ @ $NaYF_4$:Eu]	10	2	0.8	10	2	1.4
S3_C [core]	4	1		5	1	
S3_CS [core @ $NaYF_4$]	8	2	1.9	8	2	1.6
S3_CSS [core @ $NaYF_4$ @ $NaYF_4$:Eu]	10	2	1.0	9	2	0.5
S4_C [core]	4	1		5	1	
S4_CS [core @ $NaYF_4$]	9	2	2.6	10	4	2.7
S4_CSS [core @ $NaYF_4$ @ $NaYF_4$:Eu]	13	2	2.0	11	2	0.7
S5_C [core]				5	1	
S5_CS [core @ $NaYF_4$]				12	3	3.7
S5_CSS [core @ $NaYF_4$ @ $NaYF_4$:Eu]				13	3	0.4

[a]The NC composition is shown in the square brackets. Here, core stands for $NaNdF_4$ for set 1 or $NaYF_4$:$Nd_{(20mol\%)}$ for set 2. Eu^{3+} is always doped with a molar amount of 5 mol %. The denomination "_C" indicates the core NC, "_CS" indicates the core with the insulation shell and "_CSS" indicates the final NC carrying an outer shell doped with Eu^{3+}—except for Ref and S0, where no insulation shell is present and "_CS" already represents the core with the Eu^{3+} doped shell.

Ethanol (≥99.8%; 1% MEK), sodium hydroxide (≥99.9%), and cyclohexane (ROTISOLV ≥99.9%, GC Ultra Grade) were purchased from Carl Roth. All chemical reagents were used as received without further purification.

Synthesis of $NaYF_4$-Based Core and Core Shell UCNPs. *Core Synthesis of $NaY_{(1-x)}Nd_xF_4$ (x = 1 or 0.2).* The rare earth metal chlorides ($YCl_3 \cdot 6\ H_2O$; $NdCl_3 \cdot 6\ H_2O$) were used either as 1 mmol of Nd^{3+} or as 0.8 mmol of Y^{3+} and 0.2 mmol of Nd^{3+} for the sample cores. The reference core was synthesized with 1 mmol of Y^{3+}. The rare earth chlorides, OA (25.2 mmol, 8 mL, 7.12 g) and Therminol 66 (12 mL) were transferred into a 50-mL-three-necked flask. The reaction mixture was evacuated for 10 min at room temperature, then stepwise heated up to 140 °C under vacuum and vigorous stirring. The temperature was kept for 45 min, cooled down to 50 °C, and vented with argon. Sodium hydroxide (4 mmol) and ammonium fluoride (6.4 mmol) were added under an argon counter stream. The system was re-evacuated and kept at 80 °C for 30 min until the added salts had dissolved. The reaction mixture was vented with argon and heated up to 320 °C (heat rate: 25 °C/min). The temperature was kept for 15 min. The reaction mixture was cooled down to 250 °C by air, followed by cooling with a water bath to 60 °C. Nanoparticle purification was performed by washing three times with ethanol and centrifugation at 3100*g* for 8 min. Finally, the precipitate was dispersed in cyclohexane (15 mL).

Precursor Synthesis for $NaYF_4$ and $NaYF_4$:Eu Shells. Depending on the shell composition, either $YCl_3 \cdot 6\ H_2O$ (2 mmol), for the insulation shell, or $YCl_3 \cdot 6\ H_2O$ (1.8 mmol) and $EuCl_3 \cdot 6\ H_2O$ (0.1 mmol), for the second shell, were used. The trivalent metal chlorides, OA (4 mL = 3.56 g) and Therminol 66 (8 mL) were transferred into a 50-mL-three-necked flask, evacuated for 10 min and under vacuum stepwise heated up to 140 °C. This temperature was maintained for 45 min. The reaction mixture was cooled down to 50 °C. Under an argon counter stream, sodium oleate (2.5 mmol) and ammonium fluoride (4 mmol) were added. The system was re-evacuated and kept at 80 °C for 30 min until the added salts had dissolved. The reaction mixture was vented with argon and stored for later use with an argon atmosphere.

UCNP Core–Shell Synthesis. Core-UCNPs (60 mg) were transferred into a 50-mL-three-necked flask. OA (8 mL = 7.12 g) and Therminol 66 (12 mL) were added. The reaction mixture was evacuated for 30 min at 75 °C. After venting with argon, it was heated up to the injection temperature (305 °C) and 1 mL of precursor solution was added with a rate of 2 mL/h (either $NaYF_4$ precursor solution for the insulation shell or $NaYF_4$:Eu precursor solution for the second shell). For the insulation shell, the precursor solution volume was varied, depending on the desired shell thickness: 0.25 mL (for S1_CS), 0.5 mL (for S2_CS), 1.0 mL (for S3_CS), 2.0 mL (for S4_CS) and 4.0 mL (for S5_CS) were chosen. The precursor solution (1 mL) was always taken for the final Eu^{3+}-doped $NaYF_4$ shell. After finishing the precursor addition, 305 °C was maintained for further 5 min. Then, the reaction mixture was cooled down and purification was performed as described for the core-UCNPs. Finally, cyclohexane (8 mL) was added.

Photoluminescence Emission Spectroscopy. Time-gated luminescence emission spectra were recorded after excitation with a wavelength tunable pulsed Nd:YAG/OPO laser system operated at 10 Hz (26 mJ per pulse/130 mW). The laser is from Quanta Ray, Spectra Physics, Mountain View, CA, USA. The optical parametric oscillator is from GWU-Lasertechnik Vertriebsges. mbH, Erftstadt, Germany. Emitted light was recorded using an intensified CCD-camera (iStar DH720-18V-73, Andor Technology, Belfast, Great Britain) combined with a spectrograph from Shamrock (SR

https://dx.doi.org/10.1021/acs.jpcc.0c02588
J. Phys. Chem. C 2020, 124, 11229−11238

303i, Andor Technology, Belfast, Great Britain) equipped with a 600 L/mm grating blazed at 500 nm. Luminescence decay kinetics are recorded using a stroboscopic technique.[30] Each measurement was performed using an initial delay of 500 ns.

Low-Temperature Photoluminescence Emission Spectroscopy (4 K) (TLS/EEMS). Total luminescence spectroscopy (TLS) or excitation−emission-matrix spectroscopy (EEMS) was performed using the same excitation and emission recording setup as above with the only difference that the excitation light was coupled into an optical multicore Y-fiber which also collected the emission light. The sample chamber was cooled to 4 K with a cryostat system equipped with a helium compressor (Sumitomo Heavy Industries Ltd., Markt Indersdorf, Germany) and a temperature controller (331 temperature controller, Lake Shore, Westerville, OH). The sample chamber was evacuated with a turbo-vacuum pump (Leybold Vacuum Turbolab 80, Oerlikon, Köln, Germany). TLS spectra were recorded with an excitation scan from 451 to 467 nm with a scan speed of 0.4 nm/min.

Size (TEM) and Structural (XRD) Investigations. The UCNP diameter was determined with the software Image Sys Prog (version 1.2.5.16 ×64). The TEM images were recorded with a transmission electron microscope (Tecnai G2 F20 X-Twin, from FEI/Thermo Fisher Scientific) operated at 200 kV acceleration voltage.

X-ray powder diffraction patterns were recorded on a PANalytical Empyrean powder X-ray diffractometer with Bragg−Brentano geometry. The diffractometer is equipped with a PIXcel1D detector using Cu Kα radiation (with Kα wavelength λ = 1.5419 Å) operating at 40 kV and 40 mA. The pulse height distribution (PHD) level of the of the detector was set to 45−80, with an active length of 3.0061°, to reduce the fluorescence. Theta−theta scans were run over a 2θ range of 4−70° with a step size of 0.0131° and sample rotation time of 1 s within 190 min.

Theory. The migration of trivalent cations in the NC structure is investigated with the theoretical approach of the Förster resonance energy transfer (FRET) between Eu^{3+} and Nd^{3+} used as the energy donor (D) and acceptor (A), respectively. The spectral overlap in the range from 550 to 650 nm results from the Eu^{3+} luminescence transitions ($^5D_0 \rightarrow {}^7F_1$ and $^5D_0 \rightarrow {}^7F_2$) and the Nd^{3+} absorption ($^4G_{5/2} + {}^2G_{7/2} \leftarrow {}^4I_{9/2}$).[31−36] Only the $^5D_0 \rightarrow {}^7F_2$ transition of Eu^{3+} as the most intense emission band is evaluated [see Figure 4, transition (iv)].[31,34,37−41]

$$I_D(t) = I_D(0)\exp\left[-\left(\frac{t}{\tau_D}\right)^{\beta_D}\right] + y_0 \quad (1)$$

The luminescence decay kinetics of Eu^{3+} in the reference samples are analyzed with a stretched exponential in order to account for small variations in the local environment of the Eu^{3+} ions in the host lattice, eq 1. The presence of such variations is indicated by the non-monoexponential luminescence decay traces found for these samples.[42] Hence, the stretched exponential model describes the Eu^{3+} luminescence as a spatial distribution of Eu^{3+} ions in the crystal lattice.

The index D represents the donor photoluminescence in absence of the acceptor. $I_D(t)$ is the donor luminescence intensity to the given time t. $I_D(0)$ is the initial donor luminescence intensity (corresponding to the amplitude of the exponential function). τ_D is the donor luminescence decay time (in absence of A) and β_D is a heterogeneity parameter characterizing the slight variations in the environment of the donor. For $\beta_D < 1$, the function is termed stretched. For β_D = 1, a mono-exponential function would be obtained indicating non-heterogeneity with respect to the donor sites in the host lattice.

The quenched donor luminescence kinetics are analyzed using eq 2.[30,34,37] The equation was modified to consider the distribution with respect to the donor (vide supra and eq 1).

$$I_{DA}(t) = I_{DA}(0)\exp\left[-\left(\frac{t}{\tau_D}\right)^{\beta_D} - 2\gamma\left(\frac{t}{\tau_D}\right)^{\alpha/2}\right] + y_0 \quad (2)$$

$$\gamma = \frac{\sqrt{\pi}}{2} c_A \frac{4}{3}\pi {R_0}^3 \quad (2a)$$

The indices D and DA represent the donor in the absence of the acceptor and the donor in the presence of the acceptor, respectively. $I_{DA}(t)$ is the donor luminescence intensity in the presence of the acceptor at the given time t. $I_{DA}(0)$ is the initial donor luminescence intensity in the presence of the acceptor (the amplitude of the exponential function) and y_0 represents any background signal. τ_D is deduced from the reference measurements with unquenched donor luminescence. In addition to β_D, a second parameter α was introduced. α describes the heterogeneity of the acceptor distribution around the donor. Most importantly, γ is the parameter describing the acceptor concentration in a specific volume defined by the Förster radius of the particular donor−acceptor pair (see eq 2a). Here, c_A is the acceptor concentration (in acceptor molecules/ions per Å^3). The term $c_A\frac{4}{3}\pi {R_0}^3$ defines the average number of acceptor molecules (ions) in a sphere with the radius R_0. In the present case, R_0 is the Förster radius of Eu^{3+} and Nd^{3+} is donor−acceptor pair ($R_0[Eu^{3+}/Nd^{3+}]$ = 8.53 Å).[31] With the definition of a three-dimensional quenching sphere with the radius $R_0[Eu^{3+}/Nd^{3+}]$ around one Eu^{3+} donor, the term Förster volume will be used now (illustrated in the Supporting Information, Figure S1). For the further data analysis, the following assumptions are introduced: (i) the dimensionality of the system is 3D as the UCNP is a three dimensional object; (ii) the main interaction behavior between Eu^{3+} and Nd^{3+} is of dipole−dipole character as found by Joshi et al.[34]

Ln^{3+} Migration in a $NaYF_4$ Unit Cell. The $NaYF_4$ hexagonal host lattice crystalizes either in the $P6_3/m$ or $P\bar{6}2m$ or $P\bar{6}$ space group.[43] $NaNdF_4$ crystallizes in the $P\bar{6}$ space group (illustration in the Supporting Information, Figure S2).[11,43−46] Based on the X-ray diffraction (XRD) data (vide infra), for the further discussion it is suggested that in the present case, $NaYF_4$ crystallizes within the $P6_3/m$ space group (see Figure 2), in which Na^+ ions create the corners with F^- ions on the edges of the unit cell. The trivalent ions (Y^{3+} and Ln^{3+}) are centered in the unit cell. The two center positions can also be vacant (at low F^- concentration) or be occupied by Na^+ (but only with a small probability). The volume of such a unit cell is 109.2 Å^3 with the edge lengths of a = 5.97567 Å and c = 3.53053 Å.[11]

The maximum number of trivalent ions neighboring one Eu^{3+} ion within the Förster volume with R_0 is 46 (illustrated in the Supporting Information, Figure S1), which is consequently the maximum number of Nd^{3+} ions possible for neighboring one Eu^{3+}. The Förster volume contains approximately 29 unit

https://dx.doi.org/10.1021/acs.jpcc.0c02588
J. Phys. Chem. C 2020, 124, 11229−11238

cells. Most likely, the calculated acceptor number based on eq 2 will be significantly smaller than 46. With increasing insulation shell thickness, Eu-to-Nd-energy transfer is expected to decrease as the spatial separation will increase. Accordingly, the quenching of the Eu^{3+} luminescence stops with sufficient large insulation shell thickness.

Crystal Field Strength Parameter. The crystal field strength parameter is a good measure to estimate the electrostatic field properties, having most often a significant effect on d and f orbitals. With the structure sensitive Eu^{3+} optical probe, changes of the crystal field within the NC can be determined spectroscopically. TLS was performed at 4 K for the different Eu^{3+}-doped NCs. The Stark splitting of the ^7F_j levels of Eu^{3+} is a result of the crystal field created by the coordination sphere. If the coordination sphere changes, the crystal field strength parameter will change as well. For instance, the $^7F_1$ energy level can split depending on the symmetry point group at the Eu^{3+} ion into maximal three sublevels, denoted as $^7F_{1-1}$; $^7F_{1-2}$; and $^7F_{1-3}$. The crystal field strength parameter $N_v(B_{2q})$ describes the effective crystal field surrounding the Eu^{3+} ion (see eqs 3 and 3a) and depends on different parameters which alter the charge density in the surrounding of Eu^{3+} ion. This subsequently means for the present samples that the neighboring ions of the Eu^{3+} (e.g., here: Nd^{3+}, Y^{3+}, vacant lattice places, Na^+ or F^-) might influence $N_v(B_{2q})$.

$$N_v(B_{2q}) = \sqrt{\frac{\pi(2+\alpha^2)}{0.3}}\Delta E \tag{3}$$

$$\alpha = \frac{E_b - E_c}{\Delta E/2} \tag{3a}$$

The ΔE value describes the energy difference of the $^7F_{1-1}$ and the $^7F_{1-3}$ Stark levels (in cm^{-1}). E_b is the barycenter or mean energy of the $^5D_0 \rightarrow {}^7F_1$ multiplet. E_c corresponds to the $^7F_{1-2}$ peak position (in cm^{-1}). The respective peak centers are determined with a Gauss regression of the $^5D_0 \rightarrow {}^7F_1$ multiplet.[48]

RESULTS AND DISCUSSION

The sample IDs and the corresponding compositions of set 1 as well as of set 2 are given in Table 1. TEM was used to determine the overall size of the particles and to estimate the average diameter of the different layers formed around the NC cores (see Figure 1 and Table 1). The NC cores used as starting material to obtain the different samples had a diameter of approx. 4.5 nm. TEM images are shown in Figure 3 (top). The size of particles increases with shell growth. The selected samples shown are of set 1 and set 2, respectively. TEM images of all other samples can be found in the Supporting Information, Figures S6 and S7. By adapting the amount of added $NaYF_4$ shell precursor material, the thickness of the insulation shell is tailored in the range between 1 and 3.7 nm. The largest insulation shell thickness exceeds the Förster radius $R_0[Eu^{3+}/Nd^{3+}]$ by a factor of 4.

The XRD data reveal the largest differences between the core only NC (*NC*_C) and core−shell NC (*NC*_CS, $NaYF_4$ shell) (see Figure 3, bottom). Most probably, it relates to the Nd^{3+} doping of the core as well as the different synthesis conditions for the core and addition of the shell. With increasing shell thickness, the sample XRD patterns resemble stronger the reference XRD patterns of the β-$NaYF_4$; however,

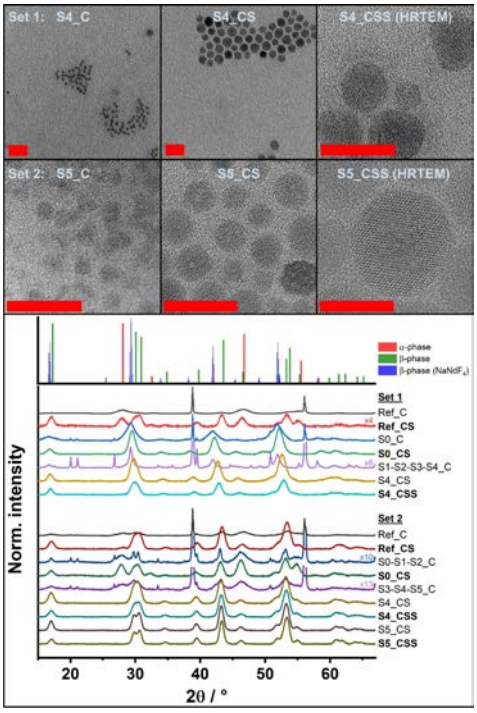

Figure 3. TEM images and XRD-patterns of NCs (top and bottom respectively). Top: Exemplary TEM images of S4 (set 1) and S5 (set 2) are shown to show the diameter increase with each additional shell starting with the core. Detailed size information can be found in Table 1. The red scale bar corresponds to 20 nm. In some sample images, different lattice planes can be seen. Bottom: Selected XRD patterns show the core $NaNdF_4$ (set 1) and $NaYF_4$:$Nd_{20mol\%}$ (set 2). The insulation shell is $NaYF_4$. The second outer shell is $NaYF_4$:$Eu_{5mol\%}$. XRD reference patterns are shown above: α-$NaYF_4$ (red, ICDD PDF #77-2042) and β-$NaYF_4$ (green, ICDD PDF #16-334) and the β-$NaNdF_4$ (blue, ICSD: 424386).[49−51] The patterns of the core NC deviate from the core−shell NC. Strong reflexes at 39 and 56° are attributed to α-NaF (ICSD: 43611). Peak tips are masked for better visibility of other reflexes. The double reflexes at 20 and 21° belong to β-Na_2SiF_6 (ICSD: 16598). Reflexes at 30 and 53° shift right with increasing shell thickness relating to Nd^{3+} doping, its crystallization in the $P\bar{6}$ space group, and its relative decrease with larger $NaYF_4$ shells. $NaYF_4$ crystallizes in the $P6_3/m$ space group. Its reflexes resemble stronger a hexagonal gagarinite structure ($P6_3/m$, ICSD: 39696). Comparison with references shows: Increasing shell thickness matches better with β-$NaYF_4$ reference patterns.

an influence of the Nd-doped core stays visible through all samples.[49−51] The shift of the reflexes at 30 and 53° to larger 2θ values corresponds to the increasing amount of $NaYF_4$ in the respective NC. Starting with Nd-doped cores, the reflexes of $NaNdF_4$ (β-phase, $P\bar{6}$ space group) are pronounced. With larger NC (thicker $NaYF_4$ insulation shells), the right shift increases as the relative fraction of $NaNdF_4$ shrinks and the relative amount of $NaYF_4$ rises in the NC. Accordingly, the XRD patterns resemble stronger the $NaYF_4$ XRD pattern (β-

https://dx.doi.org/10.1021/acs.jpcc.0c02588
J. Phys. Chem. C 2020, 124, 11229−11238

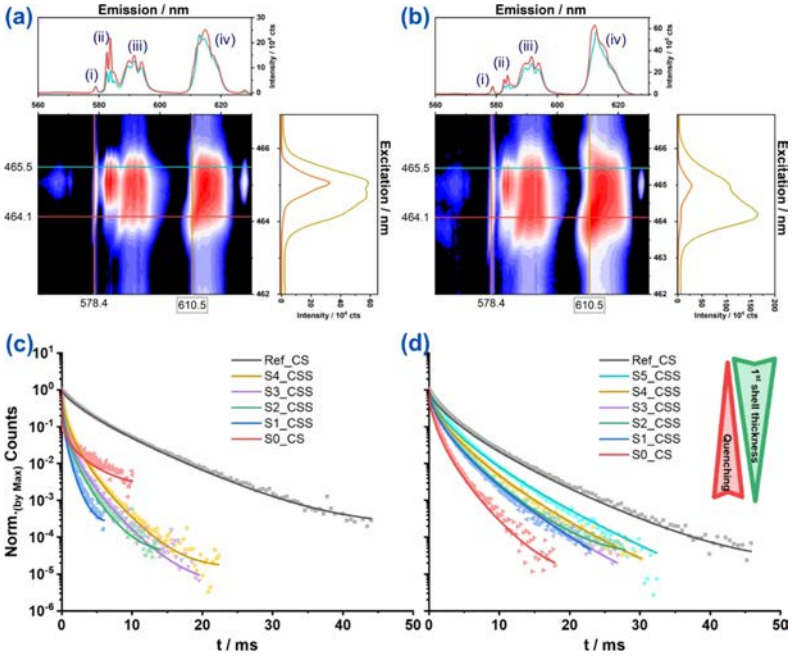

Figure 4. (a,b) TLS plot of $NaYF_4$ @ $NaYF_4$:Eu showing that deviations are present when excited either with 464.1 nm or with 465.5 nm at 4 K. Exemplarily shown: Ref_CS (a) & S1_CSS (b) of set 2. The other samples show the same major features as the same peak number in emission and excitation. The fwhm of the $^5D_0 \rightarrow {}^7F_0$ transition (i) is 0.4 nm. [Labeled transitions: (i) $^5D_0 \rightarrow {}^7F_0$; (ii) $^5D_1 \rightarrow {}^7F_3$; (iii) $^5D_0 \rightarrow {}^7F_1$; (iv) $^5D_0 \rightarrow {}^7F_2$]. For comparing the luminescence spectra of set 1 and set 2 with fully Nd^{3+}-doped or 20 mol % Nd^{3+}-doped cores see the Supporting Information, Figures S4 and S5. (c,d) Luminescence decay curves of Eu^{3+} in $NaYF_4$ NCs (c): set 1; (d): set 2. Eu^{3+} is doped in the outer shell. Nd^{3+} is doped in the core and serves as the quencher. Eu^{3+} emission is stronger quenched, when the insulation shell thickness ($NaYF_4$) decreases. The reference luminescence decay curve contains no Nd^{3+} as the quencher. (λ_{ex} = 464.55 nm; $^5D_0 \rightarrow {}^7F_2$ transition observed). Luminescence decay curves with λ_{ex} = 465.17 nm ($^5D_0 \rightarrow {}^7F_2$ transition) can be found in the Supporting Information, Figure S3.

phase, $P6_3/m$ space group). In set 1, S0_C (core = $NaNdF_4$ only) sample shows the strongest right shift. Furthermore, gagarinite ($NaCaYErF_6$; β-phase, $P6_3/m$ space group) was strongly matched by Rietveld refinement to the experimental data which also matches the reference spectra of the β-$NaYF_4$ (compare Figure 3). Other structures found by Rietveld refinement, especially in the core XRD patterns, are NaF (α-phase, very sharp peaks at 39 and 56°) that vanish again after shell addition. Most likely, this can be attributed to the subsequent synthesis steps, in which the NaF crystals served as Na^+ and F^- sources for the shell formation, which is supported by the findings of Haase et al. using small α-$NaGdF_4$ to create the β-$NaGdF_4$ NC.[52] Another structure found is Malladrite (Na_2SiF_6; tiny reflexes at 20° (double reflex) and at 27 and 39°), because of reaction of HF (intermediately formed during core synthesis at high temperature) and Si-ions of the glass reaction flask. The Malladrite XRD patterns vanished as well after shell addition. The disappearance of NaF and Malladrite can relate to the subsequent addition of the shell-precursor material and their consumption during shell-synthesis.

Eu^{3+} Luminescence for Lattice Characterization. High-resolution luminescence experiments were performed using Eu^{3+} as an optical probe in order to complement the XRD data.[53,54] Especially for the low dopant concentrations of Eu^{3+}, the detection of slight differences in the lattice (or the formation of a separate phase) can be demanding and the use of high-resolution luminescence data at ultralow temperature yields additional structural information related to the location of the Eu^{3+} ions in the lattice.[53,55,56] A typical total luminescence spectrum recorded at T = 4 K is shown in Figure 4 together with selected spectral traces for emission (top) and excitation spectra (right), respectively. The respective luminescence bands resulting from the $^5D_0 \rightarrow {}^7F_j$ transition (j = 0, 1, 2) and the $^5D_1 \rightarrow {}^7F_3$ are shown. For each luminescence band, the Stark splitting is resolved. The $^5D_0 \rightarrow {}^7F_0$ transition [marked as (i) in Figure 4a,b] forms a vertical band in the TLS plot, which means that the emission is independent of the excitation wavelength (emission spectra for λ_{ex} = 465.5 and 464.1 nm exemplarily shown as traces in the top graphs of Figure 4a,b) and one major Eu^{3+} species is dominating the luminescence of the samples. The single Gaussian-shaped $^5D_0 \rightarrow {}^7F_0$ transition indicates a relatively similar chemical environment of the Eu^{3+} ions in the lattice, although inhomogeneous line broadening can be concluded from the contribution of the peak's full width at half-maximum (fwhm = 0.4 nm). One reason for the observed inhomogeneous broadening is the different locations such as Eu^{3+} close

https://dx.doi.org/10.1021/acs.jpcc.0c02588
J. Phys. Chem. C 2020, 124, 11229−11238

Table 2. Comparison of Acceptor Number within a Three-Dimensional Sphere with the Radius of the Förster Distance of Eu^{3+} and Nd^{3+} (R_0 = 8.53 Å)[a]

Sample ID:	Ref_CS	S0_CS	S1_CSS	S2_CSS	S3_CSS	S4_CSS	S5_CSS
Set 1							
Insulation layer thickness / nm	-/-	0	1.4	1.9	1.9	2.6	
acceptor number (λ_{ex} = 464.55 nm)	0	9	3	2	2	1	
acceptor number (λ_{ex} = 465.17 nm)	0	9	4	3	3	2	
averaged acceptor number	0	8.9	3.3	2.6	2.4	1.9	
Set 2							
Insulation layer thickness / nm	-/-	0	1.0	1.5	1.6	2.7	3.7
acceptor number (λ_{ex} = 464.55 nm)	0	0.94	0.44	0.42	0.43	0.3	0.19
acceptor number (λ_{ex} = 465.17 nm)	0	1.8	1.09	0.94	0.99	0.81	0.61
averaged acceptor number	0	1.4	0.8	0.7	0.7	0.6	0.4
Trends:		Acceptor number ↘ Layer thickness					

[a]Regression parameter are obtained with eq 2 and the spectroscopic investigation of $^5D_0 \rightarrow {}^7F_2$ transition. Detailed fit-parameters are shown in the Supporting Information, Tables S2 and S3. The reference parameter used for the acceptor number calculation are: for set 1 with λ_{ex} = 464.55 nm, τ_D = (2280 ± 20) μs; with λ_{ex} = 465.17 nm, τ_D = (4060 ± 25) μs and for set 2 with λ_{ex} = 464.55 nm, τ_D = (1330 ± 5) μs; with λ_{ex} = 465.17 nm, τ_D = (3160 ± 10) μs.

to the surface or Eu^{3+} being deeper in the bulk phase, but also slight differences in the lattice parameters at the location of the Eu^{3+} ions will add to the inhomogeneous line broadening. The presence of minor differences in the near surrounding of the Eu^{3+} ions is also supported by the Stark splitting pattern and intensity distribution of the other transitions bands observed at different excitation wavelengths (see TLS spectra as well as the respective emission spectra taken as an examples and shown on top of the TLS). The emission spectra for the full set 1 and set 2 are shown in the Supporting Information, Figures S4 and S5, respectively. The tiny variations at the edges of the $^5D_0 \rightarrow {}^7F_0$ transition support the assumption of bulk and surface Eu^{3+} species. The excitation spectra with emission wavelength at 578.4 and 610.5 nm show shoulders at different positions, which can correspond to different Stark transitions for the $^5D_0 \rightarrow {}^7F_2$ transition used for excitation or to slightly different Eu^{3+} species being excited.

To further elucidate the distribution of the Eu^{3+} ions in the host lattice, the crystal field strength parameter $N_v(B_{2q})$ has been calculated and the results are summarized in the Supporting Information, Table S1. The calculation of the crystal field strength parameter has been performed based on the $^5D_0 \rightarrow {}^7F_1$ transition using eq 3. The crystal field strength parameters are found in the range of 520 $cm^{-1} < N_v(B_{2q}) <$ 560 cm^{-1}. The minor variation in $N_v(B_{2q})$ indicates that the chemical environment of Eu^{3+} ions within the different NC samples does not change significantly. The large error of the crystal field strength parameter (S0, set 1) results potentially from the strong and effective quenching by the Nd^{3+} ions and the resulting very low Eu^{3+} luminescence signal for this particular sample (pure "Nd-core").

The variation in the chemical environment according to the crystal field strength parameter and the TLS data is only small, probably because of the mixed contribution of surface- and bulk-located Eu^{3+} species. On the other hand, it shows that for the different core−shell NCs the crystal lattice stays unchanged, which is very helpful for the further evaluation of the luminescence decay kinetics within the LRET framework (vide infra).

Interlanthanide Resonance Energy Transfer. The evaluation of the luminescence decay kinetics of Eu^{3+} in the absence and the presence of Nd^{3+} in the NC core was evaluated in order to gain information on the lanthanide mixing between core and shell during synthesis (see Figure 1 for concept). The corresponding luminescence decay curves for set 1 and set 2 of the NC samples are shown in Figure 4c,d (for λ_{ex} = 464.55 nm, the data for λ_{ex} = 465.17 nm can be found in the Supporting Information). From the luminescence decays, it can be directly seen that i) the luminescence decay kinetics of the Ref_CS samples (for set 1 and set 2) is non-monoexponential and (ii) the presence of Nd^{3+} in the NC core led to an increase in the decay rate, which was dependent on the thickness of the insulation layer. The non-monoexponential decay kinetic relates to the slightly different lattice environment of the Eu^{3+} ions (vide supra). To take this heterogeneity into account, a stretched exponential function (see eq 1) was used in the data analysis. The heterogeneity parameter β_D was determined for the Ref_CS samples of both sets to be comparable (with λ_{ex} = 464.55 nm: β_D(set 1) = 0.745, β_D(set 2) = 0.671; with λ_{ex} = 465.17 nm: β_D(set 1) = 0.864, β_D(set 2) = 0.806), which indicates a rather narrow distribution or only slight differences between the sites in the NC occupied by Eu^{3+}, which is in good agreement with the TLS data (vide supra). The obtained heterogeneity parameter β_D of set 1 and set 2 was further used in the data analysis of the respective other samples. In Figure 4c,d, the fitting results are presented as well (solid lines) and it can be seen that the model is successfully applied to the experimental luminescence decay kinetics. The two different excitation wavelengths used in the time-resolved luminescence experiments account for the two subspecies of Eu^{3+} identified in the TLS: bulk and surface located Eu^{3+}. The luminescence decay times of the reference samples are: for set 1 with λ_{ex} = 464.55 nm, τ_D = (2280 ± 20) μs; with λ_{ex} = 465.17 nm, τ_D = (4060 ± 25) μs and for set 2

https://dx.doi.org/10.1021/acs.jpcc.0c02588
J. Phys. Chem. C 2020, 124, 11229−11238

with λ_{ex} = 464.55 nm, τ_D = (1330 ± 5) μs; with λ_{ex} = 465.17 nm, τ_D = (3160 ± 10) μs. The differences found in τ_D at the two different λ_{ex} for each set are supporting the idea of bulk- and surface-located Eu^{3+} species (the surface-located species being more quenched because of interactions with the solvent).

The visual analysis of the decay curves of the different core−shell−shell samples further shows immediately that even at an insulation layer thickness $\gg 2R_0$ luminescence quenching is observed. This first qualitative analysis already indicates that during the synthesis an exchange of ions (lanthanide ions as well as lattice ions (Y^{3+}, Na^+, F^-) should be taken into account) between the different layers occurs.

The results of the data evaluation using eq 2 are shown in Table 2. In the analysis, the average number of acceptors (here: Nd^{3+}) in the Förster volume was calculated as a representative parameter for comparison. For the sample S0_CS, the strongest quenching was found. For this particular sample, the Eu^{3+}-shell is directly located next to the $NaNdF_4$ core. Consequently, the highest acceptor number of nine Nd^{3+} in the Förster volume was determined for the S0_CS sample of set 1. By adding an insulation shell (see Figure 1), the quenching decreased. The observed reduction in quenching was depending on the thickness of the insulation layer. However, the quenching efficiency remained unexpectedly high—higher than it was theoretically expected with increasing shell thickness. Although for S1_CSS an insulation shell thickness of 1.4 nm (set 1) was present, still a significant quenching of the luminescence decay kinetics (see Figure 4c) was found and an average number of about three Nd^{3+} ions in the Förster volume was calculated (see Table 2). Comparing the samples with similar insulation layer thicknesses reveals stronger quenching in set 1 than in set 2. Here, the core of set 1 contained five times more Nd^{3+} ions than the core of set 2. But other than the smaller extent in overall quenching (see Figure 4c,d), the same dependence on the insulation layer thickness is observed for set 2 as for set 1 (see Table 2). The maximum acceptor number of set 2 is about two in the Förster volume (Table 2). The larger concentration gradient of set 1 can be attributed to the different initial Nd^{3+} concentration in the core. Furthermore, the fraction of acceptor numbers for set 1 and 2 is roughly in the range of the doping ratio applied in the synthesis: with 20 mol % Nd^{3+} doping (set 2) the reduced number of Nd^{3+} is reflected in the results and is roughly in the range of 1/5 up to 1/4 of the acceptor numbers determined for set 1. A summary of the fit parameters can be found in the Supporting Information, Tables S2 and S3.

CONCLUSIONS

The energy transfer between Eu^{3+} (donor) and Nd^{3+} (acceptor) ions was exploited to investigate the motion of trivalent cations during the synthesis of NCs. Two sets of $NaYF_4$-based NCs were synthesized. Both sets differ from each other in the core composition. One core was doped with only Nd^{3+} and the other one doped with 20 mol % Nd^{3+} to meet the general UCNP composition. The luminescence decay time of Eu^{3+} was evaluated and based on the FRET theory the average acceptor number around one Eu^{3+} ion in the Förster volume was calculated. It is revealed that with increasing insulation shell thickness, the acceptor number around one donor decreases; however, a total elimination of the LRET is not achieved within the two sets of NC investigated, although the thickest shell with 3.7 nm is at least four times larger than the theoretical $R_0(Eu^{3+}/Nd^{3+})$. Based on our LRET results, it can be concluded that during synthesis an exchange between rare earth ions, which were already part of the nanoparticle lattice (e.g., the core and later on in the middle shell), and rare earth ions in the reaction solution added for the shell formation occurs. Because of the dynamic resolution-crystallization process, an intermixing of rare earth ions in general (Y^{3+} as well as Ln^{3+}) is the result. This intermixing will be especially relevant for the sensitizer as well as activator ions if one intends to separate both ions from each other or to create a protection shell against surface-related quenching of the activator luminescence. The intermixing of the inner NC compartment with the outer (or better with newly formed, next layer) occurs and distinctly limits the separation of the different dopant ions between each other but also from surface effects. The fact of Ln^{3+} intermixing between different layers during synthesis is therefore a major factor to be considered for the further improvement of UCNP brightness.

Two scenarios for synthesis design are conceivable. The first approach suppresses Ln^{3+} intermixing to have as much control as possible of the NC composition and its synthesis. The second approach favors the Ln^{3+} intermixing to exploit the rare earth and Ln^{3+} diffusion. In any case, further research is needed to correlate injection temperature and rate as well as the effect of chemical different precursors with the final NC core shell structure. This opens a new research branch within the UCNP area. Next to thermal decomposition synthesis, there are microwave-assisted syntheses. Next to a hot injection method, core UCNP could be used as seeds and be transferred into a shell precursor solution. The precursor could be Ln-chlorides, Ln-trifluoracetates, or Ln-oleate, whereas it is not only restricted to these and to Ln^{3+} sources. Next to the reactants, the solvent may also play a major role. Finally, one can also think of using different host materials for the core and the shell. For the next experiments (work in progress) in addition to even thicker insulation layers, a combination with a scandium-based insulation layer is explored as well. All these factors may have a strong or a weak influence on UCNP formation and the Ln^{3+} distribution and are interesting to study. Once we have a better understanding of the interplay between parameters such as lattice phase (hexagonal, cubic and/or monoclinic), reaction temperature, reaction time, and speed of heating, it shall be possible to deduce the optimal thickness for the protection layer.

ASSOCIATED CONTENT

Supporting Information

The Supporting Information is available free of charge at https://pubs.acs.org/doi/10.1021/acs.jpcc.0c02588.

Förster volume with help of a $NaYF_4$ ($P6_3/m$) unit cell; illustration of a $NaNdF_4$ ($P\bar{6}$) unit cell; detailed crystal field strength parameters calculated from the $^7F_1$ multiplet of Eu^{3+} emission; additional photoluminescence decay curves of Eu^{3+} being excited at 465.17 nm; photoluminescence emission spectra of Eu^{3+} in $NaYF_4$ NC for sets 1 and set 2—comparison for all samples within each set; detailed fit parameters resulting from the FRET-based evaluation of quenched Eu^{3+}/Nd^{3+}-doped NC for the $^5D_0 \rightarrow {}^7F_2$ transition (for set 1 and set 2); TEM images of samples of set 1 and set 2 (PDF)

https://dx.doi.org/10.1021/acs.jpcc.0c02588
J. Phys. Chem. C 2020, 124, 11229−11238

AUTHOR INFORMATION

Corresponding Author

Michael U. Kumke − *Institute of Chemistry (Physical Chemistry), University of Potsdam, 14476 Potsdam, Germany;* orcid.org/0000-0002-3395-9379; Email: kumke@uni-potsdam.de

Authors

Philipp U. Bastian − *Institute of Chemistry (Physical Chemistry), University of Potsdam, 14476 Potsdam, Germany*

Selma Nacak − *Institute of Chemistry (Physical Chemistry), University of Potsdam, 14476 Potsdam, Germany*

Vladimir Roddatis − *German Research Centre for Geosciences (GFZ), Helmholtz-Centre Potsdam, 14473 Potsdam, Germany*

Complete contact information is available at: https://pubs.acs.org/10.1021/acs.jpcc.0c02588

Author Contributions

The paper was written through contributions of all the authors. All the authors have given approval to the final version of the paper.

Notes

The authors declare no competing financial interest.

ACKNOWLEDGMENTS

We are very thankful to Prof. Dr. Liane G. Benning and Dr. Richard Wirth of the German Research Centre for Geosciences (GFZ) for making the TEM measurements possible. V.R. acknowledges the financial support of the Helmholtz Recruiting Initiative (grant no. I-044-16-01) that supported the TEM work at the GFZ. Special thanks also go to Dr. Christina Günter (University of Potsdam, Institute of Geosciences) for her fruitful discussions, advice, and help in the context of the XRD measurements. Furthermore, we thank the Republic of Turkey, Ministry of National Education (grant no. YLSY-2010) and the Helmholtz-Graduate School Macromolecular Bioscience (MacroBio), Helmholtz-Zentrum Geesthach for the financial support of the research.

REFERENCES

(1) Bloembergen, N. Solid State Infrared Quantum Counters. *Phys. Rev. Lett.* **1959**, *2*, 84−85.

(2) Auzel, F. Upconversion and Anti-Stokes Processes with f and d Ions in Solids. *Chem. Rev.* **2004**, *104*, 139−174.

(3) Hudry, D.; Busko, D.; Popescu, R.; Gerthsen, D.; Abeykoon, A. M. M.; Kübel, C.; Bergfeldt, T.; Richards, B. S. Direct Evidence of Significant Cation Intermixing in Upconverting Core@Shell Nanocrystals: Toward a New Crystallochemical Model. *Chem. Mater.* **2017**, *29*, 9238−9246.

(4) Park, Y. I.; Kim, H. M.; Kim, J. H.; Moon, K. C.; Yoo, B.; Lee, K. T.; Lee, N.; Choi, Y.; Park, W.; Ling, D.; et al. Theranostic Probe Based on Lanthanide-Doped Nanoparticles for Simultaneous in Vivo Dual-Modal Imaging and Photodynamic Therapy. *Adv. Mater.* **2012**, *24*, 5755−5761.

(5) Xiao, Q.; Zheng, X.; Bu, W.; Ge, W.; Zhang, S.; Chen, F.; Xing, H.; Ren, Q.; Fan, W.; Zhao, K.; et al. A Core/Satellite Multifunctional Nanotheranostic for in Vivo Imaging and Tumor Eradication by Radiation/Photothermal Synergistic Therapy. *J. Am. Chem. Soc.* **2013**, *135*, 13041−13048.

(6) Chen, S.; Weitemier, A. Z.; Zeng, X.; He, L.; Wang, X.; Tao, Y.; Huang, A. J. Y.; Hashimotodani, Y.; Kano, M.; Iwasaki, H.; et al. Near-Infrared Deep Brain Stimulation via Upconversion Nanoparticle−Mediated Optogenetics. *Science* **2018**, *359*, 679−684.

(7) Sedlmeier, A.; Gorris, H. H. Surface Modification and Characterization of Photon-Upconverting Nanoparticles for Bioanalytical Applications. *Chem. Soc. Rev.* **2015**, *44*, 1526−1560.

(8) Naccache, R.; Yu, Q.; Capobianco, J. A. The Fluoride Host: Nucleation, Growth, and Upconversion of Lanthanide-Doped Nanoparticles. *Adv. Opt. Mater.* **2015**, *3*, 482−509.

(9) Würth, C.; Kaiser, M.; Wilhelm, S.; Grauel, B.; Hirsch, T.; Resch-Genger, U. Excitation Power Dependent Population Pathways and Absolute Quantum Yields of Upconversion Nanoparticles in Different Solvents. *Nanoscale* **2017**, *9*, 4283−4294.

(10) de Guereñu, A. L.; Bastian, P.; Wessig, P.; John, L.; Kumke, M. U. Energy Transfer between Tm-Doped Upconverting Nanoparticles and a Small Organic Dye with Large Stokes Shift. *Biosensors* **2019**, *9*, 9.

(11) Krämer, K. W.; Biner, D.; Frei, G.; Güdel, H. U.; Hehlen, M. P.; Lüthi, S. R. Hexagonal Sodium Yttrium Fluoride Based Green and Blue Emitting Upconversion Phosphors. *Chem. Mater.* **2004**, *16*, 1244−1251.

(12) Chen, G.; Damasco, J.; Qiu, H.; Shao, W.; Ohulchanskyy, T. Y.; Valiev, R. R.; Wu, X.; Han, G.; Wang, Y.; Yang, C.; et al. Energy-Cascaded Upconversion in an Organic Dye-Sensitized Core/Shell Fluoride Nanocrystal. *Nano Lett.* **2015**, *15*, 7400−7407.

(13) Yan, W.; Weiping, Q.; Jisen, Z.; Chunyan, C.; Jishuang, Z.; Ye, J. Synthesis and Upconversion Luminescence of LaF_3: Yb^{3+}, Er^{3+}/SiO_2 Core/Shell Microcrystals. *J. Rare Earths* **2007**, *25*, 605−608.

(14) Yi, G.-S.; Chow, G.-M. Water-Soluble $NaYF_4$:Yb,Er(Tm)/$NaYF_4$/Polymer Core/Shell/Shell Nanoparticles with Significant Enhancement of Upconversion Fluorescence. *Chem. Mater.* **2007**, *19*, 341−343.

(15) Würth, C.; Fischer, S.; Grauel, B.; Alivisatos, A. P.; Resch-Genger, U. Quantum Yields, Surface Quenching, and Passivation Efficiency for Ultrasmall Core/Shell Upconverting Nanoparticles. *J. Am. Chem. Soc.* **2018**, *140*, 4922−4928.

(16) Homann, C.; Krukewitt, L.; Frenzel, F.; Grauel, B.; Würth, C.; Resch-Genger, U.; Haase, M. $NaYF_4$:Yb,Er/$NaYF_4$ Core/Shell Nanocrystals with High Upconversion Luminescence Quantum Yield. *Angew. Chem. Int. Ed.* **2018**, *57*, 8765−8769.

(17) Hudry, D.; Popescu, R.; Busko, D.; Diaz-Lopez, M.; Abeykoon, M.; Bordet, P.; Gerthsen, D.; Howard, I. A.; Richards, B. S. Interface Disorder in Large Single- and Multi-Shell Upconverting Nanocrystals. *J. Mater. Chem. C* **2019**, *7*, 1164−1172.

(18) Hudry, D.; Busko, D.; Popescu, R.; Gerthsen, D.; Howard, I. A.; Richards, B. S. An Enhanced Energy Migration Strategy in Upconverting Nanocrystals: Color-Tuning with High Quantum Yield. *J. Mater. Chem. C* **2019**, *7*, 7371−7377.

(19) Hudry, D.; Howard, I. A.; Popescu, R.; Gerthsen, D.; Richards, B. S. Structure−Property Relationships in Lanthanide-Doped Upconverting Nanocrystals: Recent Advances in Understanding Core−Shell Structures. *Adv. Mater.* **2019**, *31*, 1900623.

(20) Dong, H.; Sun, L.-D.; Li, L.-D.; Si, R.; Liu, R.; Yan, C.-H. Selective Cation Exchange Enabled Growth of Lanthanide Core/Shell Nanoparticles with Dissimilar Structure. *J. Am. Chem. Soc.* **2017**, *139*, 18492−18495.

(21) Chen, B.; Peng, D.; Chen, X.; Qiao, X.; Fan, X.; Wang, F. Establishing the Structural Integrity of Core-Shell Nanoparticles against Elemental Migration Using Luminescent Lanthanide Probes. *Angew. Chem. Int. Ed.* **2015**, *54*, 12788−12790.

(22) Liu, L.; Li, X.; Fan, Y.; Wang, C.; El-Toni, A. M.; Alhoshan, M. S.; Zhao, D.; Zhang, F. Elemental Migration in Core/Shell Structured Lanthanide Doped Nanoparticles. *Chem. Mater.* **2019**, *31*, 5608−5615.

(23) Dühnen, S.; Haase, M. Study on the Intermixing of Core and Shell in $NaEuF_4$/$NaGdF_4$ Core/Shell Nanocrystals. *Chem. Mater.* **2015**, *27*, 8375−8386.

(24) Xu, X.; Zhou, Z.; Liu, Y.; Wen, S.; Guo, Z.; Gao, L.; Wang, F. Optimising Passivation Shell Thickness of Single Upconversion Nanoparticles Using a Time-Resolved Spectrometer. *APL Photonics* **2019**, *4*, 026104.

(25) Shi, Y.; Zhang, F.; Xu, J.; Zhou, K.; Chen, C.; Cheng, J.; Li, P. Upconversion Fluorescence Enhancement of $NaYF_4$:Yb/Re Nanoparticles by Coupling with SiO_2 Opal Photonic Crystals. *J. Mater. Sci.* **2019**, *54*, 8461−8471.
(26) Wang, S.; Ma, S.; Liu, S.; Ye, Z. Facile Post-Synthesis of a Ce^{3+}-Doped $Ca_xSr_{1-x}Sc_2O_4$ Phosphor by Means of Cation Exchange. *ChemistrySelect* **2018**, *3*, 4387−4392.
(27) Avram, D.; Colbea, C.; Florea, M.; Lazar, S.; Stroppa, D.; Tiseanu, C. Imaging Dopant Distribution across Complete Phase Transformation by TEM and Upconversion Emission. *Nanoscale* **2019**, *11*, 16743−16754.
(28) Klier, D. T.; Kumke, M. U. Analysing the Effect of the Crystal Structure on Upconversion Luminescence in Yb^{3+},Er^{3+}-Co-Doped $NaYF_4$ Nanomaterials. *J. Mater. Chem. C* **2015**, *3*, 11228−11238.
(29) Hesse, J.; Klier, D. T.; Sgarzi, M.; Nsubuga, A.; Bauer, C.; Grenzer, J.; Hübner, R.; Wislicenus, M.; Joshi, T.; Kumke, M. U.; et al. Rapid Synthesis of Sub-10 Nm Hexagonal $NaYF_4$-Based Upconverting Nanoparticles Using Therminol®66. *ChemistryOpen* **2018**, *7*, 159−168.
(30) Valeur, B. *Molecular Fluorescence—Principles and Applications*; Wiley-VCH Verlag, 2002.
(31) Horrocks, W. D.; Sudnick, D. R. Lanthanide Ion Luminescence Probes of the Structure of Biological Macromolecules. *Acc. Chem. Res.* **1981**, *14*, 384−392.
(32) Horrocks, W. D. Luminescence Spectroscopy. *Meth. Enzymol.* **1993**, *226*, 495−538.
(33) Bruno, J.; Horrocks, W. D. W.; Beckingham, K. Characterization of Eu(III) Binding to a Series of Calmodulin Binding Site Mutants Using Laser-Induced Eu(III) Luminescence Spectroscopy. *Biophys. Chem.* **1996**, *63*, 1−16.
(34) Joshi, J. C.; Pandey, N. C.; Joshi, B. C.; Belwal, R.; Joshi, J. Quantum Efficiency of Diffusion-Limited Energy Transfer from Eu^{3+} → Nd^{3+} in Borate Glass. *J. Solid State Chem.* **1978**, *23*, 135−139.
(35) Ramos-Lara, F.; C, A. L.; Ramírez, M. O.; Flores, M.; Arroyo, R.; Caldiño, U. Optical Spectroscopy of Nd^{3+} Ions in Poly(Acrylic Acid). *J. Phys. Condens. Matter* **2006**, *18*, 7951−7959.
(36) Dieke, G. H.; Crosswhite, H. M. The Spectra of the Doubly and Triply Ionized Rare Earths. *Appl. Opt.* **1963**, *2*, 675−686.
(37) Inokuti, M.; Hirayama, F. Influence of Energy Transfer by the Exchange Mechanism on Donor Luminescence. *J. Chem. Phys.* **1965**, *43*, 1978−1989.
(38) Zhang, H.; Wang, Y.; Han, L. Photoluminescence Properties and Energy Transfer between Eu^{3+} and Nd^{3+} in Polyborate $BaGdB_9O_{16}$: Eu^{3+}, Nd^{3+}. *J. Appl. Phys.* **2011**, *109*, 053109.
(39) Xie, Z.-L.; Xu, H.-B.; Geßner, A.; Kumke, M. U.; Priebe, M.; Fromm, K. M.; Taubert, A. A Transparent, Flexible, Ion Conductive, and Luminescent PMMA Ionogel Based on a Pt/Eu Bimetallic Complex and the Ionic Liquid $[Bmim][N(Tf)_2]$. *J. Mater. Chem.* **2012**, *22*, 8110−8116.
(40) Carnall, W. T.; Fields, P. R.; Rajnak, K. Electronic Energy Levels of the Trivalent Lanthanide Aquo Ions. IV. Eu^{3+}. *J. Chem. Phys.* **1968**, *49*, 4450−4455.
(41) Rabouw, F. T.; Prins, P. T.; Norris, D. J. Europium-Doped $NaYF_4$ Nanocrystals as Probes for the Electric and Magnetic Local Density of Optical States throughout the Visible Spectral Range. *Nano Lett.* **2016**, *16*, 7254−7260.
(42) Lee, K. C. B.; Siegel, J.; Webb, S. E. D.; Lévêque-Fort, S.; Cole, M. J.; Jones, R.; Dowling, K.; Lever, M. J.; French, P. M. W. Application of the Stretched Exponential Function to Fluorescence Lifetime Imaging. *Biophys. J.* **2001**, *81*, 1265−1274.
(43) Szefczyk, B.; Roszak, R.; Roszak, S. Structure of the Hexagonal $NaYF_4$ Phase from First-Principles Molecular Dynamics. *RSC Adv.* **2014**, *4*, 22526−22535.
(44) Wang, F.; Han, Y.; Lim, C. S.; Lu, Y.; Wang, J.; Xu, J.; Chen, H.; Zhang, C.; Hong, M.; Liu, X. Simultaneous Phase and Size Control of Upconversion Nanocrystals through Lanthanide Doping. *Nature* **2010**, *463*, 1061−1065.
(45) Mackenzie, L. E.; Goode, J. A.; Vakurov, A.; Nampi, P. P.; Saha, S.; Jose, G.; Millner, P. A. The Theoretical Molecular Weight of $NaYF_4$:RE Upconversion Nanoparticles. *Sci. Rep.* **2018**, *8*, 1106.
(46) Burns, J. H. Crystal Structure of Hexagonal Sodium Neodymium Fluoride and Related Compounds. *Inorg. Chem.* **1965**, *4*, 881−886.
(47) Momma, K.; Izumi, F. VESTA 3 for Three-Dimensional Visualization of Crystal, Volumetric and Morphology Data. *J. Appl. Crystallogr.* **2011**, *44*, 1272−1276.
(48) Marmodée, B.; de Klerk, J. S.; Ariese, F.; Gooijer, C.; Kumke, M. U. High-Resolution Steady-State and Time-Resolved Luminescence Studies on the Complexes of Eu(III) with Aromatic or Aliphatic Carboxylic Acids. *Anal. Chim. Acta* **2009**, *652*, 285−294.
(49) Mi, C.; Tian, Z.; Cao, C.; Wang, Z.; Mao, C.; Xu, S. Novel Microwave-Assisted Solvothermal Synthesis of $NaYF_4$:Yb,Er Upconversion Nanoparticles and Their Application in Cancer Cell Imaging. *Langmuir* **2011**, *27*, 14632−14637.
(50) Wilhelm, S.; del Barrio, M.; Heiland, J.; Himmelstoß, S. F.; Galbán, J.; Wolfbeis, O. S.; Hirsch, T. Spectrally Matched Upconverting Luminescent Nanoparticles for Monitoring Enzymatic Reactions. *ACS Appl. Mater. Interfaces* **2014**, *6*, 15427−15433.
(51) Grzechnik, A.; Friese, K. Crystal Structures and Stability of $NaLnF_4$ (Ln = La, Ce, Pr, Nd, Sm and Gd) Studied with Synchrotron Single-Crystal and Powder Diffraction. *Dalton Trans.* **2012**, *41*, 10258−10266.
(52) Dühnen, S.; Rinkel, T.; Haase, M. Size Control of Nearly Monodisperse β-$NaGdF_4$ Particles Prepared from Small α-$NaGdF_4$ Nanocrystals. *Chem. Mater.* **2015**, *27*, 4033−4039.
(53) Primus, P.-A.; Ritschel, T.; Sigüenza, P. Y.; Cauqui, M. A.; Hernández-Garrido, J. C.; Kumke, M. U. High-Resolution Spectroscopy of Europium-Doped Ceria as a Tool to Correlate Structure and Catalytic Activity. *J. Phys. Chem. C* **2014**, *118*, 23349−23360.
(54) Primus, P.-A.; Menski, A.; Yeste, M. P.; Cauqui, M. A.; Kumke, M. U. Fluorescence Line-Narrowing Spectroscopy as a Tool to Monitor Phase Transitions and Phase Separation in Efficient Nanocrystalline $Ce_xZr_{1-x}O_2$:Eu^{3+} Catalyst Materials. *J. Phys. Chem. C* **2015**, *119*, 10682−10692.
(55) Tiseanu, C.; Cojocaru, B.; Parvulescu, V. I.; Sanchez-Dominguez, M.; Primus, P. A.; Boutonnet, M. Order and Disorder Effects in Nano-ZrO_2 Investigated by Micro-Raman and Spectrally and Temporarily Resolved Photoluminescence. *Phys. Chem. Chem. Phys.* **2012**, *14*, 12970−12981.
(56) Tiseanu, C.; Parvulescu, V. I.; Boutonnet, M.; Cojocaru, B.; Primus, P. A.; Teodorescu, C. M.; Solans, C.; Dominguez, M. S. Surface *versus* Volume Effects in Luminescent Ceria Nanocrystals Synthesized by an Oil-in-Water Microemulsion Method. *Phys. Chem. Chem. Phys.* **2011**, *13*, 17135−17145.

https://dx.doi.org/10.1021/acs.jpcc.0c02588
J. Phys. Chem. C 2020, 124, 11229−11238

2.3. Trivalent Lanthanoid Cation Migration in the Sodium Yttrium Fluoride and Sodium Gadolinium Fluoride Host Lattice – Supervision via the Eu^{3+}-to-Pr^{3+} and Eu^{3+}-to-Nd^{3+} Lanthanoid Resonance Energy Transfer (Manuscript 2)

"Resonance Energy Transfer to Track the Motion of Lanthanide Ions – What Drives the Intermixing in Core-Shell Upconverting Nanoparticles?"

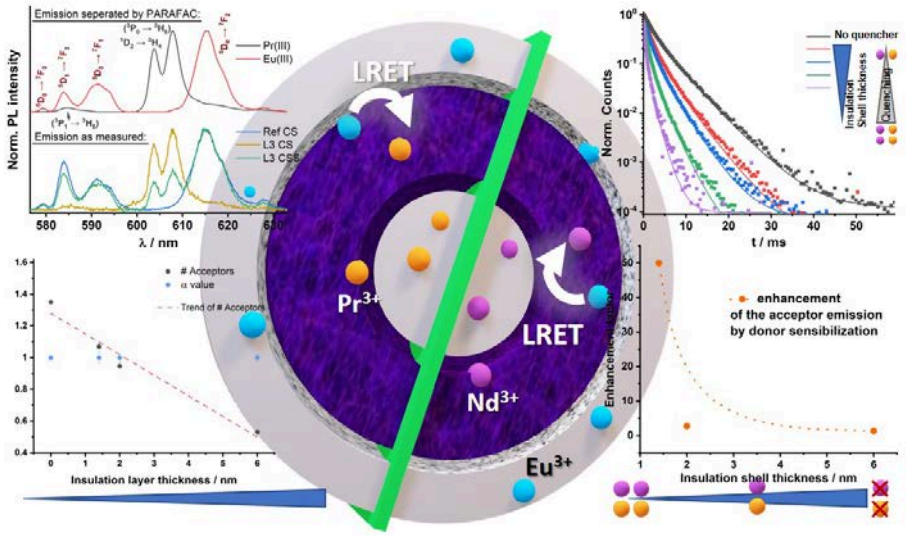

Biosensors **11** (12), 515 (2021).[100]

Link: https://doi.org/10.3390/bios11120515

biosensors

MDPI

Article

Resonance Energy Transfer to Track the Motion of Lanthanide Ions—What Drives the Intermixing in Core-Shell Upconverting Nanoparticles?

Philipp U. Bastian [1], Nathalie Robel [1], Peter Schmidt [1], Tim Schrumpf [1], Christina Günter [2], Vladimir Roddatis [3] and Michael U. Kumke [1,*]

[1] Institute of Chemistry (Physical Chemistry), University of Potsdam, 14469 Potsdam, Germany; philipp.bastian@uni-potsdam.de (P.U.B.); nathalie.robel@uni-potsdam.de (N.R.); peschmidt@uni-potsdam.de (P.S.); tschrumpf@uni-potsdam.de (T.S.)
[2] Institute of Geosciences (Mineralogy), University of Potsdam, 14469 Potsdam, Germany; guenter@geo.uni-potsdam.de
[3] Helmholtz Centre Potsdam, GFZ German Research Centre for Geosciences, 14473 Potsdam, Germany; roddatis@gfz-potsdam.de
* Correspondence: kumke@uni-potsdam.de; Tel.: +49-331-977-5209

Abstract: The imagination of clearly separated core-shell structures is already outdated by the fact, that the nanoparticle core-shell structures remain in terms of efficiency behind their respective bulk material due to intermixing between core and shell dopant ions. In order to optimize the photoluminescence of core-shell UCNP the intermixing should be as small as possible and therefore, key parameters of this process need to be identified. In the present work the Ln(III) ion migration in the host lattices $NaYF_4$ and $NaGdF_4$ was monitored. These investigations have been performed by laser spectroscopy with help of lanthanide resonance energy transfer (LRET) between Eu(III) as donor and Pr(III) or Nd(III) as acceptor. The LRET is evaluated based on the Förster theory. The findings corroborate the literature and point out the migration of ions in the host lattices. Based on the introduced LRET model, the acceptor concentration in the surrounding of one donor depends clearly on the design of the applied core-shell-shell nanoparticles. In general, thinner intermediate insulating shells lead to higher acceptor concentration, stronger quenching of the Eu(III) donor and subsequently stronger sensitization of the Pr(III) or the Nd(III) acceptors. The choice of the host lattice as well as of the synthesis temperature are parameters to be considered for the intermixing process.

Keywords: upconversion nanoparticles; lanthanoid migration; lanthanides; core-shell; energy transfer

Citation: Bastian, P.U.; Robel, N.; Schmidt, P.; Schrumpf, T.; Günter, C.; Roddatis, V.; Kumke, M.U. Resonance Energy Transfer to Track the Motion of Lanthanide Ions—What Drives the Intermixing in Core-Shell Upconverting Nanoparticles? *Biosensors* **2021**, *11*, 515. https://doi.org/10.3390/bios11120515

Received: 18 October 2021
Accepted: 9 December 2021
Published: 14 December 2021

1. Introduction

Upconversion nanoparticles (UCNP) are potential optical probes for many applications in the environmental and life science context. In order to bring UCNPs into a broad practical application, further improvements in the synthesis design, host lattices, stability in water, and surface functionalization are needed to meet the specific challenges of real-world applications. UCNPs are competing with established optical probes such as organic dyes or quantum dots. Here, a major issue is the low brightness of UCNPs which limits their use in practical applications [1–6], e.g., for imaging, diagnostics and therapy (theranostics) [5–9]. UCNPs with at least one (protective) shell around the nanoparticle core, which contains the sensitizer and activator ion, is a very frequently used strategy to improve the UCNP emission efficiency. Here, the basic idea is that the outer shell protects the doped UCNP core from unwanted quenching by the environment (e.g., quenching by OH-vibrations of water molecules). However, it has been shown that the shielding effect by this outer layer is smaller than expected. One of the limitations found is the intermixing of dopant ions from the different layers. This intermixing process has been demonstrated, e.g., by TEM investigations. Examples are given by Hudry et al. revealing an intermixing layer formed during the synthesis of core-shell

nanostructures [10–13]. A recent work by Diogenis et al. contributes to these findings and reveals a major excitation of Eu(III) in the core-shell interfacial region by an energy transfer from Gd(III) [14]. Liu et al. observed Ln(III) migration already at low temperatures, as low as 200 °C, and showed a dependency on the Ln(III) concentration [15]. In good agreement to that, Chen et al. suggested increased Ln(III) migration at higher temperatures related to vacancies in the crystal lattice and higher vibrational energy of the dopants [16]. Dong et al. suppressed triple charged Ln(III) migration by growing a CaF_2 shell with double charged Ca(II) ions [17], which is in good agreement with the Goldschmidt rules/tolerance factors [18].

The intermixing of Ln(III) ions has also been previously investigated with laser spectroscopy in our group. The monitoring concept is based on the lanthanide resonance energy transfer (LRET) [19]. Our previous work has focused on a $NaNdF_4$/$NaYF_4$ host lattice with a core-shell-shell structure. The first shell has been an insulation shell (also called insulation layer), being only composed of $NaYF_4$, to create a variable spatial separation of LRET-donor and LRET-acceptor ions in the outer shell and the core, respectively [19]. The photoluminescence (PL) emission of Eu(III) ions (donor) has been analyzed within the resonance energy transfer framework to calculate the average number of acceptor ions (being Nd(III)) around one Eu(III) ion.

Based on the previous experiments, we have extended our research on the intermixing of dopant ions between core and shell in crystalline nanoparticles. An additional LRET-pair has been used in the $NaYF_4$ host lattice. Since Nd(III) possesses only a weak luminescence in the visual spectral range, it was replaced by Pr(III). Pr(III) shows good PL emission in the visible spectral range and can be used as LRET-acceptor in combination with Eu(III) [20]. The change in the acceptor ion aims to record the acceptor (here: Pr(III)) PL emission as an additional parameter. The Pr(III) luminescence sensitization by Eu(III) is analyzed complementary to the Eu(III) PL emission, which is quenched. Additionally, the extent of intermixing behavior of Nd(III) and Pr(III) is discussed based on our previous findings with Nd(III) in the $NaYF_4$ host lattice [19]. Second, the former investigated LRET-pair (Eu-Nd) will be transferred into a $NaGdF_4$ host lattice (instead of $NaYF_4$ as in Ref. [19]) (vide infra) and the effect of the lattice on the intermixing is addressed. $NaGdF_4$ is expected to crystallize preferably in the hexagonal phase, because the $NaYF_4$ lattice forms a cubic phase at low temperatures but tends strongly to form the desired hexagonal phase upon doping with Gd(III) ions [6,21–23]. Here, the comparison of Nd(III) in $NaGdF_4$ and in $NaYF_4$ (from the previous work) shall be realized. The hexagonal crystal phase of $NaYF_4$ (and of $NaGdF_4$) is known to possess higher upconversion (UC) efficiency than the cubic crystal phase relating to the lower phonon energy and lower crystal field symmetry of the hexagonal phase [6,21,24,25]. Additionally, the $NaGdF_4$ host lattice equips the nanoparticles with magnetic properties which could be exploited in magnet resonance imaging or potentially in multidimensional diagnostic applications [24]. Therefore, the characterization of the intermixing in this particular phase is of special interest. In this work, we investigate the use of the two LRET-pairs Eu-Nd [20,25–28] and Eu-Pr [20,29–31] in different host lattices for the investigation of the migration of Ln(III).

2. Materials and Methods

2.1. Materials

All chemicals were used as received without previous purification. From Sigma Aldrich (St. Louis, MO, USA) were purchased: $RECl_3 \cdot 6H_2O$ (RE:Eu^{3+}, Pr^{3+}, Y^{3+}, Yb^{3+}, purity >99.99%) and ammonium fluoride (NH_4F, ≥99.99%). From Alfa Aesar (Kandel, Germany) were purchased: $RECl_3 \cdot 6H_2O$ (RE: Gd^{3+}, Nd^{3+}, purity > 99.99%) and oleic acid (OA, 90%). From Carl Roth (Karlsruhe, Germany) were purchased: cyclohexane (ROTISOLV® ≥ 99.9%), ethanol (≥99.8%, 1% MEK) and sodium oleate (NaOA, 90%). The solvent Therminol® 66 was bought from FRAGOL GmbH + Co KG (Mülheim, Germany).

2.2. Concept of This Study

In our current study, two main sets of nanoparticles were investigated. The nanoparticles were synthesized as core @ shell @ shell particles (=CSS). The notation is as follows:

- Set Y300: Core = $NaYF_4$:$Pr_{20\%}$ @ Shell = $NaYF_4$ @ Shell = $NaYF_4$:$Eu_{5\%}$;
- Set Gd300: Core = $NaGdF_4$:$Nd_{20\%}$ @ Shell = $NaGdF_4$ @ Shell = $NaGdF_4$:$Eu_{5\%}$;

The percentages are mol% referring to the trivalent ions in the nanocrystal. The first shell is referred to as insulation shell/layer and its thickness has been varied in order to have different distances between the core and the outer shell. The composition, nanoparticle size, and insulation shell thickness for each set is summarized in Table 1. Each set has its respective reference sample without the acceptor ions in the core (pure host lattice) and without an insulation shell, indicated as Ref CS. The Ref CS samples have only Eu(III) ions doped in the outer shell. The L0 CS samples have been synthesized the same way as the Ref CS sample except for the acceptor doping being 20 mol% in the core (and only 80 mol% of Y(III) or Gd(III)). L1 CSS, L2 CSS and L3 CSS are as L0 CS but with an additional intermediate shell (see Figure 1, inner purple shell), that has been grown prior to the donor doped outer shell. The additional intermediate shell increases in thickness, which is indicated by increasing numbers in the sample declaration. The insulation shell separates the donor and the acceptor spatially from each other. The sample L1 CSS is based on the sample L1 CS, which is derived from the core of L0 C. An overview of two main sets is given in Table 1. In Table 1, only the diameters of the nanoparticles with the first shell (so, with the insulation shell, except for L0 CS) is given, as this is the important information with respect to the distance between donor and acceptor for the application of the LRET model described below (Equations (1)–(3)). The notation for the samples L1 CS, L2 CS and L3 CS corresponds to the nanoparticles prior to the growth of the outer shell, which is doped with Eu(III). The described nanoparticle design is illustrated in Figure 1, in which the respective energy levels of the applied Ln(III) ions are shown as well [32–37]. In addition to the main sets, two subsets were synthesized in order to clarify certain effects (vide infra and Appendix A, Table A1). Briefly, the Y300_UCNP and the Gd200 subsets were synthesized according to the same protocol used in the other respective sets. The Y300-UCNP set is the same set as Y300 except for the core doping, which has been changed to the upconversion pair of Yb(III) with 18 mol% and Pr(III) with 2 mol%. With this set, the upconversion luminescence of Yb- (upconversion sensitizer) and Pr-ions (upconversion activator and LRET-acceptor) and the LRET of Eu-to-Pr was investigated. The Gd200 set differs from the Gd300 set only by the synthesis temperature used which was reduced by 100 °C.

Table 1. Overview of the sets and their sample composition with the corresponding particle sizes and their insulation shell thickness. Each set has its respective reference samples in which the LRET-acceptor is absent. The diameters are derived from the TEM images. Only the important nanoparticles for the determination of the insulation shell thickness have been examined. TEM images are shown in Figure 2 and in the Appendix A, Figure A1. Acceptor and donor doping are 20 mol% and 5 mol%, respectively, in percentage to the total amount of trivalent cations in the nanocrystal.

Set Y300 ($NaYF_4$; ϑ = 320 °C)	**Sample Composition**	**Diameter of Core-Shell (CS) Samples/nm**	**Insulation Shell Thickness/nm**
Y300 Ref CS	$NaYF_4$ @ $NaYF_4$:Eu	-/-	-/-
Y300 L0 CS [1]	$NaYF_4$:Pr @ $NaYF_4$:Eu	7.7 ± 1.5	0
Y300 L1 CSS [1]	$NaYF_4$:Pr @ $NaYF_4$ @ $NaYF_4$:Eu	6.5 ± 1.3	1.4 ± 0.7
Y300 L2 CSS [1]	vide supra	7.7 ± 1.4	2.0 ± 0.8
Y300 L3 CSS [1]	vide supra	15.7 ± 1.0	6.0 ± 0.5
Set Gd300 ($NaGdF_4$; ϑ = 320 °C)	**Sample Composition**	**Diameter of Core-Shell (CS) Samples/nm**	**Insulation Shell Thickness/nm**
Gd300 Ref CS	$NaGdF_4$ @ $NaGdF_4$:Eu	-/-	-/-
Gd300 L0 CS [2]	$NaGdF_4$:Nd @ $NaGdF_4$:Eu	8.9 ± 1.5	0
Gd300 L1 CSS [2]	$NaGdF_4$:Nd @ $NaGdF_4$ @ $NaGdF_4$:Eu	7.1 ± 0.4	0.7 ± 0.5
Gd300 L2 CSS [3]	vide supra	10.8 ± 1.5	1.0 ± 1.0
Gd300 L3 CSS [3]	vide supra	14.4 ± 1.5	2.8 ± 1.0

[1] Common core for all samples of Y300 set with a core diameter of 3.7 ± 0.4 nm. [2] Common core for Gd300 L0 CS and L1 CSS with a core diameter of 5.7 ± 0.9 nm. [3] Common core for Gd300 L2 CSS and L3 CSS with a core diameter of 8.7 ± 1.2 nm.

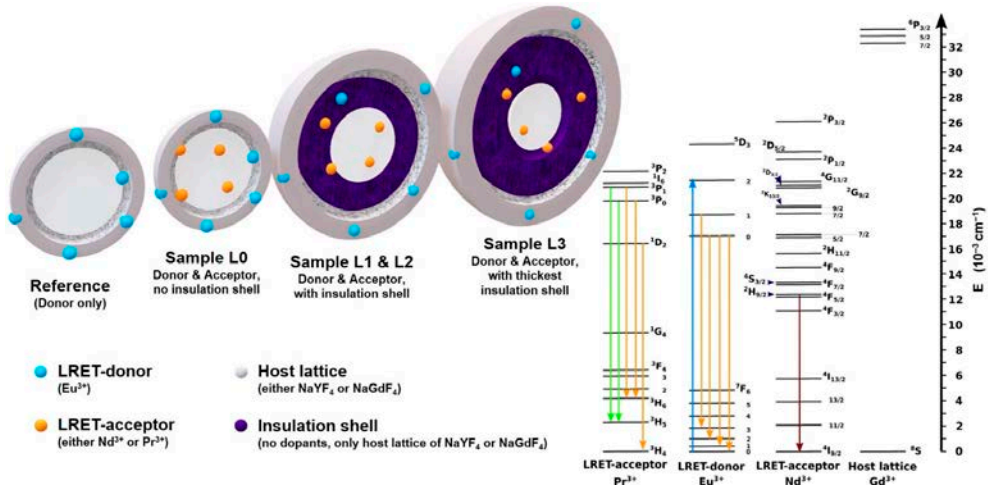

Figure 1. Illustration of the nanoparticle design and concept (**left**). Colored spheres are: Eu(III) in blue and either Nd(III) or Pr(III) in orange. Light and dark grey illustrates the host lattice of the cores and the shells being either $NaYF_4$ or $NaGdF_4$. The purple intermediate shell is the insulation shell and consists of the undoped host lattice material of the core. The acceptors Nd(III) or Pr(III) are doped in the core. The donor Eu(III) is doped in the outer shell. (**Right**) Illustration of the energy levels of Pr(III), Eu(III), Nd(III) as FRET/LRET pairs and Gd(III) as host lattice ion. The transitions for the respective Ln(III) ions are: Blue upward arrow for 465 nm absorption yields excited Eu(III) in the $^5D_2$ state, Pr(III) in the $^3P_0/^3P_1$ ($^1I_6$) state and Nd(III) in the $^4G_{11/2}$ ($^2D_{3/2}$ or $^4G_{9/2}$) [38]. Downward arrows indicate the respective Ln(III) luminescent transitions. Vide infra for corresponding emission spectra. Gd(III) on the right indicates its large energy gap and its indifference on the LRET for Eu(III) quenching.

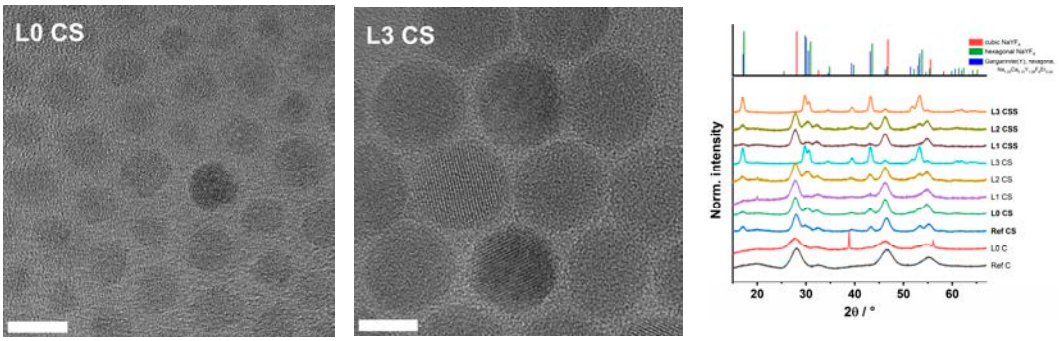

(**a**) (**b**) (**c**)

Figure 2. Set Y300: TEM images of (**a**) L0 CS, (**b**) L3 CS and (**c**) XRD data of $NaYF_4$:$Pr_{20\%}$ @ $NaYF_4$ @ $NaYF_4$:$Eu_{5\%}$. TEM images show the desired nanoparticle size increase upon shell growth. The common core L0 C is not shown for this set. An overview of all recorded TEM images is given in the Appendix A, Figure A1. The XRD data reveals the nanoparticles' hexagonal phase. The top XRD trace shows the reference diffraction patterns of cubic $NaYF_4$ (red, ICDD PDF #77-2042), hexagonal-$NaYF_4$ (green, ICDD PDF #16-334), and hexagonal Gagarinite-(Y) (blue, ICSD #39696). The sharp diffraction peaks at 39° and 56° of L0 C are attributed to cubic NaF (ICSD #43611, reference not shown). Scale bar = 10 nm.

2.3. Nanoparticle Synthesis

All syntheses were performed as previously described [19,39], whereas the amounts of the RE trivalent cations (here: Pr(III) and Y(III) or Nd(III) and Gd(III)) had been adjusted.

2.3.1. Core Synthesis of $NaREF_4$ (UCNP)

Depending on the sample (compare composition in Table 1) the RE chlorides ($YCl_3 \cdot 6H_2O$; $GdCl_3 \cdot 6H_2O$, respectively 1 mmol) were used for the reference cores or in combination with the optical active RE chlorides for the core samples (0.8 mmol of Y(III) or Gd(III) and 0.2 mmol of Nd(III) or Pr(III) or as UC pair: 0.02 mmol Pr(III) and 0.18 mmol of Yb(III)). The RE chlorides, OA (25.2 mmol, 8 mL, 7.12 g) and the solvent Therminol® 66 (12 mL) were transferred into a 50-mL-three-necked-flask. The reaction mixture was evacuated for 10 min at room temperature with subsequent heating to 140 °C under vacuum (<10 mbar) and vigorous stirring. 140 °C were maintained for at least 45 min, so that a clear solution was obtained. The reaction flask was vented with argon to add NaOA (2.5 mmol) and NH_4F (4 mmol). After re-evacuation the temperature was set to 80 °C and kept for 30 min until all salts had dissolved. The reaction flask was re-vented with argon and heated up to 320 °C (heat rate: 25 °C/min) and kept for 15 min. Finally, the temperature was decreased to 250 °C by air and then to approx. 60 °C by a water bath. The nanoparticles were precipitated by ethanol and centrifuged at 3100 g for 8 min. Further purification was performed by washing with ethanol and re-centrifugation for three times. The final precipitate was dispersed in cyclohexane (15 mL).

With respect to the nanoparticle synthesis and the changing dopants, the host lattice change from $NaYF_4$ to $NaGdF_4$ is expected to work as before, since $NaGdF_4$ crystallizes in $P\bar{6}$ space group [40] as well as $NaYF_4$ and $NaNdF_4$ [21,41–45]. A more detailed discussion can be found in Ref. [19]. It should be kept in mind, that even if the synthesis conditions are constant, it cannot be guaranteed that all the lattices crystallize in the same space group which can lead to lattice variations [46]. The trivalent ion migration within the crystal host lattice becomes possible based on those variations and on lattice vacancies, elevated temperatures, dopant concentration, as well as the synthesis approach and the design of the core-shell(-shell) systems.

2.3.2. Shell-Precursor Synthesis of $NaREF_4$ and NaREF4:Eu

The $NaREF_4$ insulation shell (first shell) was prepared either with $YCl_3 \cdot 6H_2O$ or with $GdCl_3 \cdot 6H_2O$ (2 mmol, respectively). The outer $NaREF_4$:Eu shell doped with 5 mol% Eu(III) was prepared with the same RE chlorides as before (but: 1.9 mmol of the Y/Gd chlorides; 0.1 mmol $EuCl_3 \cdot 6H_2O$). The respective RE chlorides were transferred together with OA (4 mL, 3.56 g) and Therminol® 66 (8 mL) into a 50-mL-three-necked-flask. The flask was evacuated for 10 min, subsequently heated up to 140 °C and kept at this temperature for 45 min until a clear solution had formed. The reaction mixture was cooled down to 50 °C to add under an argon counter stream NaOA (2.5 mmol) and NH_4F (4 mmol). After re-evacuation, the system was kept for at least 30 min at 80 °C until the salts had dissolved. The flask was vented with argon and the precursor was stored with an argon atmosphere.

2.3.3. Core-Shell and Core-Shell-Shell Synthesis

The respective nanoparticle cores (60 mg) were transferred into a 50-mL-three-necked-flask and OA (8 mL, 7.12 g) and Therminol® 66 (8 mL) were added. This mixture was evacuated for 30 min at 75 °C and then vented with argon. The temperature was increased to 305 °C as fast as possible and the precursor solution was added at a rate of 2 mL/h. The volume addition of the insulation shell precursor relates to the increasing shell thickness and sample number: L1 = 0.5 mL; L2 = 1 mL; L3 = 4 mL (for set Y300) and L1 = 0.4 mL; L2 = 2 mL; L3 = 4 mL (for set Gd300)—the volume of the Eu(III) doped shell precursors was 1 mL—these declarations apply for all sets. After the precursor addition was completed, the precursor addition temperature (305 °C) was maintained for 5 min. The reaction mixture was cooled down and purified as described for the core nanoparticles. The final precipitate was dispersed in cyclohexane (8 mL).

2.4. Luminescence Emission Spectroscopy

The PL spectra and decay curves were recorded using a wavelength tunable pulsed Nd:YAG/OPO laser system (10 Hz, 26 mJ per pulse/130 mW). A Quanta Ray laser from Spectra Physics (Mountain View, CA, USA) was used for the excitation of the OPO (optical parametric oscillator) from GWU-Lasertechnik Vertriebsges. mbH (Erftstadt, Germany). The experimental setup was in a 90° angle of excitation and emission light. The emitted photons were recorded with a Shamrock SR303i spectrograph from Andor Technology (Belfast, Great Britain). The spectrograph has a grating with 600 L/mm blazed at 500 nm and an iStar DH720-18V-73 intensified CCD-camera from Andor Technology. Luminescence decay curves were recorded using a stroboscopic technique [47]. The initial delays were set to 500 ns for static luminescence emission spectra and to 200 ns for recording luminescence decay curves. The delay was gradually increased by a linear time base function, so that smaller time steps in the beginning and larger time steps in the end of the decays were realized. The data analysis was made with MATLAB 2020b (The MathWorks, Inc., Natick, MA, USA) and with OriginPro 2020b (OriginLab Corporation, Northampton, MA, USA).

2.5. Size (TEM) and Structural (XRD) Characterization

Transmission electron microscopy (TEM) images were recorded with a Tecnai G2 F20 X-Twin TEM from FEI/Thermo Fisher Scientific being operated at 200 kV acceleration voltage. The images were evaluated and the nanoparticles sizes determined with help of the software ImageSP Viewer/Image Sys Prog (version 1.2.5.16 × 64).

The powder X-ray diffraction (XRD) patterns of the nanoparticles were investigated with a PANalytical Empyrean powder X-ray diffractometer in Bragg-Brentano geometry equipped with a PIXcel1D detector. The Cu Kα radiation (λ(Kα) = 1.5419 Å) was used with a voltage and current of 40 kV and 40 mA. The detector sensitivity level (PHD level) was adjusted to 45–80 to reduce fluorescence. The active length was set to 3.0061°. The theta-theta scans were performed over a 2θ range of 4–70° with a step size of 0.0131° and over 190 min.

2.6. Theory

The obtained PL time-resolved emission spectra are analyzed with a stretched exponential model, Equation (1) [48], and an equation derived from the Förster theory, that expresses the number of acceptors around one theoretical donor, Equations (2) and (3) [47]. This model is denoted as LRET model. The stretched exponential model has been chosen to account for the slight differences in the microenvironment of Eu(III). The stretched exponential model is a robust and simple approach to describe the spatial distribution of the Eu(III) in the host lattice with a small number of fitting parameters.

$$I_D(t) = I_D(0)\exp\left[-\left(\frac{t}{\tau_D}\right)^{\beta_D}\right] + y_0 \quad (1)$$

The Index D stands for the donor in absence of the acceptor. $I_D(t)$ is the donor PL emission intensity to the given time t. Hence, $I_D(0)$ is the initial PL emission intensity and the amplitude for the model. τ_D is the donor luminescence decay time and β_D is a heterogeneity parameter describing the donor's microenvironment and its tiny variations, in absence of acceptors, respectively. If $\beta_D > 1$, the model will be a stretched exponential function which can be interpreted as a continuous distribution of PL decay times [48]. If $\beta_D = 1$, the model will be a mono-exponential function indicating a homogeneous microenvironment for the emitting donors in the host lattice. y_0 accounts for the background signal.

$$I_{DA}(t) = I_{DA}(0)\exp\left[-\left(\frac{t}{\tau_D}\right)^{\beta_D} - 2\gamma\left(\frac{t}{\tau_D}\right)^{\alpha/2}\right] + y_0 \quad (2)$$

$$\gamma = \frac{\sqrt{\pi}}{2} c_A \frac{4}{3}\pi R_0^3 \quad (3)$$

The index *DA* indicates the donor in presence of the acceptor, *D* as above the donor only. $I_{DA}(t)$ is the donor PL emission intensity to the given time t. Hence, $I_{DA}(0)$ is the initial luminescence emission intensity and amplitude of the mode. y_0 accounts for the background signal. τ_D and β_D are adopted from the donor PL decay model of the respective reference sample with the absence of the acceptors. The additional heterogeneity α parameter has been introduced to account for the acceptor distribution and its related microenvironments. The parameter γ scales with the number of acceptors in a three-dimensional sphere, having a donor as center. The sphere has the radius of the Förster radius R_0 of the respective donor-acceptor pair. Here, the acceptor concentration c_A is given in ions per Å^3. The term $c_A \frac{4}{3}\pi R_0^3$ expresses the average acceptor number (number of ions) in this 3D sphere with radius equal to R_0 around the donor.

For the sake of clarity, the described model will be called LRET model, the acceptor number will be denoted as acceptor concentration (or as "#acceptors") and the applied donor-acceptor pairs are either Eu(III) and Nd(III) with R_0 = 8.53 Å or Eu(III) and Pr(III) with R_0 = 8.2 Å [20]. In case of Nd(III) the resonance condition is fulfilled, e.g., for the $^2G_{7/2}$, $^4G_{5/2} \leftarrow {}^4I_{9/2}$, $^2H_{11/2} \leftarrow {}^4I_{9/2}$, and $^4F_{9/2} \leftarrow {}^4I_{9/2}$ [28,38], while for the Pr(III) the resonance is achieved via the $^1D_2 \leftarrow {}^3H_4$ [30,38] (see Figure 1).

The LRET efficiency E_{LRET} is calculated with Equation (4) based on the donor PL decay time in presence (τ_{DA}) and in absence of the acceptor (τ_D). The parameter τ_{D} had been calculated before with Equation (1). The parameter τ_{DA} had been calculated with Equation (1) as well, but here τ_D (and β_D) was replaced by τ_{DA} (and β_{DA}), which parameters are also listed in Tables 2 and 3 and in the Appendix A, Tables A2–A4. Equation (1) would then look like:

$$I_{DA}(t) = I_{DA}(0)\exp\left[-\left(\frac{t}{\tau_{DA}}\right)^{\beta_{DA}}\right] + y_0$$

$$E_{\mathrm{LRET}} = 1 - \frac{\tau_{DA}}{\tau_D} \quad (4)$$

Table 2. Set Y300 ($NaYF_4$:$Pr_{20\%}$ @ $NaYF_4$ @ $NaYF_4$:$Eu_{5\%}$): Comparison of the insulation shell thickness, the average acceptor number, decay times τ, and LRET efficiencies $E_{\mathrm{LRET;}}$ evaluation of the Eu(III) luminescence at 616 nm ($^5D_0 \rightarrow {}^7F_2$) and of the Pr(III) luminescence at 608 nm ($^1D_2 \rightarrow {}^3H_4$) using Equations (1)–(4) (λ_{ex} = 465 nm) [1].

Set Y300	**Ref CS**	**L3 CSS**	**L2 CSS**	**L1 CSS**	**L0 CS**
Insulation shell thickness/nm	-/-	6.0	2.0	1.4	0
#acceptors	-/-	0.5	0.9	1.1	1.4
Eu(III) PL decay time τ/µs	4540	1950	1089	928	624
E_{LRET}		0.57	0.76	0.80	0.86
Pr(III) PL decay time τ_{AD}/µs (for CSS, w/Eu(III))	-/-	1.9	1.0	0.3	0.3
Pr(III) PL decay time τ_A/µs (for CS, w/o Eu(III))		1.3	0.3	0.03	0.08
Pr(III) PL enhancement by Eu(III) presence		1.5	3	11	4

[1] #acceptors within a 3D sphere with the radius of R_0(Eu/Pr) = 8.2 Å. Detailed regression parameters are shown in the Appendix A, Table A2. The Pr(III) PL enhancement (= $\tau_{(CSS)}/\tau_{(CS)} = \tau_{AD}/\tau_A$) is a factor for the increasing Pr(III) PL decay times being induced by LRET from Eu(III). (The enhancement factors of the Pr(III) PL decay times in the wavelength range of 530 nm, see Figure 3d, are given in detail in the Appendix A, Table A3).

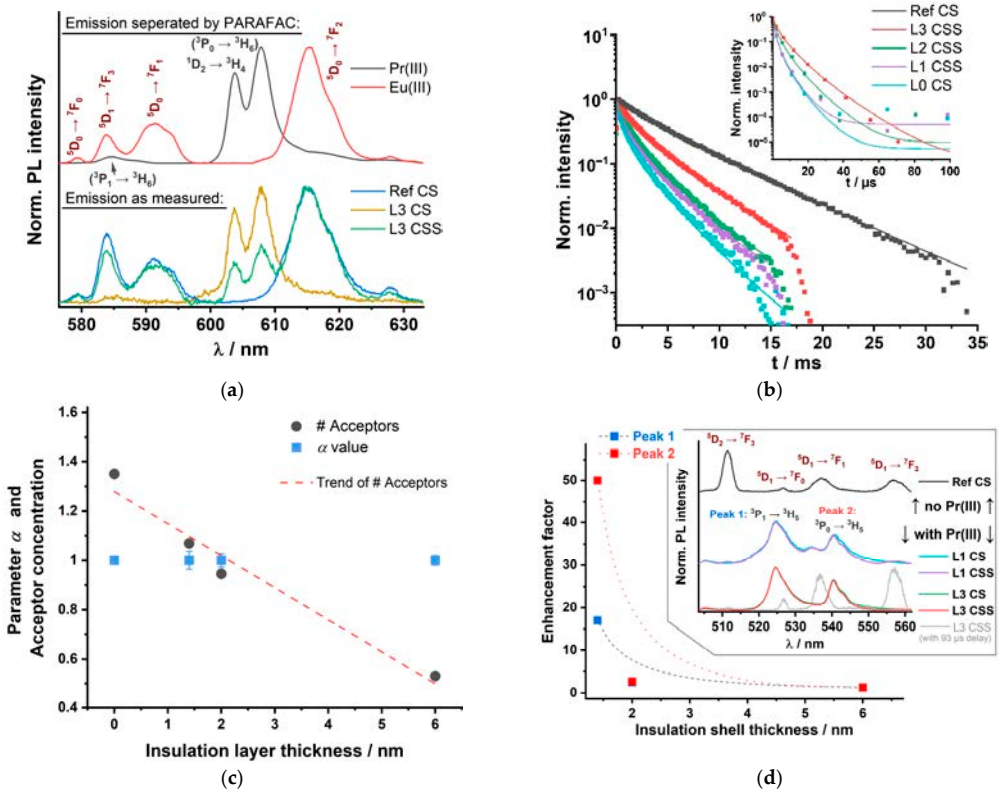

Figure 3. Set Y300 ($NaYF_4$:$Pr_{20\%}$ @ $NaYF_4$ @ $NaYF_4$:$Eu_{5\%}$): Spectroscopic investigation of the Eu(III) and the Pr(III) emission of CSS nanoparticles. (**a**) Eu(III) and Pr(III) PL emission spectra around 600 nm (red labels = Eu(III) transitions, black labels = Pr(III) transitions, λ_{ex} = 465 nm). The Pr(III) transitions labeled in brackets may result from direct excitation as well as sensitization of the $^3P_1 \leftarrow {}^3H_6$ transition by the $^5D_0$ state of Eu(III). Ref CS has no Pr(III) (no acceptor in the core, Eu(III) (donor) in the shell). L3 CS contains Pr(III) (acceptor) in the core and is equipped with the insulation shell, so no Eu(III) (donor) in the shell. L3 CSS contains both ions, Pr(III) (acceptor) in core, no doping in the insulation shell, and Eu(III) (donor) in the outer shell. The PARAFAC separated emission spectra (top part) were calculated from L3 CSS raw PL emission data. (**b**) Eu(III) luminescence decay kinetics recorded at λ_{em} = 616 nm (corresponds to the $^5D_0 \rightarrow {}^7F_2$ transition of Eu(III), λ_{ex} = 465 nm). With decreasing insulation shell thickness, the Eu(III) PL decay times decrease. In addition, from a visual inspection, it can be seen that the kinetics are no longer following a monoexponential decay as shown by Ref CS. Inset of (**b**) are the Pr(III) PL decay curves for λ_{em} = 608 nm ($^1D_2 \rightarrow {}^3H_4$) being separated by PARAFAC from the Eu(III) PL emission at 616 nm (λ_{ex} = 465 nm). (**c**) Results of the evaluation of Eu(III) kinetics based on Equation (2): average acceptor concentration within a 3D sphere (radius of R_0(Eu/Pr) = 8.2 Å) and parameters α, in dependence on the insulation shell thickness, respectively. With increasing insulation shell thickness, the average acceptor numbers decrease. Parameters α are not affected by the thickness of the insulation shell. Detailed regression parameters are shown the Appendix A, Table A2. (**d**) Enhancement factors ($\tau_{(CSS)}/\tau_{(CS)}$) of the Pr(III) PL decay times at 524 nm and at 540 nm (potentially resulting from direct excitation as well as sensitization by Eu(III) re-populating the $^3P_1$ and $^3P_0$ state, as in (a)). Inset of (**d**): PL emission with its respective transitions of Pr(III) in black and Eu(III) in red around 530 nm with λ_{ex} = 465 nm. Detailed regression parameters of the Pr(III) PL decay curves are in the Appendix A, Table A3.

Table 3. Set Gd300: Comparison of the insulation shell thickness, the acceptor numbers (#acceptors), Eu(III) decay times τ and LRET efficiencies E_{LRET}, evaluation with Equations (1)–(4) of the Eu(III) luminescence at 616 nm ($^5D_0 \rightarrow {}^7F_2$) for the core-shell-shell nanoparticles ($NaGdF_4$:$Nd_{20\%}$ @ $NaGdF_4$ @ $NaGdF_4$:$Eu_{5\%}$ nanoparticles), λ_{ex} = 465 nm [1].

Set Gd300	Ref CS	L3 CSS	L2 CSS	L1 CSS	L0 CS
Insulation shell thickness/nm	-/-	2.8	1.0	0.7	0
#acceptors	-/-	0.4	0.6	1.3	1.9
Eu(III) PL decay time τ/μs	2814	1505	1156	507	233
E_{LRET}		0.47	0.59	0.82	0.92

[1] Acceptor concentration = #acceptors within a 3D sphere with the radius of R_0(Eu/Nd) = 8.53 Å. Theoretical evaluation has been performed with the FRET derived model equation. Detailed regression parameters are shown in the Appendix A, Table A4.

Because of the Pr(III) PL decay time being shorter than the Eu(III) PL decay time [19,49–52], the PL decay curves of Pr(III) and Eu(III) were obtained by deconvolution of the respective experimental decay kinetics using parallel factor analysis (PARAFAC algorithm of MATLAB [53]), where necessary. Constrains were set to avoid negative values in the time base, wavelength and intensity. The deconvoluted decays were fitted using Equations (1) and (2) (with OriginPro) for the donor PL decay times and the acceptor PL decay times listed in the results section.

The presented acceptor PL decay times (in absence of the donor, indicated as "*A*" for CS samples, and in presence of the donor, indicated as "*AD*" for CSS samples) were also calculated with a stretched exponential decay model which transforms Equation (1) into:

$$I_{A\ (AD)}(t) = I_{A\ (AD)}(0)\exp\left[-\left(\frac{t}{\tau_{A\ (AD)}}\right)^{\beta_{A\ (AD)}}\right] + y_0$$

3. Results

3.1. Structural Characterization

Two representative examples of TEM images of set Y300 (being the $NaYF_4$:$Pr_{20\%}$ @ $NaYF_4$ @ $NaYF_4$:$Eu_{5\%}$ nanoparticles synthesized at 320/305 °C) are shown in Figure 2 (other TEM images are shown in the Appendix A, Figure A1). As expected, L3 CS has a larger diameter than L0 CS, since L0 CS has been prepared with 1 mL of Eu-doped precursor solution and L3 CS with 4 mL of the insulation shell precursor solution leading to the larger shell thickness. The TEM images of set Gd300 ($NaGdF_4$:$Nd_{20\%}$ @ $NaGdF_4$ @ $NaGdF_4$:$Eu_{5\%}$) nanoparticles synthesized at 320/305 °C are shown in the Appendix A, Figure A1. In Table 1, the nanoparticle sizes of intermediate step, the CS samples, and their respective insulation shell thicknesses are summarized.

The XRD investigations reveal good agreement between the reference XRD patterns and the patterns of the synthesized $NaYF_4$ (Figure 2c) and $NaGdF_4$ (Appendix A, Figure A2) nanoparticles. Some samples of the $NaYF_4$ samples (set Y300) show reflexes of the cubic $NaYF_4$ which vanish gradually after shell addition (see Figure 2c). Furthermore, the XRD patterns of the core nanoparticles (of set Y300) show sharp reflexes at 39° and at 56° corresponding to NaF.

3.2. Luminescence of Set Y300

Compared to our previously published work in the set Y300 the acceptor Nd(III) was exchanged for Pr(III), which is only slightly larger than the former but has the advantage to show luminescence in the visible spectral range. Since it can also serve as an acceptor in combination with Eu(III) as donor, its luminescence may also be used to gain complementary information with respect to the sensitization due to LRET.

In Figure 3a, examples for the luminescence spectra of the Y300 nanoparticle set are shown (bottom part). After excitation at λ_{ex} = 465 nm, the recorded emission spectra contained contributions of Eu(III) as well as of Pr(III) luminescence. The observed Pr(III)

luminescence is a result of sensitized and direct excitation. The direct sensitization occurs via the $^1D_2 \leftarrow {}^3H_4$ of Pr(III). The other Pr(III) luminescence bands (see Figure 1, transition in brackets, and inset of Figure 3d) observed may be a combination of direct excitation (into $^3P_1$), relaxation (e.g., into $^3H_5$ or $^3H_6$) and a (possible) subsequent sensitization (to $^3P_0$ and $^3P_1$). That a sensitization occurs can be seen from the differences in the decay times found for the nanoparticles without and with Eu(III) (see Table A3 containing the PL decay and enhancement data for the transitions $^3P_1 \rightarrow {}^3H_5$ and $^3P_0 \rightarrow {}^3H_5$ at 524 nm and 540 nm, respectively). We used PARAFAC to calculate the pure Eu(III) and the pure Pr(III) luminescence spectra (see Figure 3a, top part). Because of the fact that the Eu(III) PL emission also contains a fairly high contribution of luminescence arising from the $^5D_1 \rightarrow {}^7F_3$ transition (around λ_{em} = 585 nm) the luminescence kinetics were evaluated for the $^5D_0 \rightarrow {}^7F_2$ transition at $\lambda_{em} \approx$ 616 nm. Although emission bands of Pr(III) are also spectrally close (Pr(III) also has transitions in that spectral range: $^3P_1 \rightarrow {}^3H_6$ at 585 nm as well as $^1D_2 \rightarrow {}^3H_4$ and $^3P_0 \rightarrow {}^3H_6$ at 608 nm [38,54]), the Pr(III) PL decay kinetics are much faster (vide infra) and therefore, the Eu(III) emission decay kinetics can be evaluated selectively. The luminescence decay kinetics of Eu(III) and Pr(III) are shown in Figure 3b. It can be seen that upon decreasing the thickness of the insulation layer the Eu(III) luminescence decay kinetics became faster. The observed decrease can be attributed to the LRET process between Eu(III) and Pr(III). It is intriguing that a distinct change is also found in the L3 CSS PL decay kinetics (see Figure 3b), although the thickness of the insulation layer was more than 7-times the Förster distance (insulation layer thickness = (6.0 $\pm$ 0.5) nm compared to R_0(Eu/Pr) = 0.82 nm) (also see Table 2). Hence, mixing of Pr(III) and Eu(III) ions during synthesis into the insulation layer occurred, subsequently the average distance between donor and acceptor ions became much smaller than the insulation shell thickness, which makes the LRET possible. The inset of Figure 3b shows the Pr(III) PL decay times, that result from the PARAFAC analyzed decay curves and spectra of the emission at 608 nm. In Figure 3c the dependence of the average acceptor number on the insulation layer thickness is shown. In addition, the parameter α is shown, which is not changing with the insulation layer thickness basically indicating that there is no insulation layer related heterogeneity of the acceptor distribution. The results found for the Eu(III)/Pr(III) pair in the $NaYF_4$ host lattice are in very good agreement with our results reported for Nd(III) as the acceptor ion.

In addition to the Eu(III) emission also the luminescence of Pr(III) was investigated. Since the decay kinetics of Pr(III) luminescence are much faster than that of Eu(III), we were expecting to find an increased acceptor luminescence decay time due to LRET. However, we observed the contrary: decreasing luminescence decay time with decreasing insulation layer thickness (see inset of Figure 3b and Table 2, detailed regression parameters in the Appendix A, Table A2). In order to find an explanation for the observed trend, the Lx CS (x = 1–3) samples were investigated, in which no outer Eu(III) containing shell was present. The Lx CS samples were used as a reference for "no LRET". Interestingly, when comparing the luminescence decay times of the Lx CS with its respective Lx CSS sample (x = 1–3, see Table 2), we found that the τ-values for the Lx CSS samples were always larger. The enhancements (ratio τ-value for Lx CSS/Lx CS) are given in Table 2. The largest enhancement was found for L1 CSS, which had the thinnest insulation layer. We interpret this observation as the result of two opposing effects. High concentration of Pr(III) in the core leads to self-quenching, but due to the intermixing with the shell, the concentration in the core and subsequently the self-quenching is reduced. The extent of concentration reduction in the core is dependent on the thickness of the shell (insulation layer). Therefore, it is smallest for L1 and largest for L3. On the other hand, the LRET should be largest for L0 and L1, but smallest for L3. From our data, it may be concluded that the dilution effect is dominating. But, by using the comparison with Lx CS samples, it is possible to show the LRET effect on the acceptor luminescence. The luminescence of Pr(III) was also investigated at additional emission wavelengths, for which the enhancement factors have been plotted (see Figure 3d). In the appendix the Pr(III) decay times τ of Peak 1 at

524 nm ($^3P_1 \rightarrow {}^3H_5$) and Peak 2 at 540 nm ($^3P_0 \rightarrow {}^3H_5$) are summarized (see Appendix A, Table A3). Here, basically the same trends were found supporting our findings.

3.3. Luminescence of Set Gd300

The Eu(III) emission spectra of the set Gd300 being quenched by the Nd(III) (LRET-acceptor) are shown in Figure 4 (λ_{ex} = 465 nm). In Figure 4a, the Eu(III) PL emission spectra of set Gd300 are shown with the respective assignment of electronic state transitions. The spectra were normalized to the maximum of the $^5D_0 \rightarrow {}^7F_2$ transition. In Figure 4b, the Eu(III) PL decay kinetics are shown indicating decreasing luminescence decay times (judged by the increasing slope of the decay curves, see Table 3) with decreasing insulation shell thickness. The reference sample (no Nd(III) in the core) has the longest decay time (see Table 3). Even for the sample L3 CSS having the largest insulation shell thickness of 2.8 nm (exceeding the Förster radius R_0(Eu/Nd) = 0.853 nm by a factor >3) a distinct quenching is found.

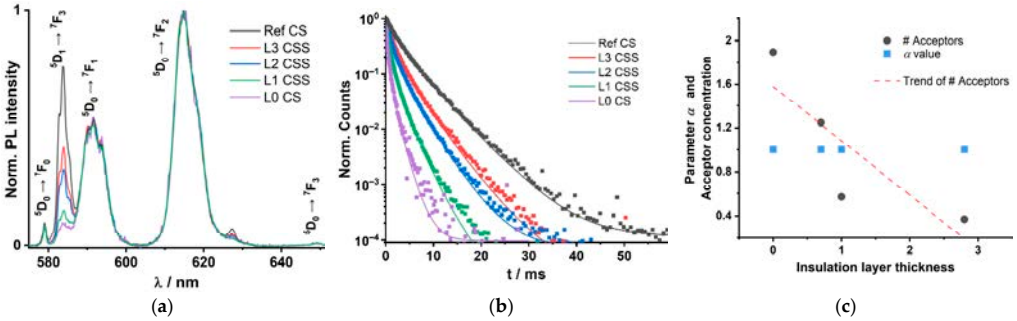

(**a**) (**b**) (**c**)

Figure 4. Set Gd300: Spectroscopic investigation of the Eu(III) emission of CSS nanoparticles ($NaGdF_4$:$Nd_{20\%}$ @ $NaGdF_4$ @ $NaGdF_4$:$Eu_{5\%}$). (**a**) Normalized (by maximum) Eu(III) emission spectra of set Gd300 (λ_{ex} = 465 nm). (**b**) Eu(III) luminescence decay kinetics, emission measured at 616 nm ($^5D_0 \rightarrow {}^7F_2$) ($\lambda_{ex}$ = 465 nm). With decreasing insulation shell thickness, the Eu(III) decay time decreases because of decreasing Eu(III)-Nd(III) distance. (**c**) Graphical presentation of the acceptor concentration within a 3D sphere with the radius of R_0(Eu/Nd) = 8.53 Å and parameters α, in dependence on the insulation shell thickness, from the evaluation of Eu(III) kinetics with the LRET model equation (Equations (1) and (2)). With increasing insulation shell thickness, the acceptor numbers decrease, whereas the parameters α result constantly at the value one.

Based on the LRET-model, the decreasing Eu(III) PL decay times translate in increasing acceptor concentrations as the insulation shell thickness decreases. The Gd300 sample Ref CS has an initial decay time of 2814 µs (λ_{ex} = 465 nm). The PL decay time decreases from L3 CSS to L0 CS from 1505 µs down to 233 µs. Therefore, the LRET efficiency and subsequently the calculated average acceptor concentrations increase from 0.4 acceptors in the 3D sphere (according to the LRET model) for L3 CSS up to 1.9 for L0 CS (see Table 3 and Figure 4c). Looking at the heterogeneity parameters α and β, no significant alterations in the microenvironments of the donor or the acceptor ions are indicated.

A striking difference between the two lattices investigated is the intensity of the $^5D_1 \rightarrow {}^7F_3$ transition, which is visible in both NP sets. The strong contribution of this transition to the overall detected emission is unusual. Comparing the Y300 set with the Gd300 set, the $^5D_1 \rightarrow {}^7F_3$ transition is (i) more intense (judged by a comparison with the intensity of the $^5D_0 \rightarrow {}^7F_j$ transitions) and (ii) it seems to be more affected by the presence of Nd(III) (compare Figures 3a and 4a). Based on the latter observation, it is tempting to assume a participation of the Eu(III) $^5D_1$ energy level in the LRET process.

Complementary to the investigation of the acceptor-related luminescence of the Y300 set doped with Pr(III), the Nd(III) luminescence around 800 nm was analyzed for the Gd300 set. In Figure 5 the luminescence decay kinetics of the respective CS and CSS samples for the smallest and largest insulation layer (L1, L3, respectively) are shown. Alike in the

case of the Y300 set, the acceptor decay kinetics were influenced by the thickness of the insulation layer (see Figure 5a). An increasing insulation layer thickness yielded also a decrease in the luminescence rate constant. That is in line with our interpretation of a partly dilution effect due to the intermixing process leading to a reduced concentration quenching of the Nd(III) ions in the core. In Figure 5b the luminescence decay kinetics of the corresponding CSS samples are shown.

Table 4. Set Gd300: Evaluation of the Nd(III) PL decay curves with Equation (1), for PL decays in Figure 5b resulting from the major Nd(III) PL emission peaks at 795 nm and 805 nm ($^2H_{9/2}$ & $^4F_{5/2} \rightarrow {}^4I_{9/2}$), ($\lambda_{ex}$ = 465 nm) [1].

Gd300	Core-Shell: no Eu(III)		Core-Shell-Shell: with Eu(III)		Nd(III) PL Enhancement
	τ_A/µs	Heterogeneity Parameter β	τ_{AD}/µs	Heterogeneity Parameter β	$\tau_{(CSS)}/\tau_{(CS)} = \tau_{AD}/\tau_A$
L3	16.0 ± 0.2	0.64 ± 0.01	19.3 ± 3.7	0.51 ± 0.04	1.2
			1036 ± 166	0.78 ± 0.06	65
L1	6.3 ± 0.1	0.86 ± 0.01	12.0 ± 2.5	0.68 ± 0.08	1.9
			374 ± 72	0.64 ± 0.05	59

[1] The CSS samples are listed with two decay times due to the abrupt change in the slope, compare inset in Figure 5b. Due to the significant change of the slope, the CSS samples have been analyzed twice with Equation (1). The shorter decay times (below 100 µs) correspond to the dashed regression curves in Figure 5 and refer to the points before the slope change [Nd(III) PL decay curve, without the influence of Eu(III)]. The longer decay times (larger than 100 µs) correspond to the solid regression curves in Figure 5b and refer to the points behind the slope change [Nd(III) PL decay curve with the influence of Eu(III)].

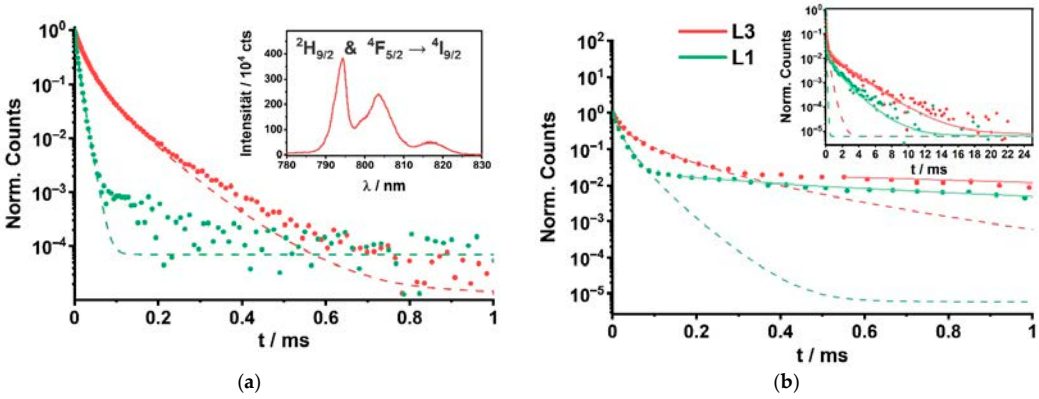

Figure 5. Set Gd300: Nd(III) PL decay curves of (**a**) CS and (**b**) CSS nanoparticles (λ_{ex} = 465 nm). Dotted curves are the experimental PL decay curves; dashed curves are the regressions of the Nd(III) PL decay; solid curves are the regressions of Nd(III) PL decay sensitized by Eu(III), regressions performed with Equation (1). (**a**) Nd(III) PL decay curves of the CS samples (inset: emission spectrum of L3 CS, representative for all recorded Nd(III) spectra of the Gd300 set). (**b**) Nd(III) PL decay kinetics of CSS samples within the first millisecond after excitation (Inset: full Nd(III) luminescence decay kinetics). Parameters listed in Table 4.

The decrease of the luminescence decay rate due to the insulation layer related dilution of the Nd(III) ion in the core is observed. However, for the CSS samples a second much slower luminescence decay process is found (see inset of Figure 5b). This can be attributed to the LRET process and the resulting decrease (increase) of the luminescence decay rate (time). However, it does not become stronger with decreasing insulation layer thickness, because the concentration related quenching seems to be larger than the Nd(III) sensitization by Eu(III)-LRET (compare inset Figure 5b and values in Table 4 in which L1 (thin insulation shell) decays faster than L3 (thick insulation shell)).

4. Discussion

4.1. Structural Characterization

The XRD experiments reveal a hexagonal crystal phase for both sets (Y300 and Gd300), because of the good match between the samples XRD reflexes and the hexagonal reference XRD reflexes. For the set Y300, the detected reflexes of the cubic $NaYF_4$ phase vanish with longer reaction time. Especially, L0 C and Ref C indicate purely cubic phased $NaYF_4$ nanoparticles. Related to the findings of the TEM investigation two ideas came up: Firstly, the cubic phased nanoparticles could have either transformed into the desired hexagonal phased nanoparticles related to the respective precursor shell additions and the associated longer reaction times, or the precursor materials have grown themselves in a hexagonal phase on the cubic phased cores. Previous research by Voss and Haase, as well as Rinkel et al. and Dong et al. give examples for that. Voss and Haase and Rinkel et al. dealt with the fabrication of hexagonal phased UCNPs by providing cubic phased UCNPs as sacrificial material yielding in a narrow size distribution of hexagonal phased UCNPs which is majorly based on Ostwald ripening [55–57]. However, the TEM investigations do not support the dissolution of the initially formed cubic phased nanoparticles. A later work by Rinkel et al. reveals a conversion of the cubic to hexagonal phase $NaYF_4$ particles [58], which could support the first idea. On the other hand, Dong et al. revealed by increasing the dosage of their Ca(II) precursors for growing the CaF_2 shell on hexagonal phased UCNPs, that the XRD reflexes changed from hexagonal $NaGdF_4$ towards CaF_2 [17], which might indicate in the case here, a certain dependency of the XRD signal on the thickness of the shell (and the associated longer reaction time). In the case for these presented experiments, with the insulation layer of the same host material but increasing shell thicknesses, it could point towards the second idea. Unfortunately, the TEM images (discussed in the following paragraph) do not reveal a difference of the cores and the shells due to the same host lattice. The dopant concentration does not seem large enough to reveal significant contrast differences in TEM. Nevertheless, it can be summarized, the samples L1 CS, L2 CS, L1 CSS, L2 CSS and Ref CS and L0 CS show a mixture of reflexes from cubic and hexagonal $NaYF_4$. The samples L5 CS and L5 CSS show only hexagonal $NaYF_4$ reflexes. We attribute this to a cubic-to-hexagonal transition, which already indicates the migration of the ions within the nanocrystal. This migration is surely not only limited to the Ln(III) ions.

The observed NaF XRD reflexes in Figure 2 relate to NaF, from which already small amounts are sufficient to provoke sharp reflexes in the XRD patterns. The NaF vanishes after the shell growth synthesis, which indicates either its consumption and integration into the nanoparticle during the reaction or its removal by the washing and centrifugation steps after the reaction.

The TEM investigation confirms increasing particle size upon shell material addition and subsequently the successful variation of the insulation layer thickness, which is the basis for the LRET analysis. Whereas, the differentiation of the core and shell structures was not possible. Here, two sets with different host lattices were synthesized at T = 320 °C for the core and at T = 305 °C for the shell growth reactions, see Figures 2 and A1 (Appendix A) and Table 1. The synthesis approach, with its applied synthesis conditions, yields spherical shaped nanoparticles, which can be seen here in the TEM images (Figures 2 and A1) and in Ref. [19].

However, it has to be kept in mind, that the changing sizes affect the luminescence properties of upconversion nanoparticles. Hence, it is very likely the same case for the nanoparticles investigated here. Although, some samples share the same core (from the same synthesis batch), their luminescence properties differ slightly as their size and shell thicknesses (insulation layer as well as donor-doped outer shell) change. An important point to note is that the largest nanoparticle (L3 CSS) possesses the thinnest outer shell and the largest surface, which may lead to stronger Eu(III) luminescence quenching.

4.2. LRET

First, we analyzed the Eu(III) luminescence (donor) with respect to the LRET formalism, which was straight forward since any possible interferences from acceptor emission

were discriminated by combining spectral and kinetic aspects in a PARAFAC analysis (vide supra, Figure 3). The analysis of the Eu(III) decay kinetics based on Equation (1) indicates, that the chemical environment does not change distinctly, since the heterogeneity parameter β decreases only slightly with decreasing insulation shell thickness (compare Table A2). This observation could be attributed to the comparable chemical behavior of the Ln(III) ions and the major presence of Y(III) ions in the $NaYF_4$ host lattice in the core as well as in the shells. The same can be observed in the $NaGdF_4$ host lattice with Gd(III) ions as a major lattice part. This is further supported by the heterogeneity parameter α, which represents the situation for the acceptor ions (vide infra). Based on Equation (2), also no change in α was found (compare Appendix A, Tables A2 and A4 for Pr(III) and Nd(III), respectively). Therefore, within the used model the observed changes in the Eu(III) luminescence decay kinetics for the different insulation layer thicknesses are attributed to an alteration of the LRET efficiency. The insulation layer thickness has a clear effect on the Eu(III) luminescence decay kinetics: the luminescence decay time increased with increasing thickness. This was found for both acceptor ions (Pr(III) as well as Nd(III)) in the respective host lattices. This distance-dependent luminescence quenching was analyzed based on the LRET formalism (see Equations (1)–(4)). The LRET from Eu(III) to Pr(III) (or Nd(III)) cannot be suppressed—even if the insulation shell thickness exceeds the Förster radius R_0 by a factor >7 (R_0(Eu/Pr) = 8.2 Å and R_0(Eu/Nd) = 8.53 Å, respectively). The average acceptor concentration (#acceptors) within the 3D sphere with the radius of R_0 (of the respective LRET-pair) increases with decreasing insulation shell thickness (see Figure 6).

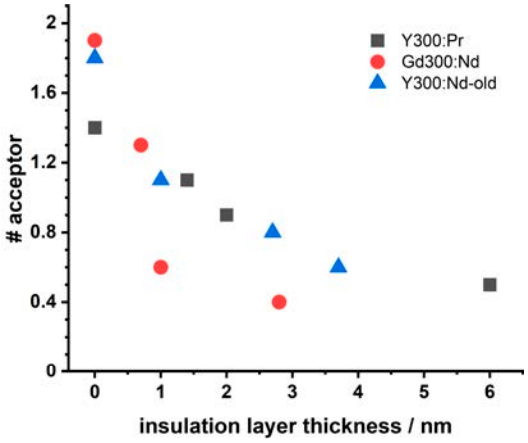

Figure 6. Comparison of the average acceptor number (#acceptor) in the respective R_0 volume for the sets Y300 and Gd300. Shown are also data of Ref. [19] (Y300:Nd-old). The analysis is based on the donor PL emission data.

In Figure 6 the #acceptor (number of acceptors) for the different host lattices and different acceptor ions are compared. Data, resulting of research from Ref. [19], are shown as well. Although the data base is small (e.g, missing of reliable errors) some trends might be seen: (i) for the same host lattice ($NaYF_4$) no difference in the intermixing of Pr(III) and Nd(III) are found and (ii) for the same acceptor ion (Nd(III)) a small influence of the host lattice is seen. It seems that in case of the $NaGdF_4$ lattice the intermixing is less for the larger insulation thicknesses. For the latter observation, differences in the lattice constants as well as lattice phase in combination with specific acceptor ion properties (e.g., ionic radius) could be the reason. Here, small differences in the heterogeneity factors found for the $NaYF_4$ and $NaGdF_4$ lattices obtained from the LRET analysis might point in this direction (vide infra, Tables A2 and A4). Furthermore, the ionic radii of Y(III) (121.5 pm), Gd(III) (124.7 pm),

Eu(III) (126 pm), Nd(III) (130.3 pm), and Pr(III) (131.9 pm) [59] are within a deviation range of 15%, which should be noted. According to Goldschmidt's theory these deviations are tolerable in terms of isomorphism for crystals [18,60]. However, the cationic radius of Y(III) deviates stronger from the Ln(III) cations. The apparent reduced intermixing of dopant Ln(III) ions in the $NaGdF_4$ host lattice could correlate with a stronger migration competition between dopant Ln(III) ions and the host lattice Gd(III) ions, that reduces stronger the dopant Ln(III) ion migration than the Y(III) ions, being smaller, in the $NaYF_4$ host lattice.

In addition to the analysis of the Eu(III) luminescence, we also analyzed the emission of the acceptor ions (Pr(III) for set Y300 and Nd(III) for set Gd300) in order to collect acceptor-based LRET data complementary to the donor results. The two donor-acceptor pairs Eu(III)/Nd(III) and Eu(III)/Pr(III) have been used before in LRET experiments [30,31,38]. However, in contrast to the analysis of the donor emission related data, for the acceptor luminescence some limitations are found with respect to selectivity in excitation and due to self-quenching because of the high local concentration of the respective acceptor ions in the core. In principle, for both acceptor ions a sensitization of their luminescence is shown. In order to quantify the sensitization effect induced by LRET (and separate contributions of direct acceptor excitation as well as self-quenching), the comparison between the CS and CSS samples of each set was necessary. Based on the data of the CS sets, it could be shown that a concentration of 20 mol% of the respective acceptor ion in the core is already high enough to induce concentration related self-quenching. The growth of an insulation layer is reducing the extent of self-quenching because acceptor ions from the core are intermixing with the shell (which is also an indication for the intermixing between core and shell). Here, this dilution effect becomes larger with increasing insulation layer thickness. Contrary to the self-quenching is the LRET based sensitization, which is largest for the L1 CSS samples with a thin insulation layer (see Tables 2 and 4). Especially for the Nd(III) luminescence, the opposing trends (self-quenching vs. sensitization) are seen in its decay kinetics, in which two components were resolved (see Figure 5b). One was attributed to Nd(III) ion in the core, which suffer from self-quenching and the other to Nd(III) ions, which were mixed into the insulation layer. For the latter, the self-quenching was reduced and in case of an outer Eu(III) containing shell (CSS samples) the sensitization was effective. The LRET-based enhancement can be quantified by the comparison between the respective CS and CSS samples, (see Table 2, last row for Pr(III) as the acceptor ion and Table 4, last column for Nd(III), respectively).

5. Conclusions

The work presented is a sequel to our investigation of core-shell UCNPs and the intermixing of ions between core and shell during the synthesis. In continuation of our previous work, we have varied the host lattice composition as well as the Ln(III) ion used as acceptor in the core. For the chosen donor/acceptor pairs the donor (Eu(III)) luminescence can be detected without interference of the acceptor-related emission. Here, we also investigated the acceptor-related luminescence in order to monitor the intermixing between core and shell. In addition to the spectral discrimination between luminescence signals from donor and acceptor, in case of Pr(III) a time gating can be used additionally, since the respective luminescence decay time of Pr(III) is much smaller. In combination with chemometry (PARAFAC) the selective detection of the acceptor's luminescence signal can be achieved. However, despite the advantages on the selective detection of the acceptor emission, we encountered a couple of draw backs in using the luminescence of Pr(III) or Nd(III) directly in the LRET analysis. Since the acceptor concentration in the core was high, we found a self-quenching, which was reduced upon adding a shell. With increasing shell thickness, the self-quenching was reduced indicated by the reference measurements using CS nanoparticles (no outer shell with Eu(III)), for which an increase in the acceptor luminescence decay time was found. This trend is opposite to the sensitization, for which also an increase in the acceptor's luminescence decay time is expected (e.g., donor τ_{Eu} >> acceptor τ_{Pr}), however here the largest sensitization is expected for the smallest

insulation layer thickness. The effect of self-quenching is also of relevance for the standard composition of UCNP containing approx. 18 mol% of Yb(III) ions as sensitizer. Maybe by determining the luminescence kinetics of Yb(III) directly, the intermixing between core and shell can also be monitored, which then would be a potential "quick check" without synthesizing nanoparticles with tailored donor-acceptor pairs for LRET analysis. We will pursuit this idea in future experiments.

Based on the evaluation of the donor PL emission using the LRET concept an average number of acceptor ions in the Förster volume around the donor ions is determined and the dependence on the insulation layer thickness is found. For the first time, we also present luminescence data of the respective acceptor (Pr(III) or Nd(III)) and how it is influenced by the intermixing. Here, two trends of opposite directions are reported: (i) reduction of concentration related self-quenching due to mixing of the acceptor ions from the core into the insulation layer and (ii) sensitization due to LRET. In order to quantify the sensitization, it is necessary to differentiate between both effects and a reference sample set is needed. Therefore, the LRET data analysis of the donor emission is preferred because here no additional samples are needed.

For the purpose of building highly protective shell structures for UCNPs, the intermixing between protective shell(s) and the sublayers has to be minimized. Here, we tested a couple of synthesis and composition parameters with respect to their influence on the intermixing. Using Pr(III) or Nd(III) as acceptor ions in the core of $NaYF_4$-based UCNP made no difference on the observed intermixing. Here, probably the difference in the ionic radii of Pr(III) and Nd(III) is too small to come into play. After all, the LRET approach is limited to certain donor acceptor pair combinations. On the other hand, the comparison of different host lattices from our data shows that the intermixing for the $NaGdF_4$ lattice is smaller for medium and large insulation layer thicknesses (see Figure 6). It is tempting to attribute the observed effect to the difference in the matching between lattice cations (either Y(III) or Gd(III)) and dopant Ln(III) ions.

Here, work is in progress to investigate this parameter further. This is important because in the composition of UCNPs the "heavier" Ln(III) ions are normally used as sensitizer and activator. We have tested NP with a regular composition for UCNP in the core using our LRET approach (core doping 2 mol% Pr(III) and 18 mol% Yb(III), these are an activator and sensitizer pair for upconversion, and outer shell doping with Eu(III) whereas the insulation layer has been applied as before). However, the 2 mol% Pr(III) (activator and LRET-acceptor) were too small to induce a significant quenching of the Eu(III) luminescence (located in the outer layer of the CSS NP) and the Yb(III) ion cannot act as LRET-acceptor due to a missing spectral overlap. We plan to look directly at the Yb(III) luminescence and monitor alterations in a (possible) self-quenching like in the case of Pr(III) or Nd(III) in order to shed light on this aspect (the required instrumentation for time-resolved NIR luminescence detection is being set up at the moment in our lab).

The host lattice in combination with the sensitizer as well as activator properties (lattice matching, lattice phase) are not the only possible parameters to be checked in the course of minimizing the intermixing between core and shell. As well, the synthesis condition or the chemical properties of the shell(s) need to be considered, e.g., using CaF_2 shells [17]. Another possible influence parameter could be the composition of the solvent mixture, e.g., the amount of oleic acid ("oleic acid etching"). For synthesis in octadecene the amount of oleic acid as well as the pH of the reaction solution had a distinct effect on the shape and growth of the nanoparticles. In addition, the reaction time will be of importance [55,61,62]. In the present work we have carried out the synthesis under constant conditions with respect to solvent/surfactant ratio and reaction time. Moreover, we used Therminol® instead of octadecene. But in the future, these parameters may be tested. We have performed first experiments, in which we synthesized the shell(s) at lower temperatures (core synthesis at 320 °C and shell synthesis at 205 °C), but first results with respect to particle size increase or monodispersity of the nanoparticles were unsatisfactory, e.g., it seemed, that in the synthesis step of shell growth, the precursor materials formed

competing seeds leading to a second generation of nanoparticles. Here, modifications in the synthesis, e.g., parameters like the addition rate of precursor materials, will be tested in future work. Additional work is in progress, in which different core and shell lattices are used (e.g., Sc(III) in the core and Y(III) or Gd(III) in the shells or Ca(II) in the outer shell). With an improved understanding of the intermixing process and how to minimize (or eliminate) it, UCNP with a higher brightness (and quantum yields) could be obtained and will make this class of optical probes even more attractive for applications in life sciences.

Author Contributions: Conceptualization and original draft preparation was carried out by P.U.B. Review and editing of writing by M.U.K., N.R., P.S. and T.S. performed the synthesis of the different NP sets and were involved in the luminescence characterization of the NP. Structural characterization was carried out by C.G. (XRD) and V.R. (TEM). C.G. and V.R. also supported the preparation of the original draft and the respective data analysis. The overall data analysis, interpretation and visualization was done by P.U.B. The project was supervised by M.U.K. All authors have read and agreed to the published version of the manuscript.

Funding: This research was partly funded by the KoUP program of the University of Potsdam.

Conflicts of Interest: The authors declare no conflict of interest.

Appendix A

Table A1. Overview of additional subsets and a choice of samples that were investigated by TEM: sets and their samples with the corresponding particle sizes and insulation shell thickness. Each set has its respective reference samples in which the LRET-acceptor is absent. The diameters are derived from the TEM images. Set Y300-UCNP is the same set as set Y300, except that the doping ratio on the core was changed to introduce the Yb-to-Pr upconversion pair instead of Pr(III) doping only. Set Gd200 was prepared exactly the same way as set Gd300 except for the decreased synthesis temperatures of 220 °C or 205 °C. Observation for set Y300-UCNP: The insulation layer thickness increases upon shell precursor addition. However, this trend is not as significant as expected. Observation for set Gd200: The insulation layer thickness does not increase, but it decreases. We relate that to an additional nucleation reaction during shell precursor addition. This additional nucleation reaction may be a consequence of the reduced temperature, which leads maybe to slower decomposition kinetics of the precursor material, so that the critical nucleation concentration can be exceeded. As a consequence, new nucleation seeds are generated on which the additional material starts growing instead of the provided core UCNPs that should actually serve as seeds.

Set Y300-UCNP ($NaYF_4$; ϑ = 320 °C)	**Sample Composition**	**Diameter of Core-Shell (CS) Samples/nm**	**Insulation Shell Thickness/nm**
Y300-UCNP L0 CS [1]	$NaYF_4$:$Yb_{18\%}$, $Pr_{2\%}$ @ $NaYF_4$:$Eu_{5\%}$	9.3 ± 2.2	$\rightarrow 0$
Y300-UCNP L1 CSS [1]	$NaYF_4$:$Yb_{18\%}$, $Pr_{2\%}$ @ $NaYF_4$ @ $NaYF_4$:$Eu_{5\%}$	9.5 ± 2.7	$\rightarrow 0.7$
Y300-UCNP L2 CSS [2]	as above	26 ± 1.7 (87%)	$\rightarrow 9.3$
		15 ± 0.9 (13%)	$\rightarrow 3.8$
Y300-UCNP L3 CSS [2]	as above	14.2 ± 4.5	$\rightarrow 3.4$
Set Gd200 ($NaGdF_4$; ϑ = 220 °C)	**Sample Composition**	**Diameter of Core-Shell (CS) Samples/nm**	**Insulation Shell Thickness/nm**
Gd200 L0 CS [3]	$NaGdF_4$:Nd @ $NaGdF_4$:Eu	3.9 ± 0.3	$\rightarrow 0$
Gd200 L1 CSS [3]	$NaGdF_4$:Nd @ $NaGdF_4$ @ $NaGdF_4$:Eu	3.8 ± 0.4	$\rightarrow (-) 3.4$
Gd200 L2 CSS [4]	as above	4.1 ± 0.5	$\rightarrow (-) 3.3$
Gd200 L3 CSS [4]	as above	4.5 ± 0.6	$\rightarrow (-) 3.1$

[1] Common core for Y300-UCNP samples L0 CS and L1 CS with a core diameter of 8.2 ± 2.5 nm. [2] Common core for Y300-UCNP samples L2 CS and L3 CS with a core diameter of 7.5 ± 0.7 nm. [3] Common core for Gd200 L0 CS and L1 CSS with a core diameter of 10.6 ± 2.0 nm. [4] Common core for Gd200 L2 CS and L3 CSS with a core diameter of 10.9 ± 1.7 nm.

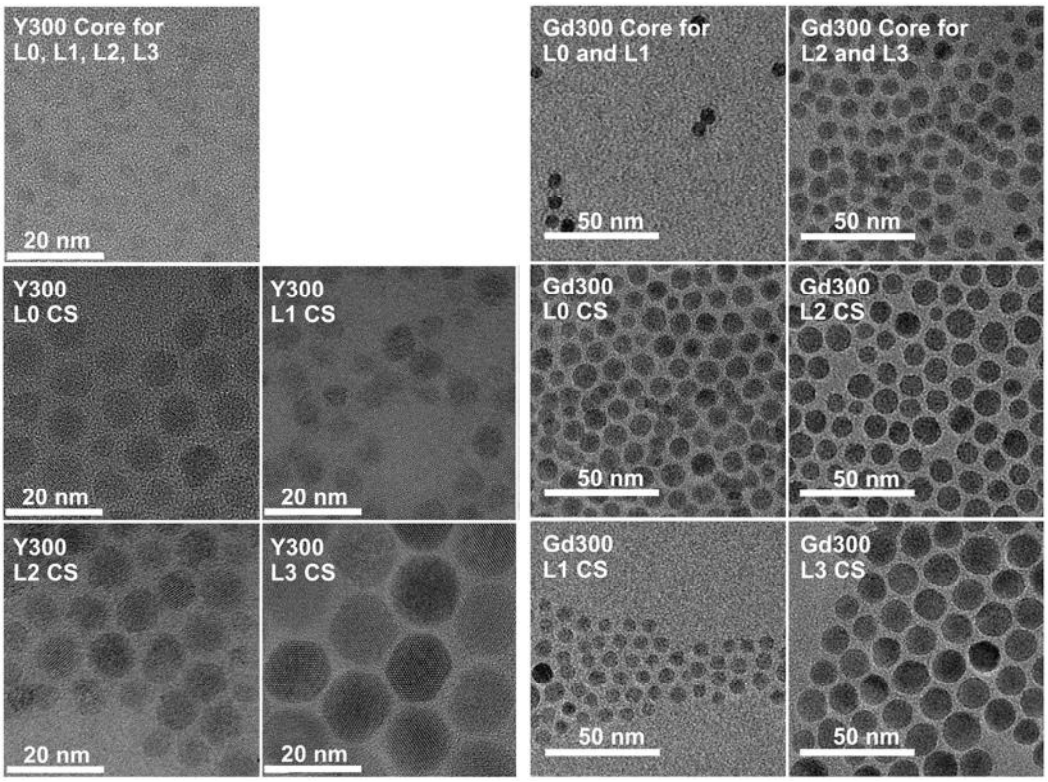

Figure A1. TEM images of the measured samples for the set (**a**) Y300 ($NaYF_4$:$Pr_{20\%}$ @ $NaYF_4$ @ $NaYF_4$:$Eu_{5\%}$, with Pr(III) doping in the core and the insulation layer thicknesses) and (**b**) Gd300 ($NaGdF_4$:$Nd_{20\%}$ @ $NaGdF_4$ @ $NaGdF_4$:$Eu_{5\%}$, with Nd(III) doping in the core and the insulation layer thicknesses). The step of the insulation shell growth synthesis results in increasing particles in comparison to the initial core particle diameter. The $NaYF_4$ based nanoparticles show a larger size distribution of particles than the $NaGdF_4$ nanoparticles.

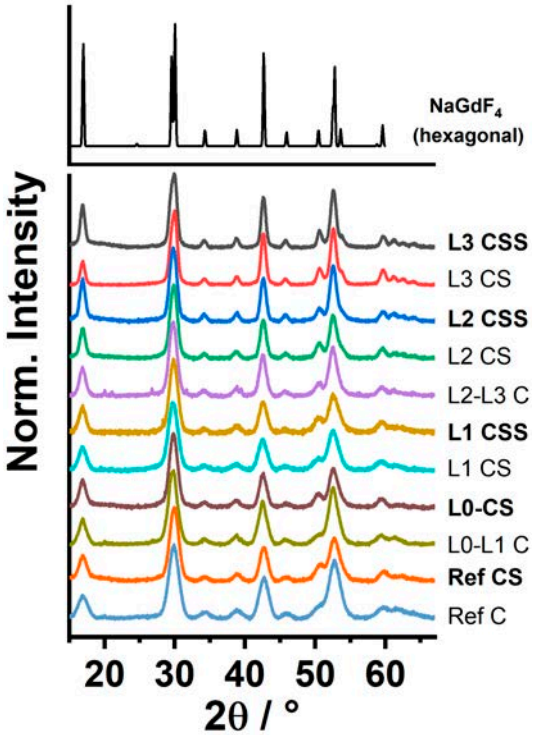

Figure A2. Set Gd300: Powder X-ray diffraction (XRD) patterns ($NaGdF_4$:$Nd_{20\%}$ @ $NaGdF_4$ @ NaGdF4:$Eu_{5\%}$). The XRD reference patterns on top = hexagonal $NaGdF_4$ (ICSD: 415868). The diffraction patterns of the samples match well with the reference patterns revealing their hexagonal crystal phases.

Table A2. Set Y300: Detailed regression parameter for the LRET model (Equation (2)). Upper part: The Eu(III) PL decay times and the Pr(III) PL decay times (with and without Eu(III)). Bottom part: Enhancement factors. Nanoparticle composition = $NaYF_4$:$Pr_{20\%}$ @ $NaYF_4$ @ $NaYF_4$:$Eu_{5\%}$, supplementary material to Table 2, α and β are heterogeneity parameters, λ_{ex} = 465 nm.

Eu(III) Luminescence at 616 nm ($^5D_0 \rightarrow {}^7F_2$)						
Ref CS (Donor Only)	**τ (Donor)/µs**	**±Er**	**β**	**±Er**		
	4540.11	**37.65**	**0.90**	**0.01**		
	#acceptor	**±Er**	**γ**	**±Er**	**α**	**±Er**
L0 CS	1.35	0.01	1.20	0.01	1.00	0.02
L1 CSS	1.07	0.02	0.95	0.02	1.00	0.04
L2 CSS	0.95	0.01	0.84	0.01	1.00	0.03
L3 CSS	0.53	0.01	0.47	0.01	1.00	0.02
	τ/µs	**±Er**	**β**	**±Er**		
Ref CS	4540.11	37.65	0.90	0.01		
L3 CSS	1949.52	18.22	0.74	0.01		
L2 CSS	1089.24	11.53	0.68	0.01		
L1 CSS	928.10	10.09	0.66	0.01		
L0 CS	623.73	16.29	0.60	0.01		

Table A2. *Cont.*

Pr(III) Luminescence at 608 nm ($^1D_2 \rightarrow {}^3H_4$) [CSS Samples, with Eu(III)]				
	τ_{AD}/µs	±Er	β_{AD}	±Er
L3 CSS	1.94	0.04	0.66	0.01
L2 CSS	1.02	0.06	0.6	0.02
L1 CSS	0.34	0.06	0.51	0.03
L0 CS	0.32	0.05	0.51	0.03
Pr(III) Luminescence at 608 nm ($^1D_2 \rightarrow {}^3H_4$) [CS Samples → No Eu(III)]				
	τ_A/µs	±Er	β_A	±Er
L3 CS	1.26	0.01	0.59	1.26
L2 CS	0.33	0.01	0.49	0.33
L1 CS	0.03	0.01	0.39	0.03
L0 C	0.08	0.04	0.52	0.08
Enhancement Factor for $\tau_{(CSS/AD)}/\tau_{(CS/A)}$ of Pr(III) Luminescence at 608 nm ($^1D_2 \rightarrow {}^3H_4$)				
L3 CSS/CS	1.94 µs/1.26 µs → 1.5			
L2 CSS/CS	1.02 µs/0.33 µs → 3.1			
L1 CSS/CS	0.34 µs/0.03 µs → 11.3			
L0 CS/C	0.32 µs/0.08 µs → 4.0			

Table A3. Set Y300: Detailed regression parameter for stretched exponential model (Equation (1)) Pr(III) PL decay times τ of Peak 1 at 524 nm ($^3P_1 \rightarrow {}^3H_5$) and Peak 2 at 540 nm ($^3P_0 \rightarrow {}^3H_5$) with λ_{ex} = 465 nm ($NaYF_4$:$Pr_{20\%}$ @ $NaYF_4$ @ $NaYF_4$:$Eu_{5\%}$ nanoparticles). Additional material for Figure 3 and Table 2.

Set Y300	**Core-Shell: without Eu(III)**		**Core-Shell-Shell: with Eu(III)**		**Pr(III) PL Enhancement**
	τ_A/µs	**Heterogeneity Parameter β_A**	τ_{AD}/µs	**Heterogeneity Parameter β_{AD}**	$\tau_{(CSS/AD)}/\tau_{(CS/A)}$
Peak 1: L3	1.51 ± 0.01	0.61 ± 0.01	1.91 ± 0.02	0.64 ± 0.01	1.3
Peak 1: L2	0.35 ± 0.01	0.49 ± 0.01	0.88 ± 0.01	0.56 ± 0.01	2.5
Peak 1: L1	0.02 ± 0.01	0.34 ± 0.02	0.37 ± 0.02	0.51 ± 0.01	17
Peak 1: L0	0.01 ± 0.01	0.35 ± 0.04	Not measured	Not measured	
Peak 2: L3	1.52 ± 0.01	0.62 ± 0.01	1.91 ± 0.02	0.64 ± 0.01	1.3
Peak 2: L2	0.37 ± 0.01	0.49 ± 0.01	1.01 ± 0.03	0.60 ± 0.01	2.7
Peak 2: L1	0.01 ± 0.01	0.43 ± 0.03	0.50 ± 0.03	0.57 ± 0.01	50
Peak 2: L0	0.01 ± 0.01	0.51 ± 0.06	Not measured	Not measured	

Table A4. Set Gd300: Detailed regression parameter for the FRET derived model equation (Equation (2)) of the Eu(III) decay times. Nanoparticle composition = $NaGdF_4$:$Nd_{20\%}$ @ $NaGdF_4$ @ $NaGdF_4$:$Eu_{5\%}$, additional material to Table 3. α and β are heterogeneity parameters.

Eu(III) Luminescence at 616 nm ($^5D_0 \rightarrow {}^7F_2$), λ_{ex} = 465 nm						
	τ (Donor)/µs	**±Er**	**β**	**±Er**		
Ref CS (Donor only)	2813.85	22.00	0.82	0.01		
	#acceptor	**±Er**	**γ**	**±Er**	**α**	**±Er**
L0 CS	1.90	0.02	1.68	0.02	1.00	0.02
L1 CSS	1.25	0.02	1.11	0.02	1.00	0.02
L2 CSS	0.57	0.01	0.51	0.01	1.00	0.02
L3 CSS	0.37	0.01	0.33	0.01	1.00	0.03
	τ/µs	**±Er**	**β**	**±Er**		
Ref CS	2813.85	22.00	0.82	0.01		
L3 CSS	1504.81	13.52	0.73	0.01		
L2 CSS	1155.81	9.73	0.72	0.01		
L1 CSS	506.79	5.97	0.65	0.01		
L0 CS	232.70	5.732	0.59	0.01		

References

1. Zhu, X.; Zhang, J.; Liu, J.; Zhang, Y. Recent Progress of Rare-Earth Doped Upconversion Nanoparticles: Synthesis, Optimization, and Applications. *Adv. Sci.* **2019**, *6*, 1901358. [CrossRef]
2. Tessitore, G.; Mandl, G.A.; Brik, M.G.; Park, W.; Capobianco, J.A. Recent insights into upconverting nanoparticles: Spectroscopy, modeling, and routes to improved luminescence. *Nanoscale* **2019**, *11*, 12015–12029. [CrossRef]
3. Naccache, R.; Yu, Q.; Capobianco, J.A. The Fluoride host: Nucleation, growth, and upconversion of lanthanide-doped nanoparticles. *Adv. Opt. Mater.* **2015**, *3*, 482–509. [CrossRef]
4. Würth, C.; Kaiser, M.; Wilhelm, S.; Grauel, B.; Hirsch, T.; Resch-Genger, U. Excitation power dependent population pathways and absolute quantum yields of upconversion nanoparticles in different solvents. *Nanoscale* **2017**, *9*, 4283–4294. [CrossRef]
5. DaCosta, M.V.; Doughan, S.; Han, Y.; Krull, U.J. Lanthanide upconversion nanoparticles and applications in bioassays and bioimaging: A review. *Anal. Chim. Acta* **2014**, *832*, 1–33. [CrossRef]
6. Chen, G.; Qiu, H.; Prasad, P.N.; Chen, X. Upconversion nanoparticles: Design, nanochemistry, and applications in theranostics. *Chem. Rev.* **2014**, *114*, 5161–5214. [CrossRef]
7. Muhr, V.; Wilhelm, S.; Hirsch, T.; Wolfbeis, O.S. Upconversion nanoparticles: From hydrophobic to hydrophilic surfaces. *Acc. Chem. Res.* **2014**, *47*, 3481–3493. [CrossRef] [PubMed]
8. Andresen, E.; Resch-Genger, U.; Schäferling, M. Surface Modifications for Photon-Upconversion-Based Energy-Transfer Nanoprobes. *Langmuir* **2019**, *35*, 5093–5113. [CrossRef] [PubMed]
9. Gorris, H.H.; Wolfbeis, O.S. Photon-upconverting nanoparticles for optical encoding and multiplexing of cells, biomolecules, and microspheres. *Angew. Chem.-Int. Ed.* **2013**, *52*, 3584–3600. [CrossRef] [PubMed]
10. Hudry, D.; Busko, D.; Popescu, R.; Gerthsen, D.; Abeykoon, A.M.M.; Kübel, C.; Bergfeldt, T.; Richards, B.S. Direct Evidence of Significant Cation Intermixing in Upconverting Core@Shell Nanocrystals: Toward a New Crystallochemical Model. *Chem. Mater.* **2017**, *29*, 9238–9246. [CrossRef]
11. Hudry, D.; Popescu, R.; Diaz-Lopez, M.; Abeykoon, A.M.M.; Bordet, P.; Gerthsen, D.; Howard, I.A.; Richards, B.S. Interface disorder in large single- and multi-shell upconverting nanocrystals. *J. Mater. Chem. C* **2019**, *7*, 1164–1172. [CrossRef]
12. Hudry, D.; Busko, D.; Popescu, R.; Gerthsen, D.; Howard, I.A.; Richards, B.S. An enhanced energy migration strategy in upconverting nanocrystals: Color-tuning with high quantum yield. *J. Mater. Chem. C* **2019**, *7*, 7371–7377. [CrossRef]
13. Hudry, D.; Howard, I.A.; Popescu, R.; Gerthsen, D.; Richards, B.S. Structure-Property Relationships in Lanthanide-Doped Upconverting Nanocrystals: Recent Advances in Understanding Core–Shell Structures. *Adv. Mater.* **2019**, *31*, 1900623. [CrossRef]
14. Diogenis, I.M.S.; Rodrigues, E.M.; Mazali, I.O.; Sigoli, F.A. Spectroscopic evidence of preferential excitation of interfacial Eu^{III} by interfacial energy transfer process on core@shell nanoparticles. *J. Lumin.* **2021**, *232*, 117848. [CrossRef]
15. Liu, L.; Li, X.; Fan, Y.; Wang, C.; El-Toni, A.M.; Alhoshan, M.S.; Zhao, D.; Zhang, F. Elemental Migration in Core/Shell Structured Lanthanide Doped Nanoparticles. *Chem. Mater.* **2019**, *31*, 5608–5615. [CrossRef]
16. Chen, B.; Peng, D.; Chen, X.; Qiao, X.; Fan, X.; Wang, F. Establishing the structural integrity of core-shell nanoparticles against elemental migration using luminescent lanthanide probes. *Angew. Chem.-Int. Ed.* **2015**, *54*, 12788–12790. [CrossRef]
17. Dong, H.; Sun, L.D.; Li, L.D.; Si, R.; Liu, R.; Yan, C.H. Selective cation exchange enabled growth of lanthanide core/shell nanoparticles with dissimilar structure. *J. Am. Chem. Soc.* **2017**, *139*, 18492–18495. [CrossRef] [PubMed]

18. Goldschmidt, V.M. Die Gesetze der Krystallochemie. *Naturwissenschaften* **1926**, *14*, 477–485. [CrossRef]
19. Bastian, P.U.; Nacak, S.; Roddatis, V.; Kumke, M.U. Tracking the motion of lanthanide ions within core–shell–shell $NaYF_4$ nanocrystals via resonance energy transfer. *J. Phys. Chem. C* **2020**, *124*, 11229–11238. [CrossRef]
20. Horrocks, W.D.W.; Sudnick, D.R. Lanthanide ion luminescence probes of the structure of biological macromolecules. *Acc. Chem. Res.* **1981**, *14*, 384–392. [CrossRef]
21. Wang, F.; Han, Y.; Lim, C.S.; Lu, Y.; Wang, J.; Xu, J.; Chen, H.; Zhang, C.; Hong, M.; Liu, X. Simultaneous phase and size control of upconversion nanocrystals through lanthanide doping. *Nature* **2010**, *463*, 1061–1065. [CrossRef] [PubMed]
22. Liu, Q.; Sun, Y.; Yang, T.; Feng, W.; Li, C.; Li, F. Sub-10 nm hexagonal lanthanide-doped NaLuF 4 upconversion nanocrystals for sensitive bioimaging in vivo. *J. Am. Chem. Soc.* **2011**, *133*, 17122–17125. [CrossRef] [PubMed]
23. Jia, H.; Zhou, Y.; Li, X.; Li, Y.; Zhang, W.; Fu, H.; Zhao, J.; Pan, L.; Liu, X.; Qiu, J. Synthesis and phase transformation of $NaGdF_4$:Yb-Er thin films using electro-deposition method at moderate temperatures. *CrystEngComm* **2018**, *20*, 6919–6924. [CrossRef]
24. Park, Y.I.; Kim, H.M.; Kim, J.H.; Moon, K.C.; Yoo, B.; Lee, K.T.; Lee, N.; Choi, Y.; Park, W.; Ling, D.; et al. Theranostic probe based on lanthanide-doped nanoparticles for simultaneous in vivo dual-modal imaging and photodynamic therapy. *Adv. Mater.* **2012**, *24*, 5755–5761. [CrossRef] [PubMed]
25. Annapurna, K.; Dwivedi, R.N.; Buddhudu, S. Energy transfer luminescence in (Eu^{3+},Nd^{3+}): Tellurite glass. *Opt. Mater.* **2000**, *13*, 381–388. [CrossRef]
26. Sharp, E.J.; Weber, M.J.; Cleek, G. Energy transfer and fluorescence quenching in Eu- and Nd-doped silicate glasses. *J. Appl. Phys.* **1970**, *41*, 364–369. [CrossRef]
27. Abad Galán, L.; Sobolev, A.N.; Skelton, B.W.; Zysman-Colman, E.; Ogden, M.I.; Massi, M. Energy transfer between Eu^{3+} and Nd^{3+} in near-infrared emitting β-triketonate coordination polymers. *Dalt. Trans.* **2018**, *47*, 12345–12352. [CrossRef]
28. Joshi, J.C.; Pandey, N.C.; Joshi, B.C.; Belwal, R.; Joshi, J. Quantum efficiency of Diffusion-Limited Energy Transfer from $Eu^{3+} \rightarrow Nd^{3+}$ in Borate Glass. *J. Solid State Chem.* **1978**, *23*, 135–139. [CrossRef]
29. Kandpal, H.C.; Tripathi, H.B. Non-radiative energy transfer from Eu^{3+} to Pr^{3+} and Eu^{3+} to Er^{3+} in DMSO. *Solid State Commun.* **1979**, *29*, 103–107. [CrossRef]
30. Chen, Y.; Wang, J.; Liu, C.; Tang, J.; Kuang, X.; Wu, M.; Su, Q. UV-Vis-NIR luminescence properties and energy transfer mechanism of $LiSrPO_4$:Eu^{2+}, Pr^{3+} suitable for solar spectral convertor. *Opt. Express* **2013**, *21*, 3161. [CrossRef]
31. Li, Y.; Wang, J.; Wang, X.M.; Pan, F.; Zhou, T.; Xie, R.J. Colour tuning via crystalline site-selected energy transfer in a Sr_2SiO_4:Eu^{2+},Pr^{3+} phosphor. *J. Mater. Chem. C* **2017**, *5*, 1022–1026. [CrossRef]
32. Da Gama, A.A.S.; De Sá, G.F.; Porcher, P.; Caro, P. Energy levels of Nd^{3+} in $LiYF_4$. *J. Chem. Phys.* **1981**, *75*, 2583–2587. [CrossRef]
33. Runowski, M.; Woźny, P.; Martín, I.R.; Lavín, V.; Lis, S. Praseodymium doped YF_3:Pr^{3+} nanoparticles as optical thermometer based on luminescence intensity ratio (LIR)—Studies in visible and NIR range. *J. Lumin.* **2019**, *214*, 116571. [CrossRef]
34. Hao, S.; Shao, W.; Qiu, H.; Shang, Y.; Fan, R.; Guo, X.; Zhao, L.; Chen, G.; Yang, C. Tuning the size and upconversion emission of $NaYF_4$:Yb^{3+}/Pr^{3+} nanoparticles through Yb^{3+} doping. *RSC Adv.* **2014**, *4*, 56302–56306. [CrossRef]
35. Dieke, G.H.; Crosswhite, H.M. The Spectra of the Doubly and Triply Ionized Rare Earths. *Appl. Opt.* **1963**, *2*, 675–686. [CrossRef]
36. Carnall, W.T.; Fields, P.R.; Rajnak, K. Electronic Energy Levels in the Trivalent Lanthanide Aquo Ions. I. Pr^{3+}, Nd^{3+}, Pm^{3+}, Sm^{3+}, Dy^{3+}, Ho^{3+}, Er^{3+}, and Tm^{3+}. *J. Chem. Phys.* **1968**, *49*, 4424–4442. [CrossRef]
37. Carnall, W.T.; Fields, P.R.; Rajnak, K. Electronic Energy Levels of the Trivalent Lanthanide Aquo Ions. IV. Eu^{3+}. *J. Chem. Phys.* **1968**, *49*, 4450–4455. [CrossRef]
38. Nakazawa, E.; Shionoya, S. Energy transfer between trivalent rare-earth ions in inorganic solids. *J. Chem. Phys.* **1967**, *47*, 3267–3270. [CrossRef]
39. Hesse, J.; Klier, D.T.; Sgarzi, M.; Nsubuga, A.; Bauer, C.; Grenzer, J.; Hübner, R.; Wislicenus, M.; Joshi, T.; Kumke, M.U.; et al. Rapid Synthesis of Sub-10 nm Hexagonal $NaYF_4$-Based Upconverting Nanoparticles using Therminol®66. *ChemistryOpen* **2018**, *7*, 159–168. [CrossRef]
40. Aebischer, A.; Hostettler, M.; Hauser, J.; Krämer, K.; Weber, T.; Güdel, H.U.; Bürgi, H.B. Structural and spectroscopic characterization of active sites in a family of light-emitting sodium lanthanide tetrafluorides. *Angew. Chem.-Int. Ed.* **2006**, *45*, 2802–2806. [CrossRef]
41. Szefczyk, B.; Roszak, R.; Roszak, S. Structure of the hexagonal $NaYF_4$ phase from first-principles molecular dynamics. *RSC Adv.* **2014**, *4*, 22526–22535. [CrossRef]
42. Grzechnik, A.; Bouvier, P.; Mezouar, M.; Mathews, M.D.; Tyagi, A.K.; Köhler, J. Hexagonal Na1.5Y1.5F6 at high pressures. *J. Solid State Chem.* **2002**, *165*, 159–164. [CrossRef]
43. Krämer, K.W.; Biner, D.; Frei, G.; Güdel, H.U.; Hehlen, M.P.; Lüthi, S.R. Hexagonal Sodium Yttrium Fluoride Based Green and Blue Emitting Upconversion Phosphors. *Chem. Mater.* **2004**, *16*, 1244–1251. [CrossRef]
44. Burns, J.H. Crystal Structure of Hexagonal Sodium Neodymium Fluoride and Related Compounds. *Inorg. Chem.* **1965**, *4*, 881–886. [CrossRef]
45. Mackenzie, L.E.; Goode, J.A.; Vakurov, A.; Nampi, P.P.; Saha, S.; Jose, G.; Millner, P.A. The theoretical molecular weight of $NaYF_4$: RE upconversion nanoparticles. *Sci. Rep.* **2018**, *8*, 1106. [CrossRef]
46. Wu, X.; Zhan, S.; Han, J.; Liu, Y. Nanoscale Ultrasensitive Temperature Sensing Based on Upconversion Nanoparticles with Lattice Self-Adaptation. *Nano Lett.* **2021**, *21*, 272–278. [CrossRef]

47. Valeur, B. *Molecular Fluorescence—Principles and Applications*; Wiley-VCH Verlag: Weinheim, Germany, 2002; ISBN 352729919X.
48. Benny Lee, K.C.; Siegel, J.; Webb, S.E.D.; Lévêque-Fort, S.; Cole, M.J.; Jones, R.; Dowling, K.; Lever, M.J.; French, P.M.W. Application of the stretched exponential function to fluorescence lifetime imaging. *Biophys. J.* **2001**, *81*, 1265–1274. [CrossRef]
49. Li, K.Y.; Liu, L.Y.; Wang, R.Z.; Xiao, S.G.; Zhou, H.; Yan, H. Broadband sensitization of downconversion phosphor YPO_4 by optimizing TiO_2 substitution in host lattice co-doped with Pr^{3+}-Yb^{3+} ion-couple. *J. Appl. Phys.* **2014**, *115*, 123103. [CrossRef]
50. Chen, X.P.; Huang, X.Y.; Zhang, Q.Y. Concentration-dependent near-infrared quantum cutting in $NaYF_4$:Pr^{3+}, Yb^{3+} phosphor. *J. Appl. Phys.* **2009**, *106*, 063518. [CrossRef]
51. Binnemans, K. Interpretation of europium(III) spectra. *Coord. Chem. Rev.* **2015**, *295*, 1–45. [CrossRef]
52. Rabouw, F.T.; Prins, P.T.; Norris, D.J. Europium-Doped $NaYF_4$ Nanocrystals as Probes for the Electric and Magnetic Local Density of Optical States throughout the Visible Spectral Range. *Nano Lett.* **2016**, *16*, 7254–7260. [CrossRef]
53. Bro, R. PARAFAC tutorial and applications. *Chemom. Intell. Lab. Syst.* **1997**, *38*, 149–171. [CrossRef]
54. Görller-Walrand, C.; Binnemans, K. Rationalization of Crystal-Field Parametrization. In *Handbook on the Physics and Chemistry of Rare Earths*; Gschneidner, K.A., Eyring, L., Eds.; Elsevier: Amsterdam, The Netherlands, 1996; pp. 173–178.
55. Voss, B.; Haase, M. Intrinsic focusing of the particle size distribution in colloids containing nanocrystals of two different crystal phases. *ACS Nano* **2013**, *7*, 11242–11254. [CrossRef] [PubMed]
56. Rinkel, T.; Nordmann, J.; Raj, A.N.; Haase, M.; Val'kovskii, M.D.; Sobolev, B.P.; Park, J.; Hwang, N.; Hyeon, T.; Cohen, B.E.; et al. Ostwald-ripening and particle size focussing of sub-10 nm $NaYF_4$ upconversion nanocrystals. *Nanoscale* **2014**, *6*, 14523–14530. [CrossRef] [PubMed]
57. Dühnen, S.; Haase, M. Study on the Intermixing of Core and Shell in $NaEuF_4$/$NaGdF_4$ Core/Shell Nanocrystals. *Chem. Mater.* **2015**, *27*, 8375–8386. [CrossRef]
58. Rinkel, T.; Raj, A.N.; Dühnen, S.; Haase, M. Synthesis of 10 nm β-$NaYF_4$:Yb, Er/$NaYF_4$ core/shell upconversion nanocrystals with 5 nm particle cores. *Angew. Chem.-Int. Ed.* **2016**, *55*, 1164–1167. [CrossRef]
59. Huheey, J.E.; Keiter, E.A.; Keiter, R.L. *Anorganische Chemie—Prinzipien von Struktur und Reaktivität*; Steudel, R., Ed.; de Gruyter GmbH: Berlin, Germany; Boston, MA, USA, 2012; ISBN 9783110249071.
60. Pfiffner, O.A.; Engi, M.; Schlunegger, F.; Mezger, K.; Diamond, L. Erdwissenschaften. In *Erdwissenschaften*; utb GmbH: Bavaria, Germany, 2016; p. 285.
61. Oh, N.; Shim, M. Metal oleate induced etching and growth of semiconductor nanocrystals, nanorods, and their heterostructures. *J. Am. Chem. Soc.* **2016**, *138*, 10444–10451. [CrossRef] [PubMed]
62. Liu, D.; Xu, X.; Du, Y.; Qin, X.; Zhang, Y.; Ma, C.; Wen, S.; Ren, W.; Goldys, E.M.; Piper, J.A.; et al. Three-dimensional controlled growth of monodisperse sub-50 nm heterogeneous nanocrystals. *Nat. Commun.* **2016**, *7*, 10254. [CrossRef]

2.4. UCNP Phase Transfer into Aqueous Solution and Bio-Conjugation with a TAMRA Dye via Click Chemistry – A Proof of Principle (Manuscript 3)

"Bioinspired Confinement of Upconversion Nanoparticles for Improved Performance in Aqueous Solution"

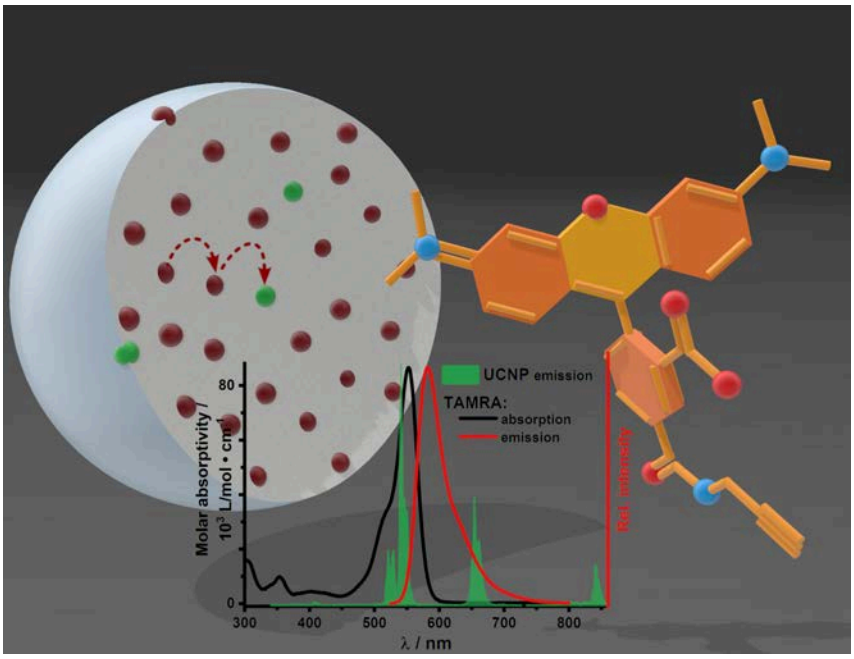

Reprinted with permission from

J. Phys. Chem. C **124** (52), 28623–28635 (2020).[101]

Link: https://doi.org/10.1021/acs.jpcc.0c09798

ACS Article on Request author-directed link:
http://pubs.acs.org/articlesonrequest/AOR-IPZAZMVNCMSCIVFPY89P

THE JOURNAL OF PHYSICAL CHEMISTRY C

pubs.acs.org/JPCC Article

Bioinspired Confinement of Upconversion Nanoparticles for Improved Performance in Aqueous Solution

Philipp U. Bastian, Leixiao Yu, Anna López de Guereñu, Rainer Haag, and Michael U. Kumke*

Cite This: *J. Phys. Chem. C* 2020, 124, 28623−28635 Read Online

ACCESS | Metrics & More | Article Recommendations | Supporting Information

ABSTRACT: The resonance energy transfer (RET) from $NaYF_4$:Yb,Er upconverting nanoparticles (UNCPs) to a dye (5-carboxytetramethylrhodamine (TAMRA)) was investigated by photoluminescence experiments and microscale thermophoresis (MST). The dye was excited via RET from the UCNPs which was excited in the near-infrared (NIR). The change of the dye diffusion speed (free vs coupled) was investigated by MST. RET shows significant changes in the decay times of the dye as well as of the UCNPs. MST reveals significant changes in the diffusion speed. A unique amphiphilic coating polymer (customized mussel protein (CMP) polymer) for UCNP surface coating was used, which mimics blood protein adsorption and mussel food protein adhesion to transfer the UCNP into the aqueous phase and to allow surface functionalization. The CMP provides very good water dispersibility to the UCNPs and minimizes ligand exchange and subsequent UCNP aging reactions because of the interlinkage of the CMP on the UCNP surface. Moreover, CMP provides N_3-functional groups for click chemistry-based functionalization demonstrated with the dye 5-carboxytetramethylrhodamine (TAMRA). This establishes the principle coupling scheme for suitable biomarkers such as antibodies. The CMP provides very stable aqueous UCNP dispersions that are storable up to 3 years in a fridge at 5 °C without dissolution or coagulation. The outstanding properties of CMP in shielding the UCNP from unwanted solvent effects is reflected in the distinct increase of the photoluminescence decay times after UCNP functionalization. The UCNP-to-TAMRA energy transfer is also spectroscopically investigated at low temperatures (4−200 K), revealing that one of the two green Er(III) emission bands contributes the major part to the energy transfer. The TAMRA fluorescence decay time increases by a factor of 9500 from 2.28 ns up to 22 μs due to radiationless energy transfer from the UCNP after NIR excitation of the latter. This underlines the unique properties of CMP as a versatile capping ligand for distinctly improving the UCNPs' performance in aqueous solutions, for coupling of biomolecules, and for applications for in vitro and in vivo experiments using UCNPs as optical probes in life science applications.

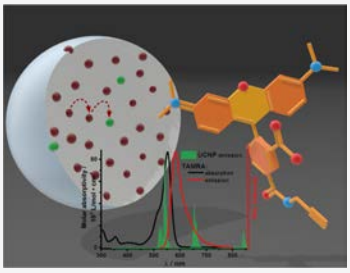

INTRODUCTION

The upconversion process based on energy transfer upconversion (ETU) was first described by Bloembergen and Auzel in 1959 and 1973.[1−3] Upconversion nanoparticles (UCNPs) are able to convert near-infrared (NIR) photons into visible photons and even up to UV photons, which is related to the ladderlike electronic structure of lanthanide(III) ions (Ln(III)).[4,5] Hence, the UCNPs are interesting candidates for bioapplications/biolabeling for bioimaging, immunoassays, and theranostics.[6−9] Biological samples are challenging for optical diagnostics, which relates to their often complex matrix composition, autofluorescence, scatter, and absorption properties. The latter two limit strongly the light penetration depth into the samples, e.g., blood or tissues. These properties are impeding factors for optical imaging or sensing, when exciting at, e.g., 400 nm and below, but they are significantly less pronounced in the NIR range. Here, the advantages of the UCNPs come into play, such as discrimination of autofluorescence by luminescence originating from long-living excited states of Ln(III) and larger penetration depth of NIR light related to the different scatter and absorption behavior of biosamples in that region.[10−13] The UCNPs could be a powerful optical probe for cancer detection and treatment via photodynamic therapy (PDT) initiated by NIR photons.[14−17] Recent research has tackled the UCNP surface modification to render them water dispersible and shows successfully different approaches.[7,13,18−22]

A cardinal point for the application of UCNPs in life science applications, in vitro as well as in vivo, is their biocompatibility. Biocompatibility accounts here for the UCNP as well as its surface ligands. Both together must have the "ability to be in contact with a living system without producing an adverse effect".[23] In the present work, the UCNPs were coated with a bioinspired PG-CatPh coating polymer[24] providing, on the one

Received: October 30, 2020
Revised: December 7, 2020
Published: December 16, 2020

https://dx.doi.org/10.1021/acs.jpcc.0c09798
J. Phys. Chem. C 2020, 124, 28623−28635

hand, excellent water dispersibility and, on the other hand, potential functional groups for straightforward biolabeling. The specially designed polymer exploits the concept of blood protein adsorption and mussel food protein adhesion on surfaces (customized mussel protein (CMP) polymer). The CMP shows promising results for surface modifications aiming at applications in biological matrices. It carries an azide functionality to open the pathway for copper-catalyzed or copper-free cycloaddition with alkynes (click chemistry).[25−29]

The UCNPs here are based on a $NaYF_4$ lattice doped with Yb(III) (sensitizer) and Er(III) (activator). An energy scheme of the donor−acceptor system used is illustrated in Figure 1.

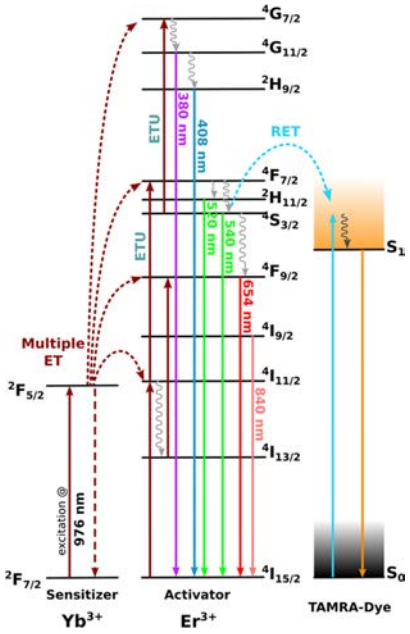

Figure 1. Illustration of energy levels of a $NaYF_4$:Yb,Er UCNP with energy transfers for ETU and resonance energy transfer (RET) to the TAMRA-5-alkyne dye. From left to right: Yb(III) is the sensitizer. Er(III) is the activator. The TAMRA-5-alkyne as RET-acceptor. Absorption and electron excitations are shown by solid dark red arrows, and the $S_1 \leftarrow S_0$ transition of the dye is shown by the solid light blue arrow. The dashed dark red arrows indicate energy transfers leading to the ETU. Downwardly waved gray arrows indicate inner relaxation processes, and downwardly solid arrows (purple, blue, green, red, peachy, orange) indicate photoluminescence (PL) emission.

The Yb(III) absorbs the incident NIR photons (976 nm laser excitation). The NIR excitation light is converted into higher-energy light (vis/UV) by several energy transfers from Yb(III) ions to Er(III) ions. The Yb(III) ions outnumber the Er(III) ions (18−2 mol %).

In this work, a resonance energy transfer (RET) from a trivalent lanthanide ion to a dye is evaluated as a showcase to demonstrate the potential of the novel ligand CMP for (bio)functionalization. The chosen dye is TAMRA-5-alkyne (5-carboxytetramethylrhodamine-alkyne, TAMRA) that serves to demonstrate the "click" functionality of CMP for linking biomarkers (antibodies or antigens) to the CMP-capped UCNPs in the future. The TAMRA absorption overlaps well with the major "green" emission peaks of Er(III). The TAMRA itself emits in a spectral region, in which Er(III) does not show photoluminescence (PL). In Figure 1, the electronic transitions of the UCNP PL emission as well as the dye absorption and its fluorescence emission are shown. The efficiency of the RET depends on the distance between the energy donor (D, here: Er(III) in UCNP) and the energy acceptor (A, here: the TAMRA-5-alkyne). No passivating shell was grown on the core UCNPs not only to keep the donor−acceptor distance as small as possible but also to show the protective potential of CMP over other capping agents in water. Although a shell enhances the upconversion quantum yield, the shell could also reduce the energy transfer efficiency due to larger donor−acceptor distances.[30]

EXPERIMENTAL SECTION

Materials. The rare-earth chlorides $RECl_3 \cdot 6\,H_2O$ (RE: Y^{3+}, Yb^{3+} with purities >99.9%), $ErCl_3$ (>99.9%), and ammonium fluoride (NH_4F, ≥99.99%), as well as poly(acrylic acid) (PAA, average M_W = 1800), diethylene glycol (≥99.0%), 3-morpholinopropane-1-sulfonic acid (MOPS, ≥99.5%), and *tert*-butanol (≥99.7%) were purchased from Sigma-Aldrich/Merck. Oleic acid (OA, 90%) was purchased from Alfa Aesar (Thermo Fisher (Kandel) GmbH). Therminol® 66 was purchased from FRAGOL GmbH + Co. KG. Ethanol (≥99.8%; 1% MEK), sodium hydroxide (≥99.9%), cyclohexane (cy) (ROTISOLV ≥99.9%, gas chromatography (GC) ultra grade), L(+)-ascorbic acid (≥99%), and $CuSO_4 \cdot 5\,H_2O$ (≥99.5%) were purchased from Carl Roth GmbH + Co. KG. The specially designed bioinspired polymer abbreviated as CMP was prepared as previously reported by Yu et al.[24] 5-Carboxytetramethylrhodamine-alkyne (TAMRA, >95%) was purchased from Jena Bioscience GmbH. The reagents were not purified prior to usage. Double-deionized water (denoted as water) was generated with a Milli-Q Advantage A10 water purification system. The MOPS buffer was prepared with MOPS and water; its concentration was set to 0.1 mol/L, and the pH value was adjusted to 6.

Upconverting Nanoparticle (UNCP) Synthesis, Phase Transfer into the Aqueous Phase via Ligand Exchange, and Click Coupling with the Dye. *Core Synthesis of $NaYF_4$:Yb,Er (UCNP\OA).* The synthesis is very similar to that previously reported, but with minor adaptions:[31] Rare-earth metal chlorides ($YCl_3 \cdot 6\,H_2O$ (0.8 mmol), $YbCl_3 \cdot 6\,H_2O$ (0.18 mmol), $ErCl_3$ (0.02 mmol)); oleic acid (OA) (25.2 mmol, 7.12 g); and Therminol® 66 (12 mL) were transferred into a 50 mL three-neck flask. The reaction mixture was evacuated for 10 min at room temperature (RT), then stepwise heated up to 140 °C under vacuum and vigorous stirring. The temperature was kept for 45 min, cooled down to 50 °C, and vented with argon. Sodium hydroxide (4 mmol) and ammonium fluoride (6.4 mmol) were added under an argon counter stream. The system was reevacuated and kept at 80 °C for at least 30 min until the added salts had dissolved. The reaction mixture was vented with argon and heated up to 320 °C (heat rate: 25 °C/min). The temperature was kept for 120 min. The reaction mixture was cooled down to 250 °C by air, followed by cooling with a water bath to 60 °C. Nanoparticle purification was performed by washing three times with ethanol and

https://dx.doi.org/10.1021/acs.jpcc.0c09798
J. Phys. Chem. C 2020, 124, 28623−28635

Scheme 1. Reaction Scheme of CMP: Intermolecular Cross-Linking and Click Reaction with TAMRA-5-Alkyne[a,34]

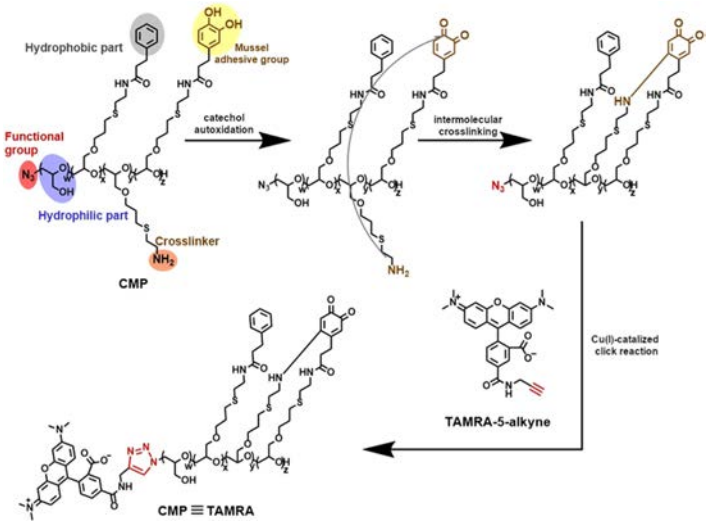

[a]Indices of CMP are $w = 110$; $x = 5$; $y = 2$; and $z = 5$. The Michael-type addition reaction is shown here for the amine-quinone reaction, although a Schiff base reaction is possible, as well.

centrifugation at 3100*g* for 8 min. The precipitate was finally dispersed in cyclohexane (15 mL).

Bioinspired PG-CatPh Coating Polymer (Customized Mussel Protein (CMP) Polymer). The CMP (see Scheme 1) is an amphiphilic block copolymer. It carries nature-inspired functional groups exploiting the concept of blood protein coagulation and the ability of mussels to stick to rock surfaces. The CMP provides water dispersibility via the hydrophilic part (blue marker). The catechol groups attach on the UCNP surface (yellow marker) via coordination bonding. Another block contains phenyl groups (gray marker) that form a monolayer on the UCNP surface via hydrophobic−hydrophobic interaction and help to prevent fast autoxidation of the catechol groups. The catechol groups oxidize to quinones on the surface. The amines can cross-link with the quinones and form a cagelike system around the UCNP. The amine groups serve as cross-linkers and displace hydrated cations from the UCNP surface (brown marker). The functional group (red marker) for further biomodification is variable. Here, it is an azide group.[24]

The cagelike system and interlinkage of the CMP were designed to use advantages like suppression of ligand exchange reactions due to dilution effects[32] or avoiding nanoparticle dissolution.[33] The hydrophilic polyglycerol block forms a brushlike conformation on the UCNPs surface after hydration. Hence, a dense hydration layer is expected to be formed and solvent molecules are kept away from the UCNP surface. The stability and water dispersibility of coated UCNPs are improved, and the nanoparticle aggregation and diffusion of outer ligands are suppressed.

The click reaction of CMP with the TAMRA-5-alkyne, also in Scheme 1, is performed using copper-catalyzed azide−alkyne cycloaddition (CuAAC) chemistry.

Ligand Exchange from OA via PAA to CMP (UCNP\CMP). The ligand exchange from OA to PAA was performed as described in the literature.[35] First, diethylene glycol (30 mL) and PAA (100 mg) were transferred into a 50 mL three-neck flask and heated up to 85 °C under an argon atmosphere until a clear solution is formed. UCNP (30 mg) dispersed in cyclohexane was added. The mixture was heated for 1 h at 85 °C. Then, the reaction mixture was cooled down naturally to room temperature, washed two times with ethanol, and centrifuged at 13 000*g* for 10 min. Finally, the precipitate containing PAA-covered UCNPs was dispersed in 10 mL of MOPS buffer. Excess PAA was removed by centrifugation at 10 000*g* for 10 min. The precipitate was dispersed in 2 mL of MOPS buffer and unified with an MOPS buffer solution containing 30 mg of CMP. The mixture was ultrasonicated for 15 min at room temperature. Afterward, the CMP-covered UCNPs were centrifuged down at 10 000*g* for 20 min and the precipitate, UCNP\CMP, was redispersed in 2.5 mL of MOPS buffer. The CMP cross-linking happens by itself overnight.

Click Reaction of TAMRA-5-Alkyne to CMP-Coated UCNP (UCNP≡TAMRA).[36] The UCNP\CMP (30 mg) and TAMRA-5-alkyne (0.5 mg) are transferred into 6 mL of a water/*tert*-butanol (1:1) solution. Then, $CuSO_4{\cdot}5\ H_2O$ (2 μmol) and a freshly prepared sodium ascorbic acid solution (1 mol/L, 20 μL) were added. The mixture was stirred in the dark for 7 h. After reaction time, it was centrifuged at 10 000*g* for 20 min. The precipitate was washed with 6 mL of water and then centrifuged at 10 000*g* for 20 min to remove free TAMRA. The washing was repeated three times. The final precipitate was dispersed in water. The RET experiments were repeated with the same sample after solvent exchange from water to MOPS buffer by centrifugation.

https://dx.doi.org/10.1021/acs.jpcc.0c09798
J. Phys. Chem. C 2020, 124, 28623−28635

Luminescence Emission Spectroscopy. Optical excitation was performed with a wavelength-tunable pulsed Nd:YAG/OPO laser system operating at 10 Hz (at 26 mJ/130 mW). The laser is from Quanta Ray, Spectra Physics, Mountain View, CA. The optical parametric oscillator (OPO) is from GWU-Lasertechnik Vertriebsges. mbH, Erftstadt, Germany. The emission light was recorded with a spectrograph from Shamrock (SR 303i, Andor Technology, Belfast, Great Britain) equipped with a 600 L/mm grating blazed at 500 nm. An intensified charge-coupled device (CCD) camera (iStar DH720-18V-73, Andor Technology, Belfast, Great Britain) was installed in the spectrograph. Luminescence decay kinetics were recorded using a box-car/stroboscopic technique.[37] Each measurement was performed using a gate width t_{gate} of 100 μs and an initial delay of 500 ns for steady-state emission measurements or 200 ns for time-resolved emission spectroscopy.

Low-temperature measurements were performed using a cryostat setup that is equipped with a helium compressor unit (CKW-21, Sumitomo Heavy Industries Ltd.), a temperature controller (331, Lakeshore), and a sample chamber, which contained a copper sample holder for NMR tubes. The chamber was set under vacuum with a turbo-molecular pump (Turbolab 80, Oerlikon Leybold Vacuum).

Time-resolved area-normalized emission spectra (TRANES) are derived from the kinetic measurement being performed with the same equipment described above in which each emission spectrum was recorded with a successively increasing delay. The respective emission peaks are normalized by the area under the emission curve. The crystal phase of $NaYF_4$ (cubic or hexagonal lattice phase) can be distinguished with help of TRANES. The hexagonal crystal phase is appreciated due to longer PL decay times and higher upconversion efficiencies.[4,22,38−41]

Absorption Spectroscopy. UV−vis investigations were realized using a Lambda 750 UV/vis spectrometer from PerkinElmer with UV WinLab software (version 5.2.0). The absorption measurements were performed with a 1 cm cuvette (3 mL volume) of the pure solvent and the samples. The sample absorption spectra were solvent- and baseline-corrected. The absorption was scanned from either 1000 or 800 to 300 nm using a slit width of 2 nm and a step width of 1 nm.

Steady-State Fluorescence Emission Spectroscopy. The emission and excitation spectra were recorded with a FluoroMax-P (JY Jobin Yvon) from Horiba. The FluoroMax-P spectrometer was operated with the software Instrument Control Center, version 2.2.13. The excitation and emission light beams were in an L-setup. The fluorescence measurements were performed with a 1 cm cuvette (3 mL volume) to characterize the TAMRA fluorescence.

Time-Correlated Single Photon Counting (TCSPC). The fluorescence decay curves were recorded using a TCSPC setup from PicoQuant GmbH (Berlin, Germany) consisting of a FluoTime 300 (fluorescence lifetime spectrometer) equipped with a PicoHarp 300 (TCSPC module and picosecond event timer), an MSH300 PQ module, and a PMA Hybrid module (single photon counting module). The setup was operated with the appropriate software FluoTime 300 "Easy Tau" (version 1.4, Build 2463). The excitation was performed with a diode laser (λ_{ex} = 375 nm, 20 MHz repetition rate) from Edinburgh Instruments (EPL, 375 ps pulsed diode laser) attached to the FluoTime 300. The obtained TCSPC fluorescence decay curves were analyzed with the PicoQuant FluoFit 4.6.6.0 software using an exponential reconvolution fit model that finally corresponds to a single exponential decay function for first-order kinetics.

Microscale Thermophoresis (MST). The microscale thermophoresis (MST) was performed with a Monolith $NT.115^{Pico}$ device from NanoTemper Technologies GmbH (Munich, Germany). The device records fluorescence time traces induced by a temperature gradient and exploits diffusion properties. The MST tool was equipped with an infrared (IR) laser beam (1475 ± 15 nm; max. power, 120 mW) for inducing a temperature gradient of 2−6 K within the sample volume. The IR beam and a coupled fluorescence light source were focused on the sample via a dichroic mirror. The experiments were performed with MST-grade standard treated capillaries. The sample volume (10 μL) was transferred into the capillary. The blue-light-emitting diode (LED) excitation power was used and set to 50%. Different runs were performed using IR laser powers for the temperature gradients of 20, 40, 60, and 80% with excitation and emission bandpass filters with λ_{ex} = 468 ± 25 nm (blue), λ_{em} = 541 ± 35 nm (green), and λ_{em} = 697 ± 35 nm (red). The temperature for all measurements was set to 22.5 °C. The fluorescence observation time windows were set to 5 s before IR laser illumination; to 30 s during IR laser illumination; and to 5 s after IR laser illumination. The MST time traces were analyzed using the temperature jump (first few seconds after the IR laser is switched on) and the thermophoresis effect. The total fluorescence intensity was normalized to one.[42]

Size (Transmission Electron Microscopy (TEM), Dynamic Light Scattering (DLS)) and Structural (X-ray Diffraction (XRD)) Characterization. The TEM images were recorded with a transmission electron microscope (TEM, Tecnai G2 F20 X-Twin, from FEI/Thermo Fisher Scientific; 200 kV acceleration voltage). The images were used to determine the UCNP diameter with help of the software Image Sys Prog (version 1.2.5.16 ×64). Furthermore, the size was determined by dynamic light scattering with a Zetasizer Nano ZS or with a Zetasizer Ultra (Malvern Instruments Ltd./Malvern Panalytical). The devices were operated with the respective appropriate software (Zetasizer, version 7.02, or ZS XPLORER, version 1.3.0.140).

The powder X-ray diffractometer was a PANalytical Empyrean powder diffractometer with a Bragg−Brentano geometry. The detector was a PIXcel1D detector, and Cu Kα radiation (with Kα wavelength λ = 1.5419 Å) was used. The diffractometer was operated at 40 kV and 40 mA. The pulse height distribution (PHD) level for the detector sensitivity was set to 45−80 with an active length of 3.0061° to reduce the fluorescence. The step size was set to 0.0131° for θ−θ scans with a 2θ range of 4−70° within 190 min. The sample rotation time was set to 1 s.

Theory. The resonance energy transfer (RET) is based on the theory formulated by Förster in 1946.[43,44] Recent research shows successful energy transfers from trivalent lanthanide ions or UCNPs to fluorescent dyes and quantum dots.[45−49] The interactions of lanthanides are not only but also of dipole−dipole character,[50] which is why the Förster resonance energy transfer (FRET) theory can be used to describe the UCNP-to-dye RET.

The time-resolved data are analyzed with the help of exponential decay models. The TAMRA fluorescence decay curves are evaluated with a single exponential decay function

https://dx.doi.org/10.1021/acs.jpcc.0c09798
J. Phys. Chem. C 2020, 124, 28623−28635

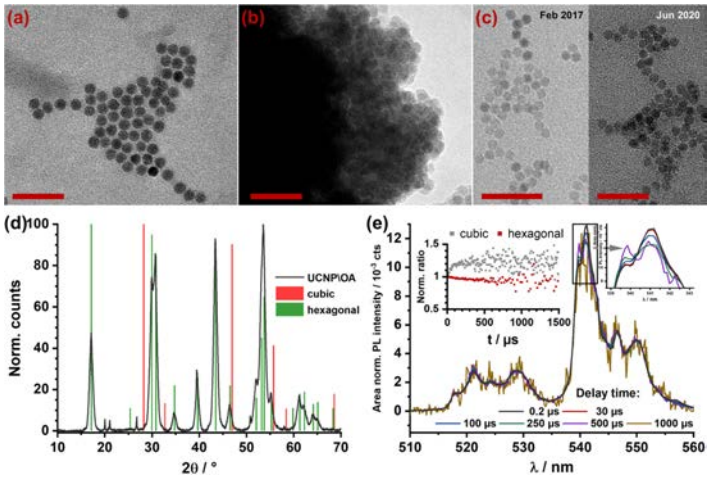

Figure 2. (a–c) TEM images of $NaYF_4$:Yb,Er UCNP, (d) XRD pattern, and (e) TRANES. The TEM images of $NaYF_4$:Yb,Er UCNPs reveal a stable dispersion, even after phase transfer: (a) UCNP\OA in cyclohexane, diameter $d = 11 \pm 1$ nm, (b) UCNP≡TAMRA in MOPS buffer, $d = 11 \pm 1$ nm, (c) UCNP\CMP in MOPS buffer stored in a fridge at 5 ± 1 °C. TEM images recorded 3 years apart from each other—particles did not agglomerate. The particle diameter did not change with storage time. Histograms are shown in Figure S2, SI. Scale bars = 50 nm. The XRD reflexes (d) of the sample (black line) match with the reflexes of $NaYF_4$ in the hexagonal crystal phase. $NaYF_4$ reference reflexes are plotted in red and green for the cubic and hexagonal phases. The TRANES in (e) support the hexagonal phase. No spectral change can be seen in the emission spectra with increasing delay time. The G1-internal-peak-ratio is nearly constant (red dots in the left inset). The gray dots show a mixture of cubic/hexagonal G1-internal-peak-ratio for comparison. The spectral range around 540 nm is shown at a higher magnification to show the iso-emissive point (right inset).

(eq 1a). The PL decay curves (excited in the NIR, 976 nm) of UCNP\OA, UCNP\CMP, and UCNP≡TAMRA are evaluated with a triple exponential decay function (eq 1b).

$$I(t) = A_1 \exp\left(-\frac{t}{\tau_1}\right) + I_\infty \tag{1a}$$

$$I(t) = \sum_{j=1}^{3}\left[F_j \exp\left(-\frac{t}{\tau_j}\right)\right] + I_\infty \tag{1b}$$

Here, $I(t)$ is the intensity to the given time t, A_1 is the amplitude corresponding to the initial intensity of the respective component of the decay model, F_j is the experimentally obtained amplitude explained below, τ_j is the decay time constant of the respective component of the decay model, and I_∞ is the baseline of the fluorescence/PL decay curve (or the noise of the detector).

The dye fluorescence curves (TAMRA being directly excited at 375 nm) have been recorded with the time-correlated single photon counting (TCSPC) technique.[51,52] The PL decay curves have been recorded with the box-car/stroboscopic technique.[37] This technique observes the PL emission of the probe with a defined delay time after the excitation pulse. This delay time increases successively with each measurement cycle. The emitted photons are recorded over a previously defined and constant time window, which is called gate width t_{gate}. The size of the gate width influences the experimentally obtained amplitude values. This will not happen with TCSPC. The following transformations are performed for the box-car technique to obtain correct/real amplitudes.

A detailed description was made by Gessner in 2010.[53] In short, all photons recorded within the gate width t_{gate} are accounted to have reached the detector at the time t. This means that due to the box-car technique itself, an integration within the borders of the time t and this time plus the gate width $(t + t_{gate})$ is conducted. It also means that the measurement points actually overlap with each other. This overlap correlates with the gate width t_{gate} requiring the correction of the experimentally obtained amplitudes. The measured PL emission intensity at time t can be described by eq 1c, in which the gate width t_{gate} is considered. Integration of eq 1c leads to eq 1d, which is valid for single exponential decays. The same logic is applied to multiexponential decays and leads to eq 1e.

$$I(t) = \int_{t}^{t+t_{gate}} A_1 \exp\left(-\frac{t}{\tau_1}\right) \mathrm{d}t \tag{1c}$$

$$I(t) = A_1\tau_1\left[1 - \exp\left(-\frac{t_{gate}}{\tau_1}\right)\right]\exp\left(-\frac{t}{\tau_1}\right) \tag{1d}$$

$$I(t) = \sum_{j=1}^{3} A_j\,\tau_j\left[1 - \exp\left(-\frac{t_{gate}}{\tau_j}\right)\right]\exp\left(-\frac{t}{\tau_j}\right) \tag{1e}$$

The superscript "3" of the sum sign $\sum$ (eq 1e) indicates the number of components in the decay model, the number of the decay times τ_j, and the amplitudes A_j. A comparison of the amplitude coefficients of eqs 1e and 1b shows that the experimentally obtained amplitude F_j (in eq 1b) depends on

https://dx.doi.org/10.1021/acs.jpcc.0c09798
J. Phys. Chem. C 2020, 124, 28623–28635

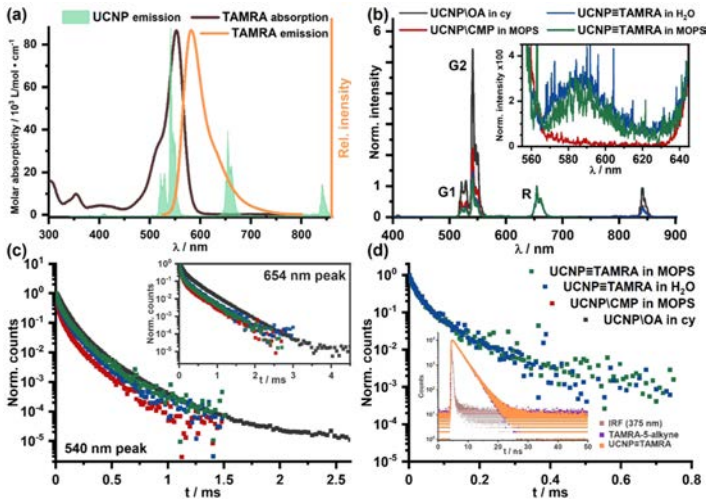

Figure 3. Norm. PL emission spectra and PL decay curves of $NaYF_4$:Yb,Er UCNP and TAMRA. (a) Basic characterization of TAMRA-5-alkyne. Molar absorptivity spectrum (dark brown) and fluorescence emission spectrum (orange, λ_{ex} = 515 nm). Green emission of $NaYF_4$:Yb,Er UCNP functionalized with CMP dispersed in aqueous MOPS buffer illustrates the spectral overlap of UCNP donor and TAMRA acceptor ($\lambda_{ex(UCNP)}$ = 976 nm as for (b)−(d)). (b) PL emission spectra of UCNPs covered with OA dispersed in cyclohexane (black, UCNP\OA), covered with CMP dispersed in MOPS buffer (red, UCNP\CMP), and covered with CMP coupled to TAMRA dispersed in water (blue, UCNP≡TAMRA) and MOPS buffer (green, UCNP≡TAMRA). Characteristic peaks are: 410 nm ($^2H_{9/2} \rightarrow {}^4I_{15/2}$), 520/540 nm (green, G1/G2: $^2H_{11/2}/{}^4S_{3/2} \rightarrow {}^4I_{15/2}$), 654 nm (red, R: $^4F_{9/2} \rightarrow {}^4I_{15/2}$), and 850 nm ($^4I_{9/2} \rightarrow {}^4I_{15/2}$). Embedded image: zoomed spectral range of TAMRA emission excited via RET. The spectra are normalized by the maximum of R serving as internal standard. The R peak does not participate in the RET (see (a), no TAMRA absorption above 600 nm). (c) PL decay curve of G2 (540 nm) and R (654 nm, embedded). (d) TAMRA PL decay curve at 600 nm. TAMRA fluorescence decay time: 22 (±1) μs with excitation via RET and 2.28 (±0.01) ns with λ_{ex} = 375 nm (embedded image, direct excitation of TAMRA being independent on coupled or not to the UCNP). Regression results are shown in Table 1. For the reference samples without TAMRA (UCNP\CMP and UCNP\OA), no emission was observed at 600 nm.

the gate width t_{gate} and on the PL decay time τ_j. Now, the true amplitude A_j can be calculated with eq 1f.

$$F_j = A_j\tau_j\left[1 - \exp\left(-\frac{t_{gate}}{\tau_j}\right)\right] \Leftrightarrow A_j = F_j \cdot \left(\tau_j\left[1 - \exp\left(-\frac{t_{gate}}{\tau_j}\right)\right]\right)^{-1} \quad (1f)$$

With the knowledge of the true amplitudes A_j, the average decay times can be formulated and it can be decided whether RET was observed or was not observed. There are two types of average decay times: the intensity-weighted average decay time $\overline{\tau}$ and the amplitude-weighted average decay time $\langle\tau\rangle$. The intensity-weighted average decay time $\overline{\tau}$ is calculated from the intensity-weighted fractions f_j (see equations in Table S1, Supporting Information (SI)). The intensity-weighted fractions f_j are proportional to the area under the curve of each single decay time contributing to the multiexponential decay curve. In contrast, the amplitude-weighted average decay time $\langle\tau\rangle$ is calculated from the amplitude-weighted fractions α_j (see eqs 2a and 2b). The amplitude-weighted fractions α_j correspond to the actual emission intensities of the components because the actual time when a photon reaches the detector is correlated.[52,54,55]

$$\alpha_j = \frac{A_j}{\sum_i A_i} \quad (2a)$$

$$\langle\tau\rangle = \sum \alpha_j\tau_j \quad (2b)$$

Time-resolved area-normalized emission spectra (TRANES) are used to distinguish between the cubic and hexagonal crystal phases of $NaYF_4$:Yb,Er UCNP. Moreover, the differentiation between multiple emissive species can be well performed with the help of TRANES.[56−59] If both crystal phases are present in one UCNP sample, TRANES will be able to unravel them because the luminescence peak ratios of Er emission in the spectra will change over time. This observable spectral alteration already happens when very tiny amounts of the second phase are present as demonstrated by Klier et al.[60] If only one emissive species (or one crystal phase) is present, the peak ratios will be constant and no change will be observed in the TRANES except deteriorating signal-to-noise ratios. For better demonstration, the ratio of the two subpeaks of the Er(III) G1 emission ($^2H_{11/2} \rightarrow {}^4I_{15/2}$) can be plotted. The ratio plot of the "G1-internal-peak-ratio" will be constant if only the hexagonal phase is present or it will rise if a mixture of cubic and hexagonal phase is present. The G1-internal-peak-ratio is calculated based on the emission peak at 529 nm and the peak at 520 nm, respectively.

https://dx.doi.org/10.1021/acs.jpcc.0c09798
J. Phys. Chem. C 2020, 124, 28623−28635

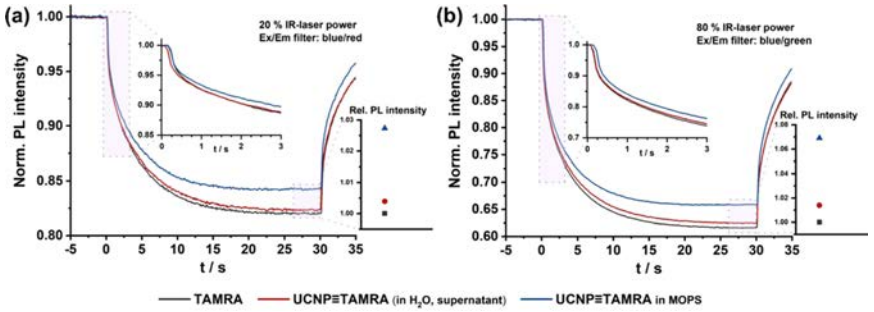

Figure 4. MST time traces of TAMRA: black curve is free TAMRA in MOPS buffer; red curve is the supernatant of UCNP≡TAMRA after centrifugation for solvent exchange; blue curve is UCNP≡TAMRA in MOPS buffer. Embedded diagrams: zoomed time window from 0 to 3 s (center) and rel. fluorescence intensity integrated from 26 to 30 s (right). IR laser power was set to (a) 20% and (b) 80%. Free TAMRA diffuses faster than UCNP≡TAMRA, which leads to faster fluorescence intensity drop for free TAMRA.

RESULTS AND DISCUSSION

General Characterization. The UCNP size is determined by TEM. The particle diameter is 11 ± 1 nm with a narrow size distribution and maintained after phase transfer (see Figure 2a,b). The polymer ligand CMP provides good water stability and suppresses agglomeration, as shown by TEM. The good water stability of UCNP\CMP in MOPS buffer is demonstrated by a stability experiment, in which the PL emission intensity decreases only moderately over 20 days. Moreover, UCNP luminescence is still easily detectable with sufficient intensity after storing the CMP-capped nanoparticles in MOPS buffer for 3 years at 5 ± 1 °C (see Figure S1, SI; two representative samples are shown). TEM also reveals that the particles did not agglomerate nor changed their size even after the long-time storage of 3 years (see Figure 2c). The UCNP stability is also confirmed by determination of the hydrodynamic diameters for UCNP\CMP in MOPS buffer (and in water) (performed with dynamic light scattering) that is around 35 ± 10 nm and shows no changes considering the margin of error during the storage time of 3 years. These findings are attributed to the protection of the UCNP by the CMP polymer-coating layer. It is noted here that for storage in phosphate-buffered saline instead, the CMP-capped UCNP precipitates within a few days.

The synthesized UCNPs are in the appreciated hexagonal crystal phase; see the XRD reflexes and the TRANES investigation in Figure 2. The XRD reflexes in Figure 2d match well with reflexes of the hexagonal $NaYF_4$. Complementary to XRD, which reports the crystal phase of the bulk, TRANES analysis of the Er(III) luminescence was performed to obtain a more Er(III)-ion-centered information on the crystal phase. The TRANES in Figure 2e show no change in the spectral signature over time, indicating the presence of only one crystal phase. In more detail, Figure 2e (left inset) shows the G1-internal-peak-ratio (529 nm over 520 nm) of Er(III)-doped UCNPs: A mixture of cubic and hexagonal crystal phase $NaYF_4$:Yb,Er UCNPs shows increasing values of the G1-internal-peak-ratio in the first 150 μs (Figure 2e, left inset, plotted in gray). A pure hexagonal crystal phase shows a nearly constant G1-internal-peak-ratio because the PL emission peaks at 520 and 529 nm are equally intense (Figure 2e, left inset, plotted in red). Due to the fact that the coupling to lattice vibrations (and the subsequent radiationless deactivation) of Er(III) is slightly more efficient in the cubic phase, the respective emission kinetics are faster compared to Er(III) in a hexagonal $NaYF_4$ lattice.[61] In case of mixed lattice phases, the observed emission kinetics are a combination of cubic and hexagonal. The increase of the G1-internal-peak-ratio can be explained by the shorter-lived cubic phase luminescence emission, which is overshined by the longer luminescence emission of the hexagonal phase—meaning that with longer delay times, the PL emission fraction of the hexagonal phase increases, whereas the PL emission fraction of the cubic phase decreases. The G1-internal-peak-ratio in Figure 2e, left inset, red dots, is constant. Following the explanations above and the results of the XRD, only the hexagonal $NaYF_4$ phase is present in the UCNP investigated here.

In the TRANES of Figure 2e, right inset, it seems as if there is an iso-emissive point at 540 nm. This can be attributed to Er(III) ions in different microenvironments, each showing a slightly different spectral intensity distribution in combination with different luminescence decay kinetics. The two Er(III) species are tentatively attributed to one being closer to the surface, the other being the bulk phase of the UCNP or by lattice imperfections.

The optical properties of the free, uncoupled dye TAMRA-5-alkyne are shown in Figure 3a. TAMRA has its absorption maximum at 553 nm and, consequently, a good spectral overlap with $^2H_{11/2} \rightarrow {}^4I_{15/2}$ (G1) and the $^4S_{3/2} \rightarrow {}^4I_{15/2}$ (G2) transition of the Er(III) PL emission in the UCNPs. No absorption at wavelengths higher than 600 nm is observed, and therefore, TAMRA is not excited at 976 nm under the experimental conditions applied (see Figure S3a, SI). The TAMRA emission maximum is around 580 nm and fits well into the emission gap of the Er(III) luminescence bands G1 and G2, and the R band around 650 nm ($^4F_{9/2} \rightarrow {}^4I_{15/2}$)—peak labels are depicted in Figure 3b. A detailed discussion of the luminescence properties is given below (vide infra).

Coupling of TAMRA to CMP-Capped UCNP. The feasibility of coupling of the CMP ligand to the intrinsic N_3 groups, when used as a capping agent for UCNPs, is demonstrated in a showcase using TAMRA. In addition to multiple centrifugation and washing steps to remove the nonlabeled TAMRA from the samples (compare Figures S3a,b and S4a–c, SI), a complementary analysis to show the successful binding of TAMRA to the CMP-capped UCNPs

https://dx.doi.org/10.1021/acs.jpcc.0c09798
J. Phys. Chem. C 2020, 124, 28623−28635

was performed. To characterize the coupling of TAMRA to the UCNP\CMP samples, investigations were performed using MST. Here, MST is used to observe the difference in diffusion speed of uncoupled and coupled TAMRA to control the dye immobilization. If the TAMRA is coupled to the UCNP, the UCNP will act like a prisoner's ball for the TAMRA and reduce its diffusion speed. This can be observed by a reduced fluorescence decrease rate, as shown by the representative runs with 20 and 80% IR laser power in Figure 4a,b. The IR laser induces the temperature gradient that triggers the TAMRA diffusion. The free TAMRA (black curve) diffuses faster out of the observation window than the UCNP≡TAMRA (blue/red curve). Accordingly, the free TAMRA fluorescence signal decreases faster. The fluorescence signal of the UCNP≡TAMRA in MOPS buffer (blue curve) drops significantly slower and ends with the highest fluorescence intensity. This indicates the smaller diffusion speed due to the UCNP hindering the TAMRA diffusion. The UCNP≡TAMRA in water (red curve)—containing residues of UCNPs coupled with TAMRA that were not centrifuged down—also hinders the TAMRA diffusion. These findings are consistent in all tested IR laser powers (20, 40, 60, and 80, only 20 and 80% are shown).

Luminescence Properties of CMP-Capped UCNP. The Er(III)-doped UCNPs show sharp and bright PL emission peaks after excitation with 976 nm (see Figure 3b). All major emission peaks of Er(III) are present, independently on the surrounding media: at 408 nm ($^2H_{9/2} \rightarrow {}^4I_{15/2}$), at 520 nm ($^2H_{11/2} \rightarrow {}^4I_{15/2}$ denoted as G1), at 540 nm ($^4S_{3/2} \rightarrow {}^4I_{15/2}$ denoted as G2), at 654 nm ($^4F_{9/2} \rightarrow {}^4I_{15/2}$ denoted as R), and at 840 nm ($^4I_{9/2} \rightarrow {}^4I_{15/2}$). The embedded graph in Figure 3b is the spectral region around 580−600 nm and shows the emission of TAMRA coupled to the UCNP (blue and green curves) at an excitation wavelength of 976 nm.

The UCNP\OA in cyclohexane shows the brightest green emission (G1 and G2). The G1 and G2 emission also suffers from the highest intensity loss after transfer into aqueous media. This effect is less pronounced on the other peaks (see Figure 3b). The PL emission spectra are normalized by the R peak as an internal standard since this peak does not participate in the UCNP-to-TAMRA RET (see Figure 3a and the red luminescence decay kinetic traces shown in the inset of Figure 3c, which show no discernable difference for the aqueous samples in contrast to the green emission kinetics). The effect of OH quenching by the aqueous media complied with the normalization. The OH vibrations quench especially the excited Er(III)'s G1/G2 energy levels as well as the Yb(III) ions, which are the energy feed for the Er(III) upconversion.[62] Moreover, comparing the normalized spectrum for CMP-capped UCNP in MOPS buffer with the respective spectrum of CMP-capped UCNP labeled with TAMRA in MOPS buffer (see Figure 3b, red and green, respectively), it can be seen that in the latter case, the green emission is further reduced. The G/R ratios were calculated by the integrals of the respective peaks. The ratios are: 5.0 (UCNP\OA); 2.1 (UCNP\CMP in MOPS buffer), 1.4 (UCNP≡TAMRA in water), and 1.1 (UCNP≡TAMRA in MOPS buffer). Especially, the loss of 50% from the UCNP\CMP to the UCNP≡TAMRA, both measured in MOPS buffer, can be emphasized because the green emission decreases strongly and indicates an energy transfer from Er(III) to TAMRA. The observed decrease of the green Er(III) emission bands is complemented by an increase of the TAMRA emission. The dye cannot be excited at 976 nm by a two-photon absorption due to the used laser system. Moreover, the depicted emission spectrum of TAMRA was recorded at a delay time of 500 ns (relative to the laser excitation pulse) (see Figure 3b, inset). At that delay time, any directly excited TAMRA fluorescence would have fully decayed. Accordingly, the operative interaction between Er(III) and TAMRA after excitation in the NIR is shown.

However, the responsible mechanism—either the reabsorption of the G emission by TAMRA or the RET from the UCNP to TAMRA—cannot be distinguished from each other based on steady-state emission measurements alone, which is why time-resolved emission spectroscopy is performed.

The PL decay curves in Figure 3c,d support the RET between Er(III) and TAMRA as the operative mechanism. The strongest indicator for RET within the UCNP≡TAMRA system is the observed distinct change of the fluorescence decay time of TAMRA. The TAMRA fluorescence decay time increases by a factor of 9500! from 2.28 ns (found for direct excitation at 375 nm; see Figure 3d inset) up to 22 μs (in water) and 18 μs (in MOPS buffer) after excitation via 976 nm and the subsequent UCNP-to-TAMRA RET (see Table 1).

Table 1. Amplitude-Weighted Decay Times of the UCNP and TAMRA Emission: 540 nm (G2), 654 nm (R), and 585 nm (TAMRA) after RET[a]

peak	UCNP\OA in cy	UCNP\CMP in MOPS	UCNP≡TAMRA in MOPS [in H_2O]
G2 (540 nm)	67 ± 1 μs	16 ± 1 μs	40 ± 1 μs [32 ± 1 μs]
TAMRA (600 nm)			18 ± 2 μs [22 ± 1 μs]
R (654 nm)	142 ± 2 μs	41 ± 1 μs	54 ± 2 μs [60 ± 2 μs]
G/R intensity ratio	5.033	2.130	1.137 [1.450]
TAMRA/R intensity ratio	0.037	0.007	0.063 [0.091]

[a] λ_{ex} = 976 nm. PL decay time decreases due to phase transfer from cyclohexane (cy) into MOPS buffer. The UCNP PL decay time increases again after click reaction with TAMRA. The TAMRA fluorescence decay time increases significantly from nanoseconds to microseconds indicating an energy transfer from Er(III) to TAMRA. TAMRA fluorescence decay time is 2.3 ns for direct excitation (λ_{ex} = 375 nm).

This clearly underlines that TAMRA is excited via the Er(III) in the UCNPs. It can also be seen in Figure 3d that the "sensitized" TAMRA luminescence decay kinetics show only little influence on the surrounding media. Water or MOPS buffer shows a minor effect on the observed decay kinetics. The embedded image in Figure 3d shows the TAMRA fluorescence decay curve (in MOPS) after direct excitation at 375 nm being equal for the TAMRA only and the UCNP≡TAMRA sample, respectively. The UCNPs are not excited at 375 nm (with the used high-repetition and low-power laser system in the TCSPC experiment), and the TAMRA fluorescence is not influenced by the presence of the UCNP and CMP ligand.

With respect to the green emission of the Er(III), the observed alteration of the corresponding luminescence decay kinetics are more complex, because here different impact factors with partly opposite effects come into play. First, the PL decay times of Er(III) shorten due to the ligand exchange of oleic acid for CMP and the phase transfer from cyclohexane into the water phase (black and red dots in Figure 3c). The

https://dx.doi.org/10.1021/acs.jpcc.0c09798
J. Phys. Chem. C 2020, 124, 28623−28635

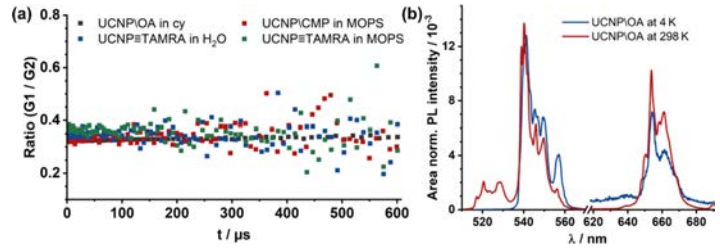

Figure 5. (a) Ratios of G1 over G2 (520/540 nm) at room temperature (RT). The ratios are constant and independent of the surrounding media and the presence or absence of TAMRA. It indicates that the G1 emission is coupled to the G2 emission since G2 supplies electrons to G1 by thermal excitation. When the G2 intensity drops, e.g., induced by RET, the G1 intensity also drops. (b) Emission spectra of $NaYF_4$:Yb,Er UCNP at RT and 4 K (solvent: cyclohexane; λ_{ex} = 976 nm). The G1 peak (at 520 nm) is not seen in the spectrum measured at 4 K.

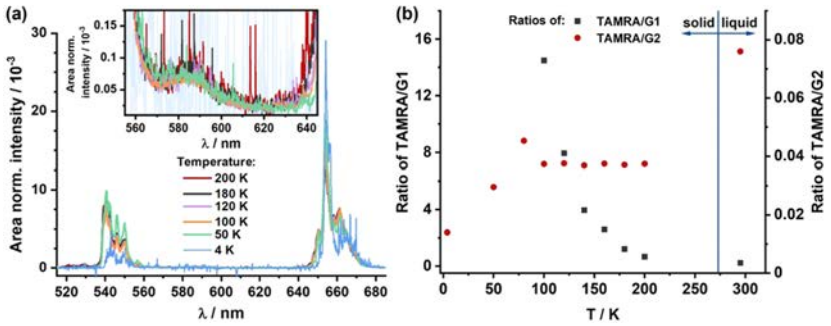

Figure 6. Low-temperature investigations of UCNP≡TAMRA. λ_{ex} = 976 nm. (a) Luminescence emission spectra normalized to the peak area of the red emission R. Only important emission spectra are shown, more data are shown in Figures S5 and S6, SI. The total luminescence emission intensity increases with increasing temperature, whereas G1 increases strongest. (b) Ratios of TAMRA over G1 and G2 emissions (at 585, 520, and 540 nm, respectively).

corresponding amplitude-weighted decay times $\langle\tau\rangle$ are shown in Table 1: $\langle\tau\rangle$ of G2 decreases by a factor of 4.2 from 67 to 16 μs. $\langle\tau\rangle$ of R decreases by a factor of 3.5 from 142 to 41 μs. Here, the quenching induced by the solvent (predominantly attributable to OH group-related quenching) can be considered as a major factor. Based on the decrease of the G- and R-related $\langle\tau\rangle$, the influence of OH-related quenching for the R band seems to be slightly smaller than the observed reduction of the respective luminescence intensities (vide supra).

After coupling the UCNP\CMP and TAMRA, the average decay time $\langle\tau\rangle$ increases. The decay times $\langle\tau\rangle$ for G2 are 32 and 40 μs and for R 60 and 54 μs (for UCNP≡TAMRA in water and for MOPS buffer, respectively, see Figure 3c and Table 1; detailed parameter are shown in Table S1, SI). The increasing decay times could indicate a stronger shielding of the UCNPs from quenching by OH groups, which could relate to better cross-linked CMP ligands. On the other hand, since RET is dependent on the effective distance between donor (Er(III) ions in UCNP) and acceptor (TAMRA coupled to the capping ligand CMP), especially Er(III) ions located in the surface will preferentially participate and will be consequently quenched more efficiently than Er(III) ions in the bulk phase of the UCNP. As a consequence, the PL emission of "bulk phase" Er(III) ions are stronger shielded from the quenching in total (surface-related quenching, which in the present case includes RET and OH quenching). As a consequence, in the box-car-based time-resolved luminescence measurement, the "bulk phase" Er(III) ions contribute more photons to the detected signal than the surface Er(III) ions, whose signal is distinctly reduced. Accordingly, the determined average decay time of the UNCP increases. Consequently, the RET evaluation based on $\langle\tau\rangle$ using eq 3 (vide infra) fails. Therefore, the best estimation for the RET efficiency is the alteration of the G emission intensity (vide supra), when the R band is used as internal reference assuming that the OH-related quenching of both emission bands is not too different (which we assume in the present case, vide supra). Using the intensity of the UCNP\CMP and the UCNP≡TAMRA (both in MOPS), an RET efficiency E of about 48% can be calculated based on eq 3.

$$E = 1 - \frac{F_{DA}}{F_D} = 1 - \frac{\int I_{DA}(t)\,dt}{\int I_D(t)\,dt} = 1 - \frac{\langle\tau\rangle_{DA}}{\langle\tau\rangle_D} = 1 - \frac{\langle\tau\rangle_{AD}}{\langle\tau\rangle_D} \quad (3)$$

The parameters in the equation are based on the basic FRET equations and are the steady-state intensities of the donor in the presence and absence of the acceptor (F_{DA} and F_D, respectively), the amplitude-weighted decay times of the donor

https://dx.doi.org/10.1021/acs.jpcc.0c09798
J. Phys. Chem. C 2020, 124, 28623−28635

Table 2. Amplitude-Weighted Decay $\langle\tau\rangle$ Times of the UCNP≡TAMRA Sample at Low Temperatures[a]

		100 K (μs)	120 K (μs)	140 K (μs)	180 K (μs)
G1 (520 nm)	τ_1	47 ± 7 [82%]	45 ± 6 [82%]	34 ± 4 [81%]	34 ± 5 [75%]
	τ_2	242 ± 30 [18%]	228 ± 21 [18%]	194 ± 11 [19%]	160 ± 8 [25%]
	$\langle\tau\rangle$	**83 ± 7**	**79 ± 6**	**63 ± 4**	**66 ± 5**
G2 (540 nm)	τ_1	43 ± 1 [83%]	42 ± 2 [83%]	42 ± 1 [82%]	39 ± 1 [82%]
	τ_2	231 ± 4 [17%]	223 ± 4 [17%]	215 ± 3 [18%]	191 ± 3 [18%]
	$\langle\tau\rangle$	**75 ± 1**	**72 ± 2**	**72 ± 1**	**66 ± 1**
TAMRA (585 nm)	τ_1	29 ± 1 [93%]	28 ± 1 [94%]	28 ± 1 [93%]	26 ± 2 [90%]
	τ_2	184 ± 8 [7%]	196 ± 10 [6%]	183 ± 7 [7%]	137 ± 7 [10%]
	$\langle\tau\rangle$	**40 ± 1**	**39 ± 1**	**39 ± 2**	**37 ± 2**

[a]The UCNP and TAMRA emissions are shown: 520 nm (G1), 540 nm (G2), and 585 nm (TAMRA) after RET. λ_{ex} = 976 nm. Percentage in brackets is the amplitude fraction α_i. PL decay times decrease with increasing temperature.

$\langle\tau\rangle_{DA}$ and $\langle\tau\rangle_D$ (in the presence and absence of the acceptor) and amplitude-weighted decay time of the acceptor being sensitized by the FRET donor $\langle\tau\rangle_{AD}$, which relates to the large difference of the UCNP donor and dye acceptor PL decay times (microsecond against nanosecond time range).[30,45,49,52]

As pointed out, the observed sensitized emission and the outstanding long fluorescence decay time, both observed for the labeled TAMRA at an excitation wavelength of 976 nm, are very strong indications for RET from the UCNP. But, since the time-resolved analysis of the Er(III) luminescence did not yield a straightforward result, an additional fundamental aspect is investigated: the contribution of the two green emission bands of Er(III) to the overall RET. Since the spectral overlap of the TAMRA absorption is larger for the G2 band, the dynamic of the G1 and G2 contribution within the UCNP≡TAMRA sample is further investigated. First, the ratio of the emission peaks G1 over G2 is shown to be dependent on the delay time after the laser excitation pulse in Figure 5a. The ratios are constant at room temperature, showing that the thermal equilibration between G1 and G2 (G1 can be populated by G2) is very fast and successfully competes with other deactivation processes such as the RET. Second, low-temperature experiments have been performed, since the G1 signal nearly vanishes at temperatures below 120 K.[63] At 4 K, the G1 emission cannot be detected anymore (see Figure 5b).

Low-Temperature Investigations. The results of low-temperature measurements of the UCNP≡TAMRA sample dispersed in MOPS buffer are shown in Figure 6, Table 2, and Figures S5 and S6 (SI). The emission of G1 and TAMRA is absent at 4 K (see Figure 6a). With increasing temperature up to 100 K, the total emission intensities increase, whereas the intensities recorded over 100 K decrease again (see non-normalized PL emission spectra, Figure S6, SI). The area-normalized emission in Figure 6a shows an increase of the emission intensities, particularly for the TAMRA emission. The G1 emission starts to appear at 100 and 120 K—100 K is very close to the limit of detection. The thermal equilibrium of G1 and G2 establishes so fast that the G1/G2 ratio stays constant with increasing delay time after the excitation pulse and the G1 emission increases significantly in relation to G2 with increasing temperature (see Figure S5, SI).

The low PL emission intensity at 4 K could relate to a less efficient energy transfer between Yb(III) and Er(III) at very low temperatures, which steadily improves with rising temperature. This relates with the thermal population of the two lower $^7F_{5/2}$ levels of Yb(III), $^7F_{5/2}|0\rangle$, and $^7F_{5/2}|1\rangle$ with an energy gap of 39 cm^{-1}, which are highly relevant in the energy transfer from Yb(III) to Er(III)).[2,64] Although at temperatures over 100 K competing multiphonon relaxation processes will occur, which add additional quenching pathways for the Er(III) luminescence, the TAMRA is stronger excited with increasing temperature. It is tempting to attribute this effect to the increasing (thermal) population of the $^2H_{11/2}$ state (which is the source for the G1 emission).

The kinetic investigations reveal decreasing luminescence decay times with increasing temperature (see Table 2). The $\langle\tau\rangle$ shows only little errors except for the G1 band at lower temperatures correlating with the very little intensity being close to the limit of detection of the applied experimental setup. The G1 regression errors decrease as the temperature (and accordingly the G1 intensity) increases. The shorter component τ_1 (of the double-exponential regression model) has always an amplitude fraction of at least 80% (see Table 2). The component τ_1 in the TAMRA emission has even a fraction higher than 90% and is always around 28 μs. After G1 appears, the second component τ_2 shows a small increase, which could either be a temperature effect or is related to the additional RET from the G1 to the TAMRA. G1-to-TAMRA RET can be neither denied nor affirmed with certainty with these results. But the G2-to-TAMRA RET is already measured at 50 K—G1 emission is absent, and TAMRA emission is already present—see Figure 6a. To further investigate this issue, the ratios of TAMRA to G1 and to G2 have been calculated and plotted (Figure 6b). The TAMRA/G1 ratios start at 100 K, because below 100 K, the G1 signal has been undetectable. Surprisingly, the TAMRA/G1 ratios decrease with increasing temperature. It reveals a relative increase of TAMRA emission in comparison to the G1 emission. In contrast, the TAMRA/G2 ratios stay constant at temperatures above 100 K, indicating an equal increase of the TAMRA and G2 emission. Based on that, the TAMRA emission should be mainly sensitized by the G2 ($^4S_{3/2} \rightarrow {}^4I_{15/2}$) band and the population of the $^2H_{11/2}$ (G1 emission) competes with the RET to TAMRA.

Another remarkable point in Figure 6b is the increasing TAMRA/G2 ratio with increasing temperature below 100 K. At low temperatures, the upconversion process works with a low efficiency due to the thermal population of the two lower Stark split energy levels of the $^7F_{5/2}$ of Yb(III). This thermal population is a preceding process, whose efficiency improves with increasing temperature. The upconversion process within the UCNP and the G2-to-TAMRA RET work very well so that the TAMRA emission increases faster than the G2 emission, in relation to G2.

https://dx.doi.org/10.1021/acs.jpcc.0c09798
J. Phys. Chem. C 2020, 124, 28623−28635

CONCLUSIONS AND OUTLOOK

The physicochemical properties of $NaYF_4$:Yb,Er UCNPs wrapped by the novel bioinspired capping ligand CMP are reported. CMP is a customized mussel protein polymer and powerful novel surface ligand for UCNPs that integrates the concepts of blood coagulation and mussel adhesion. Because of the cross-linking abilities, a tight network is formed around the UCNP, keeping them stable in MOPS buffer for very long times (up to years). The CMP cross-links on the surface of the UCNP so that a cagelike system is formed. The cross-linking of the surface ligand suppresses ligand exchange reactions, which are normally present as part of the dynamic equilibrium. Very intriguing is also the outstanding long shelf life of the UCNP in aqueous solutions, without affecting other physical−chemical properties like size or aggregation tendency negatively. The time-resolved PL measurements reveal that the UCNPs' luminescence decay time shortens due to the phase transfer from the organic to the aqueous phase, which has been observed before for UCNP in general and is attributed to the increased (surface) quenching by OH groups of the solvent. But on the other hand, it shows that the solvent molecules are still free to pass the cross-linked outer shell, which could be important for further sensing applications in which the accessibility maybe a performance issue. Especially the unique combination of properties (cross-linking and biofunctionalization via click chemistry) makes this capping ligand very promising for further future work in the field of life science applications using UCNP. As a showcase, the fluorescent dye TAMRA was coupled to the CMP-capped UCNP via click chemistry and the photophysics of this donor−acceptor system was investigated in detail. To monitor the successful coupling, MST was used as a complementary analytical tool for the first time in the context of UCNP−dye coupling. From the reduction in diffusion speed observed in the MST experiment upon coupling of TAMRA to the UCNPs, the success of the coupling could be nicely shown. Due to the TAMRA coupling, the photophysics of the UCNP is altered. Especially the distinct change in the G/R ratio and the outstanding increase of the TAMRA fluorescence decay time are strong indicators for an RET. The TAMRA fluorescence decay time increased from initial 2.28 ns up to 22 μs due to sensitization via RET, which is enhanced by a factor of 9500. Low-temperature measurements have been performed to further elucidate the RET, and it was found that the dominant sensitization originates from the G2.

The behavior of the UCNP covered with CMP, being a bioinspired PG-CatPh coating polymer, will be further investigated in biological media to figure out whether, and if, how many, biomolecules, like proteins in serum, attach nonspecific to the UCNP\CMP. Similar experiments have been performed by Nsubuga et al. with photopolymerizable capping agents (a mixture of 10,12-pentacosadiynoic acid and diyne phospholipids) in which no protein adsorption has been observed.[65] Taking further into account that in adsorption experiments of biomolecules on monolayers of CMP covering surfaces and nanoparticles as already performed by Yu et al. with very promising results,[24] the UCNP\CMP presented here in our study are promising candidates for further testing in biological applications when modified with a biomarker molecule. For use in biological systems also, the change of hydrodynamic sizes (dynamic light scattering experiments), before and after bioconjugation, can play an important role in application possibilities, which will be a subject of future research.

ASSOCIATED CONTENT

Supporting Information

The Supporting Information is available free of charge at https://pubs.acs.org/doi/10.1021/acs.jpcc.0c09798.

Additional graphics and illustrations; PL emission spectra of $NaYF_4$:Yb,Er and $NaYF_4$:Yb,Tm UCNPs after long-time storage (λ_{ex} = 976 nm) (Figure S1); histograms from TEM evaluation of the $NaYF_4$:Yb,Er UCNPs covered with CMP—same sample from 2017 and 2020 (Figure S2); PL emission spectra of the reaction mixture and supernatants of the purification and photo of the dispersions (Figure S3); fluorescence emission and absorption spectra of TAMRA after the coupling reaction and purification (Figure S4); low-temperature measurement of UCNP≡TAMRA, PL emission, and kinetics in a temperature range of 4−200 K (λ_{ex} = 976 nm) (Figure S5); detailed PL decay times of green emission G2 (540 nm), red emission R (654 nm), and TAMRA emission (600 nm) peaks excited via RET from $NaYF_4$:Yb,Er UCNP (λ_{ex} = 976 nm) (Table S1); PL emission spectra of UCNP≡TAMRA at low temperatures (4−200 K) and non-normalized spectra (λ_{ex} = 976 nm) (Figure S6) (PDF)

AUTHOR INFORMATION

Corresponding Author

Michael U. Kumke − *Institute of Chemistry (Physical Chemistry), University of Potsdam, Potsdam 14476, Germany;* orcid.org/0000-0002-3395-9379; Email: kumke@uni-potsdam.de

Authors

Philipp U. Bastian − *Institute of Chemistry (Physical Chemistry), University of Potsdam, Potsdam 14476, Germany*

Leixiao Yu − *Institute of Chemistry and Biochemistry, Freie Universität Berlin, Berlin 14195, Germany;* orcid.org/0000-0001-8804-948X

Anna López de Guereñu − *Institute of Chemistry (Physical Chemistry), University of Potsdam, Potsdam 14476, Germany*

Rainer Haag − *Institute of Chemistry and Biochemistry, Freie Universität Berlin, Berlin 14195, Germany;* orcid.org/0000-0003-3840-162X

Complete contact information is available at: https://pubs.acs.org/10.1021/acs.jpcc.0c09798

Author Contributions

The manuscript was written through contributions of all authors. All authors have given approval to the final version of the manuscript.

Notes

The authors declare no competing financial interest.

ACKNOWLEDGMENTS

P.U.B. is thankful to Helmholtz-Graduate School Macromolecular Bioscience (MacroBio, Helmholtz-Zentrum Geesthach) and to the University of Potsdam for financial support. Special thanks also go to Dr. Christina Günter (University of

https://dx.doi.org/10.1021/acs.jpcc.0c09798
J. Phys. Chem. C 2020, 124, 28623−28635

Potsdam, Institute of Geosciences) for her fruitful discussions, advice, and help in the context of the XRD measurements.

REFERENCES

(1) Auzel, F. E. Materials and Devices Using Double-Pumped-Phosphors with Energy Transfer. *Proc. IEEE* **1973**, *61*, 758−786.
(2) Auzel, F. Upconversion and Anti-Stokes Processes with f and d Ions in Solids. *Chem. Rev.* **2004**, *104*, 139−173.
(3) Bloembergen, N. Solid State Infrared Quantum Counters. *Phys. Rev. Lett.* **1959**, *2*, 84−85.
(4) Li, Z.; Zhang, Y. An Efficient and User-Friendly Method for the Synthesis of Hexagonal-Phase $NaYF_4$:Yb, Er/Tm Nanocrystals with Controllable Shape and Upconversion Fluorescence. *Nanotechnology* **2008**, *19*, No. 345606.
(5) Meijer, M. S.; Rojas-Gutierrez, P. A.; Busko, D.; Howard, I. A.; Frenzel, F.; Würth, C.; Resch-Genger, U.; Richards, B. S.; Turshatov, A.; Capobianco, J. A.; et al. Absolute Upconversion Quantum Yields of Blue-Emitting $LiYF_4$:Yb^{3+},Tm^{3+} Upconverting Nanoparticles. *Phys. Chem. Chem. Phys.* **2018**, *20*, 22556−22562.
(6) Wang, F.; Banerjee, D.; Liu, Y.; Chen, X.; Liu, X. Upconversion Nanoparticles in Biological Labeling, Imaging, and Therapy. *Analyst* **2010**, *135*, 1839.
(7) Chen, G.; Qiu, H.; Prasad, P. N.; Chen, X. Upconversion Nanoparticles: Design, Nanochemistry, and Applications in Theranostics. *Chem. Rev.* **2014**, *114*, 5161−5214.
(8) Sy, M.; Nonat, A.; Hildebrandt, N.; Charbonnière, L. J. Lanthanide-Based Luminescence Biolabelling. *Chem. Commun.* **2016**, *52*, 5080−5095.
(9) Gorris, H. H.; Resch-Genger, U. Perspectives and Challenges of Photon-Upconversion Nanoparticles - Part II: Bioanalytical Applications. *Anal. Bioanal. Chem.* **2017**, *409*, 5875−5890.
(10) Phan, T. G.; Bullen, A. Practical Intravital Two-Photon Microscopy for Immunological Research: Faster, Brighter, Deeper. *Immunol. Cell Biol.* **2010**, *88*, 438−444.
(11) Jacques, S. L. Optical Properties of Biological Tissues: A Review. *Phys. Med. Biol.* **2013**, *58*, R37−R61.
(12) Bashkatov, A. N.; Genina, E. A.; Kozintseva, M. D.; Kochubei, V. I.; Gorodkov, S. Y.; Tuchin, V. V. Optical Properties of Peritoneal Biological Tissues in the Spectral Range of 350−2500 nm. *Opt. Spectrosc.* **2016**, *120*, 1−8.
(13) Liu, Q.; Feng, W.; Li, F. Water-Soluble Lanthanide Upconversion Nanophosphors: Synthesis and Bioimaging Applications in Vivo. *Coord. Chem. Rev.* **2014**, *273*−*274*, 100−110.
(14) Swartling, J.; Axelsson, J.; Ahlgren, G.; Kälkner, K. M.; Nilsson, S.; Svanberg, S.; Svanberg, K.; Andersson-Engels, S. System for Interstitial Photodynamic Therapy with Online Dosimetry: First Clinical Experiences of Prostate Cancer. *J. Biomed. Opt.* **2010**, *15*, No. 058003.
(15) Park, Y. I.; Kim, H. M.; Kim, J. H.; Moon, K. C.; Yoo, B.; Lee, K. T.; Lee, N.; Choi, Y.; Park, W.; Ling, D.; et al. Theranostic Probe Based on Lanthanide-Doped Nanoparticles for Simultaneous in Vivo Dual-Modal Imaging and Photodynamic Therapy. *Adv. Mater.* **2012**, *24*, 5755−5761.
(16) Ai, F.; Ju, Q.; Zhang, X.; Chen, X.; Wang, F.; Zhu, G. A Core-Shell-Shell Nanoplatform Upconverting near-Infrared Light at 808 nm for Luminescence Imaging and Photodynamic Therapy of Cancer. *Sci. Rep.* **2015**, *5*, No. 10785.
(17) Zhu, X.; Zhang, J.; Liu, J.; Zhang, Y. Recent Progress of Rare-Earth Doped Upconversion Nanoparticles: Synthesis, Optimization, and Applications. *Adv. Sci.* **2019**, *6*, No. 1901358.
(18) Muhr, V.; Wilhelm, S.; Hirsch, T.; Wolfbeis, O. S. Upconversion Nanoparticles: From Hydrophobic to Hydrophilic Surfaces. *Acc. Chem. Res.* **2014**, *47*, 3481−3493.
(19) Sedlmeier, A.; Gorris, H. H. Surface Modification and Characterization of Photon-Upconverting Nanoparticles for Bioanalytical Applications. *Chem. Soc. Rev.* **2015**, *44*, 1526−1560.
(20) Wilhelm, S.; Kaiser, M.; Wurth, C.; Heiland, J.; Carrillo-Carrion, C.; Muhr, V.; Wolfbeis, O. S.; Parak, W. J.; Resch-Genger, U.; Hirsch, T. Water Dispersible Upconverting Nanoparticles: Effects of Surface Modification on Their Luminescence and Colloidal Stability. *Nanoscale* **2015**, *7*, 1403−1410.
(21) Dong, A.; Ye, X.; Chen, J.; Kang, Y.; Gordon, T.; Kikkawa, J. M.; Murray, C. B. A Generalized Ligand-Exchange Strategy Enabling Sequential Surface Functionalization of Colloidal Nanocrystals. *J. Am. Chem. Soc.* **2011**, *133*, 998−1006.
(22) Gorris, H. H.; Wolfbeis, O. S. Photon-Upconverting Nanoparticles for Optical Encoding and Multiplexing of Cells, Biomolecules, and Microspheres. *Angew. Chem., Int. Ed.* **2013**, *52*, 3584−3600.
(23) Vert, M.; Doi, Y.; Hellwich, K. H.; Hess, M.; Hodge, P.; Kubisa, P.; Rinaudo, M.; Schué, F. Terminology for Biorelated Polymers and Applications (IUPAC Recommendations 2012). *Pure Appl. Chem.* **2012**, *84*, 377−410.
(24) Yu, L.; Cheng, C.; Ran, Q.; Schlaich, C.; Noeske, P.-L. M.; Li, W.; Wei, Q.; Haag, R. Bioinspired Universal Monolayer Coatings by Combining Concepts from Blood Protein Adsorption and Mussel Adhesion. *ACS Appl. Mater. Interfaces* **2017**, *9*, 6624−6633.
(25) Rostovtsev, V. V.; Green, L. G.; Fokin, V. V.; Sharpless, K. B. A Stepwise Huisgen Cycloaddition Process: Copper(I)-Catalyzed Regioselective "Ligation" of Azides and Terminal Alkynes. *Angew. Chem., Int. Ed.* **2002**, *41*, 2596−2599.
(26) Ostermann, J.; Schmidtke, C.; Wolter, C.; Merkl, J.-P.; Kloust, H.; Weller, H. Tailoring the Ligand Shell for the Control of Cellular Uptake and Optical Properties of Nanocrystals. *Beilstein J. Nanotechnol.* **2015**, *6*, 232−242.
(27) Best, M. D. Click Chemistry and Bioorthogonal Reactions: Unprecedented Selectivity in the Labeling of Biological Molecules. *Biochemistry* **2009**, *48*, 6571−6584.
(28) Kolb, H. C.; Sharpless, K. B. The Growing Impact of Click Chemistry on Drug Discovery. *Drug Discovery Today* **2003**, *8*, 1128−1137.
(29) Han, S. S.; Yoon, H. Y.; Yhee, J. Y.; Cho, M. O.; Shim, H. E.; Jeong, J. E.; Lee, D. E.; Kim, K.; Guim, H.; Lee, J. H.; et al. In Situ Cross-Linkable Hyaluronic Acid Hydrogels Using Copper Free Click Chemistry for Cartilage Tissue Engineering. *Polym. Chem.* **2018**, *9*, 20−27.
(30) Bhuckory, S.; Hemmer, E.; Wu, Y.-T.; Yahia-Ammar, A.; Vetrone, F.; Hildebrandt, N. Core or Shell? Er^{3+} FRET Donors in Upconversion Nanoparticles. *Eur. J. Inorg. Chem.* **2017**, *2017*, 5186−5195.
(31) Hesse, J.; Klier, D. T.; Sgarzi, M.; Nsubuga, A.; Bauer, C.; Grenzer, J.; Hübner, R.; Wislicenus, M.; Joshi, T.; Kumke, M. U.; et al. Rapid Synthesis of Sub-10 nm Hexagonal $NaYF_4$-Based Upconverting Nanoparticles Using Therminol® 66. *ChemistryOpen* **2018**, *7*, 159−168.
(32) Wan, J.; Kim, Y.; Mulvihill, M. J.; Tokunaga, T. K. Dilution Destabilizes Engineered Ligand-Coated Nanoparticles in Aqueous Suspensions. *Environ. Toxicol. Chem.* **2018**, *37*, 1301−1308.
(33) Dukhno, O.; Przybilla, F.; Muhr, V.; Buchner, M.; Hirsch, T.; Mély, Y. Time-Dependent Luminescence Loss for Individual Upconversion Nanoparticles upon Dilution in Aqueous Solution. *Nanoscale* **2018**, *10*, 15904−15910.
(34) Yang, J.; Saggiomo, V.; Velders, A. H.; Stuart, M. A. C.; Kamperman, M. Reaction Pathways in Catechol/Primary Amine Mixtures: A Window on Crosslinking Chemistry. *PLoS One* **2016**, *11*, No. e0166490.
(35) Yi, Z.; Lu, W.; Liu, H.; Zeng, S. High Quality Polyacrylic Acid Modified Multifunction Luminescent Nanorods for Tri-Modality Bioimaging, in Vivo Long-Lasting Tracking and Biodistribution. *Nanoscale* **2015**, *7*, 542−550.
(36) Himo, F.; Lovell, T.; Hilgraf, R.; Rostovtsev, V. V.; Noodleman, L.; Sharpless, K. B.; Fokin, V. V. Copper(I)-Catalyzed Synthesis of Azoles. DFT Study Predicts Unprecedented Reactivity and Intermediates. *J. Am. Chem. Soc.* **2005**, *127*, 210−216.
(37) Valeur, B. *Molecular Fluorescence—Principles and Applications*; Wiley-VCH Verlag, 2002.
(38) Krämer, K. W.; Biner, D.; Frei, G.; Güdel, H. U.; Hehlen, M. P.; Lüthi, S. R. Hexagonal Sodium Yttrium Fluoride Based Green and

https://dx.doi.org/10.1021/acs.jpcc.0c09798
J. Phys. Chem. C 2020, 124, 28623−28635

Blue Emitting Upconversion Phosphors. *Chem. Mater.* **2004**, *16*, 1244−1251.
(39) Mai, H. X.; Zhang, Y. W.; Si, R.; Yan, Z. G.; Sun, L. D.; You, L. P.; Yan, C. H. High-Quality Sodium Rare-Earth Fluoride Nanocrystals: Controlled Synthesis and Optical Properties. *J. Am. Chem. Soc.* **2006**, *128*, 6426−6436.
(40) Shan, J.; Kong, W.; Wei, R.; Yao, N.; Ju, Y. An Investigation of the Thermal Sensitivity and Stability of the β-$NaYF_4$:Yb,Er Upconversion Nanophosphors. *J. Appl. Phys.* **2010**, *107*, No. 054901.
(41) Wu, K.; Cui, J.; Kong, X.; Wang, Y. Temperature Dependent Upconversion Luminescence of YbEr Codoped $NaYF_4$ Nanocrystals. *J. Appl. Phys.* **2011**, *110*, No. 053510.
(42) Sass, S.; Stöcklein, W. F. M.; Klevesath, A.; Hurpin, J.; Menger, M.; Hille, C. Binding Affinity Data of DNA Aptamers for Therapeutic Anthracyclines from Microscale Thermophoresis and Surface Plasmon Resonance Spectroscopy. *Analyst* **2019**, *144*, 6064−6073.
(43) Förster, T. Energiewanderung Und Fluoreszenz. *Naturwissenschaften* **1946**, *33*, 166−175.
(44) Förster, T. Zwischenmolekulare Energiewanderung Und Fluoreszenz. *Ann. Phys.* **1948**, *437*, 55−75.
(45) Charbonnière, L. J.; Hildebrandt, N. Lanthanide Complexes and Quantum Dots: A Bright Wedding for Resonance Energy Transfer. *Eur. J. Inorg. Chem.* **2008**, *2008*, 3241−3251.
(46) Hötzer, B.; Medintz, I. L.; Hildebrandt, N. Fluorescence in Nanobiotechnology: Sophisticated Fluorophores for Novel Applications. *Small* **2012**, *8*, 2297−2326.
(47) Geißler, D.; Linden, S.; Liermann, K.; Wegner, K. D.; Charbonnière, L. J.; Hildebrandt, N. Lanthanides and Quantum Dots as Förster Resonance Energy Transfer Agents for Diagnostics and Cellular Imaging. *Inorg. Chem.* **2014**, *53*, 1824−1838.
(48) Muhr, V.; Würth, C.; Kraft, M.; Buchner, M.; Baeumner, A. J.; Resch-Genger, U.; Hirsch, T. Particle-Size-Dependent Förster Resonance Energy Transfer from Upconversion Nanoparticles to Organic Dyes. *Anal. Chem.* **2017**, *89*, 4868−4874.
(49) Hildebrandt, N.; Wegner, K. D.; Algar, W. R. Luminescent Terbium Complexes: Superior Förster Resonance Energy Transfer Donors for Flexible and Sensitive Multiplexed Biosensing. *Coord. Chem. Rev.* **2014**, *273*−*274*, 125−138.
(50) Joshi, J. C.; Pandey, N. C.; Joshi, B. C.; Belwal, R.; Joshi, J. Quantum Efficiency of Diffusion-Limited Energy Transfer from Eu^{3+} → Nd^{3+} in Borate Glass. *J. Solid State Chem.* **1978**, *23*, 135−139.
(51) Becker, W. *Advanced Time-Correlated Single Photon Counting Techniques*; Springer-Verlag: Berlin, 2005; Vol. *81*.
(52) Lakowicz, J. R. *Principles of Fluorescence Spectroscopy*, 3rd ed.; Springer, 2006.
(53) Gessner, A. *Novel Lanthanide Doped Micro- and Mesoporous Solids Characterization of Ion−Host-Interactions, Species Distribution and Luminescence Properties Using Time-Resolved Luminescence Spectroscopy (Nauartige Lanthanoid-Dotierte Mikro- Und Mesoporöse Feststoffe)*; Universität Potsdam, 2010.
(54) Orthaus, S.; Biskup, C.; Hoffmann, B.; Hoischen, C.; Ohndorf, S.; Benndorf, K.; Diekmann, S. Assembly of the Inner Kinetochore Proteins CENP-A and CENP-B in Living Human Cells. *ChemBioChem* **2008**, *9*, 77−92.
(55) FLIM FRET Calculation for Multi Exponential Donors Summary. https://www.tcspc.com/doku.php/howto:flim_fret_calculation_for_multi_exponential_donors?s[]=amplitude&s[]=weighted (accessed March 3, 2020).
(56) Koti, A. S. R.; Krishna, M. M. G.; Periasamy, N. Time-Resolved Area-Normalized Emission Spectroscopy (TRANES): A Novel Method for Confirming Emission from Two Excited States. *J. Phys. Chem. A* **2001**, *105*, 1767−1771.
(57) Shanmugapriya, T.; Vinayakan, R.; Thomas, K. G.; Ramamurthy, P. Synthesis of CdS Nanorods and Nanospheres: Shape Tuning by the Controlled Addition of a Sulfide Precursor at Room Temperature. *CrystEngComm* **2011**, *13*, 2340−2345.
(58) Gavvala, K.; Koninti, R. K.; Sengupta, A.; Hazra, P. Excited State Proton Transfer Dynamics of an Eminent Anticancer Drug, Ellipticine, in Octyl Glucoside Micelle. *Phys. Chem. Chem. Phys.* **2014**, *16*, 14953−14960.
(59) Carlotti, B.; Benassi, E.; Cesaretti, A.; Fortuna, C. G.; Spalletti, A.; Barone, V.; Elisei, F. An Ultrafast Spectroscopic and Quantum Mechanical Investigation of Multiple Emissions in Push-Pull Pyridinium Derivatives Bearing Different Electron Donors. *Phys. Chem. Chem. Phys.* **2015**, *17*, 20981−20989.
(60) Klier, D. T.; Kumke, M. U. Analysing the Effect of the Crystal Structure on Upconversion Luminescence in Yb^{3+},Er^{3+}-Co-Doped $NaYF_4$ Nanomaterials. *J. Mater. Chem. C* **2015**, *3*, 11228−11238.
(61) Pin, M. W.; Park, E. J.; Choi, S.; Kim, Y. I.; Jeon, C. H.; Ha, T. H.; Kim, Y. H. Atomistic Evolution during the Phase Transition on a Metastable Single $NaYF_4$:Yb,Er Upconversion Nanoparticle. *Sci. Rep.* **2018**, *8*, No. 2199.
(62) Arppe, R.; Hyppänen, I.; Perälä, N.; Peltomaa, R.; Kaiser, M.; Würth, C.; Christ, S.; Resch-Genger, U.; Schäferling, M.; Soukka, T. Quenching of the Upconversion Luminescence of $NaYF_4$:Yb^{3+},Er^{3+} and $NaYF_4$:Yb^{3+},Tm^{3+} Nanophosphors by Water: The Role of the Sensitizer Yb^{3+} in Non-Radiative Relaxation. *Nanoscale* **2015**, *7*, 11746−11757.
(63) Klier, D. T.; Kumke, M. U. Upconversion Luminescence Properties of $NaYF_4$:Yb:Er Nanoparticles Codoped with Gd^{3+}. *J. Phys. Chem. C* **2015**, *119*, 3363−3373.
(64) Klier, D. T.; Kumke, M. U. Upconversion $NaYF_4$:Yb:Er Nanoparticles Co-Doped with Gd^{3+} and Nd^{3+} for Thermometry on the Nanoscale. *RSC Adv.* **2015**, *5*, 67149−67156.
(65) Nsubuga, A.; Zarschler, K.; Sgarzi, M.; Graham, B.; Stephan, H.; Joshi, T. Towards Utilising Photocrosslinking of Polydiacetylenes for the Preparation of "Stealth" Upconverting Nanoparticles. *Angew. Chem., Int. Ed.* **2018**, *57*, 16036−16040.

https://dx.doi.org/10.1021/acs.jpcc.0c09798
J. Phys. Chem. C 2020, 124, 28623−28635

3

Discussion

3.1. Migration of Trivalent Lanthanoid Cations Doped in UCNP Host Lattices

The migration of Ln(III) ions has been investigated spectroscopically by LRET in a core-shell-shell nanoparticle system. The donor-acceptor distance of two LRET-pairs has been varied by applying an insulation shell with increasing layer thickness within one set of the experiments. The insulation shell (or insulation layer) separates the acceptor doped core from the donor doped outer shell. The increasing layer thickness increases the spatial separation of the acceptors and the donors (either Nd^{3+} or Pr^{3+} in the core and Eu^{3+} in the outer shell, respectively). An illustration of the synthesis concept is given, e.g., in Fig. 1 of manuscript 1 (section 2.2). In Table 3.1, a brief overview of all main sets from both manuscripts is given.

Table 3.1.: Overview of the investigated sets.

Set naming	**Host lattice**	**LRET pair** (donor → acceptor)	**Manuscript**
Set Nd300 (= Set 1)*	$NaYF_4$†	$Eu^{3+} \rightarrow Nd^{3+}$	#1 in section 2.2
Set Y300-old (= Set 2)*	$NaYF_4$	$Eu^{3+} \rightarrow Nd^{3+}$	#1 in section 2.2
Set Y300	$NaYF_4$	$Eu^{3+} \rightarrow Pr^{3+}$	#2 in section 2.3
Set Gd300	$NaGdF_4$	$Eu^{3+} \rightarrow Nd^{3+}$	#2 in section 2.3

*corresponding to the initial sample declarations in manuscript 1.

†core being $NaNdF_4$ due to 100 mol % Nd^{3+} doping.

3.1.1. What is the reason for the Ln(III) ion migration?

The migration of the Ln(III) ions within the nanoparticle host lattice relates to the dynamic dissolution and recrystallization of the outer atom/ion layers of the nanoparticle during the nanoparticle shell growth synthesis. While the precursor solution for the

additional shell is added, already built-in trivalent cations from the core (or core-shell) nanoparticles can be exchanged against trivalent cations from the shell precursor in the reaction solution.[55] Due to the cation exchange, a transition layer between core-shell structures is formed instead of clearly separated core-shell or core-shell-shell structures.

Additionally to the described dissolution-recrystallization process, the occurrence of vacancies in the crystal lattice may favor the Ln(III) migration. The number of vacant lattice sites and the vibrational energy of the ions in the host lattice increase as the temperature increases.[51,102] These processes are important for the fabrication of UCNPs and should be kept in mind especially for core-shell systems, e.g., if the sensitizer and activator ions shall be separated from each other in a core-shell design by doping the sensitizers in the core and the activator in the shell. The dynamics of the dissolution and recrystallization can be influenced either to produce larger transition layers on purpose or to produce smaller transition layers by synthesis design, choice of precursors, and appropriate temperature. Larger transition layers or their absence may lead to improved luminescence of distinct PL emission bands due to directed energy transfer within the nanocrystal.

As mentioned earlier, not only Ln(III) ions migrate during the synthesis, but also the other ions in the nanocrystal, such as sodium, yttrium, and fluoride ions. The major driving factor of the migration process is the dissolution and recrystallization process during the synthesis. However, the investigation with laser spectroscopy can only be used to investigate the luminescent Ln(III) ions, which is going to be discussed.

3.1.2. The LRET equation / FRET derived equation

The LRET equation is used to evaluate the spectroscopic data of the Eu^{3+} donor luminescence, the Eu^{3+} PL quenching related to its nearer environment in the nanocrystal, and the influence of the insulation shell thickness resulting in different Nd^{3+}/Pr^{3+} concentrations. The LRET equation is based on a stretched exponential decay model, Eq. (3.1), in which the multi-exponential decay behavior of the donor luminescence is reflected. The donors (the Eu^{3+} ions) are distributed within the nanoparticle located either on/close to the nanoparticle surface or close to Nd^{3+} ions in the nanoparticle "bulk phase". Consequently, a mixture of luminescence from the Eu^{3+} ions is recorded, which would make the use of a multi-exponential decay model necessary. The use of the stretched exponential decay model reduces the number of needed regression parame-

ters to a minimum and still accounts for the Eu^{3+} distribution within the nanoparticle.

$$I_D(t) = I_D(0) \exp\left[-\left(\frac{t}{\tau_D}\right)^{\beta_D}\right] \qquad \text{(stretched exponential function)} \quad (3.1)$$

With Eq. (3.1), the donor only PL decay time τ_D and heterogeneity parameter β_D are calculated, which are needed for the LRET equation, Eq. (3.2). β_D ranges from 0 to 1. Ideally, β_D is close to 1. If $\beta_D = 1$, a monoexponential decay function will be obtained indicating a homogeneous Eu^{3+} distribution within the nanoparticle.

At this point, it shall be emphasized, that Eq. (3.1) is also used to calculate the donor PL decay time in presence of the acceptor (then, the parameters are τ_{DA} and β_{DA}) and the acceptor PL decay time in presence (CSS samples) and in absence (CS samples) of the donor (then, the parameters are τ_{AD} and β_{AD}, as well as τ_A and β_A, respectively). These decay times are necessary for the calculation of the donor luminescence based LRET efficiency E_{LRET} (Eq. (1.6)) and the acceptor luminescence decay time enhancement factors $\left(\frac{\tau_{AD}}{\tau_A}\right)$. For further details, please refer to the *Theory* section of the second manuscript dealing with the Ln(III) migration (manuscript 2, section 2.3).

The donor-only parameters τ_D and β_D are used as constants in Eq. (3.2) to calculate the number of acceptors within the Förster distance (also termed as acceptor concentration or acceptor number). The calculation of the acceptor number is based on the donor luminescence. The Förster distance is the Förster radius R_0 of the respective FRET/LRET pair, being either Eu→Nd or Eu→Pr.

$$I_{DA}(t) = I_{DA}(0) \exp\left[-\left(\frac{t}{\tau_D}\right)^{\beta_D} - 2\gamma\left(\frac{t}{\tau_D}\right)^{\alpha/2}\right] \qquad \text{(LRET equation)} \quad (3.2)$$

$$\gamma = \frac{\sqrt{\pi}}{2} c_A \frac{4}{3}\pi R_0^3 \qquad \text{(acceptor number calcuation)} \quad (3.3)$$

The second term in Eq. (3.2) refers to the acceptor influence on the donor luminescence decay. Therefore, the parameter α accounts for the acceptor distribution in the nanoparticles (so to say, the Nd^{3+} (Pr^{3+}) ion distribution). The parameter γ is linked to the acceptor concentration c_A, whereas the term $c_A \frac{4}{3}\pi R_0^3$ refers to the value for the acceptor number within the Förster distance (in the following termed acceptor concentration). All calculated acceptor concentrations are given in the manuscripts and a

choice is presented in Table 3.2.

These formulas can be found as well in the manuscript 1 (section 2.2), Eq. (1), (2) and (2a), and manuscript 2 (section 2.3), Eq. (1) to (3).

3.1.3. The Ln(III) migration

In subsection 1.1.3 some examples of already investigated migration parameters are mentioned. Now, the carried out research shall be set in the scientific context. It should be noticed, that the presented nanoparticle design and synthesis approach have been performed for all nanoparticles the same way. The only parameter, that was varied between the sets, is the nanoparticle composition. This variation in combination with the introduced LRET-equation Eq. (3.2) is the major tool for the following evaluation and discussion.

In Fig. 3.1, the acceptor numbers of all sets are plotted against the insulation layer thickness to compare the respective nanoparticle compositions with each other. The corresponding acceptor numbers are re-listed in Table 3.2 at the end of this section. These plots and the acceptor numbers are based on the Eu^{3+} luminescence. In Fig. 3.1 (a), the Nd^{3+} ion (= acceptor) migration in a $NaYF_4$ host lattice is reflected by the acceptor number in dependency on the insulation layer thickness. The set Nd300 (blue plot) corresponds to the samples with 100 % acceptor doping in the core (being $NaNdF_4$). The set Y300-old (yellow plot) corresponds to the samples with 20 % acceptor doping in the core (being $NaY_{80\,mol\,\%}F_4{:}Nd_{20\,mol\,\%}$). The same subsequent shell growth procedure and shell precursor materials have been applied in both cases.[98] It can be observed, that the higher acceptor concentration in the core creates a "migration pressure", which results in a higher gradient for the blue plot. The acceptor concentration gradient decreases with increasing insulation layer thickness, as it has been reported in literature before.[55,56] The initially used cores differ from the acceptor doping by a factor of 5 from 100 % to 20 % Nd^{3+} doping. This factor is reflected by the average acceptor numbers listed in Table 2 in manuscript 1 (section 2.2). However, in Fig. 3.1 (a), the respective parameters for 465 nm excitation are plotted and the factor of ca. 5 is only found up to an insulation layer thickness of approx. 1 nm. As the thickness increases further, the factor decreases, which might indicate decreasing migration pressure for Nd^{3+} ions diffusing out of the core.

The Nd^{3+} ion migration can be compared within two different host lattices: $NaYF_4$ and the $NaGdF_4$ being set Y300-old and set Gd300, respectively, compare Fig. 3.1 (b). With smaller insulation layer thicknesses, the migration behavior of the acceptor ions seems to be equal. As the insulation layer thickness increases, the deviation of the

migration behavior seems stronger pronounced, as the Nd^{3+} acceptor numbers are larger in $NaYF_4$ (yellow plot). As said in manuscript 2 (section 2.3), it is tempting to attribute this effect to the different cations in the host lattice and the better matching of Gd^{3+} with Nd^{3+} in comparison to Y^{3+} with Nd^{3+}. The respective ionic radii are 124.7 pm, 130.3 pm and 121.5 pm for Gd, Nd, and Y (with ionic charge: +3, coordination number: 9).[103] But, the initial core sizes of set Y300-old are 5 ± 1 nm (for the final S0 CS sample without an insulation layer) and 4 ± 1 nm (for the final S1 to S5 CSS samples with an insulation layer). Two batches had to be synthesized, because one synthesis does not yield in enough material to perform the experimental set with one batch. Nevertheless, these initial core diameters can be considered as equal in the given error range. For set Gd300 (red plot in (b)), the first two samples share the same core (with initial 4 ± 1 nm) and the second batch of the two samples with the larger insulation layer are based on a larger core (9 ± 2 nm diameter). The significant drop in the acceptor numbers from the samples with the insulation layers of 0 nm and 0.7 nm towards 1.0 nm and 2.8 nm relates potentially to the difference in the initial core sizes. If there is a correlation, it can be assumed, that larger nanoparticles exhibit less migration pressure leading to a less pronounced concentration gradient. Even if the small and the large nanoparticle batches have the same initial acceptor concentration (as it is here due to the synthesis strategy), the related volume of the larger particles may come into play and reduce the migration pressure.

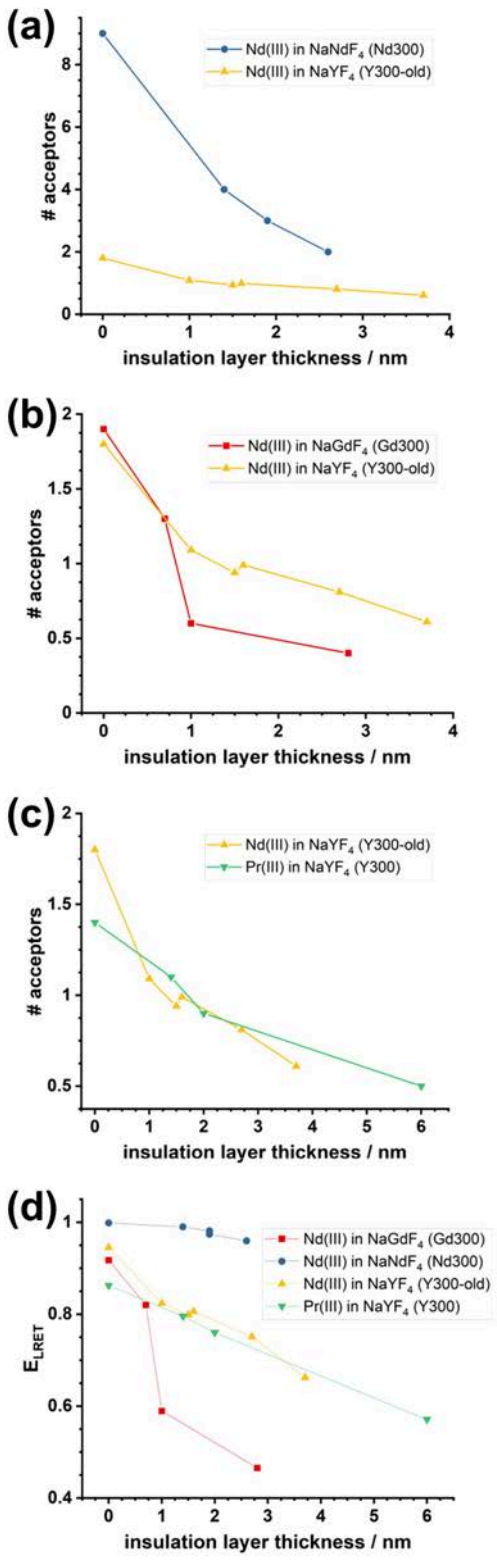

Figure 3.1.: Illustrative overview of the acceptor numbers and the LRET efficiencies E_{LRET} being based on the Eu^{3+} luminescence and its quenching (for all sets investigated).

Fig. 3.1 (c) compares the different acceptor ions
doped in the core, while anything else was maintained. The host lattice is $NaYF_4$ and only the acceptors are either Nd^{3+} or Pr^{3+} ions (yellow and green plot, respectively). Here, all samples of both sets, Y300-old as well as Y300, are based on core particles with an initial size of 4 ± 1 nm. Only minor differences of the migration behavior can be observed. The sample of Y300-old without an insulation layer (the point at 0 nm thickness, yellow plot) is the only particle batch based on a 5 nm sized core. This is also the largest difference of the nanoparticle sizes. This difference might be reflected in the acceptor numbers deviating strongest from each other with 1.8 and 1.4 acceptors for the sets Y300-old and Y300, respectively. Although, this difference could be insignificant, it is worth to mention. However, the difference of Pr^{3+} and Nd^{3+} ions could be too small to profoundly attribute these findings to different migration behavior, as these two elements are neighbors in the periodic table and have very similar ionic radii of 131.9 pm (Pr^{3+}) and 130.3 pm (Nd^{3+}) (with a coordination number of 9, respectively). [103]

In Fig. 3.1 (d), the LRET efficiencies of the four different sets are plotted. The trends and features of the decreasing efficiencies with increasing insulation layer thicknesses correspond well to the plots of the respective acceptor numbers. This is comprehensible as both calculations are based on the Eu^{3+} luminescence quenching. Nevertheless, one aspect shall be pointed out: The quenching ability of the Nd^{3+} ions seems stronger than of the Pr^{3+} ions, as the LRET efficiency of the Nd^{3+} doped sets seems higher. Especially, the Nd300 set exhibits nearly complete Eu^{3+} PL quenching, which can be attributed to the 100 % Nd^{3+} doping in the core. However, the samples with the larger initial cores (set Gd300, red plot, insulation layer thickness of 1 nm and 3 nm) indicate less LRET efficiency, which potentially correlates with larger cores and the coupled reduced migration pressure. In addition, the suppression of the Eu-to-acceptor energy transfer is not achieved, even with an insulation layer thickness of 6 nm, which exceeds the Förster radius by a factor of larger than seven (>7) in the case of Eu-to-Pr LRET.

Another aspect, which has not been considered yet, is the Ln(III) ion migration from the donors towards the acceptors. The shell growth reactions of the insulation layers and donor doped shells are realized with the respective shell precursors. Naturally, these precursors are prepared in different batches and come out in different qualities (such as moisture content or incomplete formation of Ln-oleates). These different qualities affect the migration behavior of all ions in the reaction mixture. The ions in this mixture, which are going to form the new shell, origin either from the cores/seeds or from the ions resulting from the precursor decomposition. The obtained results

were discussed in a reduced manner for reasons of simplification. It was discussed as if there was acceptor migration only, but the donor migration should not be forgotten. A separation of the donor and acceptor migration is difficult.

Related to the donor PL quenching and the LRET, the acceptor PL decay times of the sets Gd300 and Y300 (with the host lattices $NaGdF_4$ doped with Nd^{3+} and $NaYF_4$ doped with Pr^{3+}, respectively) have also been investigated, see Fig. 3.2. The luminescence decay times τ_{AD} (in (a), CSS samples, with the outer donor doped shell) and τ_A (in (b), CS samples, without the outer donor doped shell) have been calculated with the stretched exponential function (Eq. (3.1)). The acceptor PL decay enhancement factors are shown in Fig. 3.2 (c).

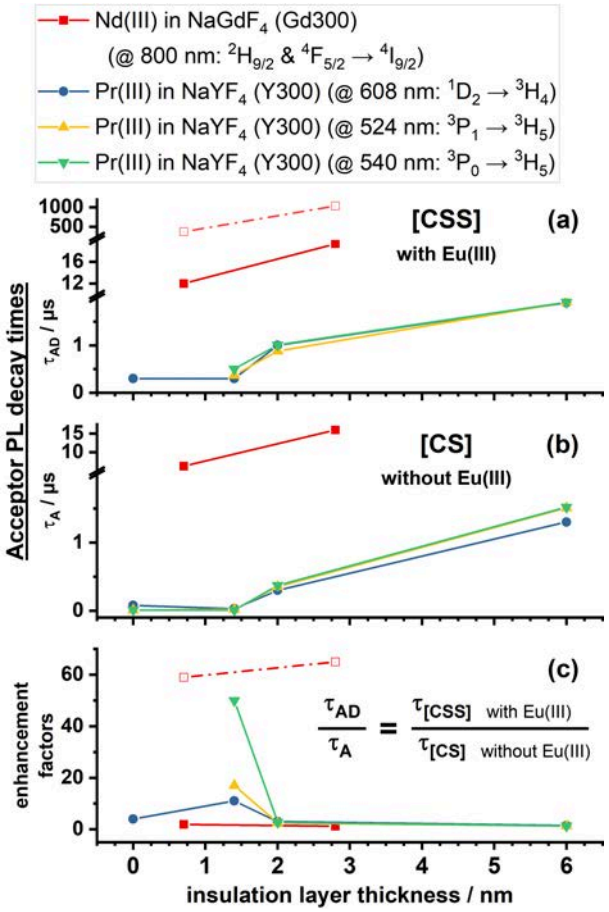

Figure 3.2.: Illustrative overview of the acceptor luminescence decay times and the respective enhancement factors in dependency of the insulation layer thickness (for all sets investigated) (Dot-dashed red plot = Nd^{3+} decay times without Eu^{3+} sensitization).

A clear trend emerges: The acceptor PL decay times increase as the insulation layer thickness increases (see Fig. 3.2 (a) and (b)). The decay time increase is small, as long as the insulation layer thickness is small. This trend can be attributed to the acceptor luminescence self-quenching, which relates to the high doping concentration. This concentration has been chosen to meet the general doping ratio of UCNPs (compare manuscript 2, section 2.3). The impact of the concentration related quenching can be seen in (b) (CS samples, acceptors in absence of donors). The Ln(III) migration leads to a dilution in the core as the insulation layer grows and "provides more space to migrate into". However, in (a) (CSS samples, acceptors in presence of donors), the expectations are not met. Instead of decreasing acceptor PL decay times with increasing insulation layer thickness, the acceptor decay times increase. The increasing spatial separation should decrease the LRET efficiency, as observed in Fig. 3.1 (d) (based on donor luminescence). However, in Fig. 3.2 (a) (based on acceptor luminescence), LRET efficiency seems to increase with increasing insulation layer thickness.

In reality, it does not. This observation can be explained with the competing acceptor sensitization by LRET and the concentration related acceptor PL self-quenching. The self-quenching is the stronger process here and has the larger rate constant, so that the dilution effect superimposes the acceptor LRET sensitization. The acceptor sensitization does increase with decreasing insulation layer thickness (because LRET efficiency increases), but this is not observed directly.

The theory of increasing acceptor sensitization by decreasing insulation layer thickness is supported by the enhancement factors, see Fig. 3.2 (c). In this figure the Eu^{3+}-to-Nd^{3+} (or Pr^{3+}) LRET sensitization is demonstrated well, as the enhancement factor increases with decreasing insulation layer thickness. The insulation layer thickness around 1.5 nm indicates a maximum and turning point for the enhancement factors (for Pr^{3+}). Below 1.5 nm insulation layer, the rate constant of the acceptor PL self-quenching is larger than for the LRET sensitization and the enhancement factors are smaller again.

Differences for Nd^{3+} in $NaGdF_4$ and Pr^{3+} in $NaYF_4$ can be seen, as the turnover point for the Nd^{3+} seems to be at even thinner insulation layers as no maximum is reached. The correlation of the two sets is difficult, because two parameters (the host lattice and the kind of acceptors) have been varied. The comparison with the previous set is not possible, because the acceptor emission was not investigated.

One more point to be mentioned is the difference of the solid red and the dot-dashed red plots of Nd^{3+} PL decay times in Fig. 3.2 (c). In manuscript 2 (section 2.3, Fig. 5 and Table 4), the Nd^{3+} emission can be separated into two Nd^{3+} species: The first ones (dot-dashed plot) are Nd^{3+} ions, which are not (or only very weakly) sensitized by Eu^{3+} LRET as those did not migrate out of the core. The second ones (solid plot) are the Nd^{3+} ions, which are sensitized by Eu^{3+} LRET as those migrated out of the core. The enhancement factors support this assumption, as the solid red plot increases towards thinner insulation layers, speaking for LRET sensitization of the Nd^{3+} ions. The dot-dashed plot decreases further towards thinner insulation layers, speaking for stronger concentration related PL self-quenching of Nd^{3+} as well as for the absence of LRET sensitization (or at least of weak LRET resulting in a smaller rate constant for LRET sensitization than for self-quenching).

The dopant dilution in the core is the major factor increasing the acceptor PL decay times. This can also be supposed to be valid for UCNPs, which results in a dilution of the sensitzer and activator dopants for core-shell UCNPs. In general, a passivating shell increases the UC efficiency. Besides the passivation, the dilution effect might induce further UC emission enhancement, but only up to a certain shell thickness.

At this point, it seems, that different synthesis strategies result in different ion migration properties. Some of them favor and others disfavor the ion migration.[51,56,58] Different sizes and concentrations alter the migration behavior already. This also means, that the investigation to particularly understand and if desired to promote, stop, or guide the Ln(III) migration will need re-evaluation, whenever any synthesis parameter changes. E.g., the effect of different shell growth strategies was demonstrated by Dühnen et al.[55] The researchers compared the usage of sacrificial nanoparticles with decomposition precursors serving as source for the shell material, respectively. Both strategies resulted in a concentration gradient. The gradient for the sacrificial nanoparticles was larger, but exhibited a smaller amount of surface Eu(III) ions.

Other researchers (Xu et al.) investigated a core-shell UCNP composition to find the optimal insulation/passivating layer thickness for improving the upconversion quantum efficiency.[104] Their particles, being $NaYF_4$:$Yb_{20\,mol\,\%}$,$Tm_{8\,mol\,\%}$ @ $NaYF_4$ UCNPs, showed best UC luminescence with a passivating layer thickness of 6.3 nm. However, the authors also communicate, that this determined thickness is only valid for their investigated nanoparticle system with their choice of their upconversion pair and their dopant concentration. Considering the results of the investigations here, one could suppose, that the optimal insulation layer thickness is 1.5 nm for the Pr^{3+} ions in the $NaYF_4$ host lattice. For Nd^{3+} no conclusion is possible, as only two samples with different insulation layer thickness were measured and no maximum was determined.

A brief paragraph shall be spend for the UCNP subset of set Y300 (shortly mentioned in manuscript 2, section 2.3). In this set, the core doping has been exchanged against the upconversion pair Yb^{3+} and Pr^{3+}. $NaYF_4$:$Yb_{18\,mol\,\%}$,$Pr_{2\,mol\,\%}$ @ $NaYF_4$ @ $NaYF_4$:$Er_{5\,mol\,\%}$ UCNPs were fabricated with a varying insulation layer thickness. In short, 2 mol % of Pr^{3+} doping is too little to observe sufficient Eu^{3+} luminescence quenching. But, it could be demonstrated, that Yb^{3+} did not quench the Eu^{3+} luminescence. Furthermore, it could be observed, that the UC emission exhibited the same trends as observed before in the sets Gd300 and Y300, but this time with 976 nm excitation (similar to Fig. 3.2, with increasing PL decay times as the insulation layer thickness increases). This could be related to the dilution of the Pr^{3+} and Yb^{3+} ions in the core.

3.1.4. Intermediate summary

As stated above, the Ln(III) migration is affected by various parameters. One of them, the insulation shell thickness, was investigated here. Small differences have been revealed, when the host lattice, the kind of dopants, or their concentration have been changed. In general, it was observed, that **the increasing insulation shell thickness leads to:**

(**1**) → decreasing acceptor numbers, which is related to the larger spatial donor-acceptor separation. (The Eu^{3+}/Nd^{3+} or Eu^{3+}/Pr^{3+} distance increases).

(**2**) → decreasing LRET efficiencies.

(**3**) → increasing Eu^{3+} PL decay times, although the initial decay times (τ_D in absence of the acceptor ions) are not reached again, which is independent of the insulation shell thickness.

(**4**) → increasing acceptor PL decay times, but trend-wise decreasing acceptor luminescence enhancement factors. In the case of thin insulation shells, a maximum of the luminescence enhancement can be observed.

The donor luminescence quenching cannot be suppressed completely, which potentially relates to the dissolution and recrystallization processes during the synthesis and which supports the Ln(III) migration effectively.

Furthermore, the correlation of the luminescence with the TEM data is mandatory in order to obtain reliable results. For instance, one of the sets investigated (but not explicitly shown) came out of the shell-growth synthesis with smaller diameter than the initially supplied cores. This indicates strongly, that the formation of core-shell particles did not work. In that case, the LRET equation does return values for the acceptor numbers, which are not reliable in terms of the applied model and the LRET equation. As a consequence, the combination of TEM and the LRET equation is necessary to keep proper indications for the Ln(III) migration and for the donor-acceptor separation by the insulation layer.

Parameters, that potentially affect the Ln(III) migration, are the *dopant concentration*, the *initial particle size* of the core (seed) particles, the *synthesis approach* (choice of precursors, reaction conditions), the *synthesis temperature*, potentially the *choice of the host lattice*, and the *kind of the dopants*. These parameters contribute to a distinct "migration pressure" and a concentration gradient of the dopants.

Table 3.2.: Comparison of acceptor numbers within a three-dimensional sphere with the Förster radii R_0(Eu/Nd) = 8.53 Å and R_0(Eu/Pr) = 8.2 Å.[105] The acceptor numbers are calculated based on the Eu^{3+} luminescence of the $^5D_0 \rightarrow {}^7F_2$ transition. *(Values from Refs. [98] and [100]).

Sample ID:	S0 CS L0 CS	S1 CSS	S2 CSS L1 CSS	S3 CSS L2 CSS	S4 CSS L2 CSS	S5 CSS L3 CSS	Ref CS
Set Nd300: $NaNdF_4$ @ $NaYF_4$ @ $NaYF_4$:$Eu_{[5\ mol\ \%]}$							
Insulation shell thicknes / nm	0	1.4	1.9	1.9	2.6		-/-
acceptor number (λ_{ex} = 465 nm)	9	4	3	3	2		0
Set Y300-old: $NaYF_4$:$Nd_{[20\ mol\ \%]}$ @ $NaYF_4$ @ $NaYF_4$:$Eu_{[5\ mol\ \%]}$							
Insulation shell thickness / nm	0	1.0	1.5	1.6	2.7	3.7	-/-
acceptor number (λ_{ex} = 465 nm)	1.8	1.09	0.94	0.99	0.81	0.61	0
Set Y300: $NaYF_4$:$Pr_{[20\ mol\ \%]}$ @ $NaYF_4$ @ $NaYF_4$:$Eu_{[5\ mol\ \%]}$							
Insulation shell thickness / nm	0		1.4	2.0		6.0	-/-
acceptor number (λ_{ex} = 465 nm)	1.4		1.1	1		0.5	0
Set Gd300: $NaGdF_4$:$Nd_{[20\ mol\ \%]}$ @ $NaGdF_4$ @ $NaGdF_4$:$Eu_{[5\ mol\ \%]}$							
Insulation shell thickness / nm	0		0.7		1.0	2.8	-/-
acceptor number (λ_{ex} = 465 nm)	1.9		1.1		0.6	0.4	0
Trends:			Layer thickness Acceptor number				

3.2. Phase Transfer and UCNP-to-Dye RET (Manuscript 3)

The manuscript 3 (section 2.4) deals with the transfer of UCNPs from the organic to the aqueous phase. Therefore, a subsequent surface modification has been realized to finally perform a resonance energy transfer (RET) from the UCNP (donor) to a dye (acceptor) (UCNP-to-dye RET). The UCNPs have been composed of $NaYF_4$:$Yb_{[18\,mol\,\%]}$, $Er_{[2\,mol\,\%]}$ core nanoparticles only, whereas the Er^{3+} ions doped into the UCNP serve as RET-donors. The RET-acceptor is the dye TAMRA immobilized on the UCNP. Prior to that, the UCNP surface was modified with the surface coating polymer abbreviated as CMP (PG-CatPh polymer). The CMP is a bio-inspired coating polymer combining mechanisms of blood-coagulation and of mussel protein adhesion. It has been used successfully for the first time to perform UCNP surface modification with subsequent coupling of a desired marker, here TAMRA.

Core-only UCNPs have been applied to obtain a homogeneous distribution of Ln(III) ions and to avoid the effect of Ln(III) ion migration, as well as keeping the donor-acceptor distance as small as possible. Although the protective shell of core-shell UCNPs leads to more brightness and an improved upconversion efficiency, the resonance energy transfer efficiency from the UCNP to the dye will suffer from the larger donor-acceptor distance. The UCNP surface modification itself increases the donor-acceptor distance as well. Previous experiments (see SI/appendix section S.2) revealed poor RET efficiency of core-shell UCNPs despite being brighter, which is in good agreement with reports in literature.[79,106]

After the phase transfer from the organic to the aqueous phase with the CMP-coating polymer, the particle sizes have been maintained. The particle diameters are found to be (11 ± 1) nm (by TEM) or (35 ± 10) nm (by DLS). The investigation with XRD revealed the hexagonal crystal phase of the flouride host, which is also confirmed by TRANES.*

The dye TAMRA is coupled via click-chemistry to the CMP-modified UCNP. The fluorescence emission of TAMRA fits well into the luminescence emission gap between the green and red PL emission of the Er^{3+} ion (compare Fig. 3 of manuscript 3).

The coupling is confirmed additionally by microscale thermosphoresis (MST). MST is a technique, that introduces a temperature gradient by a laser and simultaneously excites a fluorophore (TAMRA) with a diode, while the fluorescence signal is recorded with temporal resolution. The fluorescence intensity will decrease if the fluorophore

*TRANES = time-resolved area-normalized emission spectroscopy is a spectroscopic tool to reveal the existence of multiple emissive species. E.g., if the cubic and the hexagonal phase are present in one sample, the luminescence peak ratios will change significantly over time. If only one emissive species is present, the luminescence peak ratios will be constant over time.

diffuses out of the hot spot (observation volume). The uncoupled TAMRA diffuses quickly out of the observation volume and the fluorescence signal decreases fast. The TAMRA coupled to the UCNP diffuses slowly out of the observation volume, as the UCNP acts like a chain ball and the fluorescence signal decreases more slowly than before. The MST-experiment is reported in manuscript 3 (section 2.4, Fig. 4). Prior to that, a similar system had been investigated with MST, whose results are reported in the SI/appendix subsection S.2.2, Fig. S.5.

It is worthy to spend a closer look at the CMP-capped UCNP PL emission. The expected green and red luminescence peaks of Er^{3+} doped UCNPs can be observed clearly (in Fig. 3 (b) of manuscript 3, G1 @ 520 nm, G2 @ 540 nm, and R @ 650 nm, respectively, with λ_{ex} = 976 nm). The UCNP PL emission intensity and the PL decay time decrease due to the phase transfer into the aqueous phase and the water's strong PL quenching ability. After conjugation with TAMRA, the green UCNP PL emission decreases. This decrease could be attributed to the UCNP-to-TAMRA RET and can be seen in Fig. 3 (b), in which the PL spectra are normalized to the red PL emission. The red PL emission does not take part in the RET due to the lack of spectral overlap (compare Fig. 3 (a)).

The TAMRA conjugated and CMP capped UCNPs have been dispersed in water and in MOPS buffer, which does not reveal significant differences in terms of luminescence emission (compare TAMRA PL emission at 580–600 nm in the inset of Fig. 3 (b), with λ_{ex} = 976 nm). The observed TAMRA fluorescence indicates sensitization either via UCNP-to-dye RET or via a trivial reabsorption mechanism, as TAMRA is not excited in NIR (which was also tested). The TAMRA PL decay time has increased by a factor of 9500 from 2.3 ns up to 22 µs for free and for UCNP-coupled TAMRA, respectively (see Fig. 3 (d) for the respective PL decay curves).

Interestingly, the green and the red UCNP PL decay time increased after the UCNP had been coupled TAMRA, although the opposite effect had been expected, as the acceptor should quench the donor luminescence and shorten its PL decay time.

Two ideas are possible. The first one considers the effective encapsulation properties of the coating polymer CMP. The polymer ligand crosslinks on the UCNP surface, prevents water molecules from accessing the surface, and prevents the UCNP from PL quenching. This ability results from the CMP that creates a cage-like system around the UCNP. Hence, it also prevents ligand detachment or exchange reactions, that might occur due to dilution effects. The crosslinking needs a certain amount of time. This time span was potentially too short for the investigated sample. Accordingly, the crosslinking reaction continued during storing and during the conjugation with TAMRA. The

powerful encapsulation properties of CMP shall be emphasized with an example of a lucky coincidence: One CMP-encapsulated UCNP sample was stored in a fridge for three years. After that period, this sample still possessed sufficient upconversion luminescence for potential application.

The second idea relates to the Er-to-TAMRA RET. As indicated above, only core UCNPs had been used. However, the modification with the RET-acceptor TAMRA might lead to two Er^{3+} emitting species. The two species might be considered as "bulk phase" (inner) and "surface" (outer) Er^{3+} ions. The surface Er^{3+} ions decay already faster due to surface quenching. With the presence of the RET, their UC luminescence is quenched *additionally*. These ions receive an additional non-radiative deactivation pathway from the surface Er^{3+} point of view. In contrast to that, the "bulk phase" Er^{3+} ions are neither influenced by surface quenching nor by RET due to the distance dependency. If this assumption holds true and the "surface" Er^{3+} ions are quenched very effectively by UCNP-to-TAMRA RET (plus surface quenching), their proportion on the total PL decay time of the UCNP will decrease. In contrast to that, the proportion of the "bulk phase" Er^{3+} on the total PL decay time will increase. This results in increasing fractions of the luminescence for the already longer emitting "bulk phase" Er^{3+} ions. Therefore, the total UCNP luminescence decay time increases. The UC luminescence of Yb-Er doped UCNPs (with and without being coupled with TAMRA) shows more than one PL decay time component, which could be attributed to these "bulk phase" and "surface" Er^{3+} ions.

Previous investigations dealing with the dopant distribution within a UCNP system and indicating a significant role for the RET efficiency can be found in literature. [79,106,107] A brief overview of possible core-shell UCNP designs is given in Fig. 3.3. Fig. 3.3 (a) shows an active core design (AC) with a homogeneous distribution of sensitizer and activator ions within the core-only UCNPs. It has been found, that small-sized and core-only UCNPs already increase the RET efficiency of UCNPs to acceptors (like dyes or QDs[†]), because the donors (the activator ions in the UCNP) and the acceptors are in closer proximity than for active core-inert shell UCNP structures. The active core-inert shell design (AC-IC) is illustrated in (b). Indeed, the donor quantum yield of AC-IC UCNPs is higher than for core-only UCNPs. However, the donor-acceptor distance increases significantly and the possibility of the activators being near an acceptor decreases.[79] Therefore, also the size affects the RET efficiency, as smaller nanoparticles exhibit higher surface-to-volume ratios and the possibility of surface-located activators (RET-donors) increases.[106]

[†]quantum dot

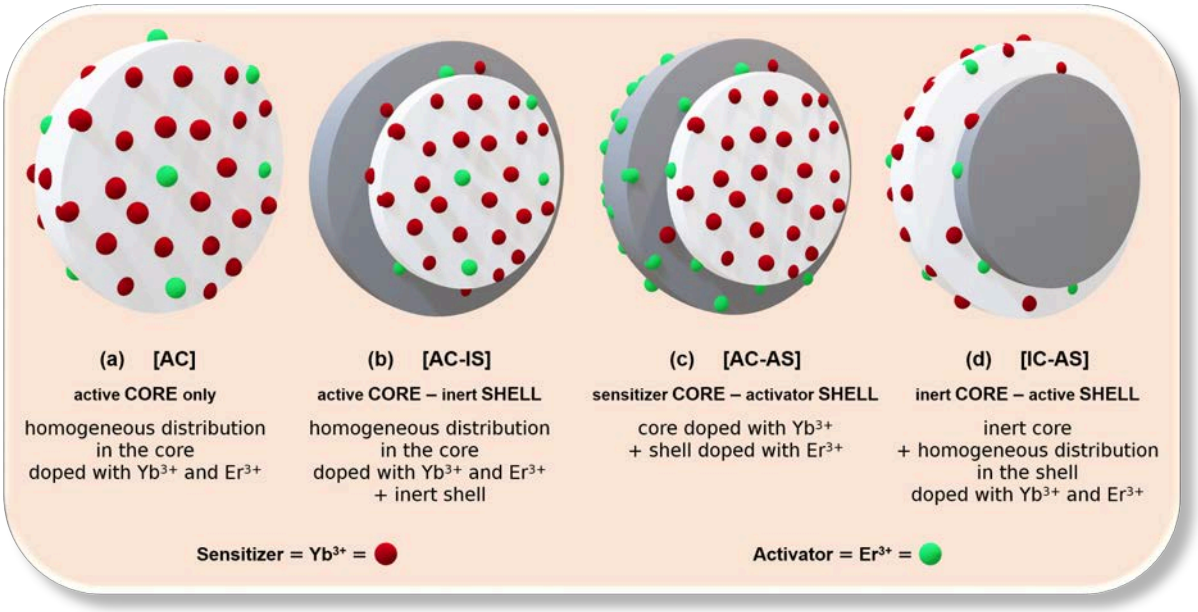

Figure 3.3.: Illustration of possible UCNP designs for enhancing RET efficiency. (a) active core (AC) corresponds to the design applied in manuscript 3 (section 2.4). (b) active core–inert shell (AC-IS), aiming at higher donor luminescence intensity. (c) sensitizer doped core–activator doped shell considered as active core–active shell (AC-AS), aiming at energy migration confinement and increasing the number of surface RET-donors. (d) inert core–active shell (IC-AS), aiming at energy migration exclusively in the outer shell and increasing the number of surface RET-donors. (The sensitizer is dark red for Yb^{3+} ions. The activator is green for Er^{3+} ions. The host lattice (e.g., $NaYF_4$) is presented in light grey (doped) and dark grey (undoped), except for (c), in which the sensitizer and activator are separated by doping in the core and the shell, respectively).

In case of the AC-IC design (b), the passivating shell cannot passivate perfectly (if so, no RET would be observable), which potentially relates to the previously discussed Ln(III) migration. The sensitizer and activator ions diffuse from the core into the inert shell. Furthermore, RET, FRET, and LRET are all very similar (same theory is used) and are long range energy transfer mechanisms (up to 7 times the Förster distance within the nanocrystal, discussed above, or up to 20 nm in solution[67]). A shell adds up to the donor-acceptor distance and decreases RET rates.

The designs in Fig. 3.3 (c) and (d) aim at high amounts of near surface activator ions (high RET-donor surface concentration) in order to decrease the donor-acceptor distance. As a consequence, the RET efficiency increases. In case of (c), all sensitizers are located in the core and all activators are located in the outer shell (sensitizer core - activator shell, AC-AS for active core-active shell). In case of (d) with an inert core-active shell (IC-AS), the sensitizers and activators are located in the outer shell. Apparently, both designs can be favorable to increase the RET efficiency as long as the outer shell does not grow too thick. This also requires a synthesis approach, that reduces the extent of Ln(III) migration to a minimum. In the best case, the chosen design is realized

and the RET-donor is confined in the outer UCNP shell only.

However, the latter IC-AS design is found to be more effective.[79,107] This can be related to the confinement of the absorbed NIR photon energy, which is only distributed within the shell.

In the case of (c), AC-AS design, the NIR photons are absorbed in the core mainly and the sensitizers are protected from surface quenching. However, the absorbed energy needs to be transferred to the activator ions (donors) in the outer shell prior to perform RET. Two drawbacks come up with the AC-AS design. First, the sensitizer ions in the core could transfer the energy among themselves until the sensitizers deactivate non-radiatively. Accordingly, the energy will be lost for RET. Second, there is only a small interface of the core and the outer shell, which allows the LRET from sensitizer to activator. Here, the Ln(III) migration comes into play again. The migration potentially increases the interface of sensitizers and activators. The sensitizer ions are able to migrate into the outer shell and the activator ions are able to migrate from the outer shell into the core. Fig. 3.3 (c) hints slightly at this Ln(III) intermixing by putting one green Er^{3+} ion into the core and some dark red Yb^{3+} ions in the shell. According to the presented design, the respective ions belong in the shell (Er^{3+}) and the core (Yb^{3+}), only. But in this case, the Ln(III) intermixing of core-shell structures could be favorable up to a certain extent to increase the RET efficiency, as the sensitizer-activator interface increases. Accordingly, the upconversion efficiency of this UCNP design could already be a limiting factor for highest RET efficiencies.

A possible work-around for that issue could be a combination of the designs (c) and (d), which is not shown, but in which the sensitizers are doped into the core and into the shell, and the activators are doped into the shell only.[106] With the mixed AC-AS/IC-AS design, a high absorption cross-section can be realized, a good LRET efficiency for the upconversion process becomes possible, and a high RET-donor surface concentration is achieved. The performance of all these designs in comparison to each other could be potential future work to create high UCNP-based RET (or FRET) probes.

3.2.1. The green Eu^{3+} luminescence and the TAMRA dye fluorescence

During the experiments for manuscript 3, the question arose, which energy level of the Er^{3+} green PL emission is the main source for UCNP-to-TAMRA RET? It can be either the G1 emission band ($^2H_{11/2} \rightarrow {}^4I_{15/2}$ transition) @ 520 nm or the G2 emission band ($^4S_{3/2} \rightarrow {}^4I_{15/2}$ transition) @ 540 nm. The two energy states $^2H_{11/2}$ (G1) and $^4S_{3/2}$ (G2) are thermally coupled.

The main source of the energy transfer is certainly the G2 emission, because the

TAMRA PL emission is visible at temperatures below 100 K, at which the G1 emission is absent and below the limit of detection. As soon as the G1 emission appears with temperatures larger than 100 K, the thermal population of the G1 energy state ($^2H_{11/2}$) competes with the RET to TAMRA, both depopulating the G2 energy state ($^4S_{3/2}$). However, it could not be determined with the performed experiments up to which extent the G1 energy state ($^2H_{11/2}$) does or does not contribute to the TAMRA excitation.

The assumption of G2 being the major donor energy state for the RET is based on the luminescence intensity ratios of the respective emission bands. The low temperature measurements range from 50 K to 200 K and demonstrate, that the UC efficiency is low at low temperatures. But, the UC efficiency increases as the temperature increases. The luminescence intensity ratio of the TAMRA and G2 emission ("TAMRA / G2") increases as well up to 100 K (see Fig. 6 in manuscript 3, section 2.4). The luminescence intensity ratio increases upon temperature increase. Additionally, this ratio increase reveals a stronger temperature dependency of the TAMRA PL emission intensity than of the "G2 emission" intensity. Consequently, the increasing luminescence intensity ratio (as the temperature increases) indicates an increasing RET efficiency from the G2 ($^4S_{3/2} \rightarrow {}^4I_{15/2}$ transition) to the dye TAMRA.

In contrast to that, the luminescence intensity ratio of the TAMRA and G1 emission ("TAMRA / G1") decreases with increasing temperature. This might correlate with the fact, that the G1 energy state is more effectively populated due to the thermal coupling of G1 and G2 than the G2-to-TAMRA RET. As the "G1 emission" intensity increases faster than the TAMRA PL intensity, the contribution of G1-to-TAMRA RET might also be small.

4

Outlook & Perspectives

In the previous chapter the investigation of the Ln(III) ion migration in the $NaYF_4$ and $NaGdF_4$ host lattices based on spectroscopic methods was discussed, which was not realized in that way before. The interlanthanoid resonance energy transfer from Eu^{3+} ions (LRET-donors) to Nd^{3+} ions or Pr^{3+} ions (LRET-acceptors) has been used as a tool, to determine the extent of the Ln(III) migration within the nanoparticle. The acceptors were doped in the core with the doping amount often used for UCNPs (being 20 mol %). A first shell served as spatial separator for the acceptors and the donors. The donors were doped in a second (outer) shell.

It was found, that the luminescence quenching of the Eu^{3+} ions could not be suppressed completely, even when the insulation shell thickness exceeded the respective Förster radii for the LRET-pairs, Eu/Nd and Eu/Pr, by more than four times and seven times, respectively. Nevertheless, the insulation shell thickness affected the migration of the Ln(III) ions. The calculated acceptor numbers, that are calculated based on the Eu-donor luminescence, decrease as the insulation shell thickness increases.

Furthermore, the acceptor luminescence has been investigated for the first time in this field. An increase of the acceptor luminescence decay times was expected, but was not observed in the first place, as the acceptors suffered from concentration related self-quenching. The self-quenching decreases with increasing insulation shell thickness. Accordingly, the acceptor luminescence decay times increase with increasing insulation shell thickness. This observation is counter intuitive, as LRET efficiency decreases clearly (based on the donor luminescence). The explanation is found in the luminescence enhancement factors of the acceptor luminescence decay times. The factors exhibit a maximum for thin insulation shells indicating that the concentration related self-quenching dominates the LRET sensitization.

These investigations can be further evaluated, as there are several parameters, that influence the Ln(III) migration. The formation of concentration gradients depends not only on the synthesis approach, synthesis temperature, and on the initial particle size, but also on the initial concentration of the dopants.[51,55,56,58] The influence of the

latter two was confirmed in this work. The influence of the synthesis conditions has not been investigated as the conditions were kept constant.

The laser-spectroscopic approach in combination with TEM is a powerful tool to calculate a diffusion length for different synthesis strategies in the future. The diffusion length as a property of different synthesis strategies, with exactly defined synthesis conditions and particular precursors, can help researchers to realize a desired nanoparticle design.

The synthesis conditions influence the migration and the crystallization dynamics as indicated above. Besides different temperatures, the usage of a sacrificial nanoparticle strategy or of a precursor decomposition strategy can be investigated and compared. It has already been reported, that different concentration gradients are found for these two strategies.[55] The investigation of nanoparticles synthesized via different strategies has not been realized yet with the LRET equation. In addition to this, different decomposition precursors could be included in the studies. With these investigations, the diffusion length property could be used to describe potential outcomes of different synthesis strategies.

Further research interest in the Ln(III) migration can be realized by e.g., changing the host lattice, which introduces lattice mismatches between the core and shell structures. Some pioneering work has already been realized by applying a CaF_2 outer shell, that suppresses the trivalent ion exchange.[51] This approach changes drastically the host lattice's nature of $NaREF_4$ (RE = trivalent rare earth ions) and also changes the oxidation state of the lattice cations from +1 (Na) and +3 (RE) to +2 (Ca). The passivation with CaF_2 could be favorable for supplying bright optical probes. This could be realized with an SiO_2 shell as well. Although both shells could hinder an energy transfer in FRET/RET applications, these shells provide a powerful basis for further bio-conjugation.

Whenever the presented analysis approach (using the LRET equation) is chosen to investigate the Ln(III) migration, an appropriate synthesis strategy shall be used. It is mandatory for the investigation, that the applied shell precursors grow homogeneously on the provided cores/seeds. The formation of "empty" shells / hollow spheres, that do not include the $NaREF_4$ nanoparticles, must be avoided. If no homogeneously covered nanoparticles are obtained, the strategy for investigating the system with the here-presented spectroscopic approach in combination with the LRET equation and TEM will have to be adapted.

The presented research generated the idea of using different trivalent cations in the fluoride host lattices of core and shell in order to introduce a small lattice mismatch and to investigate the effect on the Ln(III) migration. E.g., $NaGdF_4$ or $NaScF_4$ cores

doped with LRET-acceptors can be equipped with $NaYF_4$ based shells. The Ln(III) migration and the resulting concentration gradient can be affected. First experiments have already been performed in our group. The Ln(III) migration is observed and will be further evaluated.

Overall, the core-shell structures are an important tool to improve the UCNP up-conversion luminescence. Better understanding of either how to suppress or how to guide ion migration will surely result in better performance of UCNPs for the desired application, which can range from the bio-medical field to the technical-industrial field.

The bio-medical field has been touched with the UCNP-to-dye RET research presented in the last manuscript of the previous chapter, which can be ascribed to the sustainable development goal SDG #3.[3] Indeed, there will be a long way to realize early detection and treatment of diseases.

The outstanding encapsulation properties of the CMP coating polymer present a contribution to this higher goal. The CMP mimics mechanisms of mussel food proteins and of blood coagulation. The CMP coating polymer performed extraordinary well for the UCNP encapsulation. The CMP prevented the $NaYF_4$ core-only UCNPs doped with Yb^{3+} and Er^{3+} very effectively from coagulation and it formed an efficient polymer layer on the UCNP surface suppressing undesired luminescence quenching by solvent. Moreover, it can be further functionalized with a desired bio-functional group rendering the CMP encapsulated UCNP into a suiting tool-box for various applications in the biological field.

The relatively fast coupling reaction of the dye (TAMRA) with the CMP-capped UCNPs has been realized via click-chemistry. The CMP was equipped with an azide group and the dye with an alkyne group. The coupled system was investigated by laser spectroscopy and the Er-to-dye RET could be observed. The coupling was examined by MST, which has been one of the first published investigations on UCNPs with that technique.

It is out of question, that UCNPs exhibit unique properties with the ability to absorb NIR photons and upconvert those into higher energy photons of the Vis/UV spectral range. Due to this ability, the application of UCNPs promises bio-applications with better signal-to-noise ratios and less photodamage of bio-samples. However, there are still parameters, that need to be investigated, e.g., the performance of CMP-encapsulated UCNPs not only in buffers, but also in more realistic biological systems. This includes the evaluation of bio-compatibility and at potentially later stages e.g., evaluation of immunologic reactions, protein adsorption under physiological conditions, and body

clearance times.

In addition to the physiological point of view, there is still potential for increasing the RET efficiency by applying better suiting UCNP structures just like designs with higher RET-donor concentration on the UCNP surface, e.g., inert core-active shell or active core-active shell structures. The UCNP-to-acceptor (dye, QD, other probes) RET should be enhanced to a maximum instead of achieving the maximum upconversion luminescence intensity from the nanoparticles. This could be realized by enhancing particular emission bands of the activator via intended Ln(III) migration, nanoparticle design, and excitation power density. The experience from the Ln(III) migration with different synthesis approaches can help to favor the RET instead of increasing the UCNP brightness.

Some final ambiguous applications referring to the UCNPs in a biological environment can be related to the fabrication of UV/Vis light triggered drug release agents, which can be based on cis-trans isomerization (e.g., azo-benzenes) or on bond cleavage (e.g., spirocyclic molecules).[108,109] These mechanisms can be triggered in the NIR spectral range with help of UCNPs. Other possible drug release systems can be based on liposome interactions with UCNPs.[110] Moreover, the UCNP-to-dye RET can be applied in photodynamic therapy for cancer treatment.[96,111] The UCNPs can be surface modified, so that absorbed photon energy is transferred to a coupled singlet oxygen producing dye. The UCNP/dye system can be turned toxic and non-toxic, like a switch, by the NIR irradiation. Further surface functionalization needs to be realized to additionally introduce specific bio-recognition elements on the UCNP/dye surface. Thus, the particles accumulate at the specific target (e.g., cancer cells) and the singlet oxygen can be produced only locally in combination with the NIR irradiation. This idea will need profound revision by the specialists and further evaluation. Future questions will surely be: How can the UCNP-based photodynamic therapy be implemented realistically? Would this technique be a complementary therapy? Can this technique even serve as a replacement for chemo- or radiation therapy?

Regarding the considerations above, the upconversion process, the upconversion nanoparticles, and the NIR radiation offer a number of interesting bio-applications.

5

Bibliography

[1] Deutsche Physikalische Gesellschaft e.V., Deutsche UNESCO-Kommission e.V., „2015 Internationales Jahr des Lichtes und der Lichttechnologie – Die Deutschen Aktivitäten“, 2015, http://www.jahr-des-lichts.de/, Accessed 23. Apr. 2021.

[2] International Union of Pure and Applied Chemistry, prepared for publication by N. G. Connelly, T. Damhus, R. M. Hartshorn, A.T. Hutton, *Nomenclature of Inorganic Chemistry, IUPAC Recommendations 2005, IUPAC Red Book*, The Royal Society of Chemistry, 2005.

[3] United Nations, „Sustainable Development Goals – 17 Goals to Transform Our World“, 2016, https://sdgs.un.org/goals and https://www.un.org/ sustainabledevelopment/, Accessed 26. Apr. 2021.

[4] Wissenschaftlicher Beirat der Bundesregierung Globale Umweltveränderungen, *Welt im Wandel: Energiewende zur Nachhaltigkeit*, Springer-Verlag Berlin Heidelberg New York, 2003.

[5] K. Deng, T. Gong, L. Hu, X. Wei, Y. Chen, M. Yin, „Efficient Near-Infrared Quantum Cutting in $NaYF_4$: Ho^{3+}, Yb^{3+} for Solar Photovoltaics“, *Optics Express* **19**, 1749 (2011).

[6] R. Martín-Rodríguez, S. Fischer, A. Ivaturi, B. Froehlich, K. W. Krämer, J. C. Goldschmidt, B. S. Richards, A. Meijerink, „Highly Efficient IR to NIR Upconversion in Gd_2O_2S: Er^{3+} for Photovoltaic Applications“, *Chemistry of Materials* **25**, 1912–1921 (2013).

[7] X. Wei, S. Huang, Y. Chen, C. Guo, M. Yin, W. Xu, „Energy Transfer Mechanisms in Yb^{3+} Doped YVO_4 Near-Infrared Downconversion Phosphor“, *Journal of Applied Physics* **107** (2010).

[8] D. C. Yu, R. Martín-Rodríguez, Q. Y. Zhang, A. Meijerink, F. T. Rabouw, „Multi-Photon Quantum Cutting in $Gd_2O_2S:Tm^{3+}$ to Enhance the Photo-Response of Solar Cells“, *Light: Science and Applications* **4**, 1–8 (2015).

[9] T. C. Liu, G. Zhang, X. Qiao, J. Wang, H. J. Seo, D. P. Tsai, R. S. Liu, „Near-Infrared Quantum Cutting Platform in Thermally Stable Phosphate Phosphors for Solar Cells“, *Inorganic Chemistry* **52**, 7352–7357 (2013).

[10] X. Luo, T. Ding, X. Liu, Y. Liu, K. Wu, „Quantum-Cutting Luminescent Solar Concentrators Using Ytterbium-Doped Perovskite Nanocrystals“, *Nano Letters* **19**, 338–341 (2019).

[11] BMBF – Bundesministerium für Bildung und Forschung, „Aktionsplan Individualisierte Medizin“, 2013.

[12] Q. Liu, Y. Sun, T. Yang, W. Feng, C. Li, F. Li, „Sub-10 nm Hexagonal Lanthanide-Doped $NaLuF_4$ Upconversion Nanocrystals for Sensitive Bioimaging in Vivo“, *Journal of the American Chemical Society* **133**, 17122–17125 (2011).

[13] M. Meinhardt, R. Krebs, A. Anders, U. Heinrich, H. Tronnier, „Wavelength-Dependent Penetration Depths of Ultraviolet Radiation in Human Skin“, *Journal of Biomedical Optics* **13**, 044030 (2008).

[14] Q. Liu, W. Feng, F. Li, „Water-Soluble Lanthanide Upconversion Nanophosphors: Synthesis and Bioimaging Applications in Vivo“, *Coordination Chemistry Reviews* **273-274**, 100–110 (2014).

[15] A. Nsubuga, K. Zarschler, M. Sgarzi, B. Graham, H. Stephan, T. Joshi, „Towards Utilising Photocrosslinking of Polydiacetylenes for the Preparation of “Stealth” Upconverting Nanoparticles“, *Angewandte Chemie - International Edition* **57**, 16036–16040 (2018).

[16] T. G. Phan, A. Bullen, „Practical Intravital Two-Photon Microscopy for Immunological Research: Faster, Brighter, Deeper.“, *Immunology and cell biology* **88**, 438–444 (2010).

[17] L. A. Sordillo, Y. Pu, S. Pratavieira, Y. Budansky, R. R. Alfano, „Deep Optical Imaging of Tissue Using the Second and Third Near-Infrared Spectral Windows“, *Journal of Biomedical Optics* **19**, 056004 (2014).

[18] A. N. Bashkatov, E. A. Genina, M. D. Kozintseva, V. I. Kochubei, S. Y. Gorodkov, V. V. Tuchin, „Optical Properties of Peritoneal Biological Tissues in the Spectral Range of 350–2500 nm“, *Optics and Spectroscopy* **120**, 1–8 (2016).

[19] N. Hildebrandt, L. J. Charbonnière, M. Beck, R. F. Ziessel, H. G. Löhmannsröben, „Quantum Dots as Efficient Energy Acceptors in a Time-Resolved Fluoroimmunoassay“, *Angewandte Chemie - International Edition* **44**, 7612–7615 (2005).

[20] L. J. Charbonnière, N. Hildebrandt, R. F. Ziessel, H. G. Löhmannsröben, „Lanthanides to Quantum Dots Resonance Energy Transfer in Time-Resolved Fluoro-Immunoassays and Luminescence Microscopy“, *Journal of the American Chemical Society* **128**, 12800–12809 (2006).

[21] W. R. Algar, D. Wegner, A. L. Huston, J. B. Blanco-Canosa, M. H. Stewart, A. Armstrong, P. E. Dawson, N. Hildebrandt, I. L. Medintz, „Quantum Dots as Simultaneous Acceptors and Donors in Time-Gated Förster Resonance Energy Transfer Relays: Characterization and Biosensing“, *Journal of the American Chemical Society* **134**, 1876–1891 (2012).

[22] K. D. Wegner, N. Hildebrandt, „Quantum Dots: Bright and Versatile in Vitro and in Vivo Fluorescence Imaging Biosensors“, *Chemical Society Reviews* **44**, 4792–4834 (2015).

[23] N. Hildebrandt, C. M. Spillmann, W. Russ Algar, T. Pons, M. H. Stewart, E. Oh, K. Susumu, S. A. Díaz, J. B. Delehanty, I. L. Medintz, „Energy Transfer with Semiconductor Quantum Dot Bioconjugates: A Versatile Platform for Biosensing, Energy Harvesting, and Other Developing Applications“, *Chemical Reviews* **117**, 536–711 (2017).

[24] Y. Zhang, Y. Shen, M. Liu, Y. Han, X. Mo, R. Jiang, Z. Lei, Z. Liu, F. Shi, W. Qin, „Enhanced High-Order Ultraviolet Upconversion Luminescence in sub-20 nm β-$NaYbF_4$:0.5Doping“, *CrystEngComm* **19**, 1304–1310 (2017).

[25] P. Villanueva-Delgado, K. W. Krämer, R. Valiente, M. de Jong, A. Meijerink, „Modeling Blue to UV Upconversion in β-$NaYF_4$:Tm^{3+}“, *Phys. Chem. Chem. Phys.* **18**, 27396–27404 (2016).

[26] W. Song, X. Guo, G. He, W. Qin, „Ultraviolet Upconversion Emissions of Gd^{3+} in β-$NaLuF_4$:Yb^{3+},Tm^{3+},Gd^{3+} Nanocrystals“, *Journal of Nanoscience and Nanotechnology* **14**, 3722–3725 (2014).

[27] J. Shen, G. Chen, T. Y. Ohulchanskyy, S. J. Kesseli, S. Buchholz, Z. Li, P. N. Prasad, G. Han, „Tunable Near Infrared to Ultraviolet Upconversion Luminescence Enhancement in (α-$NaYF_4$:Yb,Tm)/CaF_4 Core/Shell Nanoparticles for in Situ Real-Time Recorded Biocompatible Photoactivation“, *Small* **9**, 3213–3217 (2013).

[28] P. W. Atkins, J. de Paula, *Physikalische Chemie, vierte, vollständig überarbeitete Auflage*, WILEY-VCH Verlag, 2006.

[29] A. Sedlmeier, H. H. Gorris, „Surface Modification and Characterization of Photon-Upconverting nanoparticles for Bioanalytical Applications“, *Chem. Soc. Rev.* **44**, 1526–1560 (2015).

[30] G. Chen, H. Qiu, P. N. Prasad, X. Chen, „Upconversion Nanoparticles: Design, Nanochemistry, and Applications in Theranostics“, *Chemical Reviews* **114**, 5161–5214 (2014).

[31] G. H. Dieke, H. M. Crosswhite, „The Spectra of the Doubly and Triply Ionized Rare Earths“, *Applied Optics* **2**, 675–686 (1963).

[32] R. T. Wegh, A. Meijerink, R.-J. Lamminmäki, J. Höslä, „Extending Dieke's Diagram“, *Journal of Luminescence* **87-89**, 1002–1004 (2000).

[33] F. Auzel, „Upconversion and Anti-Stokes Processes with f and d Ions in Solids“, *Chemical Reviews* **104**, 139–173 (2004).

[34] N. Bloembergen, „Solid State Infrared Quantum Counters“, *Physical Review Letters* **2**, 84–85 (1959).

[35] G. Liu, „Advances in the Theoretical Understanding of Photon Upconversion in Rare-Earth Activated Nanophosphors“, *Chemical Society Reviews* **44**, 1635–1652 (2015).

[36] J. Zhao, Z. Lu, Y. Yin, C. McRae, J. A. Piper, J. M. Dawes, D. Jin, E. M. Goldys, „Upconversion Luminescence with Tunable Lifetime in $NaYF_4$:Yb,Er Nanocrystals: Role of Nanocrystal Size“, *Nanoscale* **5**, 944–952 (2013).

[37] O. Ehlert, R. Thomann, M. Darbandi, T. Nann, „A Four-Color Colloidal Multiplexing Nanoparticle System“, *ACS Nano* **2**, 120–124 (2008).

[38] S. Hao, W. Shao, H. Qiu, Y. Shang, R. Fan, X. Guo, L. Zhao, G. Chen, C. Yang, „Tuning the Size and Upconversion Emission of $NaYF_4$:Yb^{3+}/Pr^{3+} Nanoparticles Through Yb^{3+} Doping“, *RSC Advances* **4**, 56302–56306 (2014).

[39] M. Quintanilla, F. Ren, D. Ma, F. Vetrone, „Light Management in Upconverting Nanoparticles: Ultrasmall Core/Shell Architectures to Tune the Emission Color“, *ACS Photonics* **1**, 662–669 (2014).

[40] M. Kaiser, C. Würth, M. Kraft, I. Hyppänen, T. Soukka, U. Resch-Genger, „Power-Dependent Upconversion Quantum Yield of $NaYF_4$:Yb^{3+},Er^{3+} Nano- and Micrometer-Sized Particles – Measurements and Simulations“, *Nanoscale* **9**, 10051–10058 (2017).

[41] C. Würth, M. Kaiser, S. Wilhelm, B. Grauel, T. Hirsch, U. Resch-Genger, „Excitation Power Dependent Population Pathways and Absolute Quantum Yields of Upconversion Nanoparticles in Different Solvents“, *Nanoscale* **9**, 4283–4294 (2017).

[42] M. Kraft, C. Würth, V. Muhr, T. Hirsch, U. Resch-Genger, „Particle-Size-Dependent Upconversion Luminescence of $NaYF_4$: Yb,Er Nanoparticles in Organic Solvents and Water at Different Excitation Power Densities“, *Nano Research* **11**, 6360–6374 (2018).

[43] M. T. Berry, P. S. May, „Disputed Mechanism for NIR-to-Red Upconversion Luminescence in $NaYF_4$:Yb^{3+},Er^{3+}“, *Journal of Physical Chemistry A* **119**, 9805–9811 (2015).

[44] W. Yan, Q. Weiping, Z. Jisen, C. Chunyan, Z. Jishuang, J. Ye, „Synthesis and Upconversion Luminescence of LaF_3: Yb^{3+}, Er^{3+}/SiO_2 Core/Shell Microcrystals“, *Journal of Rare Earths* **25**, 605–608 (2007).

[45] G. S. Yi, G. M. Chow, „Water-Soluble $NaYF_4$:Yb,Er(Tm)/$NaYF_4$/Polymer Core/Shell/Shell Nanoparticles with Significant Enhancement of Upconversion Fluorescence“, *Chemistry of Materials* **19**, 341–343 (2007).

[46] F. T. Rabouw, P. T. Prins, P. Villanueva-Delgado, M. Castelijns, R. G. Geitenbeek, A. Meijerink, „Quenching Pathways in $NaYF_4$:Er^{3+},Yb^{3+} Upconversion Nanocrystals“, *ACS Nano* **12**, 4812–4823 (2018).

[47] R. Arppe, I. Hyppänen, N. Perälä, R. Peltomaa, M. Kaiser, C. Würth, S. Christ, U. Resch-Genger, M. Schäferling, T. Soukka, „Quenching of the Upconversion

Luminescence of $NaYF_4$:Yb^{3+},Er^{3+} and $NaYF_4$:Yb^{3+} ,Tm^{3+} Nanophosphors by Water: The Role of the Sensitizer Yb^{3+} in Non-Radiative Relaxation“, *Nanoscale* **7**, 11746–11757 (2015).

[48] M. Y. Hossan, A. Hor, Q. Luu, S. J. Smith, P. S. May, M. T. Berry, „Explaining the Nanoscale Effect in the Upconversion Dynamics of β-$NaYF_4$:Yb^{3+}, Er^{3+} Core and Core-Shell Nanocrystals“, *Journal of Physical Chemistry C* **121**, 16592–16606 (2017).

[49] R. Wu, L. Lei, S. Zhang, Z. Xiao, J. Zhang, S. Xu, „Promote the Threshold of Tm^{3+} Concentration Using an Inert-Core/Active-Shell Structure“, *J. Mater. Chem. C* **4**, 9183–9186 (2016).

[50] X. Wu, S. Zhan, J. Han, Y. Liu, „Nanoscale Ultrasensitive Temperature Sensing Based on Upconversion Nanoparticles with Lattice Self-Adaptation“, *Nano Lett.* (2020).

[51] H. Dong, L. D. Sun, L. D. Li, R. Si, R. Liu, C. H. Yan, „Selective Cation Exchange Enabled Growth of Lanthanide Core/Shell Nanoparticles with Dissimilar Structure“, *Journal of the American Chemical Society* **139**, 18492–18495 (2017).

[52] D. Hudry, D. Busko, R. Popescu, D. Gerthsen, A. M. M. Abeykoon, C. Kübel, T. Bergfeldt, B. S. Richards, „Direct Evidence of Significant Cation Intermixing in Upconverting Core@Shell Nanocrystals: Toward a New Crystallochemical Model“, *Chemistry of Materials* **29**, 9238–9246 (2017).

[53] D. Hudry, R. Popescu, M. Diaz-Lopez, A. M. M. Abeykoon, P. Bordet, D. Gerthsen, I. A. Howard, B. S. Richards, „Interface Disorder in Large Single- and Multi-Shell Upconverting Nanocrystals“, *Journal of Materials Chemistry C* **7**, 1164–1172 (2019).

[54] D. Hudry, I. A. Howard, R. Popescu, D. Gerthsen, B. S. Richards, „Structure–Property Relationships in Lanthanide-Doped Upconverting Nanocrystals: Recent Advances in Understanding Core–Shell Structures“, *Advanced Materials* **31**, 1900623 (2019).

[55] S. Dühnen, M. Haase, „Study on the Intermixing of Core and Shell in $NaEuF_4$/$NaGdF_4$ Core/Shell Nanocrystals“, *Chemistry of Materials* **27**, 8375–8386 (2015).

[56] L. Liu, X. Li, Y. Fan, C. Wang, A. M. El-Toni, M. S. Alhoshan, D. Zhao, F. Zhang, „Elemental Migration in Core/Shell Structured Lanthanide Doped Nanoparticles“, *Chemistry of Materials* **31**, 5608–5615 (2019).

[57] E. Hofman, R. J. Robinson, Z. J. Li, B. Dzikovski, W. Zheng, „Controlled Dopant Migration in CdS/ZnS Core/Shell Quantum Dots“, *Journal of the American Chemical Society* **139**, 8878–8885 (2017).

[58] D. Liu, X. Xu, Y. Du, X. Qin, Y. Zhang, C. Ma, S. Wen, W. Ren, E. M. Goldys, J. A. Piper, S. Dou, X. Liu, D. Jin, „Three-Dimensional Controlled Growth of Monodisperse sub-50 nm Heterogeneous Nanocrystals“, *Nature Communications* **7**, 10254 (2016).

[59] D. Hudry, D. Busko, R. Popescu, D. Gerthsen, I. A. Howard, B. S. Richards, „An Enhanced Energy Migration Strategy in Upconverting Nanocrystals: Color-Tuning with High Quantum Yield“, *Journal of Materials Chemistry C* **7**, 7371–7377 (2019).

[60] X. Chen, L. Jin, W. Kong, T. Sun, W. Zhang, X. Liu, J. Fan, S. F. Yu, F. Wang, „Confining Energy Migration in Upconversion Nanoparticles Towards Deep Ultraviolet Lasing“, *Nature Communications* **7**, 10304 (2016).

[61] V. M. Goldschmidt, „Die Gesetze der Krystallochemie“, *Naturwissenschaften* **14**, 477–485 (1926).

[62] O. A. Pfiffner, M. Engi, F. Schlunegger, K. Mezger, L. Diamond, „Erdwissenschaften“, in *Erdwissenschaften*, 285, utb GmbH, 2016.

[63] F. Wang, Y. Han, C. S. Lim, Y. Lu, J. Wang, J. Xu, H. Chen, C. Zhang, M. Hong, X. Liu, „Simultaneous Phase and Size Control of Upconversion Nanocrystals Through Lanthanide Doping“, *Nature* **463**, 1061–1065 (2010).

[64] D. T. Klier, M. U. Kumke, „Analysing the Effect of the Crystal Structure on Up-conversion Luminescence in Yb^{3+},Er^{3+}-co-doped $NaYF_4$ nanomaterials“, *Journal of Materials Chemistry C* **3**, 11228–11238 (2015).

[65] E. Harju, I. Hyppönen, J. Hölsä, J. Kankare, M. Lahtinen, M. Lastusaari, L. Pihlgren, T. Soukka, „Polymorphism of $NaYF_4$:Yb^{3+}, Er^{3+} Up-Conversion Luminescence Materials“, *Zeitschrift für Kristallographie Proceedings* **1**, 381–387 (2011).

[66] D. T. Klier, M. U. Kumke, „Upconversion Luminescence Properties of $NaYF_4$:Yb:Er Nanoparticles Codoped with Gd^{3+}“, *Journal of Physical Chemistry C* **119**, 3363–3373 (2015).

[67] D. Geißler, S. Linden, K. Liermann, K. D. Wegner, L. J. Charbonnière, N. Hildebrandt, „Lanthanides and Quantum Dots as Förster Resonance Energy Transfer Agents for Diagnostics and Cellular Imaging“, *Inorganic Chemistry* **53**, 1824–1838 (2014).

[68] J. C. Joshi, N. C. Pandey, B. C. Joshi, R. Belwal, J. Joshi, „Quantum Efficiency of Diffusion-Limited Energy Transfer from $Eu^{3+} \rightarrow Nd^{3+}$ in Borate Glass“, *Journal of Solid State Chemistry* **23**, 135–139 (1978).

[69] E. Nakazawa, S. Shionoya, „Energy Transfer Between Trivalent Rare-Earth Ions in Inorganic Solids“, *The Journal of Chemical Physics* **47**, 3267–3270 (1967).

[70] J. R. Lakowicz, *Principles of Fluorescence Spectroscopy*, Springer, third edition, 2006.

[71] B. Valeur, *Molecular Fluorescence - Principles and Applications*, Wiley-VCH Verlag, 2002.

[72] M. Inokuti, F. Hirayama, „Influence of Energy Transfer by the Exchange Mechanism on Donor Luminescence“, *The Journal of Chemical Physics* **43**, 1978–1989 (1965).

[73] T. Förster, „Energiewanderung und Fluoreszenz“, *Naturwissenschaften* **33**, 166–175 (1946).

[74] T. Förster, „Zwischenmolekulare Energiewanderung und Fluoreszenz“, *Annalen der Physik* **437**, 55–75 (1948).

[75] R. M. Clegg, „The History of FRET: From Conception Through the Labors of Birth“, in *Reviews in Fluorescence*, C. D. Geddes, J. R. Lakowicz (Herausgeber), 3, Kapitel Chap., 1–45, Springer-Verlag GmbH, Heidelberg, New York, 2006.

[76] N. Hildebrandt, *Lanthanides and Quantum Dots – Time-Resolved Laser Spectroscopy of Biochemical Förster Resonance Energy Transfer (FRET) Systems*, doctoralthesis, Universität Potsdam, 2007.

[77] L. J. Charbonnière, N. Hildebrandt, „Lanthanide Complexes and Quantum Dots: A Bright Wedding for Resonance Energy Transfer“, *European Journal of Inorganic Chemistry* , 3241–3251 (2008).

[78] N. Hildebrandt, K. D. Wegner, W. R. Algar, „Luminescent Terbium Complexes: Superior Förster Resonance Energy Transfer Donors for Flexible and Sensitive Multiplexed Biosensing“, *Coordination Chemistry Reviews* **273-274**, 125–138 (2014).

[79] S. Bhuckory, E. Hemmer, Y.-T. Wu, A. Yahia-Ammar, F. Vetrone, N. Hildebrandt, „Core or Shell? Er^{3+} FRET Donors in Upconversion Nanoparticles“, *European Journal of Inorganic Chemistry* **2017**, 5186–5195 (2017).

[80] C. Duan, L. Liang, L. Li, R. Zhang, Z. P. Xu, „Recent Progress in Upconversion Luminescence Nanomaterials for Biomedical Applications“, *Journal of Materials Chemistry B* **6**, 192–209 (2018).

[81] I. Halimi, E. M. Rodrigues, S. L. Maurizio, H. Q. T. Sun, M. Grewal, E. M. Boase, N. Liu, R. Marin, E. Hemmer, „Pick Your Precursor! Tailoring the Size and Crystal Phase of Microwave-Synthesized Sub-10 nm Upconverting Nanoparticles“, *Journal of Materials Chemistry C* **7**, 15364–15374 (2019).

[82] L. Zhao, A. Kutikov, J. Shen, C. Duan, J. Song, G. Han, „Stem Cell Labeling Using Polyethylenimine Conjugated(α-$NaYbF_4$: Tm^{3+})/CaF_2 Upconversion Nanoparticles“, *Theranostics* **3**, 249–257 (2013).

[83] N. Bogdan, F. Vetrone, G. A. Ozin, J. A. Capobianco, „Synthesis of Ligand-Free Colloidally Stable Water Dispersible Brightly Luminescent Lanthanide-Doped Upconverting Nanoparticles“, *Nano Letters* **11**, 835–840 (2011).

[84] A. Dong, X. Ye, J. Chen, Y. Kang, T. Gordon, J. M. Kikkawa, C. B. Murray, „A Generalized Ligand-Exchange Strategy Enabling Sequential Surface Functionalization of Colloidal Nanocrystals“, *Journal of the American Chemical Society* **133**, 998–1006 (2011).

[85] J. Milton Harris, R. B. Chess, „Effect of Pegylation on Pharmaceuticals“, *Nature Reviews Drug Discovery* **2**, 214–221 (2003).

[86] V. Muhr, S. Wilhelm, T. Hirsch, O. S. Wolfbeis, „Upconversion Nanoparticles: From Hydrophobic to Hydrophilic Surfaces“, *Accounts of Chemical Research* **47**, 3481–3493 (2014).

[87] Z. Chen, H. Chen, H. Hu, M. Yu, F. Li, Q. Zhang, Z. Zhou, T. Yi, C. Huang, „Versatile Synthesis Strategy for Carboxylic Acid-Functionalized Upconverting Nanophosphors as Biological Labels“, *Journal of the American Chemical Society* **130**, 3023–3029 (2008).

[88] M. Haase, H. Schäfer, „Nanopartikel für die Aufwärtskonversion“, *Angewandte Chemie* **123**, 5928–5950 (2011).

[89] Y. Ju, J. Collins, J. Chen, W. Soboyejo, J. S. Friedberg, J. Shan, J. Meng, „Biofunctionalization, Cytotoxicity, and Cell Uptake of Lanthanide Doped Hydrophobically Ligated $NaYF_4$ Upconversion Nanophosphors“, *Journal of Applied Physics* **104**, 094308 (2008).

[90] O. Dukhno, F. Przybilla, M. Collot, A. Klymchenko, V. Pivovarenko, M. Buchner, V. Muhr, T. Hirsch, Y. Mély, „Quantitative Assessment of Energy Transfer in Upconverting Nanoparticles Grafted with Organic Dyes“, *Nanoscale* **9**, 11994–12004 (2017).

[91] J. Dong, W. Gao, Q. Han, Y. Wang, J. Qi, X. Yan, M. Sun, „Plasmon-Enhanced Upconversion Photoluminescence: Mechanism and Application“, *Reviews in Physics* **4**, 100026 (2019).

[92] S. Kim, S. H. Hwang, S. G. Im, M. K. Lee, C. H. Lee, S. J. Son, H. B. Oh, „Upconversion Nanoparticle-Based Förster Resonance Energy Transfer for Detecting DNA Methylation“, *Sensors (Switzerland)* **16**, 1–9 (2016).

[93] Q. Chen, X. Wang, F. Chen, Q. Zhang, B. Dong, H. Yang, G. Liu, Y. Zhu, C. H. Huang, X. G. Liu, „Functionalization of Upconverted Luminescent $NaYF_4$:Yb/Er Nanocrystals by Folic Acid–Chitosan Conjugates for Targeted Lung Cancer Cell Imaging“, *Journal of Materials Chemistry* **21**, 7661 (2011).

[94] L. Yu, C. Cheng, Q. Ran, C. Schlaich, P.-L. M. Noeske, W. Li, Q. Wei, R. Haag, „Bioinspired Universal Monolayer Coatings by Combining Concepts from Blood Protein Adsorption and Mussel Adhesion“, *ACS Applied Materials & Interfaces* **9**, 6624–6633 (2017).

[95] K. D. Wegner, Z. Jin, S. Lindén, T. L. Jennings, N. Hildebrandt, „Quantum-Dot-Based Förster Resonance Energy Transfer Immunoassay for Sensitive Clinical Diagnostics of Low-Volume Serum Samples“, *ACS Nano* **7**, 7411—-7419 (2013).

[96] J. Swartling, J. Axelsson, G. Ahlgren, K. M. Kälkner, S. Nilsson, S. Svanberg, K. Svanberg, S. Andersson-Engels, „System for Interstitial Photodynamic Therapy with Online Dosimetry: First Clinical Experiences of Prostate Cancer“, *Journal of Biomedical Optics* **15**, 058003–1 – 9 (2010).

[97] Y. I. Park, H. M. Kim, J. H. Kim, K. C. Moon, B. Yoo, K. T. Lee, N. Lee, Y. Choi, W. Park, D. Ling, K. Na, K. W. Moon, S. H. Choi, H. S. Park, S.-Y. Yoon, Y. D. Suh, S. H. Lee, T. Hyeon, „Theranostic probe based on lanthanide-doped nanoparticles for simultaneous in vivo dual-modal imaging and photodynamic therapy“, *Advanced Materials* **24**, 5755–5761 (2012).

[98] P. U. Bastian, S. Nacak, V. Roddatis, M. U. Kumke, „Tracking the Motion of Lanthanide Ions within Core–Shell–Shell $NaYF_4$ Nanocrystals via Resonance Energy Transfer“, *The Journal of Physical Chemistry C* **124**, 11229–11238 (2020).

[99] J. Hesse, D. T. Klier, M. Sgarzi, A. Nsubuga, C. Bauer, J. Grenzer, R. Hübner, M. Wislicenus, T. Joshi, et al. Kumke, M. U., „Rapid Synthesis of Sub-10 nm Hexagonal $NaYF_4$-Based Upconverting Nanoparticles Using Therminol® 66“, *ChemistryOpen* **7**, 159–168 (2018).

[100] P. U. Bastian, N. Robel, P. Schmidt, T. Schrumpf, C. Günter, V. Roddatis, M. U. Kumke, „Resonance Energy Transfer to Track the Motion of Lanthanide Ions – What Drives the Intermixing in Core-Shell Upconverting Nanoparticles?“, *Biosensors* **11**, 515 (2021).

[101] P. U. Bastian, L. Yu, A. López de Guereñu, R. Haag, M. U. Kumke, „Bioinspired Confinement of Upconversion Nanoparticles for Improved Performance in Aqueous Solution“, *The Journal of Physical Chemistry C* **124**, 28623–28635 (2020).

[102] B. Chen, D. Peng, X. Chen, X. Qiao, X. Fan, F. Wang, „Establishing the Structural Integrity of Core-Shell Nanoparticles Against Elemental Migration Using Luminescent Lanthanide Probes“, *Angewandte Chemie - International Edition* **54**, 12788–12790 (2015).

[103] J. E. Huheey, E. A. Keiter, R. L. Keiter, *Anorganische Chemie – Prinzipien von Struktur und Reaktivität*, de Gruyter GmbH, Berlin/Boston, völlig neu bearbeitete auflage, 4. edition, pages 114—-117, 2012.

[104] X. Xu, Z. Zhou, Y. Liu, S. Wen, Z. Guo, L. Gao, F. Wang, „Optimising Passivation Shell Thickness of Single Upconversion Nanoparticles Using a Time-Resolved Spectrometer“, *APL Photonics* **4**, 026104 (2019).

[105] W. D. W. Horrocks, D. R. Sudnick, „Lanthanide Ion Luminescence Probes of the Structure of Biological Macromolecules“, *Accounts of Chemical Research* **14**, 384–392 (1981).

[106] R. Marin, L. Labrador-Paéz, A. Skripka, P. Haro-González, A. Benayas, P. Canton, D. Jaque, F. Vetrone, „Upconverting Nanoparticle to Quantum Dot Förster Resonance Energy Transfer: Increasing the Efficiency through Donor Design“, *ACS Photonics* **5**, 2261–2270 (2018).

[107] A. López de Guereñu, P. Bastian, P. Wessig, L. John, M. U. Kumke, „Energy Transfer between Tm-Doped Upconverting Nanoparticles and a Small Organic Dye with Large Stokes Shift“, *Biosensors* **9**, 9 (2019).

[108] S. Schimka, D. T. Klier, A. López de Guereñu, P. Bastian, N. Lomadze, M. U. Kumke, S. Santer, „Photo-Isomerization of Azobenzene Containing Surfactants Induced by Near-Infrared Light Using Upconversion Nanoparticles as Mediator“, *Journal of Physics: Condensed Matter* **31**, 125201 (2019).

[109] W. Li, Z. Chen, L. Zhou, Z. Li, J. Ren, X. Qu, „Noninvasive and Reversible Cell Adhesion and Detachment via Single-Wavelength Near-Infrared Laser Mediated Photoisomerization“, *Journal of the American Chemical Society* **137**, 8199–8205 (2015).

[110] Y. Huang, E. Hemmer, F. Rosei, F. Vetrone, „Multifunctional Liposome Nanocarriers Combining Upconverting Nanoparticles and Anticancer Drugs“, *Journal of Physical Chemistry B* **120**, 4992–5001 (2016).

[111] F. Ai, Q. Ju, X. Zhang, X. Chen, F. Wang, G. Zhu, „A Core-Shell-Shell Nanoplatform Upconverting Near-Infrared Light at 808 nm for Luminescence Imaging and Photodynamic Therapy of Cancer“, *Scientific Reports* **5**, 1–11 (2015).

[112] G. Job, R. Rüffler, *Physikalische Chemie*, Springer, 2011.

[113] A. Jung, P. Berlin, B. Wolters, „Biomolecule-Compatible Support Structures for Biomolecule Coupling to Physical Measuring Principle Surfaces“, *IEE proceedings. Nanobiotechnology* **151**, 87-94 (2004).

[114] A. Jung, B. Wolters, P. Berlin, „(Bio)functional Surface Structural Design of Substrate Materials Based on Self-Assembled Monolayers from Aminocellulose Derivatives and Amino(organo)polysiloxanes“, *Thin Solid Films* **515**, 6867-6877 (2007).

[115] A. Jung, T. M. Gronewold, M. Tewes, E. Quandt, P. Berlin, „Biofunctional Structural Design of SAW Sensor Chip Surfaces in a Microfluidic Sensor System“, *Sensors and Actuators B: Chemical* **124**, 46–52 (2007).

S

Supporting Information and Appendix

S.1. Manuscripts (SI)

S.1.1. SI: Trivalent Lanthanoid Cation Migration in the Sodium Yttrium Fluoride Host Lattice – Supervision via the Eu^{3+}-to-Nd^{3+} Lanthanoid Resonance Energy Transfer (Manuscript 1)

Reprinted with permission from

J. Phys. Chem. C **124** (20), 11229–11238 (2020).[98]

Link: https://doi.org/10.1021/acs.jpcc.0c02588

Supporting Information

Tracking the Motion of Lanthanide Ions within Core-Shell-Shell $NaYF_4$ Nanocrystals *via* Resonance Energy Transfer

Philipp U. Bastian,[†] Selma Nacak, [†] Vladimir Roddatis,[‡] Michael U. Kumke[†]*

[†]Institute of Chemistry (Physical Chemistry), University of Potsdam, 14476 Potsdam (Golm), Germany

[‡]German Research Centre for Geosciences (GFZ), Helmholtz-Centre Potsdam, 14473 Potsdam, Germany

The **Supporting Information** includes additional graphics and illustrations. Illustration of the Förster volume with help of a $NaYF_4$ ($P6_3/m$) unit cell; illustration of a $NaNdF_4$ ($P\bar{6}$) unit cell; table with detailed crystal field strength parameter calculated from the $^7F_1$ multiplet of Eu^{3+} emission; additional photoluminescence decay curves of Eu^{3+} being excited at 465.17 nm; photoluminescence emission spectra of Eu^{3+} in $NaYF_4$ NC for set 1 and set 2 – comparison for all samples within each set; table with detailed fit parameter resulting from the FRET based evaluation of quenched Eu^{3+}/Nd^{3+} doped NC for the $^5D_0 \rightarrow {}^7F_2$ transition (for set 1 and set 2); TEM images of samples of set 1 and set 2.

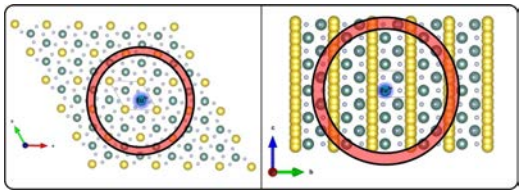

Figure S1 Illustration of Förster volume in the hexagonal $NaYF_4$ host lattice. Bonds are skipped for better illustration, yellow = Na^+; grey = F^-; green = trivalent ions (e.g. Y^{3+}, Eu^{3+}, Nd^{3+}). Red circle shall illustrate the size of the Förster volume being defined by the Förster radius $R_0[Eu^{3+}/Nd^{3+}]$ = 8.53 Å. The Förster volume includes 46 locations next to the center Eu^{3+} ion (highlighted in blue), either for other Eu^{3+}, for Nd^{3+} or for vacancies. The unit cells included in one Förster volume are approximately 29. Images are created with open-source software package VESTA[47].

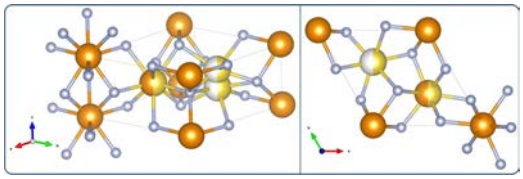

Figure S2 Hexagonal $NaNdF_4$ NC unit cell ($P\bar{6}$ space group). Yellow = Na^+; Grey = F^-; Orange = Nd^{3+} and other Ln^{3+} or Y^{3+}. The positions in the hexagonal unit cell are available either for vacancies or Y^{3+} or Ln^{3+} ions. Half-filled spheres indicate either Na^+ or vacancy or Nd^{3+} occupation. Images are created with open-source software package VESTA[47].

Table S1 Crystal field strength parameter $N_v(B_{2q})$ derived from the $^7F_1$ multiplet Eu^{3+} luminescence emission with eq. (3). Comparison of set 1 and set 2 and the excitation wavelength 465.5 nm and 464.1 nm. Values are given in wavenumbers (cm^{-1}).

	Crystal field strength parameter $N_v(B_{2q})$ / cm^{-1}			
λ_{ex}	465.5 nm	464.1 nm	465.5 nm	464.1 nm
Sample	Set 1		Set 2	
S0_CS	580 ± 260	560 ± 240	550 ± 40	560 ± 40
S1_CSS	520 ± 60	520 ± 40	560 ± 40	580 ± 30
S2_CSS	520 ± 30	530 ± 30	560 ± 30	580 ± 30
S3_CSS	540 ± 30	530 ± 30	540 ± 20	570 ± 20
S4_CSS	540 ± 50	550 ± 40	550 ± 20	570 ± 20
S5_CSS	-/-	-/-	540 ± 20	570 ± 20
Ref_CS	540 ± 40	560 ± 30	540 ± 20	560 ± 20

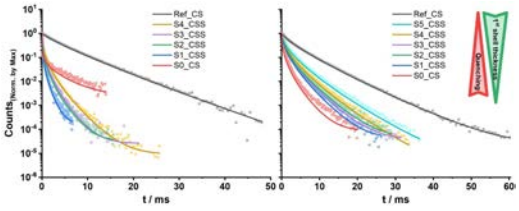

Figure S3 Luminescence decay curves of Eu^{3+} in $NaYF_4$ nanocrystals (left: set 1; right: set 2, λ_{ex} = 465.17 nm; $^5D_0 \rightarrow {}^7F_2$ transition).

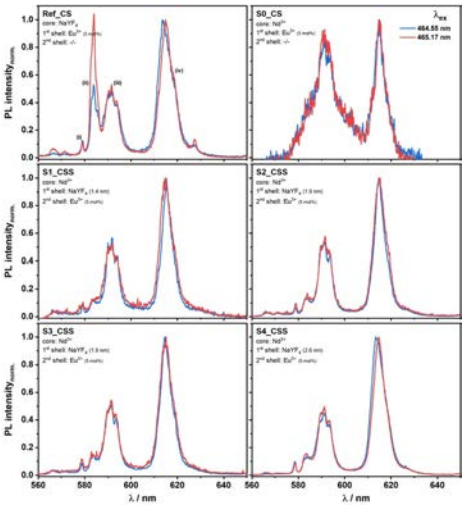

Figure S4 Comparison of luminescence spectra of Eu^{3+} in $NaYF_4$ nanocrystals (set 1). Eu^{3+} is doped in the outer shell, Nd^{3+} is doped in the core. Eu^{3+} signal-to-noise ratio is improving with increasing insulation shell thickness ($NaYF_4$). Ref_CS is not doped with Nd^{3+}; S0_CS is doped with Nd^{3+} and has no insulation shell resulting in maximum quenching efficiency and lowest signal-to-noise ratio. The insulation shell thickness increases from S1_CSS to S5_CSS and Eu^{3+} is less quenched. Transitions shown: (i) $^5D_0 \rightarrow {}^7F_0$; (ii) $^5D_1 \rightarrow {}^7F_3$; (iii) $^5D_0 \rightarrow {}^7F_1$; (iv) $^5D_0 \rightarrow {}^7F_2$.

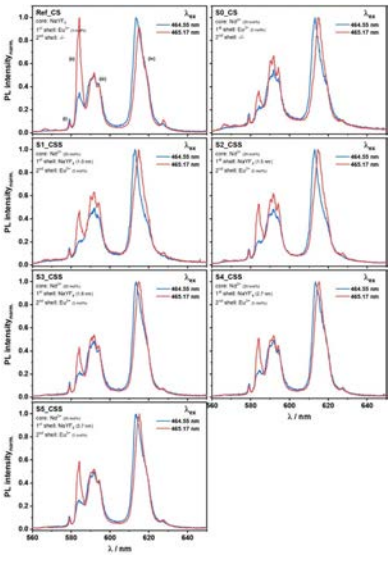

Figure S5 Luminescence spectra of Eu^{3+} in $NaYF_4$ nanocrystals (set 2). Eu^{3+} is doped in the outer shell, Nd^{3+} is doped in the core. Eu^{3+} signal-to-noise ratio is improving with increasing insulation shell thickness ($NaYF_4$) due to the reduced quenching of the Eu^{3+} emission. Ref_CS is not doped with Nd^{3+}; S0_CS is doped with Nd^{3+} and has no insulation shell resulting in maximum quenching efficiency and lowest signal-to-noise ratio. The insulation shell thickness increases from S1_CSS to S5_CSS and Eu^{3+} is less quenched. Transitions shown are: (i) $^5D_0 \rightarrow {}^7F_0$; (ii) $^5D_1 \rightarrow {}^7F_3$; (iii) $^5D_0 \rightarrow {}^7F_1$; (iv) $^5D_0 \rightarrow {}^7F_2$.

Table S2 Detailed fit parameter of the evaluation of the LRET quenched Eu^{3+}/Nd^{3+} doped NC for the $^5D_0 \rightarrow {}^7F_2$ transition for set 1. The heterogeneity parameter α differs significantly for the S0 sample. α is close to 0 which correlates with the large concentration of Nd^{3+} ions and induces a strongly changing chemical environment of the Eu^{3+} ions.

Set 1	**Ref_CS**	**S0_CS**	**S1_CSS**	**S2_CSS**	**S3_CSS**	**S4_CSS**	**S5_CSS**
α	-/-	0.05	0.90	0.75	0.72	0.88	
±Er [%]	-/-	1%	2%	1%	1%	1%	
Number of acceptor within Förster volume	0	9.0383	2.8237	2.1743	1.9587	1.4911	
±Er [%]	-/-	2%	1%	1%	1%	1%	
acceptor number (λ_{ex} = 464.55 nm)	0	9	3	2	2	1	
α	-/-	0.05	0.82	0.80	0.85	0.85	
±Er [%]	-/-	1%	1%	1%	1%	1%	
Number of acceptor within Förster volume	0	8.6895	3.8537	2.9210	2.7395	2.2760	
±Er [%]	-/-	2%	1%	1%	1%	1%	
acceptor number (λ_{ex} = 465.17 nm)	0	9	4	3	3	2	
averaged acceptor number	0	8.9	3.3	2.6	2.4	1.9	
Insulation layer thickness / nm	-/-	0	1.4	1.9	1.9	2.6	
Trends:		Acceptor number ↘ Layer thickness ↗					

Table S3 Detailed fit parameter of the evaluation of the LRET quenched Eu^{3+}/Nd^{3+} doped NC for the $^5D_0 \rightarrow {}^7F_2$ transition for set 2. α is always 1 except for S0_CS which correlates with the lack of an insulation shell and the small distance between Nd^{3+} and Eu^{3+} ions inducing a moderate change in the chemical environment of the Eu^{3+} ions.

Set 2	Ref_CS	S0_CS	S1_CSS	S2_CSS	S3_CSS	S4_CSS	S5_CSS
α	-/-	0.95	1.00	1.00	1.00	1.00	1.00
±Er [%]	-/-	1%	3%	2%	3%	4%	6%
Number of acceptor within Förster volume	0	0.9388	0.4370	0.4195	0.4324	0.3032	0.1921
±Er [%]	-/-	1%	2%	2%	3%	4%	6%
acceptor number (λ_{ex} = 464.55 nm)	0	0.94	0.44	0.42	0.43	0.3	0.19
α	-/-	0.80	1.00	0.93	0.97	0.90	0.85
±Er [%]	-/-	1%	1%	1%	1%	1%	1%
Number of acceptor within Förster volume	0	1.7990	1.0884	0.9430	0.9926	0.8072	0.6145
±Er [%]	-/-	1%	1%	1%	1%	1%	1%
acceptor number (λ_{ex} = 465.17 nm)	0	1.80	1.09	0.94	0.99	0.81	0.61
averaged acceptor number	0	1.4	0.8	0.7	0.7	0.6	0.4
Insulation layer thickness / nm	-/-	0	1.0	1.5	1.6	2.7	3.7
Trends:		Acceptor number ↘ Layer thickness ↗					

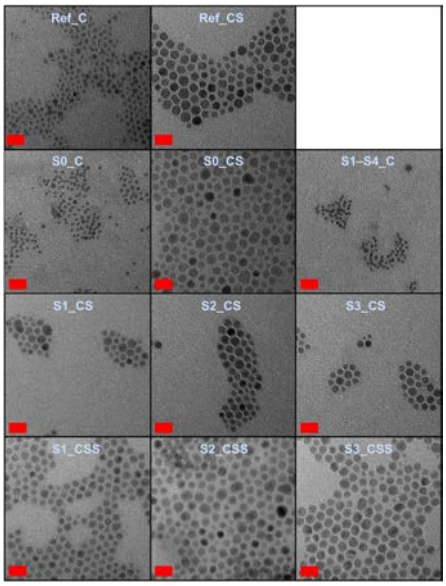

Figure S6 TEM images of samples of set 1 ($NaNdF_4$ core only, $NaYF_4$ shell with increasing shell thickness per sample and outer shell of $NaYF_4$ with 5 mol% Eu^{3+}). The red scale bar corresponds to 20 nm. The samples S1, S2, S3 and S4 are based on the same core NC, (S1–S4_C). The size increase of each sample corresponds to the shell addition, compare with Table 1.

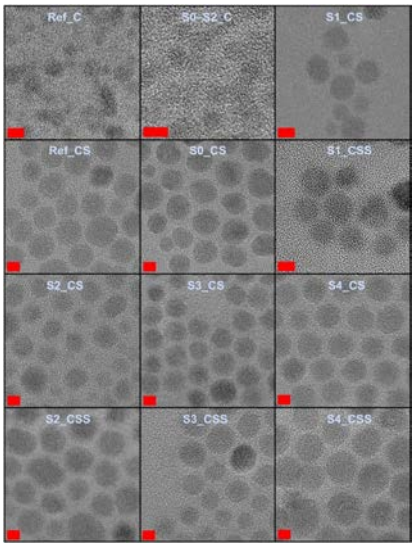

Figure S7 TEM images of samples of set 2 ($NaYF_4$ core doped with 20 mol% Nd^{3+}, $NaYF_4$ shell with increasing shell thickness per sample and outer shell of $NaYF_4$ with 5 mol% Eu^{3+}). The red scale bar corresponds to 5 nm. The samples S0, S1, S2 (S0–S4_C) and S3, S4, S5 (S3–S5_C) are based on the same core NC batch. The TEM image S3–S5_C can be found in Figure 3, there named as S5_C. The size increase of each sample corresponds to the shell addition, compare with Table 1.

S.1.2. SI: UCNP Phase Transfer into Aqueous Solution and Bio-Conjugation with a TAMRA Dye via Click Chemistry – A Proof of Principle (Manuscript 3)

J. Phys. Chem. C **124** (52), 28623–28635 (2020).[101]

Link: https://doi.org/10.1021/acs.jpcc.0c09798

Supporting Information

Bioinspired Confinement of Upconversion Nanoparticles for Improved Performance in Aqueous Solution

Philipp U. Bastian,[†] Leixiao Yu,[‡] Anna López de Guereñu,[†] Rainer Haag,[‡] Michael U. Kumke[,†]*

[†]Institute of Chemistry (Physical Chemistry), University of Potsdam, Potsdam (Golm) 14476, Germany

[‡]Institute of Chemistry and Biochemistry, Freie Universität Berlin, Berlin 14195, Germany

Keywords: *Upconversion Nanoparticles, RET, UCNP-to-dye-RET, TAMRA, biofunctionalization*

Supporting information include additional graphics and illustrations. Figure S1, PL emission spectra of $NaYF_4$:Yb,Er and $NaYF_4$:Yb,Tm UCNPs after long time storage (λ_{ex} = 976 nm); Figure S2, Histograms from TEM evaluation of the $NaYF_4$:Yb,Er UCNPs covered with CMP – same sample from 2017 and 2020; Figure S3, PL emission spectra of the reaction mixture and supernatants of the purification and photo of the dispersions; Figure S4, Fluorescence emission and absorption spectra of TAMRA after the coupling reaction and purification; Figure S5, Low temperature measurement of UCNP≡TAMRA, PL emission and kinetics in a temperature range of 4–200 K (λ_{ex} = 976 nm); Table S1, detailed PL decay times of the green emission G2 (540 nm), the red emission R (654 nm) and the TAMRA emission (600 nm) peaks excited via RET from $NaYF_4$:Yb,Er UCNP (λ_{ex} = 976 nm); Figure S6, PL emission spectra of UCNP≡TAMRA at low temperatures (4–200 K), non-normalized spectra (λ_{ex} = 976 nm).

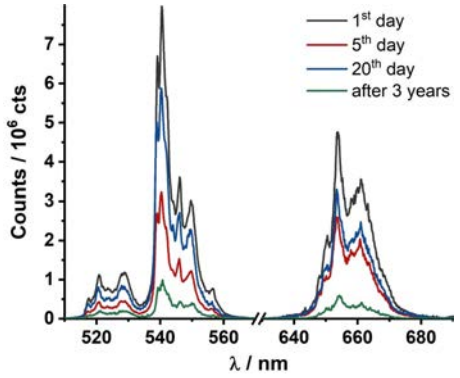

Figure S1. PL emission spectra of $NaYF_4$:Yb,Er UCNP encapsulated in CMP. The total PL emission is shown, the recording settings were almost kept constant but the laser excitation power was not controlled. (λ_{ex} = 976 nm; emission from 500–700 nm not measured). Both plots show, that the PL emission intensity decreases moderately over time which can be attributed to the extraordinary properties of CMP described in the corresponding publication.[1]

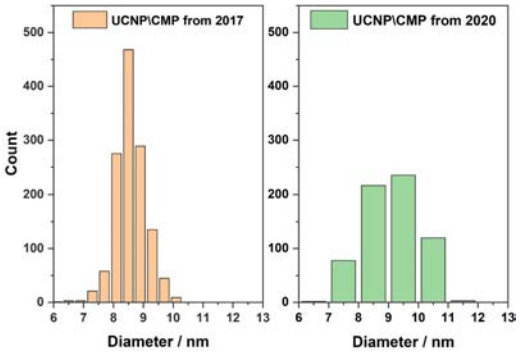

Figure S2. Histograms from TEM size evaluation of the $NaYF_4$:Yb,Er UCNPs covered with CMP. Sample from 2017 and the same sample after storage in a fridge at (5 ± 1) °C from 2020 is shown.

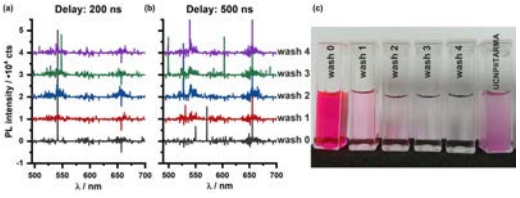

Figure S3. PL emission spectra of the reaction mixture (wash 0) and the washes 1–4 recorded with **(a)** 200 ns and **(b)** 500 ns delay time. It demonstrates that TAMRA cannot be excited in the NIR (976 nm). Some UCNP residues can be identified by its green G1 & G2 and red R emission. But, the amount is insufficient to excite the TAMRA via RET. **(c)** Photograph of the reaction mixture (wash 0), the washes 1–4 and the final sample UCNP≡TAMRA ($NaYF_4$:Yb,Er covered with CMP and coupled with TAMRA-5-alkyne). The solvent is water. It shows: The color intensity decreases with each washing step and the sample has higher color intensity than the washes. That means, the final sample contains more TAMRA than the washes.

It was excluded that TAMRA could be accidentally excited with 976 nm by testing the supernatants luminescence emission. Furthermore, a concentration decrease with each purification step can be seen in the fluorescence and absorption spectra with a strong hyperchromic effect,[2–4] which can also be observed by eye. These finding are illustrated in the SI Figure S3 and Figure S4. It is worth to mention that roughly 5 nmol dye are coupled to 30 mg UCNP\CMP so that the TAMRA concentration is roughly 0.16 nmol per mg of UCNP\CMP (based on the absorbance of UCNP≡TAMRA at 554 nm in the SI Figure S4).

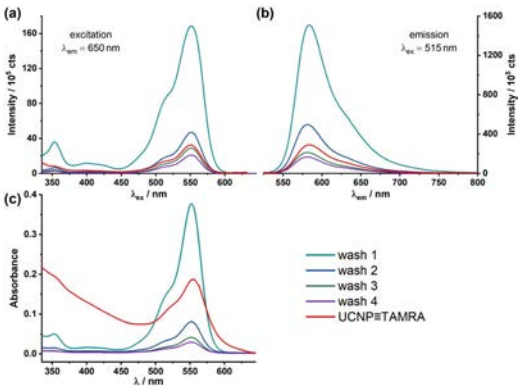

Figure S4: Fluorescence emission and absorption spectra of TAMRA after the coupling reaction. Supernatants from the purification after centrifugation (washes 1–4) and the final product UCNP≡TAMRA in water are shown. **(a)** Steady-state fluorescence excitation spectra with λ_{em} = 650 nm. **(b)** Steady-state fluorescence emission spectra with λ_{ex} = 515 nm. **(c)** Absorption spectra. The final sample has higher absorption and higher fluorescence intensity than the last washes.

Table S1. Detailed PL decay times of the green emission G2 (540 nm), the red emission R (654 nm) and the TAMRA emission peak (600 nm) excited via RET from $NaYF_4$:Yb,Er UCNP (λ_{ex} = 976 nm). The intensity weighted average PL decay time $\bar{\tau}$ is shown: $\bar{\tau} = \sum f_j \tau_j$ with $f_j = \frac{A_j \tau_j}{\sum_i (A_i \tau_i)}$. The amplitude weighted average PL decay time $\langle\tau\rangle = \sum a_j \tau_j$ with $a_j = \frac{A_j}{\sum_i A_i}$. The PL decay time decreases due to phase transfer from cyclohexane (cy) into water. The UCNP PL decay time increases again after click reaction with TAMRA being independent on the dispersion media (water or MOPS buffer with pH=6, .1mol/L).

λ_{ex}	UCNP\OA in cy	UCNP\CMP in MOPS	UCNP⊒TAMRA in H_2O	UCNP⊒TAMRA in MOPS	UCNP⊒TAMRA in H_2O	UCNP⊒TAMRA in MOPS
976 nm	Peak = 540 nm (G2)				Peak = 600 nm (TAMRA)	
τ_1	59 µs	10 µs	21 µs	26 µs	0.01 µs	11 µs
±ER(τ_1)	2 µs	1 µs	1 µs	2 µs	4 µs	3 µs
α_1	93 %	82 %	84 %	79 %	0 %	75 %
f_1	82 %	50 %	57 %	52 %	0 %	44 %
τ_2	160 µs	37 µs	77 µs	80 µs	17 µs	35 µs
±ER(τ_2)	17 µs	2 µs	4 µs	7 µs	1 µs	8 µs
α_2	7 %	17 %	15 %	19 %	91 %	23 %
f_2	18 %	39 %	37 %	38 %	70 %	44 %
τ_3	538 µs	126 µs	181 µs	175 µs	74 µs	122 µs
±ER(τ_3)	755 µs	4 µs	14 µs	15 µs	3 µs	28 µs
α_3	0.05 %	2 %	1 %	2 %	9 %	2 %
f_3	0.04 %	12 %	6 %	10 %	30 %	12 %
$\bar{\tau}$	79 µs	34 µs	52 µs	62 µs	34 µs	35 µs
±ER($\bar{\tau}$)	2 µs	1 µs	1 µs	1 µs	0.6 µs	2 µs
$\langle\tau\rangle$	67 µs	16 µs	32 µs	40 µs	22 µs	18 µs
±ER($\langle\tau\rangle$)	1 µs	1 µs	1 µs	1 µs	1 µs	2 µs

λ_{ex}	UCNP\OA in cy	UCNP\CMP in MOPS	UCNP⊒TAMRA in H_2O	UCNP⊒TAMRA in MOPS
976 nm	Peak = 654 nm (R)			
τ_1	0 µs	27 µs	37 µs	34 µs
±ER(τ_1)	0 µs	2 µs	2 µs	2 µs
α_1	0 %	84 %	87 %	89 %
f_1	0 %	56 %	54 %	56 %
τ_2	90 µs	73 µs	142 µs	147 µs
±ER(τ_2)	3 µs	7 µs	38 µs	27 µs
α_2	78 %	13 %	7 %	6 %
f_2	49 %	24 %	18 %	17 %
τ_3	325 µs	309 µs	316 µs	328 µs
±ER(τ_3)	7 µs	7 µs	25 µs	16 µs
α_3	22 %	3 %	5 %	4 %
f_3	51 %	21 %	28 %	26 %
$\bar{\tau}$	209 µs	97 µs	133 µs	131 µs
±ER($\bar{\tau}$)	2 µs	1 µs	2 µs	2 µs
$\langle\tau\rangle$	142 µs	41 µs	60 µs	54 µs
±ER($\langle\tau\rangle$)	2 µs	1 µs	1 µs	2 µs

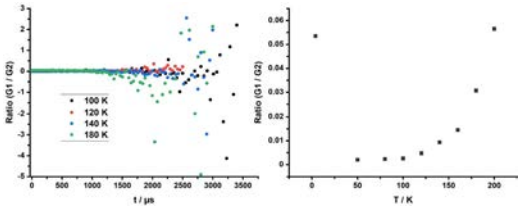

Figure S5. Low temperature measurements of UCNP⊒TAMRA. PL emission and kinetic investigations, λ_{ex} = 976 nm. **Left:** Ratios of G1/G2 emission from kinetic measurements. The time dependent ratios are constant. Only 140 K and 180 K show deviations, upwards and downwards, respectively. **Right:** Ratios of G1/G2 emission from emission measurements. They show clearly that the G1 emission increases in intensity with increasing temperature. The exemption for the 4 K ratio, whose total intensity emission is very low, correlates with very little G2 emission. G1 emission cannot be detected below 100 K.

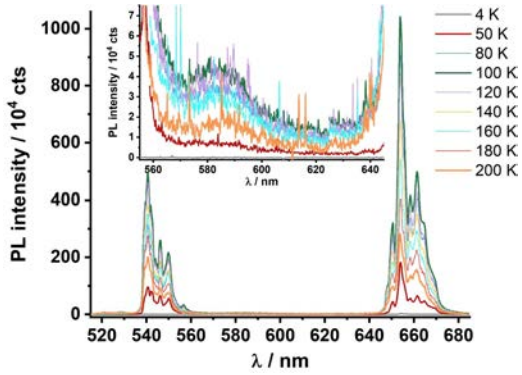

Figure S6. PL emission spectra of UCNP⊒TAMRA at low temperatures with T in K. The PL emission intensities increase with increasing temperature up to 100 K – accounting for all emission bands of G1 (520 nm), G2 (540 nm), TAMRA (585 nm) and R (654 nm). When T exceeds 100 K the PL emission intensities decrease with T increasing, which could relate to stronger pronounced multiphonon relaxation processes.

References

(1) Yu, L.; Cheng, C.; Ran, Q.; Schlaich, C.; Noeske, P.-L. M.; Li, W.; Wei, Q.; Haag, R. Bioinspired Universal Monolayer Coatings by Combining Concepts from Blood Protein Adsorption and Mussel Adhesion. *ACS Appl. Mater. Interfaces* **2017**, *9*, 6624–6633.

(2) Sabaté, R.; Freire, L.; Estelrich, J. Influence of Dielectric Constant on the Spectral Behavior of Pinacyanol. A Spectrophotometric Experiment for Physical Chemistry. *J. Chem. Educ.* **2001**, *78*, 243.

(3) Ackerman, M. M.; Ricciardi, C.; Weiss, D.; Chant, A.; Kraemer-Chant, C. M. Analyzing Exonuclease-Induced Hyperchromicity by UV Spectroscopy: An Undergraduate Biochemistry Laboratory Experiment. *J. Chem. Educ.* **2016**, *93*, 2089–2095.

(4) Winter, R.; Noll, F.; Czeslik, C. *Methoden der Biophysikalischen Chemie*; Vieweg+Teubner Verlag, Springer Fachmedien Wiesbaden, 2011.

S.2. Additional Experiments

The additional experiments have been performed more or less to develop an understanding as well as a handling for phase transfer reactions and to optimize reaction conditions. Some of these reactions were project related experiments, which are not further described.

S.2.1. Surface modification and phase transfer reactions

The phase transfer reactions are reactions to transfer the oleic acid covered UCNPs into the aqueous phase with the aim to prepare the UCNPs for bio-conjugation.

Phase transfer with PAA: The phase transfer with polyacrylic acid (PAA) replaces the initial oleic acid with PAA on the UCNP surface. This entropy driven process correlates with the polydentate property of PAA. PAA with a molar mass of M_W = 1800 g/mol carries 25 acrylic acid monomers (whereas oleic acid carries only one carboxy group). Accordingly, PAA exceeds oleic acid by 24 carboxy groups and replaces it. If more mass of PAA than of oleic acid (on the UCNP surface) is provied, the equilibrium will shift from oleic acid covered UCNPs towards PAA covered UCNPs (Le Chatelier's and Braun's principle).[112]

Two possible ways for the ligand exchange have been examined. One is stirring over night in tetrahydrofuran. The other one is described in section 2.4.[101] In both cases a milky and relatively optically dense dispersion is obtained. The PAA covered UCNPs can be dispersed in MOPS buffer and are stable for some weeks, although the PAA covered UCNP precipitate without agglomerating. UCNP dispersions in phosphate buffered saline (PBS) agglomerated within days. This can be attributed to the strong affinity of phosphates to the UCNP surface. Hence, the phosphates displace the PAA. The hydrodynamic diameter of a representative sample is determined via DLS:* (35 ± 4) nm (UCNP covered with oleic acid, dispersed in cyclohexane) and (190 ± 20) nm (UCNP covered with PAA, dispsersed in water). The size increase by a factor of 5 correlates with the different capping agents on the UCNP surface and with the larger solvation shell in water than in cyclohexane.

*Dynamic light scattering (DLS) is (not only) a size determination method. DLS returns the hydrodynamic radius or diameter. The method is based on the time correlation of intensity fluctuations of scattered laser light. The scattered light stems from a sample consisting of dispersed particles or polymers. The diffusion coefficient is obtained via an auto correlation function that results from the scattered laser light intensities. With the help of the Stokes-Einstein equation, the hydrodynamic radius is obtained.

Phase transfer with HCl: The phase transfer with hydrochlorid acid (HCl) protonates the oleic acid and results in ligand-free UCNPs. At pH 4 the oleic acid detaches from the UCNP surface and the sterical stabilization by oleic acid is removed. The ligand-free UCNPs remain electrostatically stabilized. The strength of the electrostatic double layer depends on the pH value and surface coordinated water molecules. The best stability is observed at a pH value of 4.[83]

The phase transfer via ligand-free UCNPs is a tempting approach, since the ligand-free UCNPs are already dispersed in water and further surface modifications can be applied directly. The performed experiments resulted in UCNPs dispersed in deionized water, sometimes with good yields and more often with agglomareted UCNPs. One good UCNP sample being covered with oleic acid and dispersed in cyclohexane showed a hydrodynamic diameter of (42 ± 3) nm with a zetapotential of (34 ± 4) mV. After ligand removal and dispersion in DI-water, the hydrodynamic diameter was (87 ± 12) nm with a zetapotential of (32 ± 1) mV. The size increase can be attributed to the water molecules coordinated on the UCNP surface forming a hydrodynamic shell. Minor agglomeration is indicated by the increase of the standard deviation. The zetapotential being far from zero indicates a stable dispersion.

Phase transfer with DMSA The phase transfer with dimercaptosuccinic acid (DMSA) equips the UCNP with carboxy and thiol groups. This opens in principle two possible bio-conjugation pathways via the carboxy or the thiol group. The idea was, that DMSA could create a cage-like system on the UCNP surface suppressing ligand exchange reactions. The carboxy groups could be accessible for esterification to introduce bio-recognition elements.[93]

The experiments performed have yielded water-dispersible, DMSO-stabilized UCNPs. However, the dispersions have only been stable for a few days. One UCNP sample showed a significant increase of the hydrodynamic diameter after three days, which indicated strong agglomeration (from 200 nm to 1700 nm). This revealed a poor stability of the UCNP dispersion, which is not good enough for further experiments.

Polymer bead encapsulation There are two ways to realize polymer bead encapsulation of UCNPs. One can be soaking, the other one can be encapsulation during the polymerization. Both have been tested in project related purposes. The inclusion of oleic acid capped UCNPs during the polymerization resulted in a hydrodynamic radius of approximately 100 nm. The upconversion luminescence emission has been weak but always detectable (see Fig. S.1). It was observed, how the PL decay times increase after

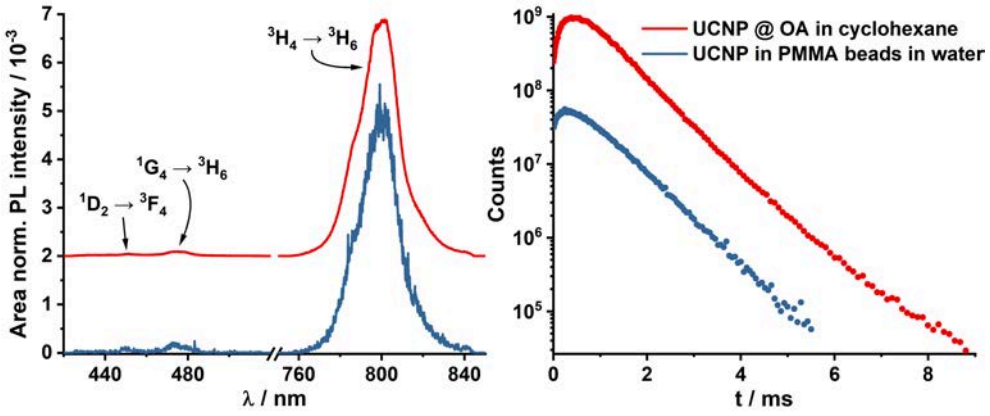

Figure S.1.: PL emission spectra (left) and PL decay curves (right) of the 800 nm PL emission band of core-shell UCNPs ($NaYF_4$:$Gd_{[30\,mol\,\%]}$,$Yb_{[19\,mol\,\%]}$,$Tm_{[1\,mol\,\%]}$ @ $NaYF_4$), before (red curves) and after (blue curves) polymer inclusion (λ_{ex} = 976 nm). The PL emission intensity decreases due to the phase transfer from the organic phase (red) to the aqueous phase (blue) and probably due to the inclusion polymerization. Instead, the luminescence decay time increases: (440 ± 8) µs (red, organic phase) and (700 ± 5) µs (blue, aqueous phase).

bead encapsulation and the accompanied phase transfer. It could relate either to a certain extend of UCNP aggregation or to better shielding from the environment/solvent due to the inclusion. The resulting polymer beads carried bio-modifiable groups.

Polymer encapsulation Also, PEG-PLGA[†] has been applied to transfer the hydrophobic UCNPs into the aqueous phase for a project related cooperation. The block copolymer replaced the oleic acid on the UCNP surface to render the UCNPs water-dispersible. The UC PL emission intensity was low, but still it was a promising approach. The applied shell on the UCNPs consisted of $NaGdF_4$ enabling the possibility for magnetic resonance imaging, in which the particles performed surprisingly well. The respective UC PL emission spectra are shown in Fig. S.2.

Another example are cellulose derivatives (not exclusively of course), which are often applied in immunology for monolayer surface coatings and subsequent antibody immobilization.[113–115] One cellulose derivative has been applied as UCNP surface ligand providing bio-conjugatable groups. The PL emission spectrum of such coated UCNPs is shown in Fig. S.3 indicating sufficient upconversion efficiency.

[†]Poly(ethylene glycol) methyl ether-*block*-poly(lactide-*co*-glycolide)

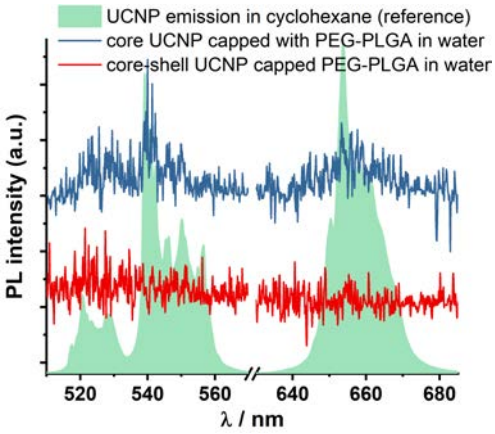

Figure S.2.: PL emission spectra of $NaYF_4$:$Yb_{[18\,mol\,\%]}$,$Er_{[2\,mol\,\%]}$ @ $NaGdF_4$ UCNPs ($\lambda_{ex} = 976\,nm$). The green filled background curve serves as reference spectrum for the strong Er^{3+} UC PL emission in cyclohexane. After PEG-PLGA encapsulation and dispersion in water, the signal-to-noise ratio is low. The Er^{3+} UC PL emission of the core UCNPs (blue) is weak but surprisingly stronger than for the core-shell UCNPs (red). PL decay times were determined due to too little PL emission intensities.

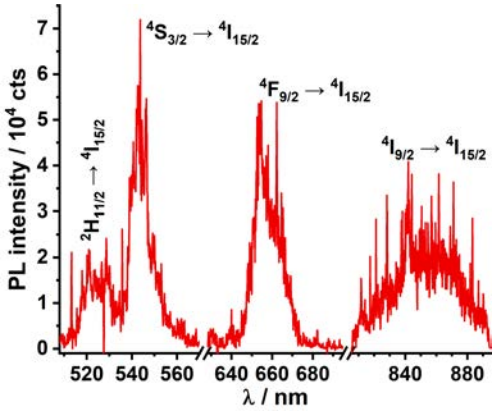

Figure S.3.: UC PL emission spectrum of $NaYF_4$:$Yb_{[18\,mol\,\%]}$,$Er_{[2\,mol\,\%]}$ UCNPs coated with a cellulose derivative ($\lambda_{ex} = 976\,nm$). Excited with a relatively weak, focused cw-laser diode (ca. 800 mW).

S.2.2. Bio-conjugation reactions – proof of principle for coupling antibodies

Next to the surface modification and bio-conjugation reactions being published (section 2.4), additional bio-conjugation reactions had been realized within a project-related idea with the aim to test a coupling strategy for proteins via an N-terminal group. Therefore, an AlexaFluor™ 488 NHS[‡] (RET-acceptor) was coupled to Tm^{3+} doped UCNPs[§] (RET-donor) via an esterification reaction. The donor-acceptor spectral overlap is illustrated in Fig. S.4 (a).

In a first trial, the AlexaFluor™ dye was directly coupled to the UCNP covered with the PG-CatPh coating polymer (which has also been used in the publication in section 2.4). Here, the unbound primary amine group of CMP was addressed via the NHS group of AlexaFluor™ 488 NHS. *In a second trial*, the aim was to couple a dye with an amine group to the UCNP. Therefore, some chemistry on the AlexaFluor™ 488 NHS dye was coupled with N-Boc-ethylenediamine and Boc-deprotected resulting in an AlexaFluor dye with a primary amine. Instead, the UCNP donor was equipped with an NHS group instead (by coupling propanedioic acid-NHS = propanedioic acid 1-(2,5-dioxo-1-pyrrolidinyl) ester). The introduced carboxy groups were modified to NHS-groups by activation with a Steglich-like esterification (with EDC and Sulfo-NHS). Finally, the donor-acceptor coupling was performed. *A third trial* was investigated, in which the UCNP donor was covered with PAA (instead of the CMP coating polymer). The modified AlexaFluor™ 488 dye (with a terminal amine group) was coupled via Steglich-like esterification with the UCNP donor. *In a fourth trial*, the UCNP donor was exchanged against Er^{3+} doped UCNPs[¶]. PAA was kept as coating polymer. Related to the donor exchange, the dye had to be changed to TAMRA amine, 5-isomer dye ($\lambda_{max–emission}$ = 583 nm).

The corresponding spectroscopic data are summarized for trial 2 (Fig. S.4 (a) & (b)) and for trial 4 (Fig. S.4 (c) & (d)). The respective spectral overlap of the Tm^{3+} doped UCNP luminescence with the AlexaFluor™ 488 dye absorption is illustrated in (a) and for Er^{3+} doped UCNP luminescence with the TAMRA amine,5-isomer in (c). In (b) and (d), the respective PL emission of the coupled dyes and UCNPs upon excitation with λ_{ex} = 976 nm are shown.

The first trial apparently seemed to work, but it is not sure. The coupling could not be

[‡]AlexaFluor™ 488 NHS is a rhodamine derivative with two sulfonate groups on the anthracene part and with the NHS group on the benzoic acid part as succinimidyl ester. Its PL intensity maximum is at $\lambda_{max–emission}$ = 542 nm.

[§]UCNP composition = $NaYF_4$:$Gd_{[30\,mol\,\%]}$,$Yb_{[19\,mol\,\%]}$,$Tm_{[1\,mol\,\%]}$.

[¶]UCNP composition = $NaYF_4$:$Gd_{[30\,mol\,\%]}$,$Yb_{[18\,mol\,\%]}$,$Er_{[2\,mol\,\%]}$.

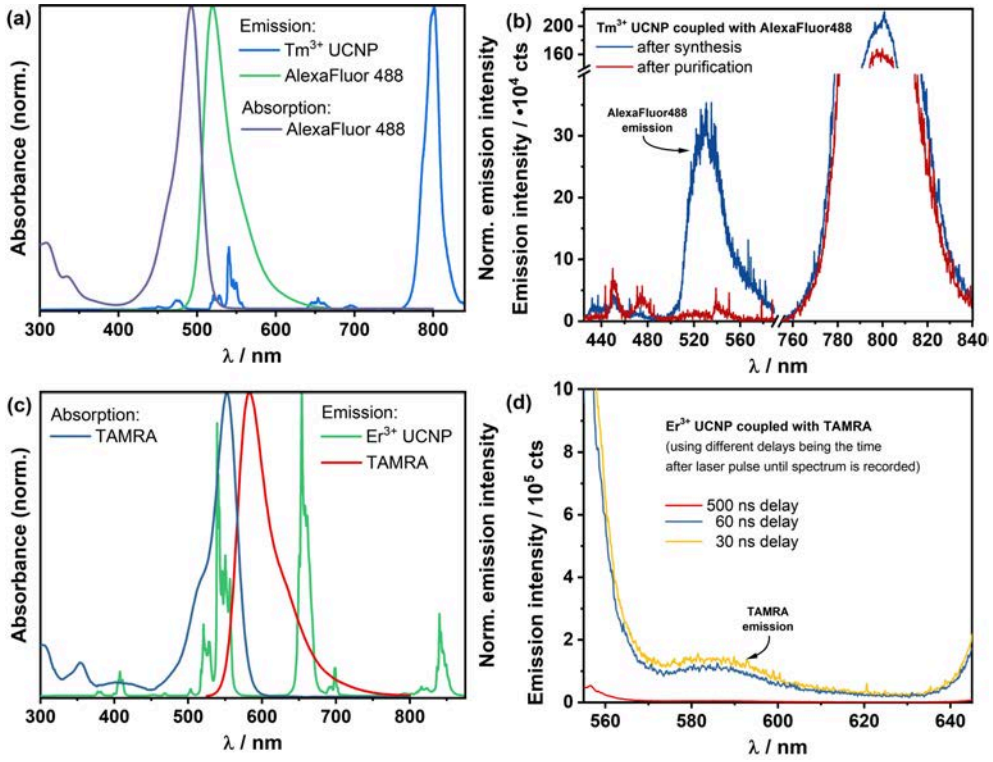

Figure S.4.: UC PL emission and absorption spectra of core-shell UCNPs coupled with appropriate dyes for FRET/RET. (a) UC PL emission of $NaYF_4$:$Yb_{[19\,mol\,\%]}$,$Tm_{[1\,mol\,\%]}$ @ $NaYF_4$ UCNPs (λ_{ex} = 976 nm) and absorption and fluorescence emission of AlexaFluor™ 488 NHS dyes (λ_{ex} = 460 nm) indicating its absorption ability of Tm^{3+} PL emission. (b) PL Emission spectra of AlexaFluor™ 488 coupled with Tm^{3+}-doped UCNPs (capped with PG-CatPh-polymer modified with carboxy surface functionality), after the synthesis (blue) and after the purification (red). (λ_{ex} = 976 nm) (c) UC PL emission of $NaYF_4$:$Yb_{[18\,mol\,\%]}$,$Er_{[2\,mol\,\%]}$ @ $NaYF_4$ UCNPs (λ_{ex} = 976 nm) and absorption and fluorescence emission of TAMRA amine, 5-isomer (λ_{ex} = 515 nm) indicating its absorption ability of the major Er^{3+} PL emission by TAMRA and its fluorescence emission between the green and red PL emission of Er^{3+}. (d) PL emission spectra of TAMRA amine coupled with Er^{3+} doped UCNPs (capped with PAA), recorded at different delay times exceeding the initial TAMRA fluorescence decay time in absence of the UCNPs. (λ_{ex} = 976 nm).

confirmed spectroscopically, as PL emission traces of Er^{3+} (which are always present in our Tm^{3+} doped UCNPs) have interfered with the dye (AlexaFluor™ 488) PL emission at 540 nm (Fig. S.4 (a), blue curve). Nevertheless, coupling was likely, as the final sample (UCNPs coupled with the dye) had the coloration of the dye. This coloration did not vanish after purification by centrifugation and washing. The spectroscopic data of this trial are not shown, as the blue Tm^{3+} PL emission was too weak to sensitize the AlexaFluor™ 488 dye via RET effectively. Only weak dye fluorescence was detected, which is influenced by and difficult to distinguish from the Er^{3+} UC PL emission. If the detected luminesence at 540 nm was the dye emission, it surely would be either RET or a trivial emission-reabsorption process, because the dye does not absorb 976 nm (being the excitation light) and the detection of the supposed dye luminescence started after 200 ns. The dye itself has a fluorescence decay time of (5.5 ± 0.1) ns, which would have already after 200 ns.

The second trial was surely not successful. The chemical reactions were too optimisticly planned and probably need better handling and training. The results of the second set are shown in Fig. S.4 (b). It indicates, that the dye has been in the reaction mixture, but is washed out after the purification process. In Fig. S.4 (b) a very strong AlexaFluor™dye PL emission at 540 nm can be seen before the purification (blue curve), whereas the Tm^{3+} PL emission at 475 nm is very weak. After the purification (red curve), the Tm^{3+} PL emission at 475 is significantly higher, but the dye PL emission at 540 nm vanished. It indicates washing out of the dye and no successful coupling of the UCNP and the dye. Nervertheless, it apparently indicates, that the AlexaFluor™dye absorbs the photons of the Tm^{3+} PL emission at 475 nm more strongly than at 450 nm, also being a trivial mechanism instead of LRET.

The third trial has been a failure as well. Very poor luminescence intensity has been detected after the UCNP phase transfer and coupling reaction. It is related to UCNP agglomeration and as before to the preparation of the dye.

The fourth trial worked fine and best of the given examples. The spectral overlap of Er^{3+} UC PL emission (RET-donor) and of the dye TAMRA amine, 5-isomer (RET-acceptor) illustrated in Fig. S.4 (c) also indicates that TAMRA is not excited upon irradiation with 976 nm. But in (d), the TAMRA luminescence at 583 nm relates to RET (or a trivial mechanism). The increasing PL emission intensities below 560 nm and above 640 nm belong to the upconverted green (520/540 nm) and red (655 nm) Er^{3+} PL emission bands. It can be seen, that the TAMRA emission is very weak and has already vanished with a delay 500 ns. In contrast to the UCNP in the manuscript 3 (section 2.4), in which core-only UCNPs were used, here, core-shell UCNPs were

used, as the awareness of too high donor-acceptor distance outcompeting the RET and brighter UCNPs luminescence was not present yet—it just came later.[79] Nevertheless, there are three indications for successful coupling: (i) TAMRA PL emission is detected under 976 nm irradiation at which TAMRA does not absorb. (ii) The initial TAMRA fluorescence decay time of (2.4 ± 0.1) ns increased up to (68 ± 1) ns, as the UCNP donor was present (and that in Fig. S.4 (d) the TAMRA luminescence was detected even at delay times of 30 ns and 60 ns. (iii) Microscale thermophoresis (MST, as in manuscript 3, section 2.4) revealed a faster diffusion speed of the free TAMRA than for the TAMRA coupled to the UCNP due to the faster drop of the TAMRA fluorescence intensity, see Fig. S.5. The large and heavy UCNP hinders fast TAMRA diffusion and slows it down. Accordingly, coupling between TAMRA and the PAA covered UCNPs is very likely.

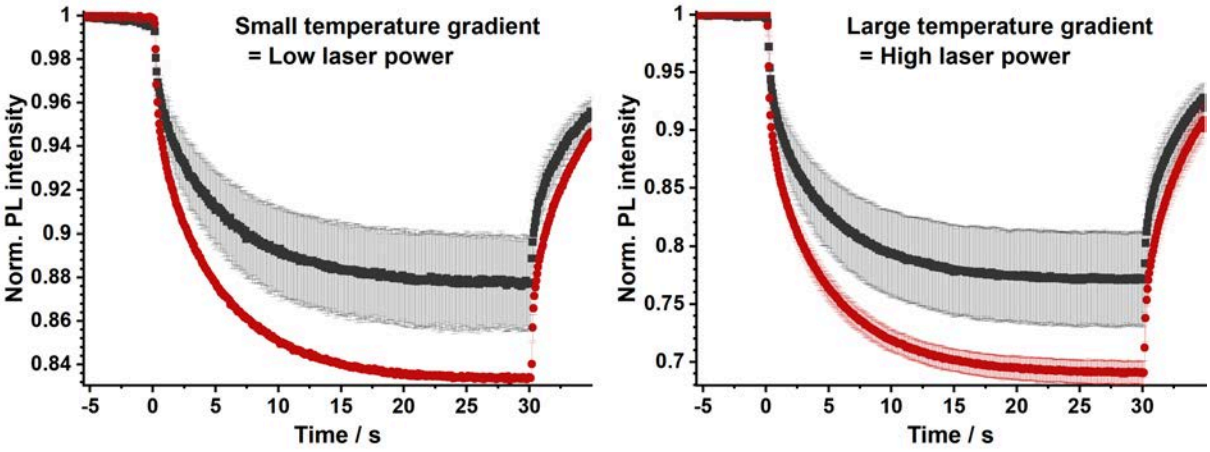

Figure S.5.: MST of TAMRA coupled to $NaYF_4$:$Yb_{[18\,mol\,\%]}$,$Er_{[2\,mol\,\%]}$ @ $NaYF_4$ UCNPs illustrating different diffusion speeds upon IR-laser irradiation to induce a temperature gradient. The TAMRA fluorescence is observed. Red bullets = uncoupled, free TAMRA; black bullets = TAMRA coupled to the UCNP.

S.3. Additional Figures and Illustrations

⟹ *continued on next page*

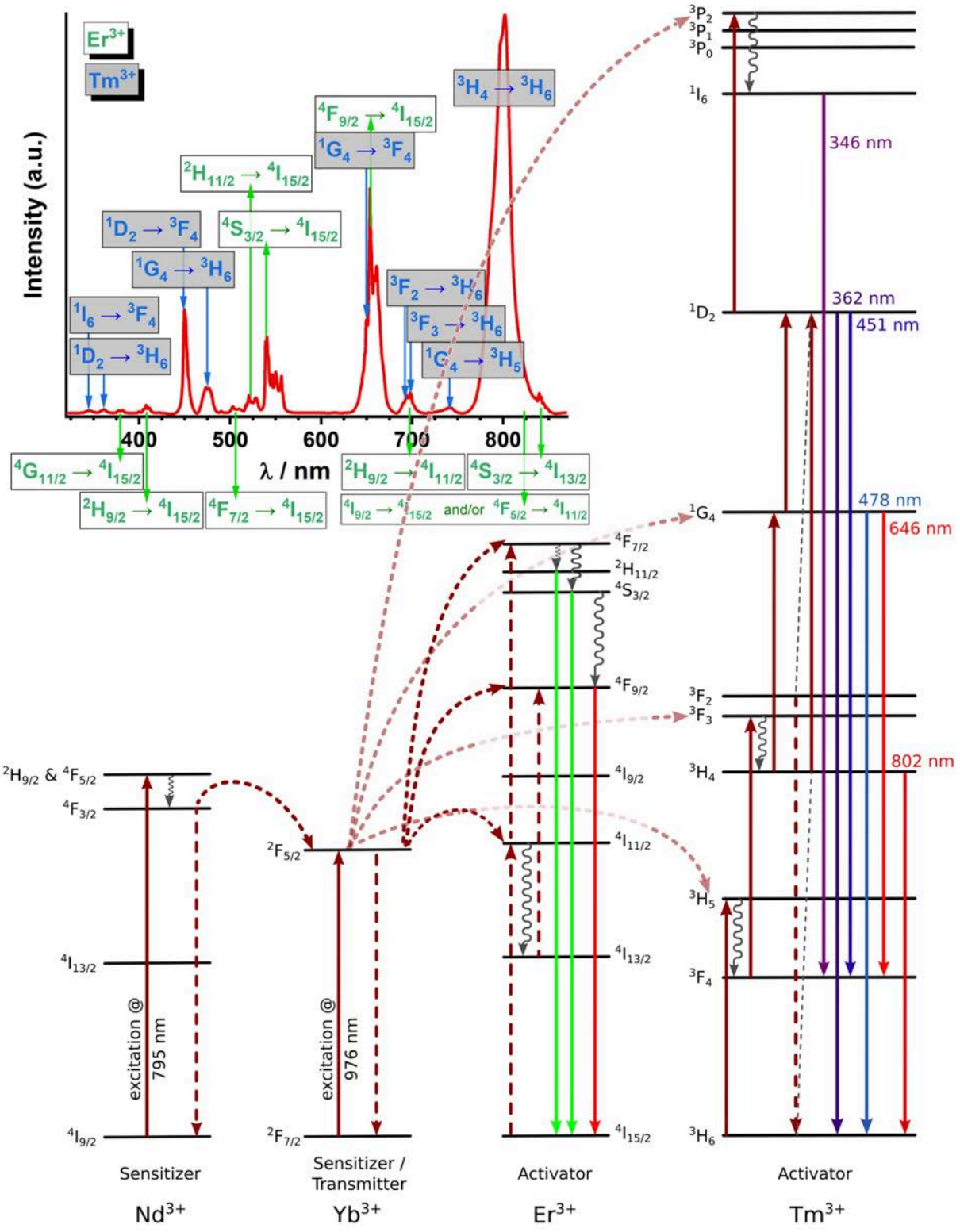

Figure S.6.: Energy transfer upconversion scheme with energy levels of the sensitizers Nd^{3+} and/or Yb^{3+} for 795 nm or 976 nm excitation, respectively. The upconversion luminescence spectrum in the top left corner is given for the activators Er^{3+} and Tm^{3+}. The energy levels are taken from Dieke's diagram showing free lanthanoid ion energy levels.[31,32]

Glossary of Acronyms

APTE	addition de photon par transfers d'énergie
CMP	bioinspired PG-CatPh coating polymer (customized mussel protein polymer)
DC	frequency downconversion
DI-water	deionized water
DLS	dynamic light scattering
DMSA	dimercaptosuccinic acid
ETU	energy transfer upconversion
FRET	Förster resonance energy transfer
IR	infrared light
Ln(III)	trivalent lanthanoid ions (cations)
LRET	(inter-) lanthanoid/lanthanide resonance energy transfer
MOPS	3-(N-morpholino)propanesulfonic acid
MRI	magnetic resonance imaging
MST	microscale thermosphoresis
NIR	near-infrared light
OA	oleic acid
PAA	polyacrylic acid
PBS	phosphate buffered saline
PDT	photodynamic therapy
PEG-PLGA	poly(ethylene glycol) methyl ether-*block*-poly(lactide-*co*-glycolide)
PL	photoluminescence emission (synonym = luminescence)
PMMA	poly(methyl methacrylate)
PSA	prostate serum albumin
RET	resonance energy transfer
SDG	sustainable development goal
SI	supporting information
TLS	total luminescence spectroscopy performed at 4 K
UC	frequency upconversion (process)
UCNP	frequency upconversion nanoparticle
UV	ultraviolet light
Vis	visible light

List of Figures

List of Tables

Declaration of Independence

(Selbstständigkeitserklärung)

I hereby confirm: The submitted work was carried out independently and only explicitly listed sources and means were used.

Furthermore, I confirm that this thesis has not been submitted elsewhere for the purpose of obtaining a doctoral degree.

(Hiermit versichere ich: Die vorliegende Arbeit wurde selbständig durchgeführt. Es wurden keine anderen Quellen und Hilfsmittel als die ausdrücklich aufgeführten verwendet.

Weiterhin versichere ich, dass diese Arbeit noch nicht an anderer Stelle zur Erlangung des Doktorgrades eingereicht worden ist.)

Place (Ort), Date (Datum)

Philipp U. Bastian